UPGRADES FOR AN IMPROVED MEASUREMENT OF THE PERMANENT ELECTRIC DIPOLE MOMENT OF RADIUM

By

Tenzin Rabga

A DISSERTATION

Submitted to
Michigan State University
in partial fulfillment of the requirements
for the degree of

Physics – Doctor of Philosophy

2020

ABSTRACT

UPGRADES FOR AN IMPROVED MEASUREMENT OF THE PERMANENT ELECTRIC DIPOLE MOMENT OF RADIUM

By

Tenzin Rabga

A non-zero Electric Dipole Moment (EDM) in a non-degenerate system violates time-reversal (T-)symmetry and consequently also charge-parity (CP-)symmetry. EDM measurements are therefore sensitive searches for new CP-violating interactions. The octupole deformation and nearly degenerate nuclear parity doublet in ^{225}Ra make it an attractive candidate for probing CP-violations in the hadronic sector. Our latest measurement limits the EDM of ^{225}Ra to be less than $1.4 \times 10^{-23} e \cdot \text{cm}$ (95%C.L.), and is the first ever measurement of an EDM limit using laser cooled and trapped atoms. Further experimental upgrades are being implemented to enhance the current EDM sensitivity for ^{225}Ra. This includes more than a factor of three enhancement in the electric field from our electrode upgrade, a STIRAP-based electron shelving for improved state detection efficiency, and an improved atom slowing scheme for enhancing our atom trapping efficiency by two orders of magnitude. With these upgrades in place our EDM sensitivity should increase by about three orders of magnitude and allow us to substantially improve constraints on certain CP-violating processes within the nucleus.

This work is supported by the U.S. DOE, Office of Science, Office of Nuclear Physics, under contract DE-AC02-06CH11357 and the Michigan State University.

ACKNOWLEDGEMENTS

TABLE OF CONTENTS

LIST OF TABLES

LIST OF FIGURES

CHAPTER 1

INTRODUCTION

"The most incomprehensible thing about the world is that it is comprehensible."

— Albert Einstein

Thomas Kuhn, in his *The Structure of Scientific Revolutions*, describes the history of scientific development as characterized by phases of what he calls "normal" and "revolutionary" sciences. The revolutionary science is qualitatively different from the normal science and is accompanied by short periods of drastic revisions of our existing scientific practices and assumptions that form the paradigm of scientific enquiry. These are often preceded by the inability of the prevailing scientific theories to address certain critical questions in the field. The new normal, developed following such a "paradigm shift", is markedly distinct from the former in many ways. At the outset, developments in the early twentieth century physics appear to have this characteristic. For instance, the failure of classical theories to explain, such phenomena as, the spectrum of the black body radiation, the photoelectric effect, the Compton effect, and generally the structure of atoms and the quantization of atomic emission lines, among others, led to the development of the quantum theory of radiation and matter. As evidenced by the subsequent - over half a century's worth of - physics research, it has irreversibly altered how we think of phenomena at the atomic and subatomic scales.

The quantum field theories that make up the standard model (SM) of particle physics, and Einstein's general theory of relativity, form the current paradigm through which we engage with and understand the physical Universe. As successful as they have been in elucidating many features of the microscopic as well as the macroscopic world, many fundamental questions still remain unaddressed and have so far evaded any signs of resolutions. It is reasonable to think that answers to these questions might lead to a type of revolutionary paradigm shift in physics witnessed early in the twentieth century. One such question that puzzles many physicists is the origin of the matter that constitutes the world around us. Our physical theories at the present moment, do not allow for a satisfactory explanation as to why our Universe is dominated by matter over its counterpart,

antimatter. It is strongly believed that the solution to this problem might lead to physics beyond the current paradigm of the standard model. This question and its implications for measurable properties of atomic and molecular systems called the electric dipole moment (EDM), motivate the subject matter of this thesis.

This thesis is divided into nine chapters. chapter 2 provides the essential overview of EDM search experiments and the fundamental questions that motivate their searches. chapter 3 motivates this particular experiment and provides the context for the radium EDM search experiment. In chapter 4, we outline the foundations of laser cooling and trapping of neutral atoms as applied for trapping radium atoms and elaborates of the different laser systems used in this experiment. In chapter 5, we highlight a broadband laser frequency stabilization technique that has found widespread application in our different laser systems and we show its application to precision spectrsocopy in radium. chapter 6 gives an overview of the experimental apparatus for measuring the radium EDM and reviews the latest results. chapter 7 and 8 elaborate on two upgrades currently underway for improving the limit on the measured atomic EDM of ^{225}Ra. These include the improvement of our detection efficiency and the upgrade to our atom slowing scheme for trapping more radium atoms. chapter 9 concludes this thesis and provides the outlook for future developments.

CHAPTER 2

WHY SEARCH FOR ELECTRIC DIPOLE MOMENTS?

This chapter explains the motivation behind electric dipole moment (EDM) search experiments, emphasizing the role they play in probing some of the most fundamental questions we can ask of our physical theories. It also provides an overview of the current status of the various EDM search experiments in a number of different systems.

2.1 The Matter-Antimatter Asymmetry

In his seminal paper published in 1928[1], Paul Dirac introduced - what is now known as - the Dirac equation for describing the quantum electrodynamics of spin-1/2 particles such as an electron. It was immediately noted that the equation predicted the presence of a particle with exactly the same mass as an electron, the same spin quantum number, but with the opposite electric charge. This particle, called the positron, was experimentally observed by Carl Anderson in 1932[2] and was recognized as Dirac's anti-electron. Since then, a plethora of antiparticles have been observed and their existence has been recognized as a necessary consequence of uniting quantum mechanics with special relativity. Although produced and observed in laboratory settings, in the natural world, there is almost no evidence of antimatter. Moreover, from astronomical observations, our visible Universe appears to be matter dominated. One of the most compelling evidence for this is provided by the seven year Wilkinson Microwave Anisotropy Probe (WMAP7) observation data that studied the power spectrum of the temperature fluctuations in the cosmic microwave background (CMB)[3]. The matter-antimatter asymmetry, or the baryon asymmetry of the Universe (BAU) can be quantified by the ratio of the difference between the number of baryons (N_B) and antibaryons ($N_{\bar{B}}$) to the number of photons (N_γ):

$$\eta = \frac{N_B - N_{\bar{B}}}{N_\gamma} \tag{2.1}$$

The WMAP7 data alone gives

$$\eta_{\mathrm{CMB}}/10^{-10} = 6.160^{+0.153}_{-0.156} \tag{2.2}$$

That this number is non-zero points to one of two things. Either the Universe began with an initial condition that was baryon-antibaryon number asymmetric, or certain dynamical processes led the Universe into a matter dominated state. Assuming the latter - and there are good reasons to believe this is more likely - then the natural question to ask is what are the conditions necessary for baryogenesis in the early Universe? Andrei Sakharov in 1967, enumerated a set of conditions that would have to be present in the early Universe for successful baryogenesis[4]. These are:

1. Baryon number violating processes
2. Mechanisms for *C*- and *CP*-violation
3. Departure from thermal equilibrium

As will be elaborated later in this chapter, violations of fundamental symmetries has been observed already. In fact, the weak nuclear force is known to violate both *C*- and *CP*- symmetries. However, the amount of *CP*-violation allowed in the Standard Model (SM) is not sufficient to account for the observed BAU[5].

This is where the EDM search experiments play an important role. They provide us with unique avenues for identifying new sources of *CP*-violations in nature and potentially help us understand why our Universe is dominated by matter. But before we get to EDMs, we elaborate a little on the different discrete symmetries of our physical theories and their observed violations.

2.2 *P*-Violation

It is reasonable to expect our physical theories to be invariant under an inversion of our physical dimensions. There should be no way of distinguishing the two parity (*P*) states (inverted and the non-inverted) states solely on the basis of the physical laws. Although this is true for the gravitational, electromagnetic and the strong nuclear forces, it was not clear if this was also true for

the weak interaction. In fact, this led Lee and Yang, in 1956, to propose a test of *P*-conservation in weak nuclear force[6]. This experiment was carried out by C.S. Wu later that year[7]. In her famous experiment, she studied the beta decay of spin polarized radioactive ^{60}Co nuclei. The nuclei were prepared to have their spins aligned along a specific direction. Her group observed that after the decay the electrons were preferentially ejected along the direction of the nuclear spin. Clearly, under a parity transformation, the nuclear spin, being an axial vector, remains unchanged, while the direction of the electrons emitted is spatially inverted. This then suggests in this "mirror" image, the electrons are preferentially ejected in the direction opposite to the nuclear spin. If parity was conserved under the weak interaction, we should therefore observe an isotropic distribution of the ejected electrons. The observation of anisotropy in the emitted electrons was a clear indication of *P*-violation in the weak interaction. In fact, parity is maximally violated by the weak interaction, as shown by the fact that all the observed neutrinos are left-handed and all the antineutrinos are right-handed.

2.3 *C*-Violation

Charge (*C*) conjugation refers to the reversal of all the signs of the charges of a particle. Here, by charges we refer not only to the electric charge, but also to the baryon number, lepton number, strangeness, charm, bottom, and top. Essentially the charge conjugation operator turns a particle into its antiparticle, and vice versa. *C*-symmetry refers to the fact that a physical theory is invariant under charge conjugation. This happens to be true for the gravitational, electromagnetic and the strong interactions. However, the weak interaction violates *C*-symmetry. As noted in the previous paragraph, so far we have only observed left-handed neutrinos. Under the charge conjugation operator, we turn a left-handed neutrino into a left-handed antineutrino, which does not exists in nature. Hence, the weak interaction is said to maximally violate *C*-symmetry as well.

2.4 *CP*-Violation

The simultaneous violations of charge conjugation (C) and parity (P) symmetries in the weak interaction led Lev Landau, in 1957, to propose that the weak interactions are invariant under the combined operation of *CP*-transformation - what he called the "combined inversion"[8]. In fact, the cleanest example is provided by the emission of an antimuon in a pion decay.

$$\pi^+ \rightarrow \mu^+ + \nu_\mu \tag{2.3}$$

Here, all the antimuons produced are observed to be left-handed. Under the operation of the *CP*-transformation, we get the following process

$$\pi^- \rightarrow \mu^- + \bar{\nu}_\mu \tag{2.4}$$

This predicts the emission of right-handed muons in the decay of an antipion, as is observed. So may be, *CP*-symmetry is what is actually preserved by all the interactions, and when we speak of the "mirror" image of a process, we ought to invert not only the spatial directions but also the charges of the particles involved.

If *CP* were a conserved symmetry, it would have important implications for the decay of neutral K mesons. Gell-Mann and Pais in their 1955 paper showed that this meant the weak interaction allowed K^0 to turn into its antiparticle $\bar{K}^0$[9]. This implies that these are not the neutral K mesons observed in the laboratories, but some linear combination of the two. In fact, we can create the following linear combinations that are eigenstates of *CP*:

$$|K_1\rangle = \frac{1}{\sqrt{2}}\left(\left|K^0\right\rangle - \left|\bar{K}^0\right\rangle\right) \tag{2.5}$$

$$|K_2\rangle = \frac{1}{\sqrt{2}}\left(\left|K^0\right\rangle + \left|\bar{K}^0\right\rangle\right) \tag{2.6}$$

such that

$$CP\,|K_1\rangle = |K_1\rangle \tag{2.7}$$

$$CP\,|K_2\rangle = -\,|K_2\rangle \tag{2.8}$$

$$\tag{2.9}$$

Now if CP were a good symmetry of the weak interaction, K_1 should decay into products with a total $CP = +1$, and K_2 should decay into products with a total $CP = -1$. It is well known that the neutral kaons decay into two or three pions. the two pions carry a total CP of +1, while three pions have a total CP of -1. This means, K_1 decays into 2π while K_2 decays into 3π. Since the decay of K_1 releases more energy, it has a significantly shorter lifetime than K_2. This implies that if we begin with a beam of neutral kaons, $\left|K^0\right\rangle = \left(|K_1\rangle + |K_2\rangle\right)/\sqrt{2}$, the K_1s should decay rapidly and sufficiently far down the beamline, we should only observe K_2s. This would mean, we should only observe 3π events down the beamline. In short, if we create a long enough beam of the neutral kaons, we should have a pure beam of the long-lived K_2s by the end. This was put to test by Cronin and Fitch in 1964[10]. What they observed at the end of their 57 feet long beam line is about 45 two pion events in a total of 22,700 decays. This meant that the beam contained some amount of the short-lived kaons K_1. This was the first indication that CP is in fact, violated in weak interactions.

2.5 *T*-Violation, the *CPT* Theorem and EDMs

Let's consider a simple process. Two balls start off in certain initial states, collide elastically and end up in their respective final states. It would seem obvious that the laws of collisions should be the same whether we run the movie forward or in reverse. In other words, just by studying the physical process of collision, we would not be able to identify the "initial" states of the balls. Such a process, and therefore the underlying physical laws, are said to be symmetric under the reversal of the direction of time. It was thought that this should be true of all physical interactions, that T-symmetry was conserved by all processes in nature. Now, from the CPT theorem we know that all the interactions as described in the Standard Model are invariant under the combined action of C, P and T transformations. This is one of the most fundamental results in quantum field theory - a

consequence of the requirement that the quantum field theories be Lorentz invariant. The observed *CP*-violation in the weak interactions therefore implies a compensating amount of *T*-violation. This was therefore taken as an indirect evidence for *T*-violation. However, more recently, direct observations of *T*-violations have been made, for instance, by the BaBar collaboration in the decay of B mesons[11].

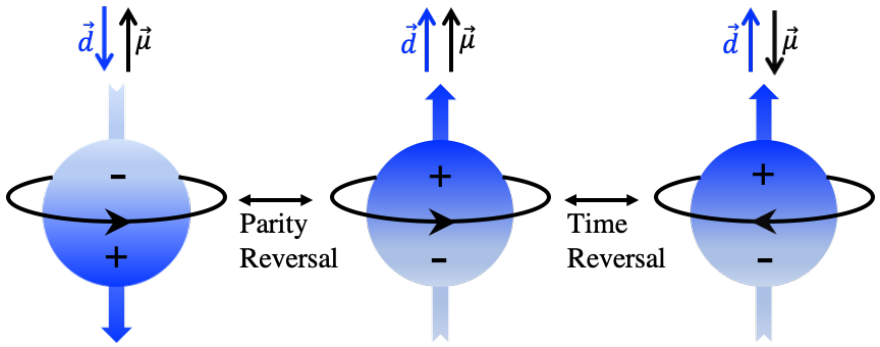

Figure 2.1: Figure depicting how a non-degenerate system with a permanent EDM $\vec{d}$ and a magnetic moment $\vec{\mu} \propto \vec{S}$ behave under parity and time-reversal transformations. The presence of the non-zero EDM violates both *P*- and *T*-symmetry.

We now introduce our quantity of interest, the electric dipole moment (EDM). Suppose, as shown in Fig. 2.1, a particle, that represents a non-degenerate system, has a non-zero, permanent EDM, $\vec{d}$, and a non-zero spin $\vec{S}$ ($\vec{S} \propto \vec{\mu}$). It is easy to see that the only component of the EDM that is non-zero is the component that lies along the direction of the spin

$$\vec{d} = d\frac{\vec{S}}{S} \tag{2.10}$$

where $d = |d|$, and $S = |S|$. The interaction of the EDM with an external electric field $\vec{E}$ is given by

$$\begin{aligned} H_{EDM} &= -\vec{d} \cdot \vec{E} \\ &= -d\frac{\vec{S}}{S} \cdot \vec{E} \end{aligned} \tag{2.11}$$

The behavior of this interaction under the different symmetry transformations is determined by the dot-product $\vec{S} \cdot \vec{E}$. We notice that the spin $\vec{S}$ is even under a parity transformation, but odd under

a time reversal transformation. The electric field $\vec{E}$ on the other hand is odd under P, and even under T. Clearly, this interaction, and therefore the presence of a non-zero EDM, violates both P- and T-symmetries. Given that CPT is a conserved symmetry, the existence of EDMs also implies CP-violation.

The CP-violation as present in the Standard Model comes predominantly from the weak sector, and in particular from the quark mixing, Cabibbo-Kobayashi-Maskawa (CKM) matrix. The resultant SM predictions for the EDMs in the different systems are many orders of magnitude smaller than the current experimental limits[12]. Therefore, any observation of a non-zero EDM would be a SM "background" free signature of CP-violation and potentially point towards physics beyond the SM (BSM).

2.6 Measuring an EDM

Given their importance, how do we then measure an EDM? As a rule of thumb, when trying to measure a very small quantity, it is advisable that we convert it into a property of a system we can measure the most precisely. One of the things we can measure the most precisely happens to be frequency. In Arthur Schawlow's own words, "Never measure anything but frequency!"[13] Which is why we often observe that EDM experiments such as the radium EDM experiment relate the EDM to some frequency of the system that can be measured. To illustrate this, let's assume we want to measure the EDM of a neutral atom in its ground state. Suppose the ground state has a total angular momentum $F = 1/2$. The atom has a magnetic moment $\vec{\mu}$ that precesses in the presence of an external magnetic field $\vec{B}$. The precession frequency ω is given by

$$\hbar\omega = 2\mu B \tag{2.12}$$

Now, suppose the atom has a non-zero EDM $\vec{d}$. It couples to an external electric field E to create a vector shift in the precession frequency. The sign of the shift depends on whether the electric field is parallel (+) or antiparallel (−) to the magnetic field. The precession frequency is

therefore given by

$$\hbar\omega_{\pm} = 2\mu B \pm 2dE \tag{2.13}$$

The quantity of interest, the EDM d is given by

$$d = \frac{\hbar\Delta\omega}{4E} \tag{2.14}$$

where $\Delta\omega = \omega_{+} - \omega_{-}$ is the EDM induced frequency shift.

2.7 Current Best Limits on EDMs in Different Systems

In this section, we give a brief overview of the EDM search experiments conducted in a number of different systems, probing different sources of SM and BSM *CP*-violations. Although EDM limits have been placed on other particles such as, the muon[14], tau[15], and Λ[16], we focus primarily on the EDM searches in the neutron, and in paramagnetic and diamagnetic atoms and molecules, as currently these are the most active sectors for EDM search experiments. However, we note that the search for a non-zero EDM is an actively growing area of research and more experiments are expected to emerge in the near future.

2.7.1 The EDM Unit

For historical reasons, the EDM limits in the experimental searches are cited with the unit $e \cdot$ cm. Here, $e = 1.602 \times 10^{-19}$ C is the elementary electric charge. Therefore, $1\, e \cdot$ cm is the electric dipole moment of two charges (e and $-e$) displaced by 1 cm with respect to each other.

2.7.2 Neutron EDM

EDM search experiments have a 70 years long history. It began in 1950, when Ramsey and Purcell proposed an experiment for measuring the neutron's EDM[17]. Although their experiment was initially motivated as a test of parity conservation, they also noted that a neutron EDM would be

forbidden by time reversal symmetry. In 1957, their experiment at Oak Ridge National Laboratory yielded the first limit on the size of the neutron EDM[18]. They found that their measurement was consistent with zero, and limited the size of the neutron EDM to be $|d_n| < 5 \times 10^{-20} e \cdot \text{cm}$. The experimental sensitivity of the neutron EDM measurement is predominantly limited by the motion of the neutrons. Initially thermal beams of neutrons were used, which were later replaced by ultra cold neutrons (UCNs) that helped reduce the motional systematic effects. Since the first measurement, several more experiments have further improved the limit, with the current best limit at $|d_n| < 1.8 \times 10^{-26} e \cdot \text{cm}$ (90% C.L.), obtained by the nEDM experiment at the Paul Scherrer Institute (PSI) [19]. Several other experiments such as at the Spallation Neutron Source at Oak Ridge National Laboratory, and at the Paul Scherer Institute in Switzerland are also attempting to further improve the neutron EDM measurement. The current limit on the size of neutron EDM is still ~ 6 orders of magnitude greater than the SM prediction.

2.7.3 Electron EDM

The electron EDM search experiments are generally conducted in paramagnetic species. The presence of the unpaired electron ensures that the shielding of the electron EDM from the externally applied field is imperfect. So far all the measurements of the electron EDM are consistent with zero. In the SM the electron EDM arises at the four-loop level and is therefore extremely suppressed and predicted to be $\sim 10^{-38} e \cdot \text{cm}$. Most of the electron EDM search experiments use polar molecules such as YbF[20], ThO[21], HfF^+[22]. Such molecules provide highly enhanced internal effective electric fields (on the scales of 100GV/cm) for moderate levels of applied external fields. Currently the best limit on the size of the electron EDM is set by the ACME collaboration, where they use a beam of ThO molecules to set the electron EDM to be $|d_e| < 1.1 \times 10^{-29} e \cdot \text{cm}$ (90% C.L.)[21], which is still many orders of magnitude larger than the SM limit.

2.7.4 Diamagnetic Atomic EDM

The diamagnetic atoms probe the hadronic contribution to an EDM and therefore *CP*-violation. Due to the paired electrons, the contribution from the electron EDM is greatly suppresed. An EDM of a diamagnetic atom d_A arises predominantly from the nuclear Schiff moment, and the EDMs of the individual nucleons, and the nuclear-spin-dependent electron-nucleon interactions[23].

$$d_A = \kappa_S S - [k_T^{(0)} C_T^{(0)} + k_T^{(1)} C_T^{(1)}] \tag{2.15}$$

where S, $C_T^{(0)}$, and $C_T^{(1)}$ are the nuclear Schiff moment, the isoscalar and the isovector electron-quark interaction terms. The coefficients κ_S, $k_T^{(0)}$, and $k_T^{(1)}$ are the respective sensitivities of the atomic EDM to these terms. The Schiff moment - described in detail in the next chapter - can be expressed in terms of the contributions from the EDMs of the individual unpaired nucleons (d_p, d_n), as well as the long-range pion-nucleon couplings ($\bar{g}_\pi^{(0)}$, $\bar{g}_\pi^{(1)}$) as

$$S = a_p d_p + a_n d_n + a_0 \bar{g}_\pi^{(0)} + a_1 \bar{g}_\pi^{(1)} \tag{2.16}$$

As can be seen from the above discussion, the EDM of a diamagnetic atom has a complicated dependence on the underlying *CP*-violating physics. This makes the interpretation of the EDM limits on diamagnetic species heavily reliant on the precision of the nuclear and atomic theory calculations and the theoretical uncertainties on the coefficient of the various *CP*-violating parameters (for example, the coefficient as in Eq. 2.16).

Currently, the best limit on the EDM of a diamagnetic atom comes from the ^{199}Hg experiment at U. Washington at Seattle. They limit the atomic EDM of ^{199}Hg to be $\left|d_{\mathrm{Hg}}\right| < 7.4 \times 10^{-30} e \cdot$ cm (95%C.L.)[24]. This, along with the limit on the size of the neutron EDM sets a stringent limit on the amount of *CP*-violation allowed in the strong interaction. The strong interaction allows for *CP*-violation via the $\theta-$term in the QCD lagrangian[23]:

$$\mathcal{L}_{\bar{\theta}} = -\frac{\alpha_S}{16\pi^2} \bar{\theta} \mathrm{Tr}(G^{\mu\nu} \tilde{G}_{\mu\nu}) \tag{2.17}$$

where α_S is the strong coupling constant. $G^{\mu\nu}$ is the gluon field with a dual given by $\tilde{G}_{\mu\nu}$. The limits on the neutron EDM, and the ^{199}Hg atomic EDM limit the dimensionless parameter $\bar{\theta} < 10^{-10}$. That this $CP-$violating parameter in the strong interaction is so "unnaturally" small is referred to as the "strong CP problem". Famously, as a solution to this, Peccei and Quinn postulated the existence of a scalar (axion) field with a non-zero vacuum expectation value which allows the $\bar{\theta}$ term to vanish and therefore conserves the *CP*-symmetry in strong interactions[25]. However, such a particle is yet to be observed in nature and therefore this problem still remains unresolved.

2.8 Interpreting the EDM Limits

Fig. 2.2 shows how the measurable atomic and molecular EDMs relate to the different *CP*-violating parameters at different energy scales, and eventually to the underlying fundamental SM ($\bar{\theta}$, CKM) and BSM (SUSY, Multi-Higgs, LR-symmetry) physics. As can be seen, for most of the experiments that probe atoms and molecules, the EDM of the system depends on many different *CP*-violating parameters. For instance, the EDM of a diamagnetic atom/molecule depends on the tensor electron-nucleon interaction parameter (C_T), as well as the nuclear Schiff moment, which in turn depends on the individual EDMs of the nucleons as well as the pion-nucleon couplings ($\bar{g}_\pi^{(0)}$, $\bar{g}_\pi^{(1)}$, $\bar{g}_\pi^{(2)}$). Although heavily suppressed, it also depends on the scalar electron-nucleon coupling (C_S) and the electron EDM (d_e). This then raises the question; having measured the limit on the EDM of one of these species, how do we interpret the contributions from the underlying *CP*-violating parameters? The traditional method has been to use the "sole-source" assumption. Given the measured limit on the EDM of a system, one assumes that the contribution comes entirely from one of the underlying parameters. This is then used to set the limits on the maximum size of the *CP*-violating parameters. This model-dependent "single-source" analysis however, ignores the possible correlations between the contributions from the different *CP*-violating parameters. To address this, Chupp & Ramsey-Musolf [26] developed a model-independent, "global analysis" of EDM searches. In this, simultaneous limits are set on the set of six parameters that contribute to the EDM: d_e, C_S, C_T, $\bar{g}_\pi^{(0)}$, $\bar{g}_\pi^{(1)}$, and the short-range component of the neutron EDM $\bar{d}_n^{\mathrm{sr}}$.

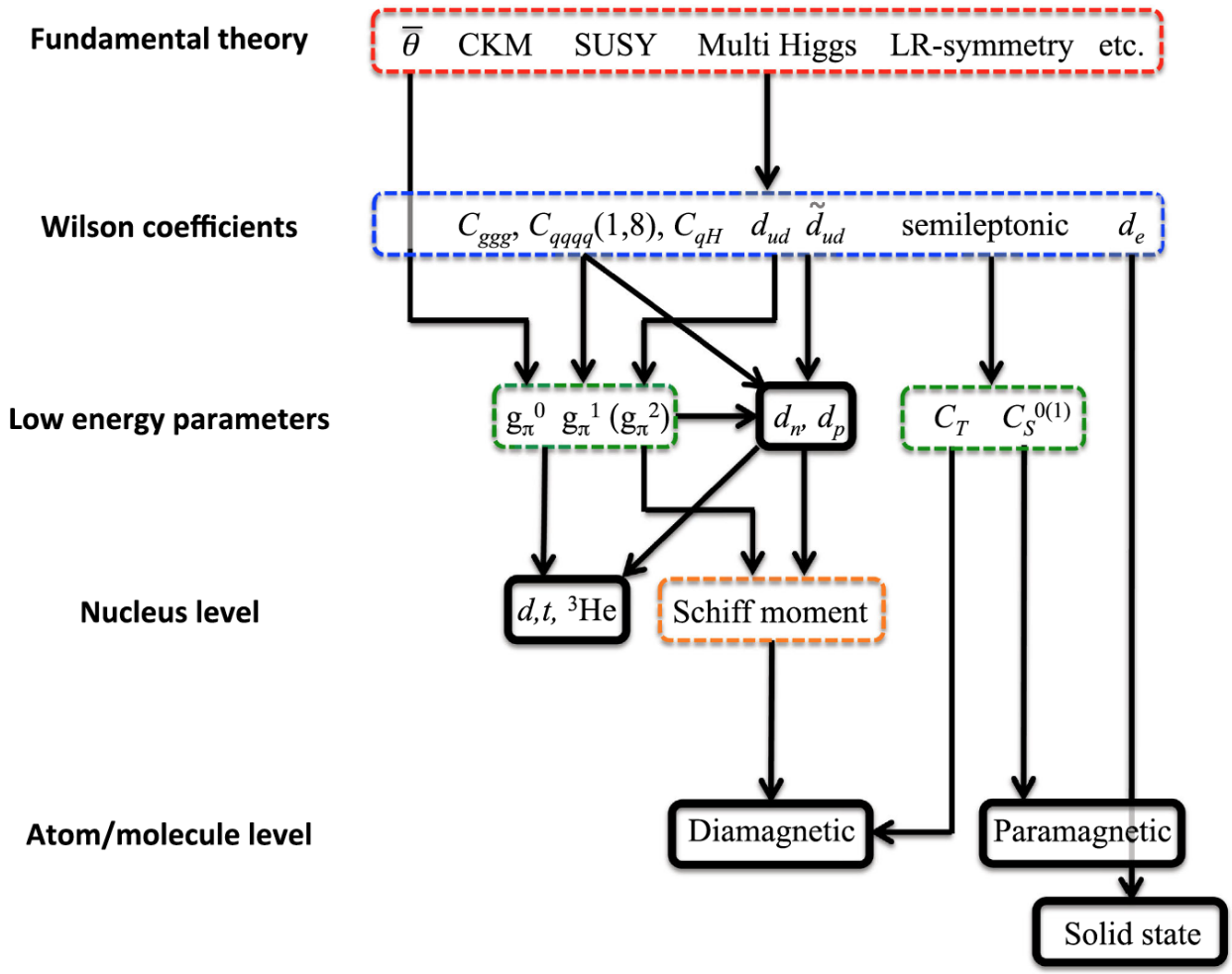

Figure 2.2: The dependence of the observable atomic/molecular EDMs to the different underlying *CP*-violating mechanisms. The low energy parameters connect the experimental limits on the EDMs to the allowed fundamental *CP*-violating SM and BSM theories. The paramagnetic sytems probe the contributions from the electron EDM d_e and the scalar electron-nucleon coupling (C_S), and the diamagnetic systems probe the hadronic contributions to the EDM from the individual nucleon EDMs (d_n, d_p), the tensor electron-nucleon coupling (C_T), the nuclear Schiff moment (S), and the long-range pion-nucleon couplings ($\bar{g}_\pi^{(0)}$, $\bar{g}_\pi^{(1)}$). Figure taken from Ref. [23]

The constraints on the electron EDM 'd_e' and the scalar electron-nucleon interaction parameter, 'C_S' are set by the paramagnetic experiments that are most sensitive to these parameters. The diagmagnetic systems set the bounds on the other four hadronic parameters. To estimate the range

of allowed values that these four parameters can take, a χ^2 is defined as

$$\chi^2(C_j) = \sum_i \frac{\left(d_i^{\rm exp} - d_i\right)^2}{\sigma^2_{d_i^{\rm exp}}} \tag{2.18}$$

where $d_i^{\rm exp}$ are the experimentally determined central value of the size of the EDM in each system, with total uncertainties $\sigma_{d_i^{\rm exp}}$. The theoretically calculated values of the EDMs in each system is given by

$$d_i = \sum_j \alpha_{ij} C_j \tag{2.19}$$

where C_j are the four hadronic *CP*-violating parameters, and $\alpha_{ij} = \frac{\partial d_i}{\partial C_j}$ rely on the atomic and nuclear calculations that relate the underlying *CP*-violating parameters to the observable EDM. In their analysis, Chupp *et al.* [23] consider the four of five experiments probing hadronic sources of *CP*-violation: neutron, ^{199}Hg, ^{129}Xe, and ^{225}Ra EDM experiments. Inverting the matrix α_{ij}, they determine the sensitivity of the different experiments to the various *CP*-violating parameters.

$$\begin{pmatrix} \bar{d}_n^{\rm sr} \\ \bar{g}_\pi^{(0)} \\ \bar{g}_\pi^{(1)} \\ C_T \end{pmatrix} = \begin{pmatrix} 5.2 & 4.7\times10^4 & 9.5\times10^3 & 21 \\ -2.8\times10^{14} & -3.1\times10^{18} & -6.3\times10^{17} & -1.4\times10^{15} \\ -7.0\times10^{13} & -7.7\times10^{17} & -1.6\times10^{17} & -4.8\times10^{14} \\ 1.9\times10^{16} & 1.4\times10^{19} & 3.6\times10^{19} & 8.4\times10^{16} \end{pmatrix} \begin{pmatrix} d_n \\ d_{\rm Xe} \\ d_{\rm Hg} \\ d_{\rm Ra} \end{pmatrix} \tag{2.20}$$

where they take the best values of the α_{ij} parameters as given in Table IV of Ref. [23], with $\alpha_{{\rm Hg},\bar{g}_\pi^{(1)}} = 1.6\times10^{-17}$ and $\alpha_{{\rm Ra},\bar{d}_n^{\rm sr}} = -8\times10^{-4}$.

As a consequence of this cumulative analysis, as can be seen from the above equation, there is significant correlation between the bounds set on the different parameters. Therefore the limits on the parameter sizes from the "global analysis" is slightly less stringent than a purely "sole-source" treatment. This also highlights the complementary nature of the different EDM search experiments. In the case of the diamagnetic species, at the current level of experimental limits, ^{225}Ra and ^{129}Xe

have similar sensitivities to the underlying *CP*-violation. Moreover, improving the experimental limit on the EDM of one of the systems helps improve the impact of the others [26].

CHAPTER 3

MOTIVATING THE RADIUM EDM SEARCH EXPERIMENT

This chapter motivates the radium EDM search experiment. As a diamagnetic atom, as explained in the previous chapter, ^{225}Ra is sensitive to the hadronic contributions to the EDM and therefore the underlying *CP*-violating physics. We elaborate on the advantages and challenges associated with using ^{225}Ra for an EDM experiment. Its enhanced nuclear Schiff moment makes it particularly sensitive to hadronic sources of *CP*-violation, while its short half-life, low supply and low vapor pressure make it challening to work with.

3.1 The Nuclear Schiff Moment

Unlike elementary particles, the EDM of an atomic nucleus is shielded from detection by the surrounding electron cloud. This is famously known as the 'Schiff Theorem'[27], which in essence states that under the limit of a point-like, non-relativistic nucleus, under the influence of the electrostatic interaction, the electron cloud rearranges itself - in response to the nuclear EDM - in such as way as to cancel it, resulting in a zero net atomic EDM. To illustrate this shielding, we follow the treatment as outlined in Ref. [12]. Consider a non-relativistic, structure-less system (electrons and nucleus) held together by the electrostatic interaction $V(r)$. The atomic Hamiltonian is then given by

$$H = \sum_j \frac{p_j^2}{2m_j} + \sum_j V(\vec{r}_j) - \sum_j \vec{d}_j \cdot \vec{E}_j \tag{3.1}$$

$$= H_0 + \sum_j \frac{1}{e_j} \vec{d}_j \cdot \vec{\boldsymbol{\nabla}} V(\vec{r}_j) \tag{3.2}$$

$$= H_0 + i \sum_j \frac{1}{e_j} \left[\vec{d}_j \cdot \vec{p}_j, H_0 \right] \tag{3.3}$$

where p_j, r_j, e_j, and d_j are the respective momentum, coordinate, charge and the EDM of each constituent component (nucleus and the electrons). In the above derivation, H_0 - comprising

of the kinectic and the Coulomb interaction terms - is the unperturbed atomic Hamiltonian, and the interaction of the EDM with the electric field E is taken to be the perturbation to the system and therefore much smaller than the Coulomb interaction.

Using first order perturbation theory, we can calculate the collective dipole moment $\vec{d}'$ induced by this perturbation in the ground state of the system.

The first order shift to the unperturbed ground state $|g\rangle$ is given by

$$|g\rangle' = |g\rangle + \sum_k \frac{|k\rangle \langle k| \, i \sum_j \frac{1}{e_j} \left[\vec{d}_j \cdot \vec{p}_j, H_0\right] |g\rangle}{E_g - E_k} \tag{3.4}$$

$$= |g\rangle + \sum_k \frac{|k\rangle \langle k| \, i \sum_j \frac{1}{e_j} \vec{d}_j \cdot \vec{p}_j \, |g\rangle \, (E_g - E_k)}{E_g - E_k} \tag{3.5}$$

$$= \left(1 + i \sum_j \frac{1}{e_j} \vec{d}_j \cdot \vec{p}_j\right) |g\rangle \tag{3.6}$$

The induced dipole moment $\vec{d}'$ in this perturbed ground state is given by

$$\vec{d}' = \langle g|' \sum_j e_j \vec{r}_j \, |g\rangle' \tag{3.7}$$

$$= \langle g| \left(1 - i \sum_k \frac{1}{e_k} \vec{d}_k \cdot \vec{p}_k\right) \sum_j e_j \vec{r}_j \left(1 + i \sum_l \frac{1}{e_l} \vec{d}_l \cdot \vec{p}_l\right) |g\rangle \tag{3.8}$$

$$= i \langle g| \left[\sum_j e_j \vec{r}_j, \sum_k \frac{1}{e_k} \vec{d}_k \cdot \vec{p}_k\right] |g\rangle \tag{3.9}$$

$$= - \langle g| \sum_k \vec{d}_k \, |g\rangle = -\vec{d} \tag{3.10}$$

As we can see, the induced dipole moment is equal and opposite to the total permanent dipole moment of the system, resulting in a total zero net EDM.

However, it was shown that this cancellation is incomplete when the finite size of the nucleus, and the relativistic electrons are taken into account [27–29]. The lowest order component of the

T-, *P*- odd nuclear electromagnetic potential that survives this shielding and therefore contributes to the atomic EDM is called the 'Schiff moment'. It can be written as

$$\vec{S} = \frac{1}{10}\int \left(r^2\vec{r} - \frac{5}{3}\left\langle r^2\right\rangle_{\text{ch}}\vec{r}\right)\rho(\vec{r})d^3\vec{r} \tag{3.11}$$

where $\rho(\vec{r})$ is the ground state nuclear charge density, and $\left\langle r^2\right\rangle_{\text{ch}}$ is the nuclear charge mean square radius.

3.2 Enhanced Schiff Moment in ^{225}Ra

We now focus our attention on nuclei with static octupole deformation in their nuclear structure, and illustrate how a measurable collective nuclear Schiff moment is generated. As shown in Ref. [30], in the body-fixed frame of the nucleus, it can have collective *P*-,*T*- odd moments, such as the Schiff moment, even without any *P*-,*T*-violating forces. However, in the absence of such interactions, in the laboratory frame, the Schiff moment vanishes. The reason for this is as follows. The intrinsic Schiff moment - oriented along the nuclear axis $\hat{n}$ - is given by $\vec{S}_{int} = S_{int}\hat{n}$. In the laboratory frame, a nucleus with a non-zero spin $\vec{I}$, has no preferred orientation. This means, in the laboratory frame, to have a non-zero Schiff moment, we require $\hat{n} \propto \vec{I}$, which violates both *P*-,*T*-symmetry.

Take for instance the ground state parity doublets observed in reflection asymmetric nuclei. These states have the same angular momenta but opposite parities, and can be expressed as

$$|\Psi_\pm\rangle = \frac{1}{\sqrt{2}}\left(|IM,+K\rangle \pm |IM,-K\rangle\right) \tag{3.12}$$

where I is the nuclear spin with z-component M. $K = \vec{I}\cdot\hat{n}$ is the projection of the nuclear axis along the spin quantization. As can be seen, $\langle\Psi_\pm|K|\Psi_\pm\rangle = 0$, and so there is no net orientation of the nuclear axis in the laboratory frame.

However, in the presence of a *P*-,*T*- odd interaction, due to the mixing of the parity doublet states, there is a non-zero average orientation of the nuclear axis along the nuclear spin, $\langle\hat{n}\rangle \neq 0$. The

T-,P- violating interaction V_{PT}, for instance, creates an admixed state, $|\Psi\rangle$, that is predominantly the positive parity state with a small mixture of the negative parity state

$$|\Psi\rangle = \Psi_+ + \alpha\Psi_- \tag{3.13}$$

where α is the parity mixing amplitude given by

$$\alpha = \frac{\langle\Psi_+|V_{PT}|\Psi_-\rangle}{E_+ - E_-} \tag{3.14}$$

The average-value of the nuclear axis vector is non-zero and given by

$$\langle n\rangle = 2\alpha\frac{KM}{I(I+1)} \tag{3.15}$$

The resultant Schiff moment in the laboratory frame is therefore non-zero and given by

$$S = S_{int}\,\langle n\rangle = 2\alpha\frac{KM}{I(I+1)}S_{int} \tag{3.16}$$

The electrostatic potential generated by the Schiff moment then generates the atomic EDM that can be measured in diamagnetic systems.

Given the above formulation of the nuclear Schiff moment, there are two main reasons that make ^{225}Ra particularly sensitive to this quantity and therefore the atomic EDM generated by it.

First, due to nuclear octupole deformation in its nuclear structure, the intrinsic Schiff moment, S_{int}, in ^{225}Ra is significantly larger than other more symmetric nuclei, such as ^{199}Hg. Second, the presence of the nearly-degenerate rotational parity doublet in the ground state of ^{225}Ra enhances the parity mixing amplitude α.

3.2.1 Nuclear Octupole Deformation

It has been noted that the collective Schiff moment in nuclei with octupole deformation may be two to three orders of magnitude larger than in spherically symmetric nuclei. In fact, the deformation need not even be static. Soft octupole vibrational modes in heavy nuclei are suspected to lead to similar enhancements in the Schiff moment [31].

To see how the nuclear octupole deformation leads to an enhanced Schiff moment, we follow the treatment presented in Ref.[31]. The surface of an axis symmetric deformed nucleus can be written in terms of the spherical harmonics Y_{l0} as

$$R(\theta) = R\left(1 + \sum_{l=1} \beta_l Y_{l0}(\theta)\right) \tag{3.17}$$

where β_l is the $l-$th multipole deformation parameter. β_3 for instance is the octupole deformation parameter. To ensure that the electric dipole moment vanishes, $e\,\langle\vec{r}\rangle = 0$, we require that the center of the charge distribution coincides with the center of mass (as required by the Schiff theorem). This fixes the parameter β_1 to be

$$\beta_1 = -3\sqrt{\frac{3}{4\pi}} \sum l = 2\frac{(l+1)\beta_l\beta_{l+1}}{\sqrt{(2l+1)(2l+3)}} \tag{3.18}$$

where constant charge density is assumed for $r < R(\theta)$. The intrinsic Schiff moment S_{int} is then given by

$$\begin{aligned} S_{int} &= eZR^3\frac{3}{20\pi} \sum l = 2\frac{(l+1)\beta_l\beta_{l+1}}{\sqrt{(2l+1)(2l+3)}} \\ &\approx \frac{9}{20\pi\sqrt{35}} eZR^3\beta_2\beta_3 \end{aligned} \tag{3.19}$$

where the second line stresses that the dominant contribution to the intrinsic Schiff moment comes from the product of the static quadrupole, β_2, and octupole, β_3, deformations. As we can see, the intrinsic Schiff moment is linearly proportional to the static octupole (and the quadrupole) nuclear deformation. This means, greater the reflection asymmetry, larger the sensitivity of the nucleus to this quantity.

As shown in Fig. 3.1, ^{225}Ra exhibits deformations in its nuclear structure. Compared to ^{199}Hg ($\beta_2 = -0.122$, $\beta_3 = 0$) for instance, ^{225}Ra has both a larger quadrupole and octupole deformation ($\beta_2 = 0.138$, $\beta_3 = 0.104$) [33]. This results in a larger intrinsic Schiff moment than ^{199}Hg and therefore its contribution to the atomic EDM.

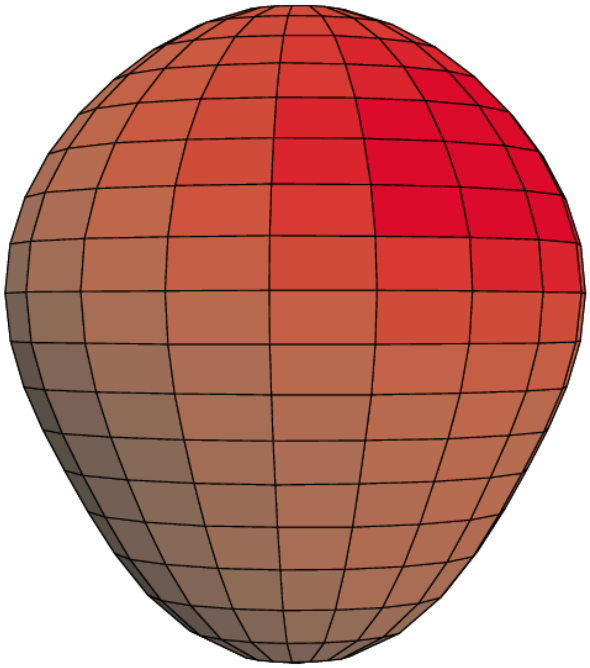

Figure 3.1: The shape of ^{225}Ra nuclei as taken from Ref. [32]. It exhibits a pear-shaped reflection asymmetry indicative of large nuclear octupole deformation.

3.2.2 Nearly-Degenerate Parity Doublet

As mentioned earlier, static nuclear octupole deformation is accompanied by the presence of nearly-degenerate parity doublet. Fig. 3.2 shows the parity doublet corresponding to the $I = 1/2$ ground state in ^{225}Ra. The energy difference between these two opposite parity states is 55 keV. This near degenarcy of the opposite parity states enhances the parity mixing amplitude α which results in a larger Schiff moment in the laboratory frame. This provides an additional, complementary enhancement to the Schiff moment.

It is worth noting that from a theoretical point of view, the calculation of the Schiff moment is remarkably more accurate and easier in ^{225}Ra compared to a soft nucleus such as ^{199}Hg. In fact, in the calculations, due to their near degeneracy, in the perturbative expansion of the Schiff moment, only the opposite parity doublet in the ground state of ^{225}Ra are taken into account. This is unlike ^{199}Hg, where sums over many unperturbed opposite parity states have to be considered. Also, given the rigid deformation, the density of the ^{225}Ra nucleus is very well approximated by a

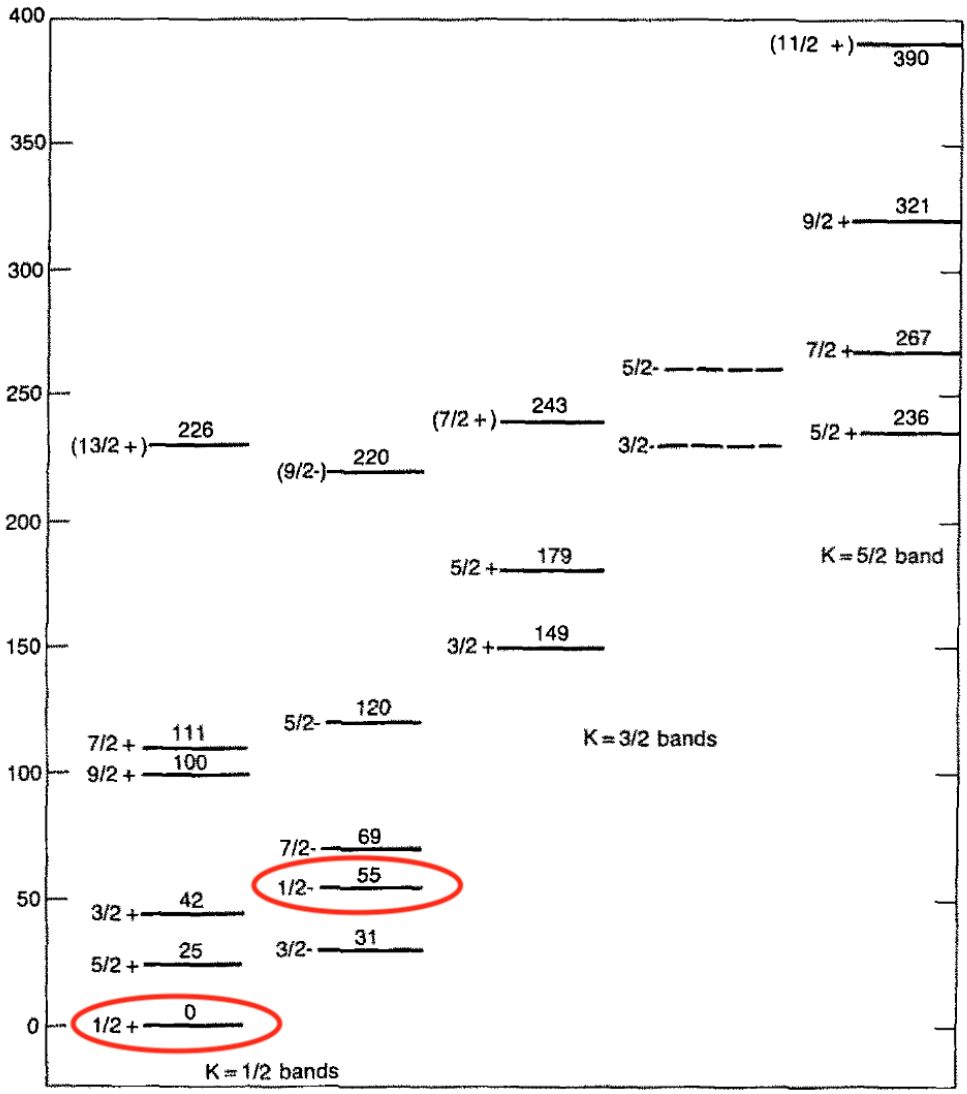

Figure 3.2: The ground state parity-doublet observed in ^{225}Ra. The two states are separated by 55keV. The figure is taken from Ref. [34].

single mean field, which greatly facilitates nuclear calculations [12].

3.2.3 Relativistic Enhancement of the Atomic EDM

The nuclear Schiff moment polarizes the electron cloud to generate the atomic EDM. The atomic theory calculations that relate the Schiff moment to the measurable atomic EDM is beyond the scope of this thesis and so only the relevant results are presented here. As mentioned in Eq. 2.15,

the atomic EDM can be written solely in terms of the Schiff moment as

$$d_A = \kappa_S S \tag{3.20}$$

where κ_S determines the sensitivity of the atomic EDM to the underlying nuclear Schiff moment. Table 3.1 summarizes the atomic theory calculations for the value of κ_S in mercury and radium in units of $\left(\frac{10^{-17}}{e\cdot\text{fm}^3}\right) e \cdot \text{cm}$.

Table 3.1: Calculated values of the κ_S coefficient in ^{199}Hg and ^{225}Ra.

Atom	$\kappa_S \left[\left(\frac{10^{-17}}{e\cdot\text{fm}^3}\right) e \cdot \text{cm}\right]$	Ref.
Hg	-2.6	[35]
	-2.16	[36]
	-1.8	[37]
Ra	-8.8	[35]
	-6.8	[38]
	-6.22	[37]
	-6.3	[39]

As can be seen, the enhancement of the κ_S coefficient in ^{225}Ra compared to ^{199}Hg is a factor of 2-3. This, along with the enhanced nuclear Schiff moment of ^{225}Ra, makes it an extremely sensitive probe of $CP-$violation emanating from the atomic nucleus.

3.3 C_T parameter

Diamagnetic atoms and molecules are also sensitive to the spin-dependent nucleon-electron tensorpseudotensor (Ne-TPT) interaction characterized by the low energy parameter C_T. Again, in a sole source approximation, we can write the resultant atomic EDM as

$$d_A = R_T C_T \tag{3.21}$$

where the coefficient R_T is the atomic interaction constant. For detailed discussions on the derivation of this coefficient, see Ref. [40]. Table 3.2 shows a list of calculations of R_T done in

^{225}Ra and ^{199}Hg. As can be seen, on average, ^{225}Ra is a factor of 3-5 more sensitive to the C_T parameter compared to ^{199}Hg.

Table 3.2: Calculated values of the R_T coefficient in ^{199}Hg and ^{225}Ra.

Atom	$R_T \left[\left(10^{-20} \langle\sigma\rangle\right) e \cdot \mathrm{cm}\right]$	Ref.
Hg	-4.3	[41]
	-5.1	[35]
	-4.4	[36]
	-3.4	[37]
	-4.43	[40]
Ra	-18	[35]
	-16.59	[42]
	-10.01	[38]
	-9.93	[37]
	-15	[40]
	-13	[39]

As discussed in Sec. 2.8, the phenomenological consequences of the various EDM measurements can be interpreted in two ways: *(i)* setting the contributions from all but one parameter to zero and setting bounds on that parameter. This is the sole-source interpretation. *(ii)* In the model-independent global analysis, the experimentally determined limits (assuming the values are consistent with zero) simultaneously constrain the global phase space of allowed values the different *CP*-violating parameters can take. This incorporates potential cancellations from the contributions to the EDM from the different parameters.

In the sole-source interpretation, the bounds placed on C_T by the ^{225}Ra EDM limit is still ~7 orders of magnitude less stringent than the bounds imposed by the ^{199}Hg limit. However, in the global analysis, as shown by Chupp & Ramsey-Musolf [26], even with 2-3 orders of magnitude improvement in the ^{225}Ra EDM limit, it will help further constrain the C_T parameter. In this sense, the upgrades detailed in this dissertation that are expected to result in at least 2 orders of magnitude improvement in the ^{225}Ra EDM limit, will have significant impact on the *CP*-violating parameters.

3.4 Using ^{225}Ra for an EDM Experiment

With its octupole deformed nucleus and the nearly-degenerate ground state parity doublet, ^{225}Ra is a very sensitive probe for *CP*-violations in the atomic nucleus. This is what motivated the ^{225}Ra EDM search experiment at Argonne National Laboratory (ANL). However, given it's short half-life and low vapor pressure, such an experiment presents a unique set of challenges.

^{225}Ra is a radioactive isotope of radium with a half life of $\tau_{1/2} = 14$ days. Currently, Oak Ridge National Laboratory serves as the only source of ^{225}Ra, where it is produced through the $\alpha-$decay of ^{229}Th. Typically, we obtain about 10 mCi of ^{225}Ra every two months. The radioactivity of the isotope sets the limit on the amount of ^{225}Ra we can load into our atomic beam oven.

Radium, unlike mercury, has a low vapor pressure. It has a vapor pressure of 8 mTorr at 560 C, compared to 2 mTorr for mercury at room temperature. This makes building a gas vapor cell for radium particularly challenging. However, as an alkaline-earth element, it is amenable to the techniques of laser cooling and trapping of atoms. This is what was chosen for the ^{225}Ra EDM experiment at ANL and is the subject of the next chapter. This makes the experiment susceptible to a very different set of systematic effects compared to the mercury vapor cell based ^{199}Hg EDM experiment.

CHAPTER 4

LASER COOLING AND TRAPPING OF RADIUM ATOMS

This chapter outlines the technique of laser cooling and trapping of neutral atoms and its application to radium. We begin with an overview of the underlying physical concepts that allow laser cooling and trapping to work, we then explain how this technique is applied to radium to trap a cold cloud of radium atoms for our experiment, and finally, we finish this chapter by discussing in detail the different laser systems and the frequency stabilization schemes implemented on some of them.

4.1 Laser Cooling and Trapping Theory

It was shown by James Clerk Maxwell, in as early as the nineteenth century, that electromagnetic radiation carried momentum and therefore exerted force on incident matter[43]. For instance, a radiation with intensity I, exerts a force on a surface with area A given by

$$F_{rad} = \frac{IA}{c} \tag{4.1}$$

where c is the speed of light. However, it was not until the advent of lasers that this concept found applications in cooling and trapping of neutral atoms for preparing ultracold ensembles of atoms. For their pioneering work in this field, Steven Chu, William Phillips and Claude Cohen-Tannoudji were awarded the Nobel Prize in Physics in 1997. Since then, laser cooling and trapping of atoms has become a standard workhorse in the field of atomic, molecular, and optical (AMO) Physics with applications ranging from - but not limited to - the creation of Bose-Einstein Condensates (BEC), probing ultra-cold chemistry with cold molecules, optical atomic clocks for precise time-keeping, precision measurements and test of fundamental symmetries, and quantum computation and simulation.

We now provide a basic overview of this technique and the underlying physical concepts. Readers interested in a more in-depth discussion should refer to Ref. [44, 45]. To understand this technique, we adopt the photon picture of electromagnetic radiation as is customary. For

simplicity, we consider a two-level atom moving with a speed v in the direction of a laser with angular frequency ω. The scattering force F_{scatt} exerted by the laser on the atom is given by

$$F_{scatt} = p_\gamma \times R_{scatt} \tag{4.2}$$

where $p_\gamma = \hbar k$ is a single photon momentum, with $k = \omega/c$, and R_{scatt} is the photon scattering rate given by

$$R_{scatt} = \frac{\Gamma}{2} \frac{\Omega^2/2}{\delta^2 + \Omega^2/2 + \Gamma^2/4} \tag{4.3}$$

where $\Gamma = \tau^{-1}$, called the natural linewidth of the transition, is the inverse of the lifetime τ of the excited state. Ω is the Rabi frequency of the transition induced by the laser field, and $\delta = \omega - \omega_0 + kv$ is the detuning of the laser frequency from the two-level resonance ω_0, taking the Doppler shift into account. At this point, it is more common to express the scattering rate in terms of the laser intensity I than the Rabi frequency Ω, both of which are related by $I/I_{sat} = 2\Omega^2/\Gamma^2$. Here, I_{sat} is the saturation intensity given by

$$I_{sat} = \frac{\pi}{3} \frac{hc}{\lambda^3 \tau} \tag{4.4}$$

where λ is the wavelength of the transition. We can then write the photon scattering force as

$$F_{scatt} = \hbar k \frac{\Gamma}{2} \frac{I/I_{sat}}{1 + I/I_{sat} + 4\delta^2/\Gamma^2} \tag{4.5}$$

Here we note that as $I \to \infty$, the force tends towards the maximal value of $F_{max} = \hbar k \Gamma/2$. The maximal acceleration produced by the radiation on the atom with mass M is then given by

$$a_{max} = \frac{F_{max}}{M} = \frac{\hbar k}{M} \frac{\Gamma}{2} = \frac{v_{rec}}{2\tau} \tag{4.6}$$

where v_{rec} is the recoil velocity and is equal to the photon momentum divided by the atomic mass. For a ^{226}Ra atom with $M = 226$ a.m.u., using the $\lambda = 714$ nm transition with an excited

state ($^3P_1$) lifetime of 422 ns, we have a maximum acceleration of $a_{max} = 2930\,\mathrm{m/s^2}$, which is about 300 times the acceleration due to gravity ($g = 9.8\,\mathrm{m/s^2}$).

Now suppose if we were to slow the atoms to rest using this photon scattering force. An atom with an initial speed v_0, experiencing a constant acceleration $a = a_{max}/2$, comes to rest at a distance given by

$$L_0 = \frac{v_0^2}{2a} = \frac{v_0^2}{a_{max}} \tag{4.7}$$

where we set $a = a_{max}/2$, as it is typically done to compensate for random fluctuations of the scattering force due to spontaneous emissions. The starting velocity v_0 is usually determined by the temperature at which the oven for the atomic beam is operated. This determines the most probable velocity of the atoms in the beam, which is typically set as the starting velocity of the fastest atoms stopped by the light force. However, in certain cases, as is the case with radium in its "red slower" scheme (this is explained later in this chapter), to keep the distance over which atoms are slowed to a practical length, the starting velocity of 60 m/s is chosen, which is much less than the most probable velocity of 315 m/s at $T = 673.15$ K.

The above results holds only when the atom experiences a constant acceleration. However, as we know from Eq. 4.5, the photon scattering force is dependent on the frequency detuning term δ, which in turn relies on the atomic velocity via the Doppler shift kv. Now, as the atom slows down and its velocity decreases, the size of the photon Doppler shift in the atomic frame of reference decreases as well. At some point, the Doppler shift decreases enough to put the atom out of resonance with the incident laser beam. To put it mathematically, the atom experiences the strong scattering force only in the velocity range $\Delta v \sim \Gamma/k$. From here onward the atom no longer scatters the photons and is therefore no longer slowed.

4.1.1 Zeeman Slower

As a solution this problem, Phillips & Metcalf [46] devised an ingenious tool - the Zeeman Slower. Their idea was quite simple but effective. To keep the slowing atomic beam in resonance with the

Doppler shifted laser beam, they adjusted the differential Zeeman shift of the two levels to ensure that the laser was always resonant with the cooling transition. This was achieved by surrounding the atomic beam with a tapered solenoid to create a $B-$field profile that matched the Zeeman shift with the changing Doppler shift of the incident laser beam, as shown in Fig. 4.1.

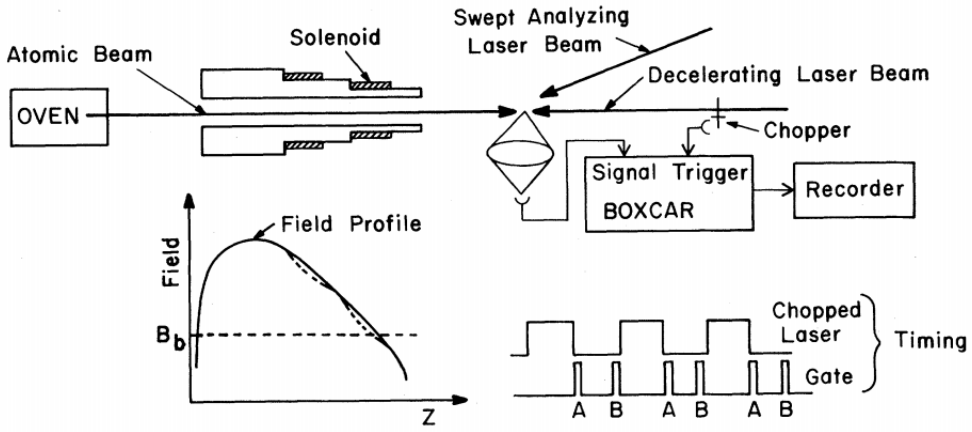

Figure 4.1: The schematic of the setup used by Phillips & Metcalf [46] for demonstrating the slowing of an atomic beam using a counter propagating laser beam. The tapered solenoid creates the required $B-$field profile for adjusting the Zeeman shift of the cooling transition to match the changing Doppler shift of the decelerating laser beam. Figure taken from [46].

To determine what the $B-$field profile should be, we write the spatial dependence of the atomic velocity along the atomic beam axis (and therefore the axis of the tapered solenoid).

$$v(z) = v_0\sqrt{\left(1 - \frac{z}{L_0}\right)} \tag{4.8}$$

The Zeeman shift for an atom with a transition magnetic moment μ in a spatially varying magnetic field $B(z)$ is given by $\Delta\nu_B = \mu B/\hbar$. To ensure that the decelerating laser beam is resonant on the Zeeman shifted atomic transition, we require

$$\omega_0 + \frac{\mu B(z)}{\hbar} = \omega + kv(z) \tag{4.9}$$

The required $B-$field is then given by

$$B(z) = B(0)\sqrt{\left(1 - \frac{z}{L_0}\right)} + B_{bias} \tag{4.10}$$

for $0 \leq z \leq L_0$, with $B(0) = h\nu_0/\mu\lambda$, and $B_{bias} \approx \hbar(\omega - \omega_0)$. The bias field is adjusted to tune the exit velocity of the atomic beam. It is often desirable to leave the atoms moving at a small velocity for the subsequent section of the experiment. Such a Zeeman slower can achieve slowing of atomic beams, as was demonstrated in early experiments with cooling of beams of atomic Na[47], as shown in Fig. 4.2.

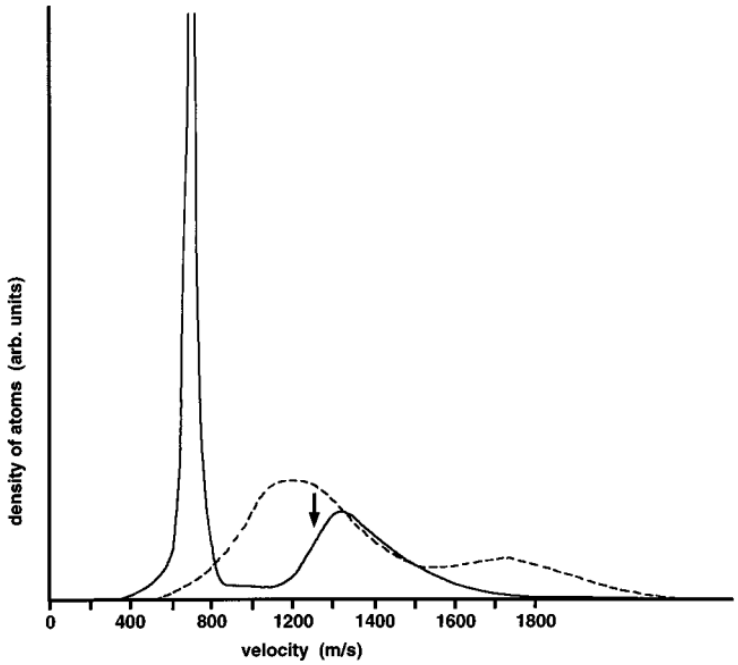

Figure 4.2: The slowing of a beam of Na atoms in a Zeeman slower. The solid(dashed) line shows the density of atomic population as a function of the atom velocity after(before) Zeeman slowing. Figure adapted from [47].

4.1.2 Magneto-Optical Trap (MOT)

The slowing of beams of neutral atoms played a pivotal role in enabling the trapping of these atoms and creating ultracold samples of atomic clouds. Following the development of atom slowing techniques, such as the Zeeman slower described in the previous section, it was quickly realized that with a magnetic field gradient in the presence of counter-propagating laser beams of opposite circular polarization, one could achieve a trap for neutral atoms[48].

To explain the workings of such a trap, we focus on a one-dimensional realization of this set

up. The operating principle of the typically used three-dimensional setup follows naturally. The trap consists of a pair of counter-propagating laser beams with opposite circular polarization, and a pair of magnetic coils in the anti-Helmholtz configuration.

This generates a quadrupolar magnetic field that is linear along the coil axis: $B = B_0\hat{z}$. Considering a two-level system with a ground state angular momentum of $J = 0$ and an excited state with angular momentum $J = 1$, Fig. 4.3 shows the Zeeman splitting of the excited state levels along the coil axis z. The counter-propagating laser beams at frequency ω are red-detuned from the transition frequency, $\omega < \omega_0$. As can be seen, the $m_J = +1$ and the $m_J = -1$ sublevels of the excited states are resonant with the laser beams at different positions along the trap. The $m_J = +1$ sublevel for instance, is resonant with the laser beams at some $z < 0$. An atom in the ground state then selectively scatters the laser beam with the σ^+ polarization - dictated by angular momentum selection rule - and is therefore pushed toward the trap center. While at some $z > 0$, the $m_J = -1$ sublevel is resonant with the laser frequency and therefore the atom in the ground state selectively scatters the beam with the σ^- polarization. This then ensures that at either side of the trap center, the atoms are pushed toward the center and are therefore trapped. Such a trap constructed with counter-propagating lasers beams with opposite circular polarization in the presence of a quadrupolar magnetic field is called a magneto-optical trap (MOT).

To express this point mathematically, we consider the scattering forces experienced by an atom in a MOT. Here the Zeeman shift at the axial position z is given by

$$\beta z = \frac{g\mu_B}{\hbar}\frac{\mathrm{d}B}{\mathrm{d}z}z \tag{4.11}$$

where g is the g-factor of the transition in this case given by $g = g_J$. Typically for ground states with a non-zero angular momentum, it is given by

$$g = g_{F'}m_{F'} - g_F m_F \tag{4.12}$$

where the primed(unprimed) quantities refer to the excited(ground) states. μ_B is the bohr magneton, and $\mathrm{d}B/\mathrm{d}z$ is the magnetic field gradient.

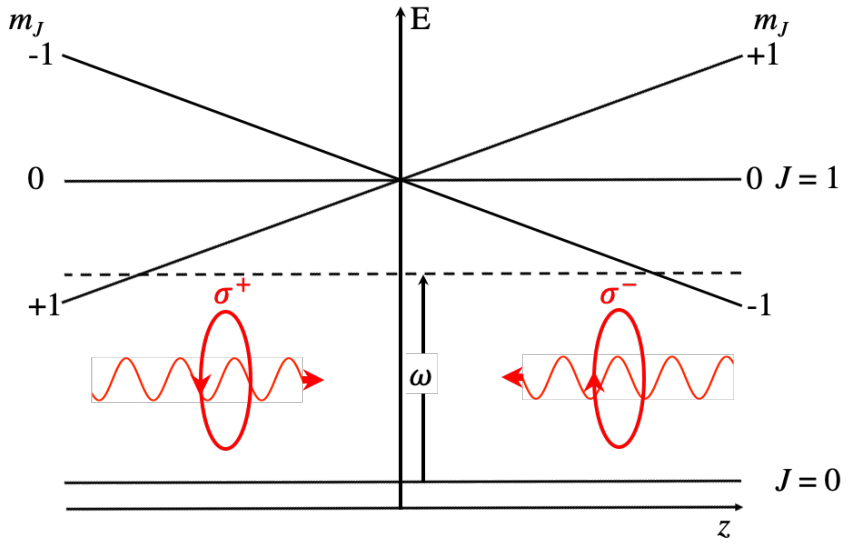

Figure 4.3: The linear $B-$field generated by the anti-Helmholtz coils splits the $m_J = \pm 1$ Zeeman magnetic sublevels of the excited state such that the laser beams are selectively resonant with a sublevel at either side of the trap center. The opposite polarization of the laser beams ensure that the atom scatters only one of the two counter-propagating beams at either side of the trap center and is therefore pushed back to the center.

The MOT scattering force F_{MOT}, only up to the linear terms[1], is then given by

$$F_{MOT} = F^{\sigma^+}_{scatt}(\omega - kv - (\omega_0 + \beta z)) - F^{\sigma^-}_{scatt}(\omega + kv - (\omega_0 - \beta z)) \tag{4.13}$$

$$\simeq -2\frac{\partial F}{\partial \omega} kv + 2\frac{\partial F}{\partial \omega_0}\beta z \tag{4.14}$$

$$= -2\frac{\partial F}{\partial \omega}(kv + \beta z) \tag{4.15}$$

$$= -\alpha v - \frac{\alpha\beta}{k} z \tag{4.16}$$

Eq. 4.16 describes a damped oscillator, with a damping factor $\alpha = -2(\partial F/\partial\omega)k$, and a

[1]Here we assume that the Zeeman shift $\beta z \ll \Gamma$ and the Doppler shift $kv \ll \Gamma$.

restoring factor $\alpha\beta/k$. Typically the atomic motion is overdamped and therefore the atoms are quickly confined to the center of the trap with a certain trap lifetime. This damped restoring force from the selectively scattering of the two laser beams in the presence of a magnetic field gradient is what allows for the trapping of neutral atoms in a MOT. It is then quite straightforward to see that the presence of three pairs of such counter-propagating laser beams achieve a three-dimensional MOT, for spatial confinement of the atoms along all the spatial dimensions.

4.1.3 Optical Dipole Trap (ODT)

Another method for neutral atom confinement that has found widespread applications is the optical dipole trap (ODT). Such a trap usually consists of a high intensity laser beam that employs the induced electric dipole interaction between the atom and the laser to create an almost conservative potential for confining the atoms. The laser is also chosen to have a frequency far off-resonance from any of the electronic transitions in the atom to reduce the photon scattering rate and therefore atom heating. We now present a semi-classical description of the optical dipole trap of atoms that closely follows the treatment provided in Ref. [49].

We begin by deriving the force exerted by the laser field on an atom with an induced electric dipole moment. Here we adopt the classical 'oscillator' description of the atom-light interaction. An atom illuminated by a laser with an electric field $\vec{E}$ with frequency ω polarized along $\hat{\varepsilon}$ given by

$$\vec{E}(\vec{r},t) = \hat{\varepsilon}\tilde{E}(\vec{r})e^{-i\omega t} + c.c. \tag{4.17}$$

has an induced electric dipole $\vec{d}$ given by

$$\vec{d} = \hat{\varepsilon}\tilde{d}(\vec{r})e^{-i\omega t} + c.c. \tag{4.18}$$

The amplitude of the dipole $\tilde{d}$ is proportional to the magnitude of the electric field $\tilde{E}$ and can be written as

$$\tilde{d} = \alpha\tilde{E} \tag{4.19}$$

where $\alpha = \alpha(\omega)$ is the frequency dependent complex polarizability of the atom.

The atom-light interaction potential is then given by $U_{dip} = -\left\langle \vec{d} \cdot \vec{E} \right\rangle /2$, where the brackets indicate time averaged value over the rapidly oscillating terms, and the factor of 1/2 accounts for the fact that the dipole is induced and not permanent. We find that the interaction potential in terms of the laser intensity I is given by

$$U_{dip} = -\frac{1}{2\epsilon_0 c}\mathrm{Re}(\alpha) I(\vec{r}) \tag{4.20}$$

where we make the substitution $I = 2\epsilon_0 c\left|\tilde{E}\right|^2$. Here ϵ_0 is the vacuum permittivity, and c is the speed of light.

This interaction potential results in a force exerted on the induced dipole of the atoms by the laser light, which can be expressed as

$$\vec{F}_{dip} = -\vec{\boldsymbol{\nabla}} U_{dip} = \frac{1}{2\epsilon_0 c}\mathrm{Re}(\alpha)\vec{\boldsymbol{\nabla}} I(\vec{r}) \tag{4.21}$$

As can be seen, the dipole force is proportional to the intensity gradient of the laser field and is in phase with the oscillations.

Next, we calculate the scattering rate of the laser photons by the atom. The scattering rate is given by the power absorbed by the oscillator - the atom in our case - divided by the single photon energy

$$R_{scatt} = \frac{P_{abs}}{\hbar\omega} = \frac{1}{\hbar\omega}\left\langle \dot{\vec{d}} \cdot \vec{E} \right\rangle = \frac{1}{\hbar\epsilon_0 c}\mathrm{Im}(\alpha) I(\vec{r}) \tag{4.22}$$

We observe that the scattering rate is out of phase with the oscillation and depends on the imaginary part of the polarizability α, and is proportional to the intensity of the laser I.

We now calculate the polarizability of the atom α at a given laser frequency ω. For this purpose we use the Lorentz's model of the atom as a classical harmonic oscillator. In the presence of

frequency dependent damping γ_ω, the motion of the bounded electron, with mass m_e and charge $-e$, in the center-of-mass frame is described by

$$m_e\ddot{\vec{x}}(t) + m_e\gamma_\omega\dot{\vec{x}}(t) + m_e\omega_0^2\vec{x}(t) = -\hat{\varepsilon}e\tilde{E}\exp\{-i\omega t\} \tag{4.23}$$

Assuming a solution of the form $\vec{x}(t) = \hat{\varepsilon}\tilde{x}\exp\{-i\omega t\}$ gives

$$\tilde{x} = \frac{e\tilde{E}/m_e}{\omega^2 - \omega_0^2 + i\gamma_\omega\omega} \tag{4.24}$$

The resultant induced dipole of the atom is

$$\vec{d} = -e\vec{x} \tag{4.25}$$

However, since the dipole is induced by the external laser field, we can define the polarizability α as a response of the atom to the field as

$$\vec{d} = \alpha(\omega)\vec{E} \tag{4.26}$$

From Eq. 4.25 and Eq. 4.26, we find that the atomic polarizability is therefore given by

$$\alpha(\omega) = \frac{e^2/m_e}{\omega_0^2 - \omega^2 - i\gamma_\omega\omega} \tag{4.27}$$

Classically the damping term due to dipole radiative energy loss is given by

$$\gamma_\omega = \frac{e^2\omega^2}{6\pi\epsilon_0 m_e c^3} \tag{4.28}$$

Rewriting the expression for the polarizability in terms of the on-resonance damping $\gamma \equiv \gamma_{\omega_0} = (\omega_0/\omega)^2\gamma_\omega$ gives

$$\alpha(\omega) = 6\pi\epsilon_0 c^3 \frac{\gamma/\omega_0^2}{\omega_0^2 - \omega^2 - (\omega^3/\omega_0^2)\gamma} \tag{4.29}$$

It is worth noting that Eq. 4.28, and Eq. 4.29 are valid only in the limit of low photon scattering. Only a full quantum mechanical treatment captures the saturation effects seen when the excited

state is significantly populated. In our case, we are interested in highly-intense but far-detuned lasers that keep the scattering rate low, $R_{scatt} \ll \gamma$, so this treatment is still valid.

With the expression for the atomic polarizability as derived above, we can rewrite our interaction potential and the photon scattering rate as

$$U_{dip}(\vec{r}) = -\frac{3\pi c^2}{2\omega_0^3}\left(\frac{\gamma}{\omega_0 - \omega} + \frac{\gamma}{\omega_0 + \omega}\right) I(\vec{r}) \tag{4.30}$$

$$R_{scatt}(\vec{r}) = \frac{3\pi c^2}{2\hbar\omega_0^3}\left(\frac{\omega}{\omega_0}\right)^2 \left(\frac{\gamma}{\omega_0 - \omega} + \frac{\gamma}{\omega_0 + \omega}\right)^2 I(\vec{r}) \tag{4.31}$$

Under most circumstances, the the laser frequency detuning $\Delta = \omega - \omega_0$ satisfies the condition: $|\Delta| \ll \omega_0$. This allows us to simplify the above expressions[2]

$$U_{dip}(\vec{r}) = \frac{3\pi c^2}{2\omega_0^3}\frac{\gamma}{\Delta} I(\vec{r}) \tag{4.32}$$

$$R_{scatt}(\vec{r}) = \frac{3\pi c^2}{2\hbar\omega_0^3}\left(\frac{\gamma}{\Delta}\right)^2 I(\vec{r}) \tag{4.33}$$

These two equations contain the necessary underlying physics for understanding the interaction of the atoms with a far-detuned laser ODT. First and foremost, note how that the dipole interaction potential U_{dip} depends on the sign of the frequency detuning Δ. For $\Delta < 0$ or far red-detuned lasers - as is the case for radium - the potential is negative everywhere and the potential minima are found at the intensity maxima. This means the atoms are attracted to the highest intensity regions. For an intense, focused, red-detuned laser beam, the atoms are trapped at the focus of the beam. Secondly, we note that the dipole interaction potential scales as (I/Δ) but the scattering rate scales as (I/Δ^2). Therefore, optical dipole traps are far-detuned to ensure low scattering rate, but also have high intensities to maintain a reasonable trap-depth.

[2]The approximation we make here is known as the rotating wave approximation where we assume $\omega/\omega_0 \approx 1$.

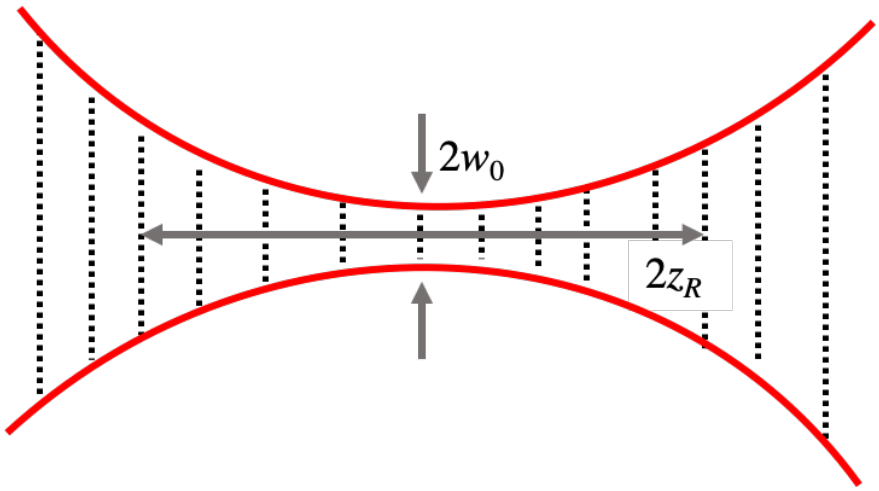

Figure 4.4: A far red-detuned gaussian laser beam with a beam waist w_0 and Rayleigh range z_R.

We conclude this section by studying a focused red-detuned laser beam, as shown in Fig. 4.4, that has a gaussian intensity profile given by

$$I(r,z) = \frac{2P}{\pi w^2(z)} \exp\left(-2\frac{r^2}{w^2(z)}\right) \tag{4.34}$$

where P is the laser power, r and z are the respective radial and axial coordinates in a cylindrical coordinate system. $w(z)$ is the $1/e^2$ radius of the beam given by

$$w(z) = w_0\sqrt{1+\left(\frac{z}{z_R}\right)^2} \tag{4.35}$$

w_0 is the minimum beam radius, also called the beam waist, and $z_R = \pi w_0^2/\lambda$ is the Rayleigh length for the beam with wavelength λ. The trap-depth is then defined as $U_0 = U_{dip}(r=0, z=0)$. Assuming that the thermal energy of the atoms $k_B T$ is much smaller than trap-depth U_0, the dipole interaction potential can be written as

$$U(r,z) \simeq -U_0\left(1 - 2\left(\frac{r}{w_0}\right)^2 - \left(\frac{z}{z_R}\right)^2\right) \tag{4.36}$$

A typical characteristic of such far red-detuned optical dipole trap is the stronger confinement of the atoms along the radial direction than long the axial direction. This is because the Rayleigh length z_R is larger than the beam waist w_0. To ensure long trap lifetimes and stable atom traps, the

beams are generally aligned horizontally to minimize the perturbations due to gravity. For such traps, under the harmonic potential approximation, the trapped atoms experience radial oscillations with frequency $\omega_r = \sqrt{4U_0/mw_0^2}$ and axial oscillations with frequency $\omega_z = \sqrt{2U_0/mz_R^2}$. For instance, for an ODT used for trapping radium with a beam waist of $w_0 = 65\,\mu$m, $\lambda = 1550$ nm, $P = 50$ W, we have $\omega_r = 297$ Hz, and $\omega_z = 1.6$ Hz.

4.2 Laser Cooling and Trapping Radium Atoms

As mentioned in the previous chapter, radium's low vapor pressure makes the fabrication of a glass vapor cell challenging. However, the presence of certain transitions make it amenable to laser cooling and trapping. Therefore, with the above arsenal of tools for laser cooling and trapping of neutral atoms we now discuss their applications for cooling and trapping radium atoms.

As is evident from our discussion so far, laser cooling and trapping methods are sensitive to the internal electronic structure of the atoms. Fig. 4.5 presents the relevant lowest lying electronic states in radium. According to Eq. 4.6, the 483 nm transition, with a linewidth of $2\pi \times 30$ MHz, from the ground state $^1S_0$ to $^1P_1$ state allows for the largest atom deceleration. However, the $^1P_1$ state has significant decay channels to the metastable $^1D_2$, $^3D_1$, and $^3D_2$ states that limit the number of photon scattering events to only about $\sim$ 1000 photons/atom before it is lost from the cooling cycle. The straightforward solution would be to depopulate these $D-$ states and close the cooling cycle. However, the addition of three more repumping lasers proves quite a practical challenge. A potentially economical and effective scheme for using the 483 nm transition for atom slowing or the "blue slower scheme" - as it will be refered to - is presented in Ch.8 and is the subject of active research in our lab. However, currently, owing to the limitations of using the blue slower scheme, we use the much narrower ($2\pi \times 380$ kHz), 714 nm transition from $^1S_0$ to $^3P_1$. For ^{226}Ra the laser is tuned to the $(J = 0) \leftrightarrow (J = 1)$ transition, while for ^{225}Ra it is tuned to the $(F = 1/2) \leftrightarrow (F = 3/2)$ transition. This spin-forbidden, inter-combination transition is weaker than the dipole allowed 483nm transition, and therefore a 1 m long Zeeman slower based on the 714 nm transition only slows atoms moving below 60 m/s, compared to a 20 cm long 483 nm Zeeman

slower that can slow atoms with speeds up to 300 m/s. However it has the practical advantage of only requiring one laser at 1428 nm for depopulating the atoms that have decayed into the $^3D_1$ state. Additionally, the atoms that decay into the $^3P_0$ state are repumped by the thermal blackbody radiation [50].

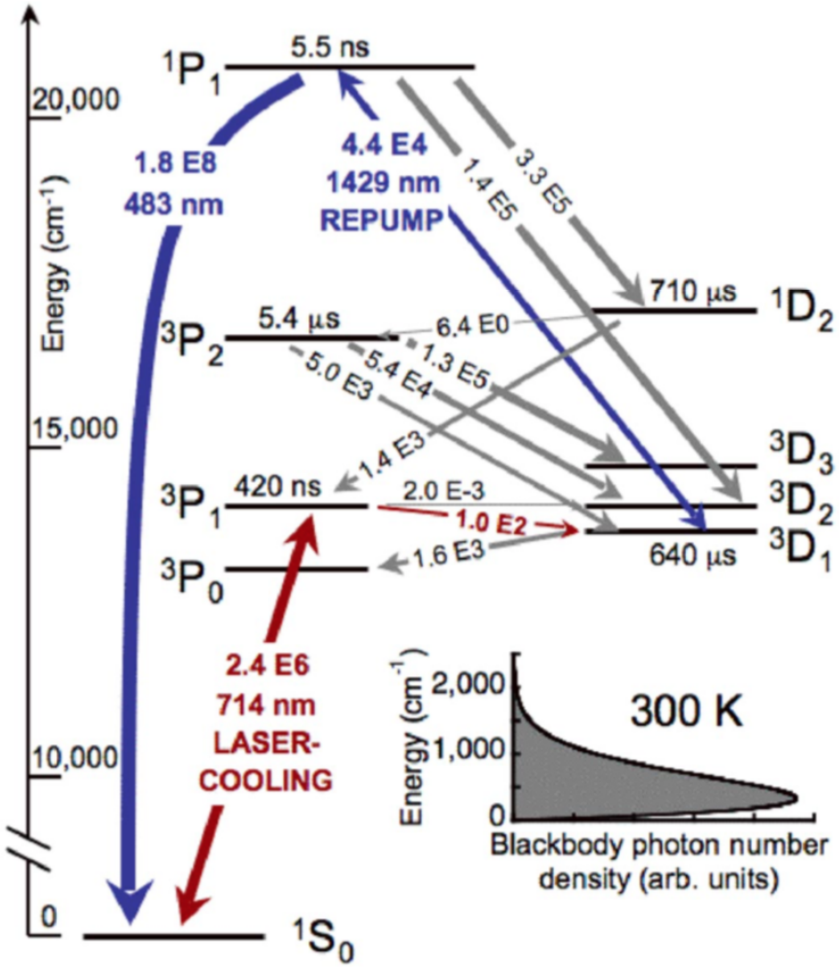

Figure 4.5: The lowest-lying energy levels of radium relevant to atom cooling and trapping. Figure taken from[50].

4.3 Laser Systems Used in the Experiment

Currently, we use seven different lasers in the lab for various purposes, ranging from laser cooling and trapping of radium atoms, state preparation via electron shelving and for atom absorption imaging.

Table 4.1: The different Lasers Used in the Radium EDM Search Experiment.

Laser	λ (nm)	P_{max} (W)	Notes
Lighthouse Photonics Sprout DPSS	532	18	Pump laser for the Ti:Sa ring cavity laser.
Matisse TS ring cavity laser (Ti:Sa)	700 - 990	3.2	Atom cooling and trapping laser.
Toptica DL Pro ECDL	483	0.03	STIRAP pump laser.
Moglabs CEL002	483	0.04	Atom imaging laser.
FBG 1428 laser	1428	0.3	STIRAP Stokes laser.
FBG 1428 laser	1428	0.3	Repump laser for atom cooling and trapping.
IPG Photonics Fiber Laser ELR-100-WC-Y14	1550	100	Bus ODT laser.
IPG Photonics Fiber Laser ELR-50-1550-SF-LP	1550	30	Holding ODT laser.
Thorlabs Tunable Diode Laser M9-915-0300	910-920	0.1	Laser used for determining the $^1D_2 \leftrightarrow {}^3F_2$ transition resonance.

Here we describe the different laser systems used in the radium EDM apparatus, as shown in Table 4.1.

4.3.1 714 nm Laser

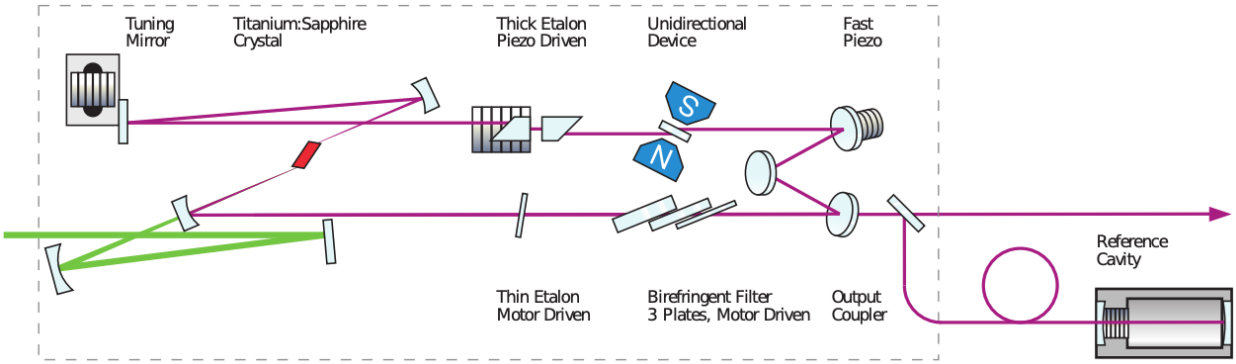

Figure 4.6: The Ti:Sapphire ring cavity laser used for producing the 714 nm light required for laser cooling and trapping of radium. The green laser light is generated by a pump laser and is incident on the Ti:Sapphire crystal that generates the 714 nm light. Figure taken from [51].

The atom cooling and trapping light at 714 nm is generated by a Sirah Matisse Ti:Sapphire ring cavity laser, shown in Fig. 4.6, pumped using a diode-pumped solid state (DPSS) laser (Lighthouse Photonics, Sprout). With the pump laser set to 9.5 W, we typically get about 1.2 W at 714 nm out of the laser.

As shown in Fig. 4.7, most of the power is sent to the vacuum chamber for laser cooling and trapping of radium atoms. This consists of the transverse cooling, Zeeman slowing, the 3D MOT and the 1D MOT beams. Some of the remaining power is sent to the Bristol wavemeter for wavelength monitoring and to an ultra-low expansion (ULE) glass cavity for frequency stabilization. Although we elaborate more on the frequency stabilization schemes later in this chapter, it is worth mentioning here that the Matisse frequency used to be locked to one of the ULE cavity resonant modes using the reflection Pound-Drever-Hall (PDH) technique until it was recently replaced by the Electronic-Sideband (ESB) technique, which allows for larger frequency tunability. This required the use of a high bandwidth, temperature controlled, fiber-coupled electro-optic modulator (EOM) (EOSpace, Phase Modulator) to allow several GHz of tunability. The thick piezo driven etalon, and

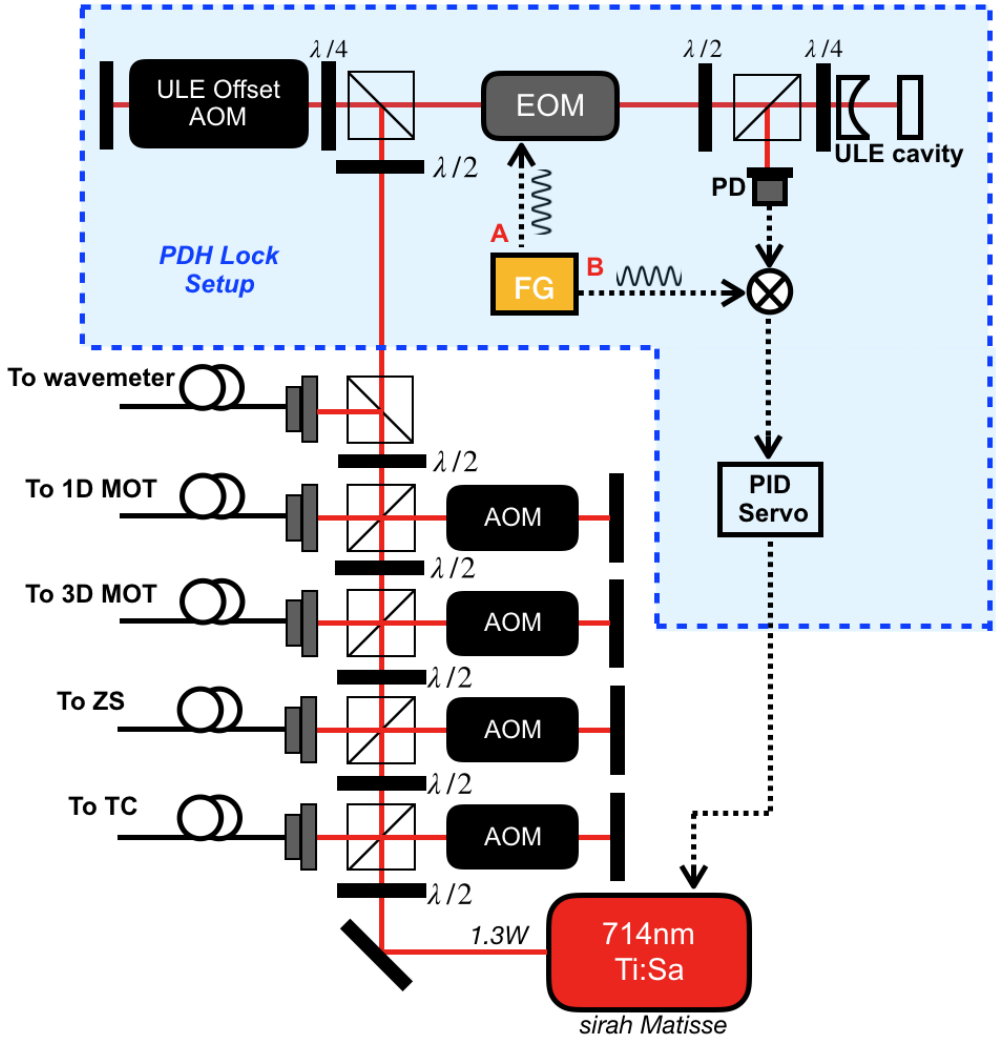

Figure 4.7: The 714 nm laser setup. Much of the output power from the Ti:Sapphire ring cavity laser is sent to the atom cooling and trapping apparatus. Some of the power is sent to the wavemeter for laser frequency monitoring. The rest is sent to the ULE optical reference cavity for frequency stabilization. This figure depicts the PDH-scheme used for laser frequency stabilization that has recently been replaced by an ESB lock setup.

the thin motor driven etalon are internally locked after fine adjustments of the laser wavelength. The fast piezo driven etalon is feedback controlled to reduce the fast laser linewidth to be within 70 kHz. As shown in the shaded portion of Fig. 4.7, in the PDH scheme for laser frequency stabilization, the laser beam incident on the cavity is double-passed through an acousto-optic modulator (AOM), labeled the 'ULE Offset AOM'. This serves two purposes. First, it allows us to shift between the laser cooling and trapping frequencies required for ^{226}Ra and ^{225}Ra. Second, it also helps

compensate for the slow drift in the cavity resonance frequency - mostly due to slow thermal and mechanical drifts of the cavity. To minimize thermal drifts, we implement a two-stage temperature control of our ULE cavity, housed inside a vacuum chamber held at ultrahigh vacuum. With this, we notice that the ULE cavity resonance drifts can be controlled to < 10 kHz/day. Fig. 4.8 shows the recorded drift of the resonance frequency of the relevant TEM_{00} mode of the ULE cavity used for frequency stabilizing the 714 nm Ti:Sapphire laser for laser cooling and trapping ^{226}Ra. The drift is very uniform except for certain discontinuities due to instances when the power supply for the ULE temperature controller had reset and the output had turned off. The details of the cavity temperature control is similar to what is implemented in our zerodur cavity, and will be discussed later in this chapter.

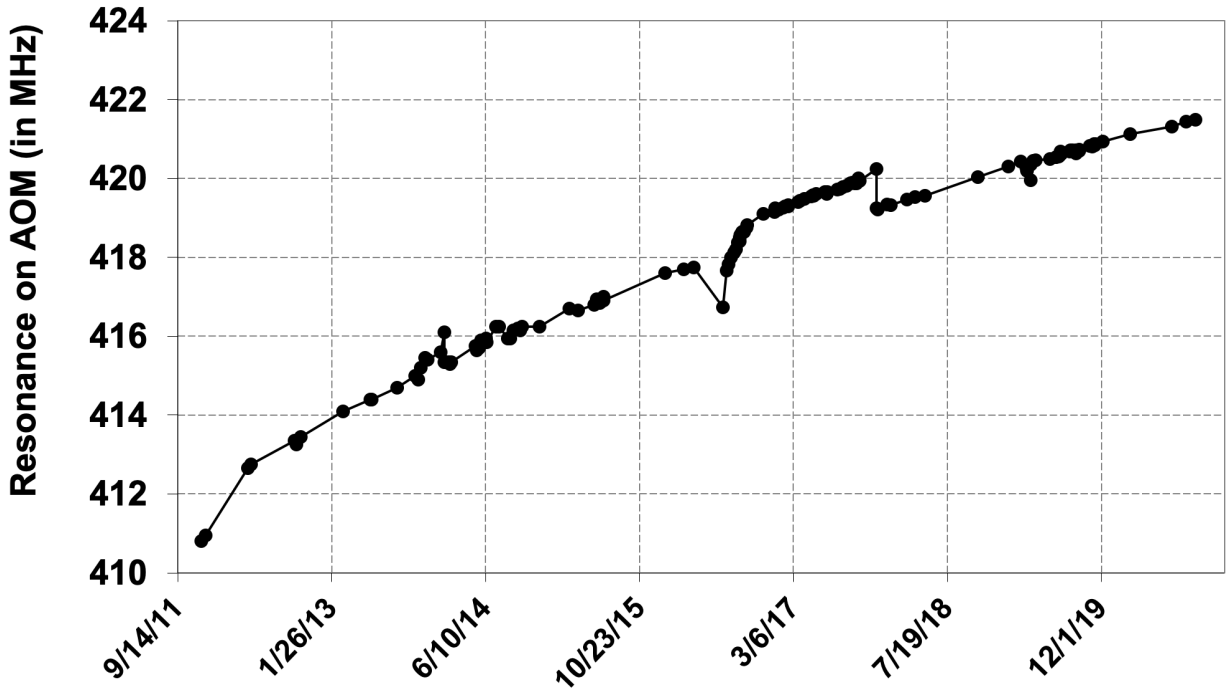

Figure 4.8: The drift of the resonant frequency of the relevant TEM_{00} mode of the ULE cavity used for frequency stabilizing the 714 nm Ti:Sapphire laser for trapping ^{226}Ra atoms.

4.3.2 1428 nm Lasers

4.3.2.1 1428 nm STIRAP IR Laser

The 1428 nm light required in our experiment are generated by two Fara-Banafsh FBG (Fiber Bragg Grating) lasers. One of the lasers, called the 'STIRAP IR laser' from here onward, supplies the 1428nm beam necessary for ground state preparation via electron shelving using the STIRAP technique. This technique is explained in detail in chapter 7. The laser easily generates about 300 mW of power at 1428 nm. The coarse tuning of the laser frequency is achieved by changing the laser temperature, while it can be fine tuned by changing the injection current. As shown in Fig. 4.9, most of the output power is sent to the atoms. Some of it is sent to the optical beatlock setup for frequency stabilizing the other 1428 nm laser, called the 'Repump IR laser'. This will be discussed later. The remaining power is shared between the wavemeter and the cavity for frequency stabilization. Here we also display the relevant components for the ESB lock setup implemented on the 1428 nm STIRAP IR laser. The details of this technique is the subject of chapter 5, and therefore not reproduced here. However, we mention the role played by the double-passed AOM before the temperature controlled, fiber-coupled EOM (EOSpace, Phase Modulator) that creates the necessary modulations on the laser light for the ESB scheme. This AOM allows us to avoid potential "mode collisions", or shift the laser frequency enough to avoid different sidebands of the lasers from colliding and causing lock degradation. This is typically seen when the laser tuning frequency (LOM) is set to half the free spectral range of the cavity.

Similar to what is implemented on the ULE optical reference cavity, the zerodur cavity is housed inside a vacuum chamber held at ultrahigh vacuum, and has a two-stage temperature control to minimize the thermal drifts of the cavity. Fig. 4.10 shows the different segments of the zerodur reference cavity thermal stabilization. Fig. 4.10a shows the zerodur cavity block with three cavities arranged in parallel to each other, housed inside a six-way vacuum cube. The input windows (not shown in the figure) are AR-coated at the appropriate laser wavelengths. The vacuum chamber is pumped by an ion pump (Gamma Vacuum, 3S-CV-1V-5K-N-N) and maintains a pressure of low

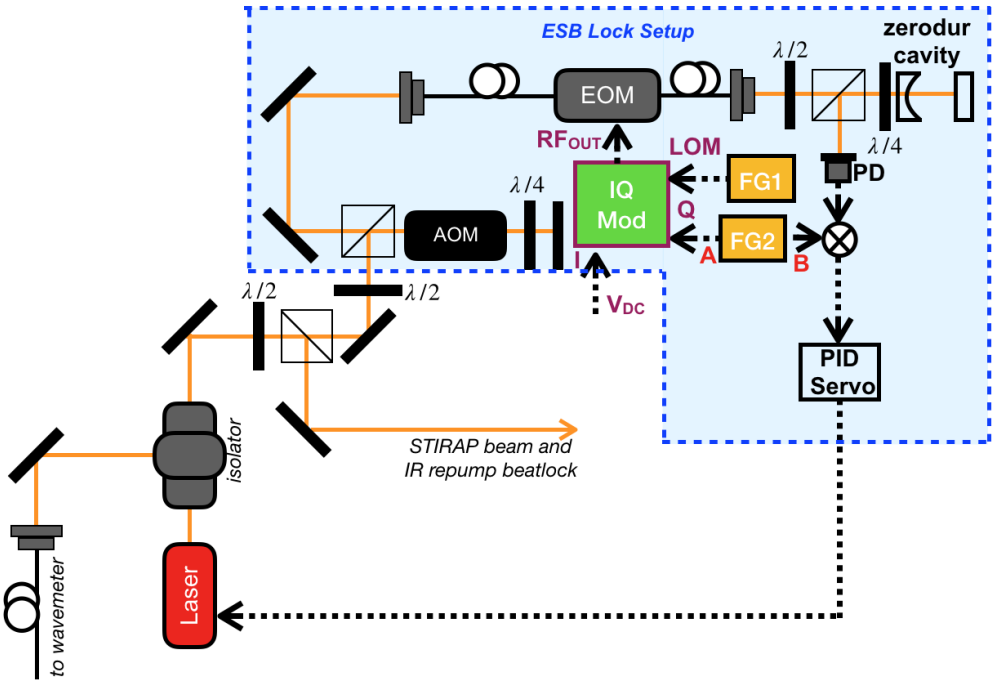

Figure 4.9: The 1428 nm STIRAP IR laser setup. Much of the power generated is sent to the STIRAP beam pathway, and to the repump IR laser optical beatlock setup. Some of the power is sent to the wavemeter and the rest to the zerodur optical cavity for frequency stabilization.

10^{-7}Torr.

Fig. 4.10b shows the vacuum chamber wrapped in heater wires that help regulate the temperature of the chamber body, providing the first stage of temperature control. The chamber is held at a temperature setpoint several degree centigrade above the ambient room temperature. We use a home-built temperature controller circuit shown in Fig. 4.11 powered by a bench-top power supply. A 100 $k\Omega$ thermistor R_{TH} attached to the chamber body monitors its temperature. The temperature setpoint is adjusted using the potentiometer R_{SET}. A drift in the temperature from the setpoint creates a potential difference across the input terminals of the instrumentation amplifier (INA128P). Consequently it outputs a voltage determined by the gain set by R_G that is integrated and fed into the tuning ports of an external power supply (HP3245), which supplies the current through the heater wires for heating the chamber body. As is evident, this circuit can only heat the chamber body, hence the setpoint is selected to be higher than the room temperature.

The vacuum chamber is encased in a temperature controlled copper box, as shown in Fig. 4.10c.

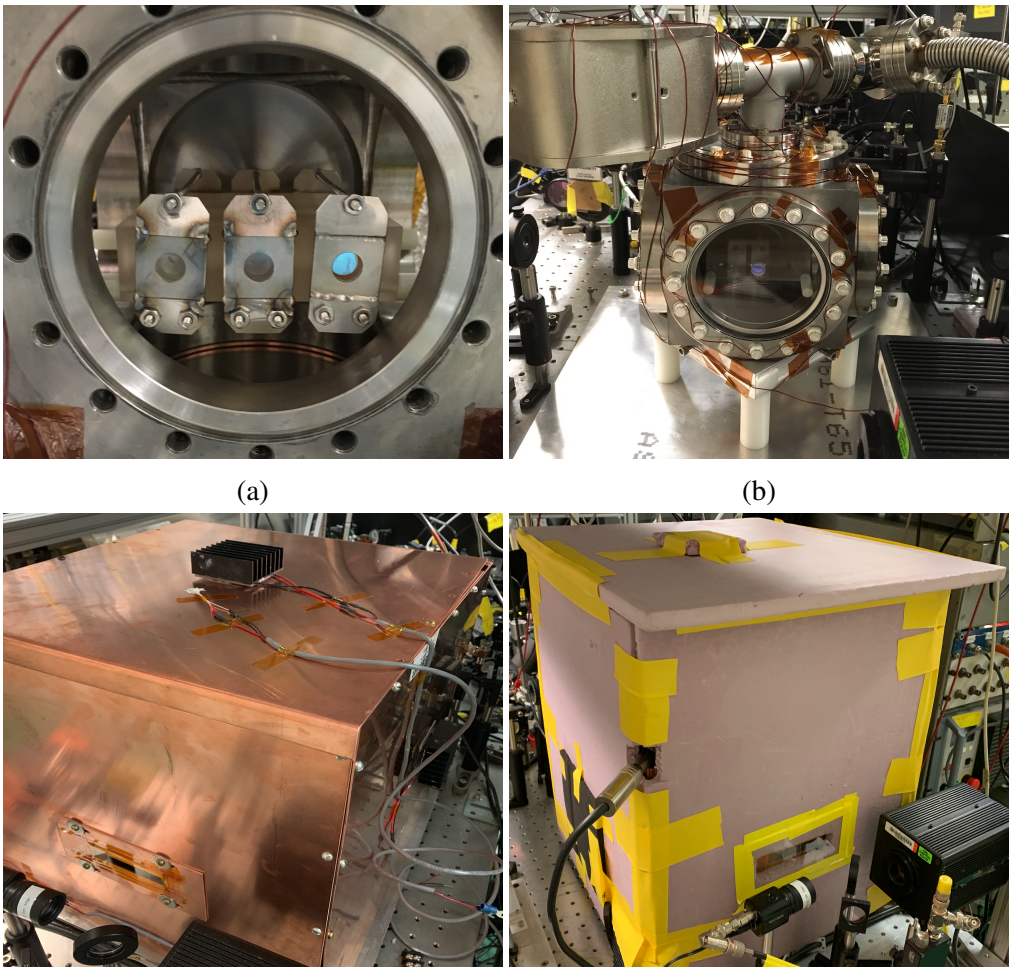

(a) (b)

(c) (d)

Figure 4.10: The zerodur optical reference cavity thermal stablization setup. (a) shows three optical cavities setup in parallel on the zerodur block, as seen through a 6" view-port of the vacuum chamber pumped to low 10^{-7} Torr. (b) the cavity chamber is wrapped in heater wires for temperature control. (c) shows the copper box that covers the zerodur vacuum chamber and is in turn temperature controlled by three TEC modules attached to three sides of the box. (d) the entire setup is covered by insulating panels to reduce the perturbations from room temperature fluctuations.

As can be seen in the figure, three peltier thermo-electric cooler (TEC) modules with heat sinks are attached to three sides of the copper box using thermally conductive epoxy. The three TECs are set in parallel and the temperature controlling current is provided by a TEC controller (ILX Lightwave, LDT-5416). We then apply a final layer of insulation to reduce the effects of room temperature fluctuations, as shown in Fig. 4.10d, that completes our temperature control setup for the zerodur optical reference cavity. Fig. 4.12a shows the temperature data recorded for over a week

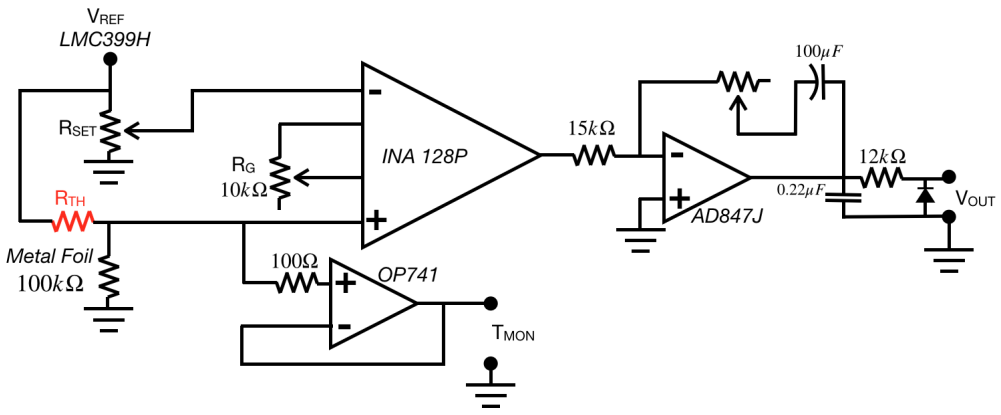

Figure 4.11: The temperature control circuit used for heating and stabilizing the zerodur cavity vacuum chamber. The thermistor R_{TH} senses the chamber temperature. Any deviation from the setpoint set by R_{SET} results in a voltage difference across the inputs of the instrumentation amplifier INA128P, which consequently outputs a voltage that is integrated and sent to the tuning port of an external power supply for heating the chamber.

on a high-precision multi-meter (HP3458A). Fig. 4.12b plots the Allan deviation of the same data over different time-scales. As can be seen, the largest deviation is $\sim 650\,\mu$K/day, and $< 100\,\mu$K over an hour. The daily fluctuation is due to the thermal load generated by the resumption of lab activities every morning. This corresponds to a largest thermal drift of 50 kHz/day in our 1428 nm laser optical reference cavity.

4.3.2.2 1428 nm Repump IR Laser

The Repump IR laser provides the required radiation at 1428 nm for depopulating the $^3D_1$ state and repumping the atoms back into the cooling cycle via the $^3D_1$ to $^1P_1$ transition, for the red-slowing scheme. Fig. 4.13 shows the relevant components of this laser. Most of the light is sent to the atoms for cooling and trapping of radium. Some of the light is picked off of the polarizing beamsplitter (PBS) and combined with the light from the STIRAP IR laser on a beamsplitter (BS) to generate an optical beat pattern for frequency stabilization. The STIRAP IR laser frequency, as described above, is stabilized to a zerodur optical reference cavity. The beat signal is collected on a fast photodiode (Thorlabs, DET08CL) and sent to a phase discriminator (RF Bay, PDF-150) via a directional coupler. The signal out of the coupled port is sent to a spectrum analyzer to monitor

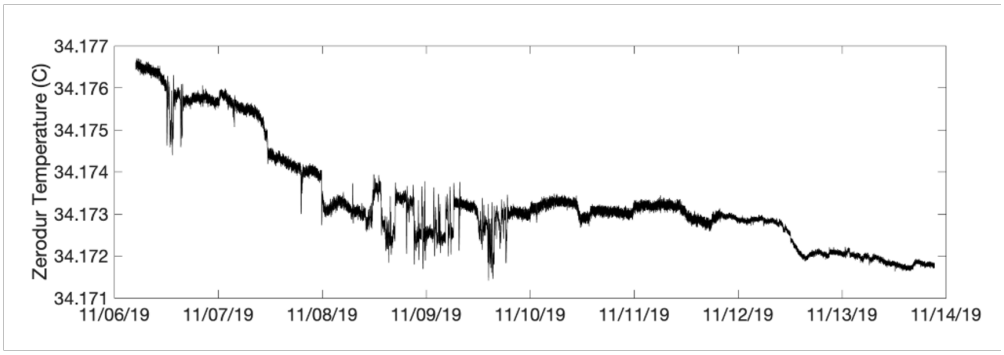

(a)

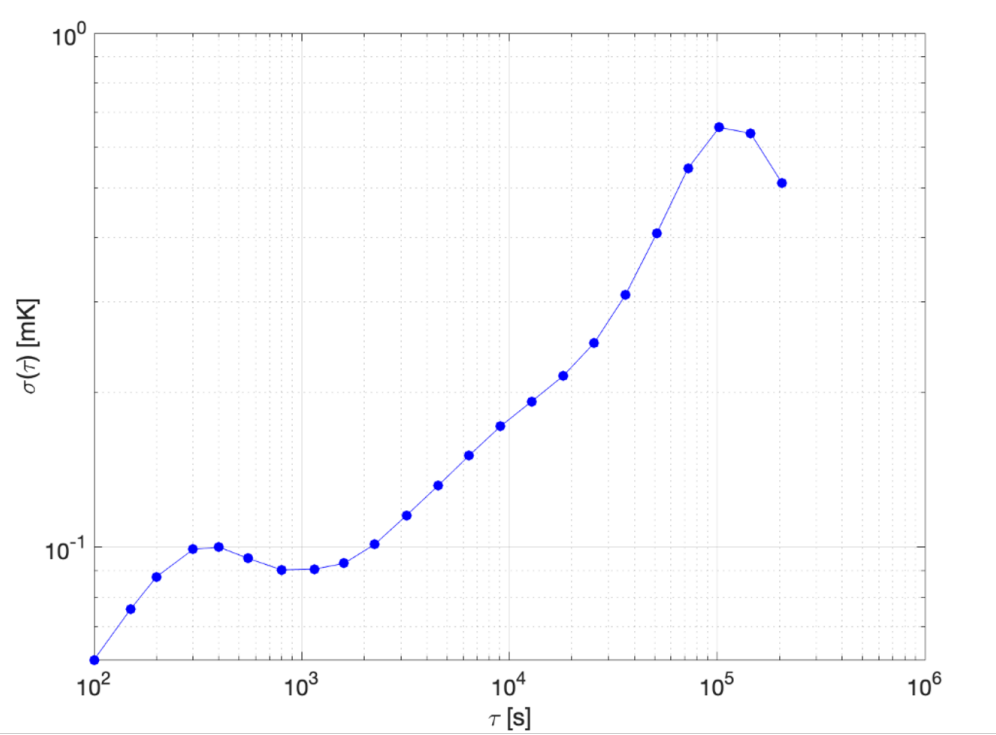

(b)

Figure 4.12: (a) shows the temperature of the zerodur cavity vacuum chamber from 11/06/2019 to 11/14/2019. (b) The plot of the Allan deviation $\sigma(\tau)$ at different observation times τ. With the temperature control in place, the largest deviation is seen at $\sim 650\,\mu$K/day.

the beat signal. The reference frequency for the phase discriminator is supplied by a function generator (Windfreak, USBSynthII). On scanning the Repump IR laser frequency and therefore the beat frequency across the reference frequency, the phase discriminator generates the necessary error signal that is fed into a PID servo (Vescent Photonics, D2-125) that feedbacks on the laser current to stabilize the Repump IR laser frequency.

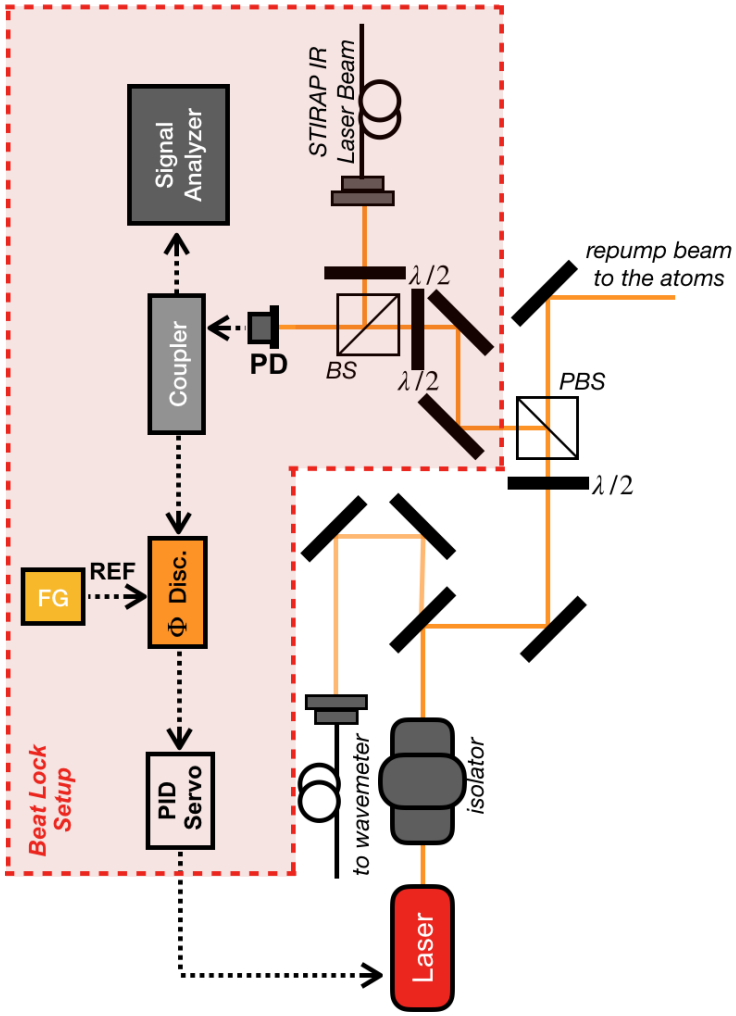

Figure 4.13: The 1428 nm Repump IR laser setup. We show the relevant components of the optical beatlock setup for frequency stabilizing the Repump IR laser. Light from the STIRAP IR laser is combined with portion of the Repump IR laser light on a beamsplitter (BS) and the optical beat pattern collected on a fast photodiode. The phase discriminator compares the beat frequency to a reference frequency and generates the error signal required to lock the Repump IR laser.

4.3.3 483 nm Lasers

Currently, two 483 nm lasers are operational in our lab, as shown in Fig. 4.14. The first, called the STIRAP Blue laser, generates the 483 nm light required for the STIRAP technique for state preparation of the ground state. The second, called the Imaging Blue laser, generates the 483 nm light required for atom absorption imaging in the science chamber.

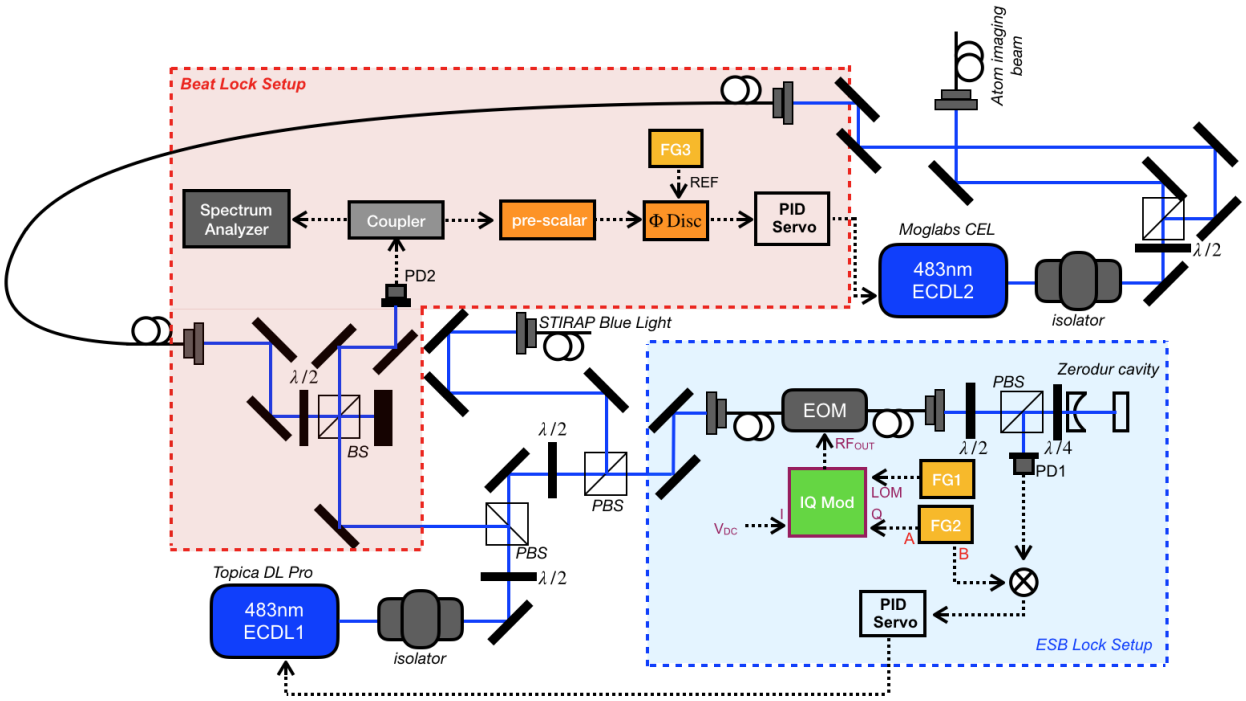

Figure 4.14: The 483 nm laser setups for ECDL1 and ECDL2 are shown. ECDL1 supplies the STIRAP blue light and is frequency stabilized to a zerodur cavity. ECDL2 supplies the imaging beam and is beatlocked to ECDL1.

4.3.3.1 483 nm STIRAP Blue Laser

The STIRAP Blue laser is generated by a Toptica DL Pro external cavity diode laser in littrow configuration, labelled ECDL1 in Fig. 4.14. Fig. 4.14 shows the relevant components of the laser setup. Most of the light is sent to the STIRAP blue beam. Some of the light is sent to the zerodur optical reference cavity for frequency stabilization using the ESB laser frequency locking scheme. The cavity is constructed using a channel on the zerodur block parallel to the cavity for the STIRAP IR laser. The light to the cavity is modulated by a phase modulator (AdvR) which is temperature controlled by a Peltier TEC module. Rest of the light is sent to the wavemeter (not shown in the figure), and the optical beatlock setup for frequency stablizing the Imaging Blue laser.

4.3.3.2 483 nm Imaging Blue Laser

The 483nm imaging light is generated by a Moglabs Cateye Laser (CEL), labelled ECDL2 in Fig. 4.14. Most of the light is sent to the atoms for absorption imaging on the $^1S_0$ to $^1P_1$ transition. Some of the light is sent to the wavemeter for frequency monitoring, and some of the light to the optical beatlock stup. The setup is almost identical to what we use on the 1428 nm Repump IR laser and shown in Fig. 4.14. We do add a pre-scaler (RF Bay, FPS-10-6) before the phase discriminator. This ensures that we scale down the beat frequency into the dynamic range of the phase discriminator, allowing us to set the beatlock offset between the Imaging Blue laser and the STIRAP Blue laser to over 1GHz.

4.3.4 1550 nm Lasers

We use two 1550 nm lasers in our lab. The first of the two, called the 'Bus ODT' laser, is a 100 W, water-cooled, Erbium fiber laser (IPG Photonics), typically operated at 50 W, for transporting atoms from the MOT to our science chamber. This laser, installed in late-2019, replaced our old 50 W Erbium fiber laser (IPG Photonics) due to deterioration in laser output power. This laser is neither polarized nor single-mode.

The second 1550 nm laser, called the 'Holding ODT' laser, is a 30 W, linearly polarized, Erbium fiber laser (IPG Photonics) that is operated in either traveling wave or standing wave configuration for trapping the atoms in between our high voltage electrodes for experimentation in our science chamber.

4.3.5 912 nm Laser

For our spectroscopic study of the $6d7p\,^3F_2$ state in radium, we required 912 nm laser light for probing the $^1D_2 \leftrightarrow {}^3F_2$ transition. For this purpose we used a tunable 915 nm laser diode (Thorlabs M9-915-0300) with a tuning range of 910 nm - 920 nm and an output power of 300 mW. The diode was installed inside a temperature controlled diode mount (Thorlabs LDM90) and

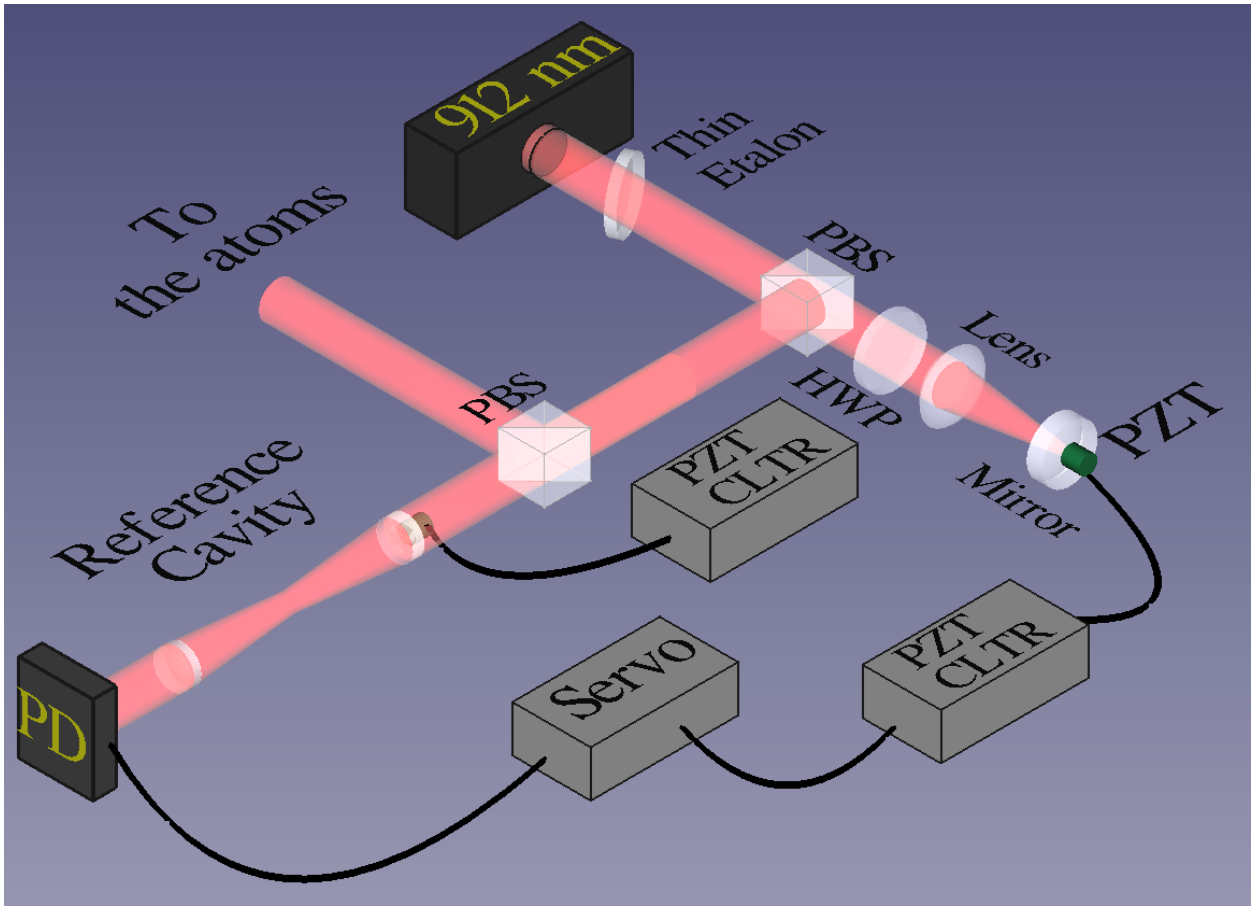

Figure 4.15: The 912 nm laser setup. The laser diode frequency linewidth is narrowed using an external cavity that employs a thin etalon for frequency discrimination. The cavity length is adjusted using a piezo element on the reflecting mirror mount. The PBS and the HWP form the output coupler. A portion of the laser light is sent to an external Invar cavity that can be used both as a scanning cavity to study the laser frequency mode, and for locking the laser frequency using a side-of-the-fringe technique. Most of the power is sent to the atoms.

connected to a laser diode current supply and a TEC controller (ILX Lightwave LDT-3724b) for temperature stabilization.

Our initial search for the above resonance revealed that the laser power density at 912 nm was not high enough to see the atomic fluorescence signal. In order to narrow the laser diode frequency linewidth, we created an external cavity as shown in Fig. 4.15. The cavity is $\sim 10''$ long and consists of a thin etalon ($\sim 200\,\mu$m thick), a polarizing beam splitter (PBS), a half-wave plate (HWP), a cateye lens, and a reflecting mirror mounted on a mirror mount on a translation stage that has a piezo element for controlling the overall length of the cavity. Using a thin etalon for

laser frequency narrowing is an economical solution and has been demonstrated in Refs. [52, 53]. The HWP and the PBS serve as our output coupler. As the laser power builds up inside the cavity, a portion of the power couples out through the PBS. The proper functioning of the cavity can be achieved by tuning the tilt of the thin etalon, the cavity length, the reflecting mirror tilt which controls the retro-reflection into the cavity, and the HWP which controls the balance between the laser power inside the cavity and power that leaves the cavity through the PBS. To test the laser diode frequency linewidth narrowing due to the external cavity, we send some of the output power through an external scanning Invar reference cavity and monitor the output power on a photodiode (PD).

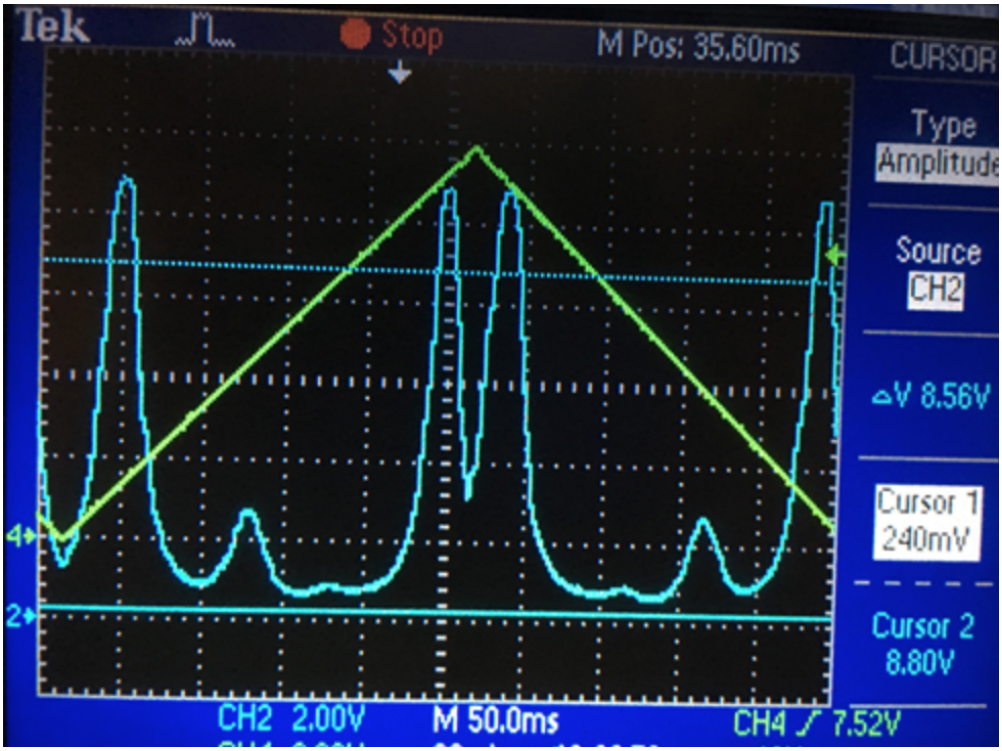

Figure 4.16: The green trace shows the scanning voltage used to scan the Invar cavity length and therefore the cavity resonance. The blue trace is the cavity transmission as recorded on a photodiode (PD).

As shown in Fig. 4.16, the laser beam sent into the cavity is almost single-mode. The green trace in the plot shows the scanning of the Invar cavity length by an externally modulated voltage applied to a piezo actuator mounted on one of the cavity mirrors. The blue trace shows the cavity

transmission. Each peak corresponds to one of the transverse modes of the cavity. We estimate that $\sim$ 80% of the output power is in the desired laser mode (large peak) which is scanned in order to find the resonant frequency for the above mentioned transition. For our purposes we find that using the piezo actuator on the reflecting mirror mount for controlling the laser cavity length allows for fine enough adjustment of the laser frequency. In fact, we can typically tune the laser frequency by $\sim$ 1 GHz without any mode-hops. To further stabilize the laser frequency fluctuations, we use the scanning Invar cavity to loosely "lock" the laser frequency.

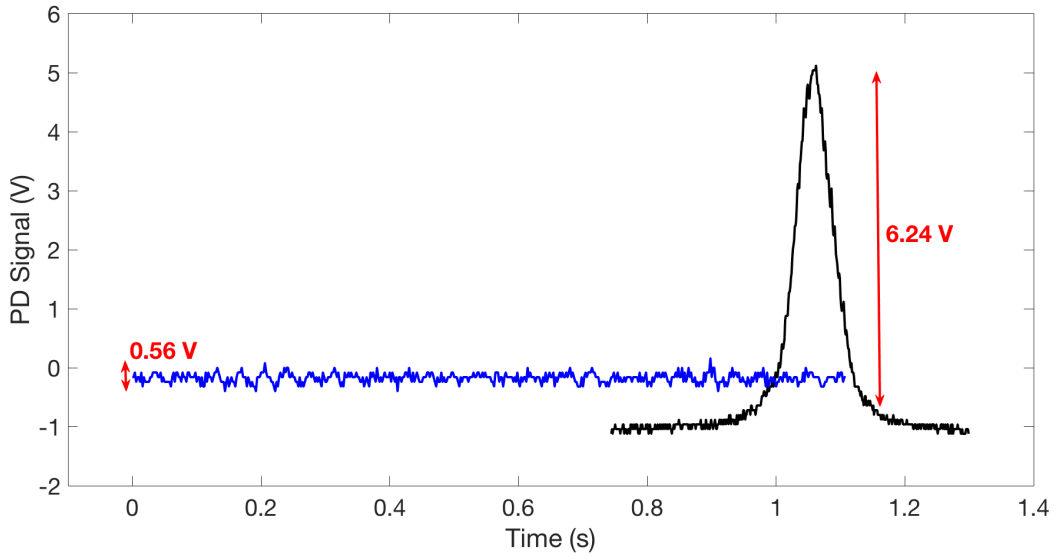

Figure 4.17: The cavity transmission with the laser frequency scanning over a cavity resonance (black trace), and when locked to side of the peak (blue trace), as recorded on a photodiode (PD).

For this, we lock the laser frequency to one side of the fringe, as shown in Fig. 4.17. The cavity transmission signal (black trace) from the PD is fed into a laser controller servo (Vescent Photonics D2-125). We adjust the transmission signal offset and lock the laser frequency to one of the sides of the fringe. The locked cavity transmission signal (blue trace), along with the cavity finesse (14) and the free spectral range (500 MHz), suggest that we can reduce the laser frequency fluctuation to $\sim$ 3 MHz. This quickly assembled setup for the 912 nm laser was enough for the first ever observation of the $^1D_2 \leftrightarrow {}^3F_2$ transition in radium. However, the laser setup required frequent significant maintenance which led us to use the Matisse Ti:Saph instead for generating the 912 nm laser light required for completing the spectroscopic study of the $^3F_2$ state. This is the subject of chapter 8

and is described in much detail there. We believe that this simple external cavity setup using a thin etalon could be made more stable and less sensitive to external perturbations by encasing the cavity in a box, reducing thermal noise and vibrations, and experimenting with a range of etalon thicknesses.

4.4 Pound-Drever-Hall Laser Frequency Locking Scheme

Most of the lasers operational in our lab are frequency stabilized to optical frequency reference cavities. The technique of choice for frequency locking is either the Pound-Drever-Hall (PDH) scheme or the Electronic Sideband (ESB) scheme, both of which are very similar in their operating principle. Here we discuss the PDH scheme and defer the discussion on the ESB scheme to the next chapter. Our treatment closely follows the discussion in Ref. [54]. To illustrate how the PDH scheme works, we take the 714 nm laser setup as an example. Fig. 4.7 shows the implementation of the reflection PDH lock on this laser.

Traditionally, one can use an optical fabry-perot cavity as a frequency filter. Unless the wavelength of the incident beam is twice the cavity length, we do not observe cavity transition. The early laser locks used the slope of the transmission peak for side-of-the-fringe locking. Despite the simplicity of the technique, it suffers from serious drawbacks such as, it couples the laser intensity fluctuations to frequency instability. The PDH scheme, on the other hand, uses the reflection off of the cavity. Unlike the transmission signal, the reflected signal displays a minimum at cavity resonance. And instead of locking to the side-of-the-fringe, this scheme uses the minimum of the signal for frequency locking. The idea is as follows. The derivative of the reflected signal with respect to the laser frequency is opposite on either side of the cavity resonance. This enables us to determine which side of the resonance we are on. This 'error signal' can then be fed into a PID servo for stabilizing the laser frequency.

To see how the error signal is generated, we consider a phase modulated laser beam with an

electric field given by

$$E_i(t) = E_0 e^{(i\omega t + b\sin(\Omega t))} \tag{4.37}$$

where ω is the laser carrier frequency, Ω is the modulation frequency and b the modulation depth. To see the sidebands created on the laser beam, we expand this in terms of the Bessel functions as

$$E_i(t) \approx E_0 \left[J_0(b) e^{i\omega t} + J_1(b) e^{i(\omega+\Omega)t} - J_1(b) e^{i(\omega-\Omega)t} \right] \tag{4.38}$$

where $J_0(b)$ and $J_1(b)$ are the zeroth and the first order Bessel functions of first kind. Here we can see that there are three separate beams incident on the cavity. There is the carrier with frequency ω and the two sidebands at $\omega \pm \Omega$.

The electric field of the reflected portion of a beam incident on a cavity is given by

$$E_r(t) = E_1 e^{i\omega t} \tag{4.39}$$

and the reflection coefficient $F(\omega)$ is given by

$$F(\omega) = E_r/E_i = \frac{r\left(\exp\left(i\frac{\omega}{\Delta\nu_{fsr}}\right) - 1\right)}{1 - r^2 \exp\left(i\frac{\omega}{\Delta\nu_{fsr}}\right)} \tag{4.40}$$

where r is the reflectivity of the cavity mirrors, and $\Delta\nu_{fsr} = c/2L$ is the free spectral range of the cavity with length L.

The electric field of the reflected portion of the phase modulated beam is then given by

$$E_r = E_0 \left[F(\omega) J_0(b) e^{i\omega t} + F(\omega+\Omega) J_1(b) e^{i(\omega+\Omega)t} - F(\omega-\Omega) J_1(b) e^{i(\omega-\Omega)t} \right] \tag{4.41}$$

The corresponding power carried by the reflected beam as measured on a photodiode is given by $P_r = |E_r|^2$, which can be written as

$$
\begin{aligned}
P_r \approx\ & P_c|F(\omega)|^2 + P_s\left(|F(\omega+\Omega)|^2 + |F(\omega-\Omega)|^2\right) \\
& + 2\sqrt{P_c P_s}\left(\mathrm{Re}\left[F(\omega)F^*(\omega+\Omega) - F^*(\omega)F(\omega-\Omega)\right]\cos\Omega t\right. \\
& \left.+\mathrm{Im}\left[F(\omega)F^*(\omega+\Omega) - F^*(\omega)F(\omega-\Omega)\right]\sin\Omega t\right)
\end{aligned} \tag{4.42}
$$

where we ignore terms of order 2Ω and above. $P_c = J_0^2(b)|E_0|^2$ is the power in the carrier, and $P_s = J_1^2(b)|E_0|^2$ is the power in the first-order sidebands. We notice two terms oscillating at Ω in the above expression. These terms sample the phase of the reflected beam and therefore determine which side of the cavity resonance the laser frequency is on. Suppose we operate under the assumption that the carrier is resonant on the cavity and the sidebands are not. Moreover, the modulation frequency is large[3] enough that the sidebands are fully reflected; $F(\omega \pm \Omega) \approx -1$ and we have

$$
F(\omega)F^*(\omega+\Omega) - F^*(\omega)F(\omega-\Omega) \approx -i2\mathrm{Im}(F(\omega)) \tag{4.43}
$$

.

In this case only the $\sin\Omega t$ survives, and can be isolated using a mixer. Demodulating the signal at $\sin\Omega t$, and low-pass filtering it, we get an error signal given by

$$
\epsilon = -2\sqrt{P_c P_s}\mathrm{Im}\left[F(\omega)F^*(\omega+\Omega) - F^*(\omega)F(\omega-\Omega)\right] \tag{4.44}
$$

For the 714 nm laser, the laser beam incident on the ULE cavity is phase modulated by an EOM (Thorlabs, EO-PM-NR-C1) to create 10MHz sidebands about the carrier frequency. The modulation is provided by channel A of a function generator (Rigol, DG-4000). The reflected signal off of the cavity is collected on a photodiode and demodulated by mixing with the phase-locked output from channel B of the function generator. The relative phase is adjusted to obtain an optimal error signal similar to what is shown in Fig. 4.18. The lock point is selected at $(\omega - \omega_0)/\Delta\nu_{fsr} = 0$. The

[3]More precisely, we assume $\Omega >> \Delta\nu_{fsr}/\mathcal{F}$, where $\mathcal{F} = \pi\sqrt{r}/(1-r)$ is the finesse of the optical cavity.

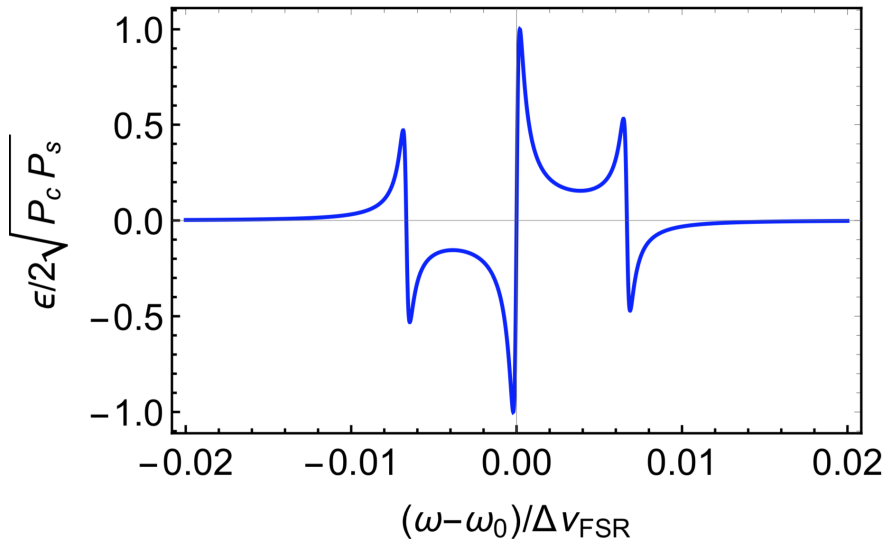

Figure 4.18: Normalized error signal $\epsilon/2\sqrt{P_c P_s}$ plotted as a function of the detuning of the laser frequency ω from the cavity resonance ω_0 in terms of the free spectral range $\Delta\nu_{fsr}$ = 1500MHz. The modulation frequency Ω is set to 10MHz, and the finesse is 31,000.

error function is fed into the matisse laser control module which feeds back on the fast piezo driven etalon to keep the laser locked to a TEM_{00} mode of the ULE cavity. Typically, when optimized, the laser linewidth is measured to be $\sim$ 70 kHz.

CHAPTER 5

ELECTRONIC SIDEBAND (ESB) OFFSET LOCK FOR PRECISION SPECTROSCOPY IN RADIUM

Laser frequency stabilization techniques are ubiquitous in applications such as precision spectroscopy, laser cooling and trapping of atoms and molecules, and quantum information science. Laser frequency is stabilized by comparing the frequency of the laser to a stable frequency reference; converting deviations of the laser frequency from the stable reference into an “error signal" that allows feed-back on to the laser to keep it “locked" to that reference. The choice of a frequency reference can be a stabilized optical cavity, atomic transitions in a saturated absorption spectroscopy setup, another frequency stabilized laser, or some other reference. There are many ways of generating the error signal. In a side-of-the-fringe locking scheme, one locks the laser frequency to the side of an optical cavity transmission peak - using the slope of the cavity resonance as the error signal. This has certain drawbacks, most importantly, it couples any laser intensity fluctuations to its frequency instability. A preferred and an improved method is the Pound-Drever-Hall (PDH) locking scheme [54, 55]. This involves the phase modulation of the laser beam incident on a optical cavity reference. The reflected signal off of the cavity is collected on to a photo detector and demodulated to generate an error signal. This method overcomes some of the difficulties associated with the side-of-the-fringe locking scheme. It is often desirable to have a tunable laser frequency lock. There are a variety of ways to achieve this. Most simply, with an acousto-optic modulator (AOM), one can achieve several hundreds of MHz of frequency tunability[56]. A tunable reference cavity length[57], and an offset phase locking to another frequency stabilized laser[58], achieve similarly tunable frequency locks. Here we present a locking scheme that can have multiple GHz of frequency tunability and is a simple extension to the PDH lock setup. The electronic side-band (ESB) offset lock allows for a broadband tunable laser frequency lock[59, 60]. With a fiber coupled EOM, frequency tunability up to 4 GHz has been demonstrated[60]. In our case, we describe the use of an IQ modulator for generating the complex frequency modulation required for the ESB

offset lock. This enables us to lock our laser to the same cavity mode, offset by as much as 6 GHz, which is the limit set by the bandwidth of our IQ modulator (Analog Devices, LTC5588-1). This allows us to compare the frequencies of different transitions to the same cavity mode and determine the differences very precisely, enabling very precise spectroscopy of rare isotopes.

Here we describe a method for implementing a broadband ESB offset lock using an optical cavity frequency reference and apply it to the precision spectroscopy of radium isotopes. We perform an improved measurement of the frequency difference between the $^1S_0$ to $^3P_1$ transition in ^{226}Ra and $^1S_0$ [F=1/2] to $^3P_1$ [F=3/2] transition in ^{225}Ra. The relevant energy levels for slowing and trapping of a radium MOT are shown in Fig. 8.1a.

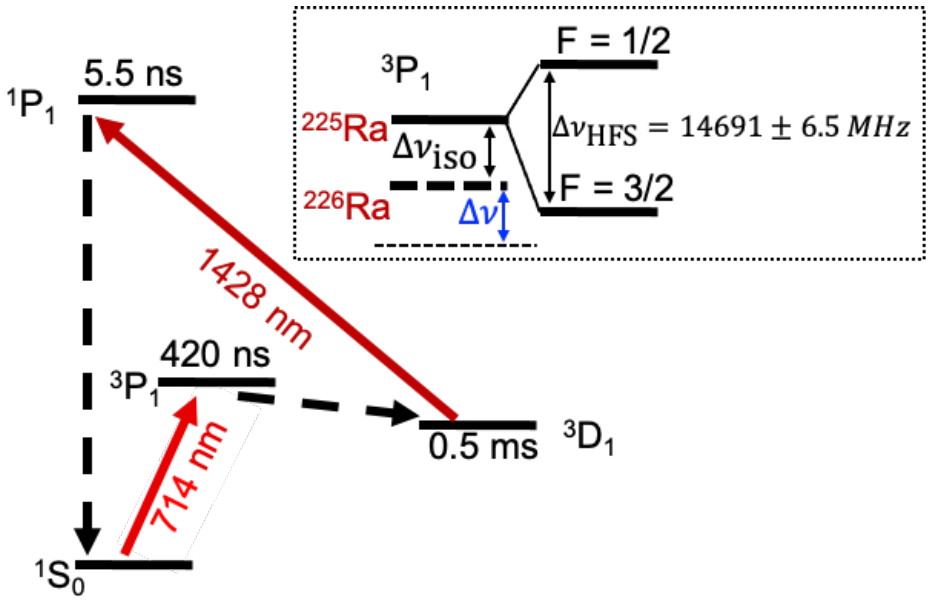

Figure 5.1: The atom slowing and cooling scheme used to trap a MOT of ^{226}Ra and ^{225}Ra. The $^1S_0 \rightarrow {}^3P_1$ transition requires a single repump laser 1428 nm for the $^3D_1 \rightarrow {}^1P_1$ transition to close the cooling cycle. Inset: The frequency difference $\Delta\nu$ between the MOT transitions for the two isotopes is shown. Also shown are the isotope shift for the transition, $\Delta\nu_{\mathrm{iso}}$, and the hyperfine splitting $\Delta\nu_{\mathrm{HFS}}$.

5.1 Generating the Sidebands

An IQ modulator splits the input carrier RF signal into its in-phase and quadrature components. With appropriate choices of inputs into the I and Q ports it can approximate frequency modulation

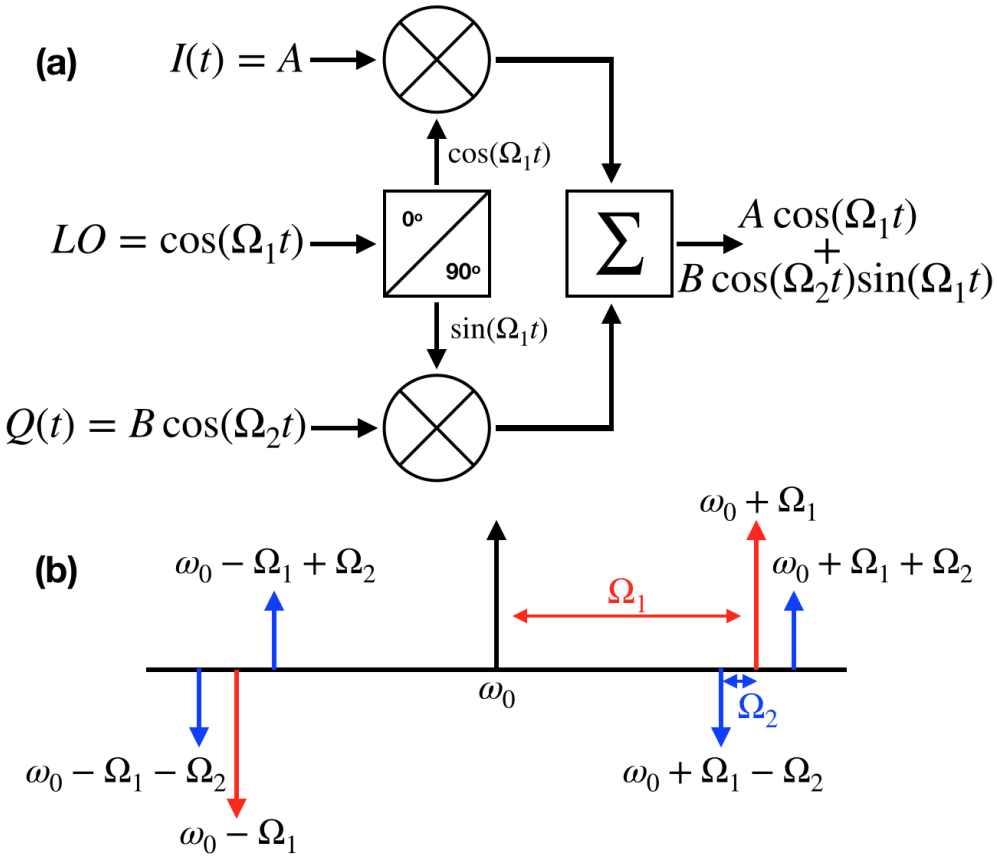

Figure 5.2: (a) A schematic showing the generation of sidebands using an IQ modulator. An RF signal at Ω_1 fed into the LO port is split into the in-phase and quadrature components. The quadrature part is modulated with an RF signal at Ω_2 and combined with the in-phase component. (b) The frequency sidebands created on an input laser frequency at ω_0 by the IQ modulated EOM up to $O(J_1)$ in Eq. 5.2.

in a broadband application. In our case, to generate the necessary frequency sidebands, the carrier with frequency Ω_1 is fed into the LO port of the IQ modulator. A constant DC voltage is fed into the I port, while a modulation signal at Ω_2 is fed into the Q port. The resultant combination of the in-phase and quadrature signals is then applied to the EOM. The principle of operation of an IQ modulator is shown in Fig. 5.2.

The electric field of a laser beam of frequency ω and amplitude E_0 can be written as

$$E(t) = E_0 e^{i\omega t} \tag{5.1}$$

For the ESB offset lock scheme, the IQ modulated signal $A\cos(\Omega_1 t) + B\cos(\Omega_2 t)\sin(\Omega_1 t)$ is

amplified and applied to the EOM. The modulated electric field of the laser beam is then given by

$$E(t) = E_0 e^{i\{\omega t + A\cos(\Omega_1 t) + B\cos(\Omega_2 t)\sin(\Omega_1 t)\}} \tag{5.2}$$

Where, Ω_1 and Ω_2 are the respective modulations into the LO and the Q ports of the IQ modulator with associated modulation depths A and B. Expanding the above expression in terms of Bessel functions, up to terms of $O\left(J_1^2\right)$, enables us to see the associated sidebands generated.

$$\begin{aligned}
E(t) \approx E_0 \Big\{ & J_0(A)J_0^2(B/2)e^{i\omega t} && (5.3)\\
& + iJ_0^2(B/2)J_1(A)\left(e^{i(\omega+\Omega_1)t} + e^{i(\omega-\Omega_1)t}\right) && (5.4)\\
& + J_0(A)J_1^2(B/2)\left(e^{i(\omega+2\Omega_1)t} + e^{i(\omega-2\Omega_1)t} - e^{i(\omega+2\Omega_2)t} - e^{i(\omega-2\Omega_2)t}\right) && (5.5)\\
& + J_0(B/2)J_1(B/2)\left[J_0(A) - 2J_1(A)\sin(\Omega_1 t)\right]\times && (5.6)\\
& \left(e^{i(\omega+\Omega_1-\Omega_2)t} + e^{i(\omega+\Omega_1+\Omega_2)t} - e^{i(\omega-\Omega_1+\Omega_2)t} - e^{i(\omega-\Omega_1-\Omega_2)t}\right)\Big\} && (5.7)
\end{aligned}$$

Here we see the carrier at ω and the different sidebands generated. Up to terms linear in J_1, we see the six sidebands generated as shown in Fig. 5.2. We also note that up to the $O\left(J_1^2\right)$ terms in Eq. 5.7, we observe amplitude modulations at Ω_1. This is a consequence of using an IQ modulator for phase-modulations, there is always some amplitude modulation. For the current purposes, we focus our attention on the modulation at $\omega - \Omega_1$ and the two sidebands generated at $\omega - \Omega_1 - \Omega_2$ and $\omega - \Omega_1 + \Omega_2$. This is similar to the sidebands generated for the PDH scheme. The modulation at Ω_2 generates the error signal, while the modulation at Ω_1 provides the tunability of the lock. Compared to a PDH scheme with a modulation at frequency Ω_1 and with modulation-depth A, the relative size of the error signal (up to $O\left(J_1^2\right)$) is given by

$$D_{ESB}/D_{PDH} = J_0^3(B/2)J_1(B/2)\left[1 - \frac{2J_1(A)}{J_0(A)}\sin(\Omega_1 t)\right] \tag{5.8}$$

By tuning Ω_1 we change the offset of the laser frequency from the resonant optical cavity mode and therefore tune the laser frequency. The collision of the different sidebands as you tune the EOM offset frequency Ω_1 poses a potential issue for broadband applications. In the above case,

for large $\Omega_1 = \Delta\nu_{FSR}/2$, we notice the collision of the sidebands with opposite phases at $\omega + \Omega_1$ and $\omega - \Omega_1$, where $\Delta\nu_{FSR}$ is the free spectral range of the optical cavity. This can be remedied by adding an AOM in the pathway to move the relevant mode away from a potential collision to keep it at the desired frequency and prevent any lock degradation as a result.

5.2 Characterizing the ESB Lock Performance

To characterize the performance of the ESB offset lock we test it in our 483 nm Toptica DL Pro external cavity diode laser (ECDL1) setup. The setup is shown in Fig 5.3.

5.2.1 ESB Lock Test Setup

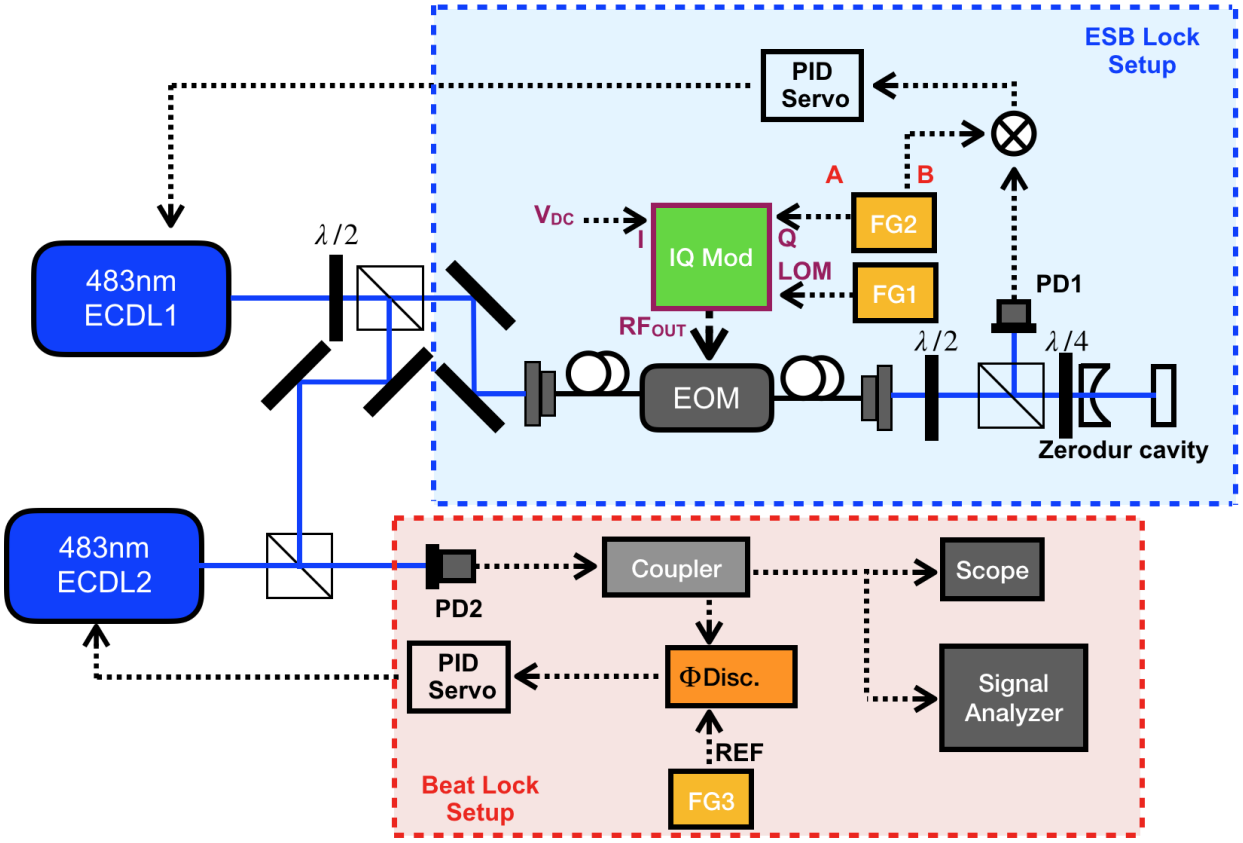

Figure 5.3: ESB offset lock setup for 483 nm ECDL1 laser and the beat-lock setup for ECDL2.

Portion of the 483 nm ECDL1 laser power is sent to a fiber coupled EOM (AdvR, KTP phase modulator). The modulated light is sent to a zerodur optical reference cavity housed in a vacuum

chamber held at $\sim 10^{-9}$torr and temperature controlled to a drift of less than 1mK/day. The IQ modulation scheme for generating the sidebands and locking is identical to what is described for the 714 nm laser setup. Here we feedback on the DC component of the laser current to stabilize its frequency. We beat-lock another 483 nm (ECDL2) (Moglabs, CEL) to the locked ECDL1. The beat pattern is collected on a fast photo detector (PD2), and sent to a phase comparator (RF Bay, PDF-150) via a directional coupler. The reference for the phase comparator comes from an RF synthesizer (FG3) (Windfreak, USBSythnII). This generates an error signal for locking the ECDL2 laser. The beat pattern is sampled using the coupled port of the directional coupler and monitored on a signal analyzer, as well as a scope. For this test, the beat reference was set to 100 MHz, and down converted to 20 kHz by mixing the beat pattern with a function generator output at 99.98 MHz. We noticed that locking the ECDL2 introduced extra noise in the beat pattern, so for the purposes of testing the ESB offset lock's performance, it was kept free-running.

To test the performance of the ESB offset locking scheme, we compare it to the PDH lock. For the PDH lock, we simply bypass the EOM and send the laser beam straight to the cavity. The AC component of the laser current for ECDL1 is dithered using channel A of FG2, and the cavity reflection signal demodulated using channel B to generate the PDH error signal, which is then low-pass filtered and fed to the same PID servo (SRS, SIM960) as for the ESB offset lock. Fig. 5.4 shows the power spectral density (PSD) for the beat pattern with the ECDL1 laser locked using either the PDH or the ESB offset locking scheme. On the ESB lock noise spectrum, we note the PID servo drop-off at 100 kHz. We also note that the sub-MHz noise in the ESB lock is about 1.5 dB higher than the noise in the PDH lock. We have not tested the ESB locked ECDL1 for atomic spectroscopy, but when implemented in our atom cooling and slowing setup using the 714 nm transition, we do not notice any significant enhancement of the measured laser linewidth, which is consistently ~70 kHz, or any significant adjustments required in our day to day operations. It is possible that due to the difference in the phase modulators, and the overall setup used for the 714 nm and the 483 nm laser locks, the noise on the ESB lock might be different in the two systems. We intend to study the effects of the higher noise in the ESB lock on narrow transitions (few MHz

wide) in our 483 nm system, for instance in our stimulated raman adiabatic passage (STIRAP) spectroscopy in radium isotopes.

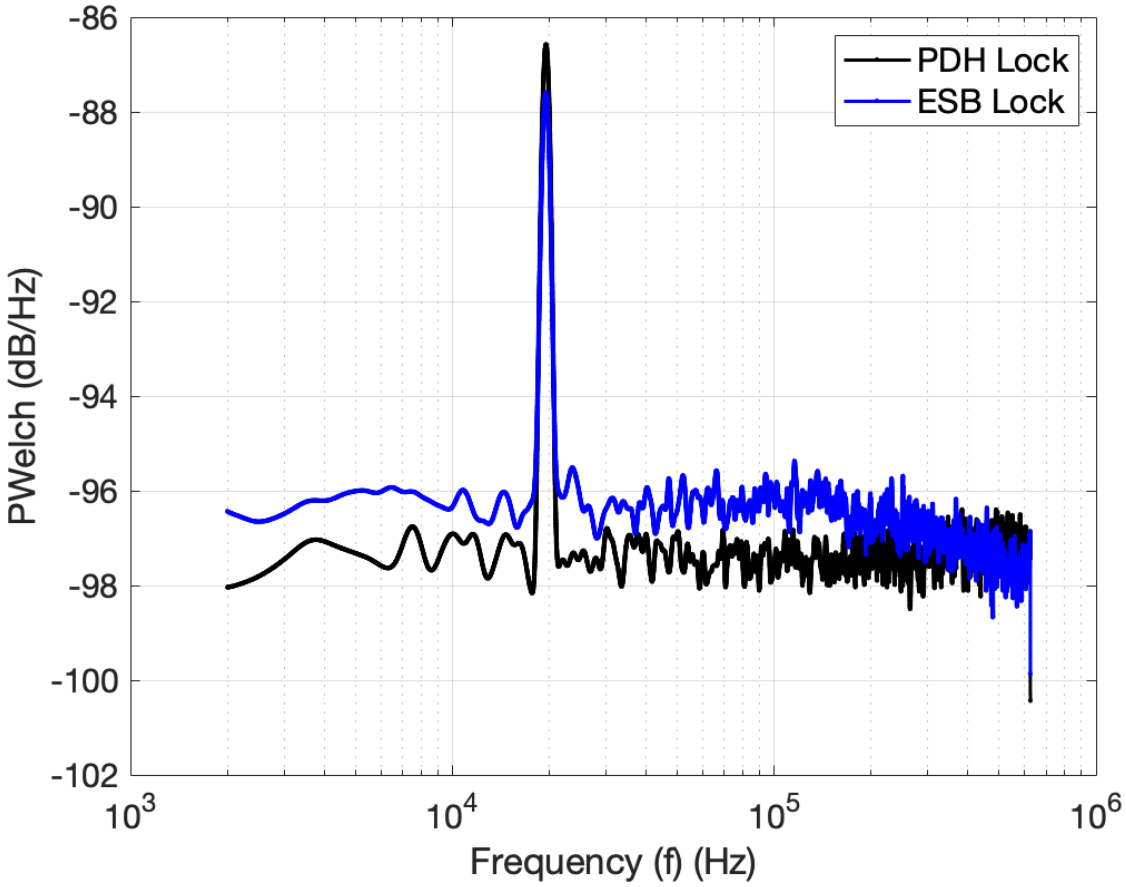

Figure 5.4: Beat pattern power spectral density (PSD) for the ESB offset lock and the PDH lock. The optical beat pattern at 100MHz is collected on a fast photo-detector PD2 and down converted to 20kHz to study the sub-MHz noise in our laser locks.

5.2.2 Optimizing the Lock

Since the ESB locking scheme utilizes an EOM for the laser beam modulation, it is susceptible to certain sources of lock instabilities. One of the most prominent source of noise in the lock is residual amplitude modulation (RAM). The dependence of the RAM from an EOM on its temperature and the input polarization of the incident beam has been studied extensively[61]. There are a number of ways for reducing the RAM in the laser beam, ranging from active stabilization[62] to tuning of the

EOM temperature and laser input polarization for controlling the RAM[61]. For this purpose, the EOMs used for our ESB locks are thermally stabilized. The EOMs are attached to a base plate that is temperature controlled using a peltier module and a TEC controller (LDT-5412, ILX). The RAM in our laser beam manifests as a DC offset drift of our error signal. We tune the temperature set point of the EOM base-plate to minimize the offset drift. In addition to the temperature of the EOM, input polarization of the incident laser beam has to be optimized. This aligns the polarization of the beam along one of the principal axes of the crystal. This can be achieved, in our case, by using a quarter wave-plate ($\lambda/4$) followed by a half wave-plate ($\lambda/2$). Currently, we do not implement any active suppression of RAM since it is well controlled using the above methods.

Certain EOMs, such as the one used in our 714 nm ESB lock setup, are susceptible to significant photo refractive effect at high input optical powers. In our case, as the input power exceeds 6 mW, we notice a reduction in the cavity transmission due to destructive interference in the bulk of the crystal. Therefore, the input power needs to be set below the threshold where the photo refractive effect occurs - which is more than sufficient for our needs.

5.3 MOT Cutoff Measurements in ^{225}Ra and ^{226}Ra

We now describe the implementation of the ESB offset locking in our 714 nm laser and its application to precision spectroscopy in ^{226}Ra and ^{225}Ra.

5.3.1 ESB Offset Lock Setup

The experimental setup for the ESB offset locking of the 714 nm laser and the MOT cutoff frequency measurements is shown in Fig 5.5. We generate ~1.3 W of 714 nm light from a Sirah Matisse Ti:Sapphire ring cavity laser pumped using a diode-pumped solid state (DPSS) laser (Lighthouse Photonics, Sprout) set to 9.5 W. Most of the light is sent to our laser slowing and trapping setup to trap the radium atoms. A small sample of ~4 mW, is sent to a fiber-coupled EOM (EOSpace). The EOM provides the modulation to the laser beam which is sent to a high finesse ULE optical cavity for its frequency stabilization. The ULE cavity is held inside a ultrahigh vacuum (UHV) chamber

and temperature stabilized such that the cavity resonance frequency drifts less than 50 kHz every 2 weeks.

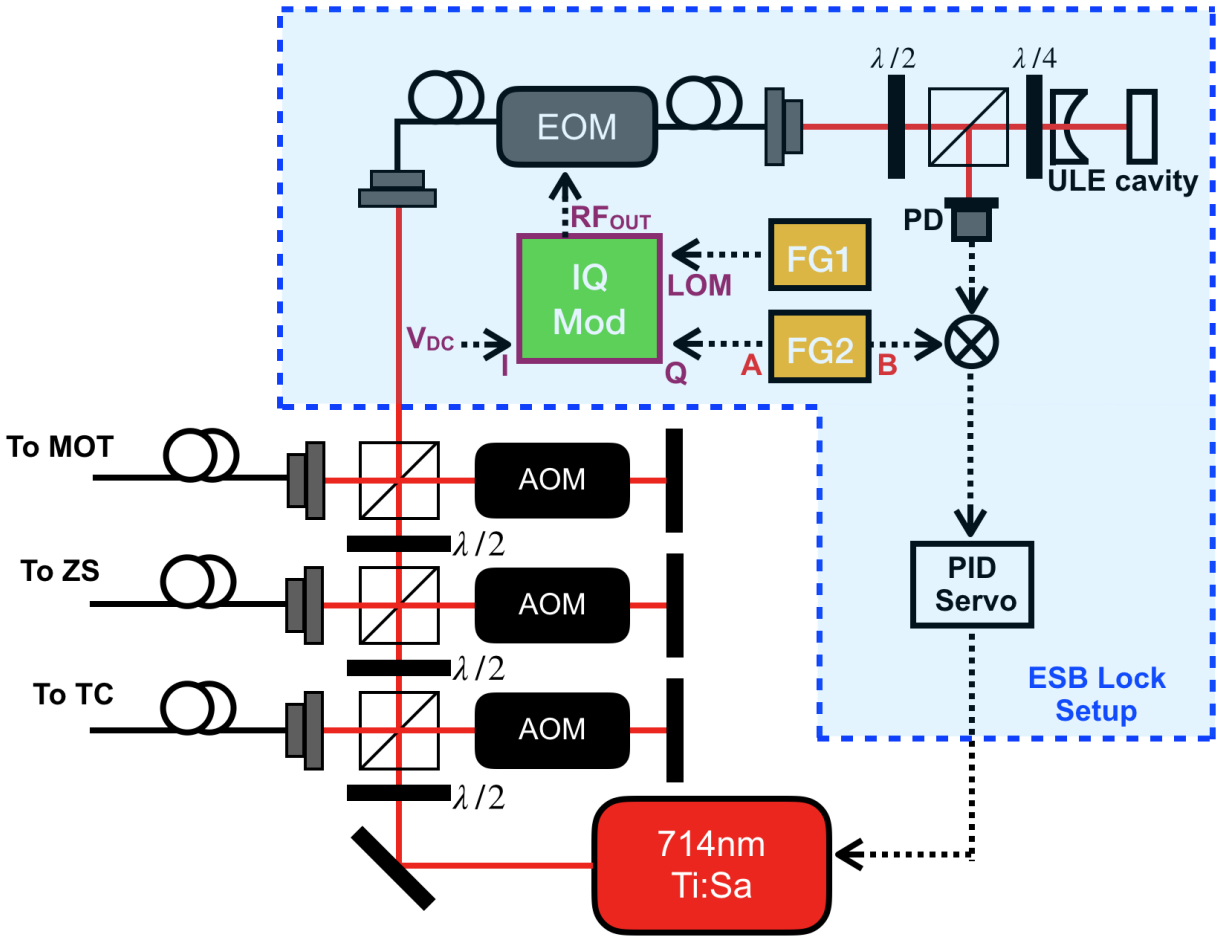

Figure 5.5: ESB Lock setup for our 714 nm Ti:Sa ring cavity laser. The EOM is driven with the output of the IQ modulator that modulates the laser beam incident on the ULE reference cavity.

The modulation of the RF signal sent to the EOM is generated from by an IQ modulator (Analog Devices, LTC5588-1). The output of an RF synthesizer (Windfreak, SynthUSBII) (FG1) is sent into the LOM port of the IQ modulator. This provides the modulation at Ω_1 which offsets the laser frequency from one of the resonant cavity modes. A constant 0.5 VDC is applied to the BBPI and the BBMQ ports. The output of one of the channels (A) of our two-channel RF generator (Rigol DG4162) (FG2), at 10 MHz and 0.5 VDC offset, is fed into the BBQI port of the IQ modulator. This provides the modulation at Ω_2 for generating the error signal for the laser lock. The BBPM and the LOP ports are terminated at 50 Ω.

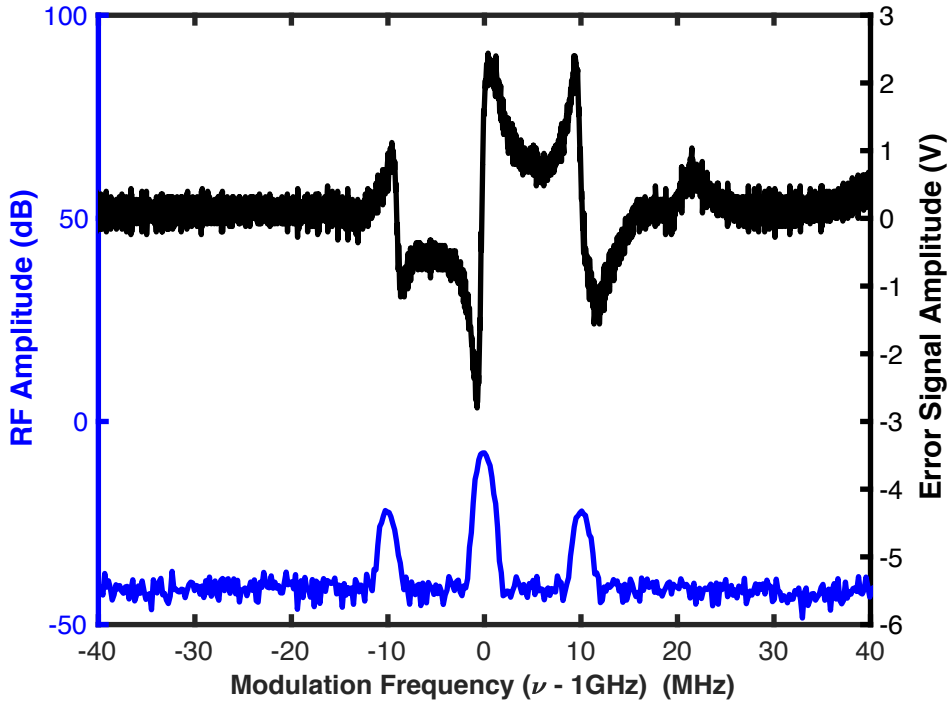

Figure 5.6: Blue Trace: Output of the IQ modulator showing the modulation sideband at Ω_1 with the two sidebands at $\Omega_1 \pm \Omega_2$. Ω_1 is set to 1 GHz and Ω_2 to 10MHz. Black Trace: The error signal generated after demodulating the reflected optical signal at Ω_2.

The output of the modulator is sent to an RF amplifier (Mini-Circuits, ZHL-4W-422+) and then to the EOM. The blue trace in Fig. 5.6 shows a typical output from the IQ modulator. Here we see the offset sideband at 1 GHz (Ω_1) and the corresponding sidebands about it at 10 MHz (Ω_2). The reflected light from the cavity is collected on a fast photodiode (PD). The signal is sent to a mixer and demodulated using the output from the second channel (B) on our RF generator (FG2), which is phase-locked to the first channel (A). By tuning the relative phase, the error signal is optimized to look as shown by the black trace in Fig. 5.6. The error signal is low-pass filtered and sent to a PID servo inside the Sirah Matisse laser control box, which feeds-back on the fast etalon in the ring cavity and locks the laser frequency to a ULE cavity's TEM_{00} mode. While the long term drifts are greatly reduced by the temperature stabilized ULE cavity, the fast laser linewidth, when locked, is typically measured to be ~70 kHz, limited by the bandwidth of the laser controller servo.

5.3.2 MOT Cutoff Measurement Setup

Most of the 714 nm laser power is sent to the transverse cooling (TC) chamber for collimating the atomic beam coming out of the oven, followed by the Zeeman slower (ZS) to slow the atoms down to MOT capture velocities, and finally to the magneto-optical trap (MOT) to trap the radium atoms. More details about the experimental design and the slowing and trapping of atoms can be found in Ref. [63] The acousto-optic modulator (AOM) for the MOT beam is switched between the probe and the loading phase using an RF switch. An experimental cycle is set to 25 s, of which we probe for 300 ms, as set by the camera exposure. During the loading phase, the MOT laser frequency is set 2×79 MHz red-detuned from resonance using a voltage controlled oscillator (VCO). During the probe phase, we scan the RF frequency applied to the MOT AOM using an RF synthesizer (Windfreak, USBsynthII) and measure the MOT fluorescence on an EMCCD camera (Andor, Luca).

For ^{225}Ra, we further offset the laser frequency from the cavity reference mode by 2629.95MHz. This is achieved by increasing the offset frequency Ω_1 (FG1) by the same amount. This then highlights the broadband tunability of this lock. Locking to the same cavity reference mode, we simply increase the laser frequency offset to probe transitions that are several GHz apart. Using the same cavity mode eliminates any systematic or statistical frequency errors introduced by referencing the laser to different cavity modes.

5.3.3 Data Analysis

We measure the MOT fluorescence signal for ^{225}Ra and ^{226}Ra during the probe phase. For each isotope, we collect 5 background images before and after the frequency scan. We scan the MOT probe frequency in steps of 20kHz - 50kHz, by scanning the RF drive frequency of the MOT AOM during the probe phase, and take atom fluorescence images at each frequency. The atom images are background subtracted to extract the atom fluorescence counts.

The MOT cutoff frequency is defined as the frequency at which the MOT fluorescence vanishes. As shown in Fig. 5.7a, after a certain frequency the MOT fluorescence counts drop to the background

level. To determine the MOT cutoff frequency, we assume the fluorescence signal is linear in the region of the cutoff, and fit the following fit function to the segment of the MOT fluorescence curve containing several data points just before the fluorescence curve plateaus:

$$y(\nu) = \text{Max}\left[a_1(\nu - a_2), a_1(a_3 - a_2)\right] \tag{5.9}$$

Here we fit the fluorescence counts $y(\nu)$ as a function of the MOT AOM frequency ν to the maximum of a line with an adjustable slope a_1, and an x-intercept a_2 and a line with a constant y-offset. a_3 is the frequency at which the two lines intersect and in this case, defined as the MOT cutoff frequency. Only data points near the cutoff are useful to the fit, since beyond this the linear approximation fails. Thus, we studied the effects of the number of data points included on the fit values of the MOT cutoff frequency a_3. This is discussed in the following section.

5.3.4 Results and Discussion

The MOT fluorescence data for the two isotopes are shown in Fig 5.7. From the fits we determine the MOT cutoff frequency a_3 for ^{226}Ra with their statistical uncertainties to be $\nu_{226} = 162.862(20)$ MHz, and for ^{225}Ra to be $\nu_{225} + 2629.95\text{MHz} = 162.785(102)\text{MHz}$. The frequency difference for the MOT transition between the two isotopes is therefore determined to be 2630.037MHz with a statistical uncertainty of $\sigma_{\Delta\nu,stat} = 0.104\text{MHz}$

To select the number of data points to include in our fit, we study the effects of including certain number of data points on the fit values of MOT cutoff frequency a_3. For example, for our ^{226}Ra dataset at 25.8 mW MOT probe power, we fit the dataset containing data points between the peak of the dataset and the eighth from the last data point and observe how the fit values for a_3 change. We expect the fit values for a_3 to converge to the true value near the actual MOT cutoff frequency, where the linear approximation holds, and to diverge as we include more points and as this approximation breaks down. As shown in Fig. 5.8, the MOT cutoff frequency fit values diverge by more than one standard deviation after more than 15 data points are included in the fit (including the last 8 data points). We therefore fit for the MOT cutoff frequency a_3 using the last

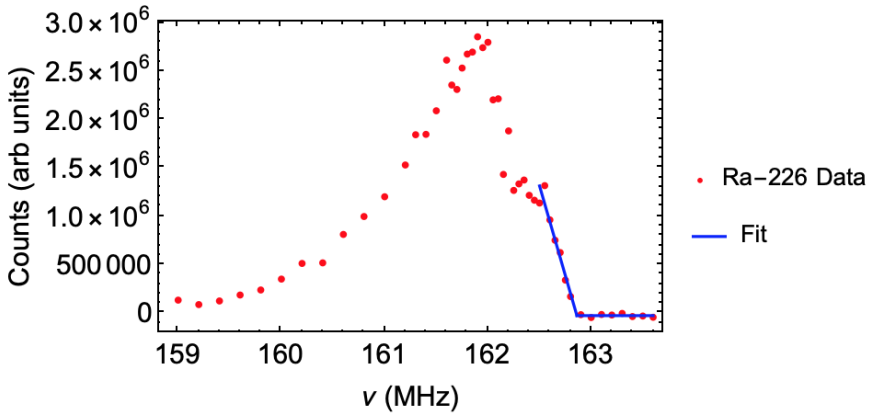

(a) MOT cutoff data for ^{226}Ra

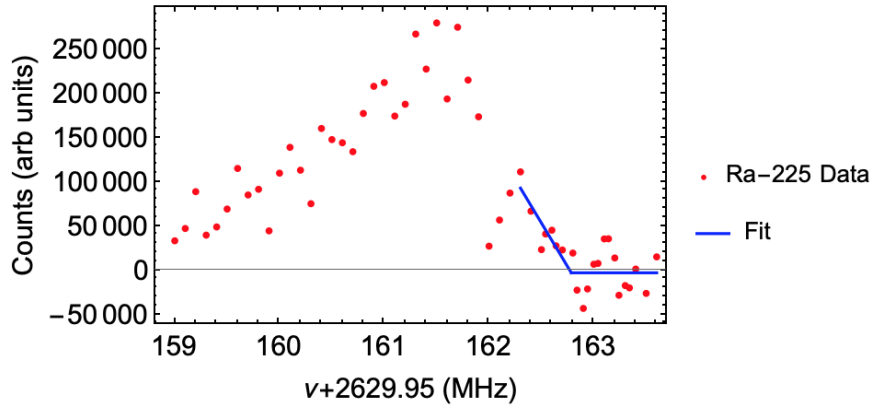

(b) MOT cutoff data for ^{225}Ra

Figure 5.7: The MOT fluorescence counts for ^{226}Ra and ^{225}Ra are plotted against the MOT AOM RF frequencies (ν). The laser frequency for ^{225}Ra is further offset from the cavity resonance relative to ^{226}Ra laser frequency by increasing the EOM offset frequency Ω_1 by 2629.95MHZ.

15 data points for the above dataset. The data and the resultant fit is as shown in Fig. 5.7a. This method for determining the cutoff frequency is repeated for all the MOT cutoff datasets taken for ^{226}Ra and ^{225}Ra.

We studied the potential systematic effects of the MOT probe power and the MOT gradient B-fields on our MOT cutoff frequency determination in ^{226}Ra. For the MOT power dependent effect, we keep the MOT gradient B-field the same and alter the MOT probe power and take a MOT fluorescence spectrum. The dependence of MOT cutoff frequency on the MOT probe power for ^{226}Ra is shown in Fig. 5.9a. We estimate the size of this effect by using the largest possible difference in the MOT cutoff fit values from the four different MOT probe powers studied. This

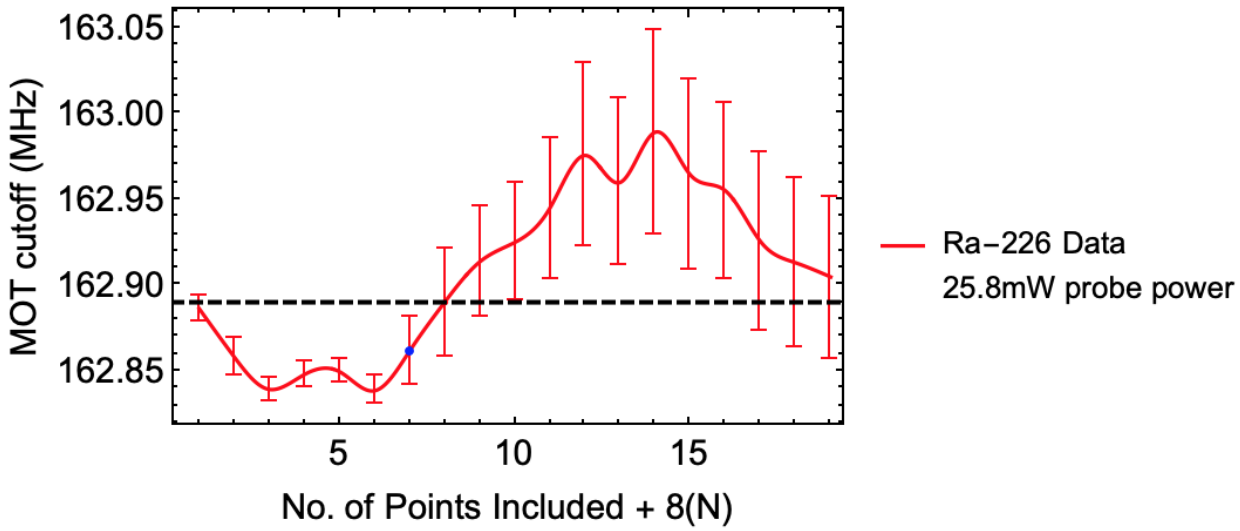

Figure 5.8: MOT cutoff frequency a_3 for ^{226}Ra (probe power at 25.8 mW) as a function of the number of data points included in the fit, including the 8 last data points, up to the peak of the fluorescence spectrum. We fit the data up to the point before the MOT cutoff frequency value diverges by more than a standard deviation. In this case, as indicated by the dashed line, the N = 8 data point is where the value of a_3 diverges and only up to the N = 7 data point (blue data point) are included in the fit.

puts the effect at the level of 180kHz.

We then study the effect of the MOT B-field gradient on the MOT cutoff frequency by keeping the MOT probe power the same while changing the MOT B-fields during the probe phase by tuning the MOT B-field power supply current. The plot of the MOT cutoff frequency fit values for the different MOT B-field currents are shown in Fig. 5.9b. We similarly estimate the size of this effect at 180kHz. Cumulatively, adding in quadrature, the total systematic effect is $\sigma_{\Delta\nu,sys}$ = 0.254MHz. Adding this in quadrature to the statistical uncertainty of $\sigma_{\Delta\nu,stat}$ = 0.104MHz gives a total uncertainty on our MOT cutoff frequency difference between the two isotopes of $\sigma_{\Delta\nu}$ = 0.274MHz. The frequency difference for the MOT transitions between ^{226}Ra($^1S_0 \rightarrow {}^3P_1$) and ^{225}Ra($^1S_0$ [F=1/2] $\rightarrow {}^3P_1$ [F=3/2]) is therefore determined to be

$$\Delta\nu = \nu_{226} - \nu_{225} \tag{5.10}$$

$$= 2630.0 \pm 0.3\,\text{MHz} \tag{5.11}$$

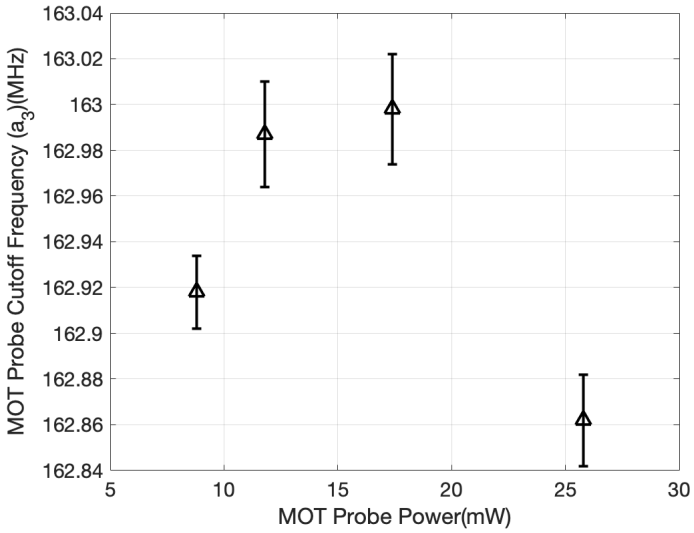

(a) MOT cutoff frequency dependence on the MOT probe laser power in ^{226}Ra.

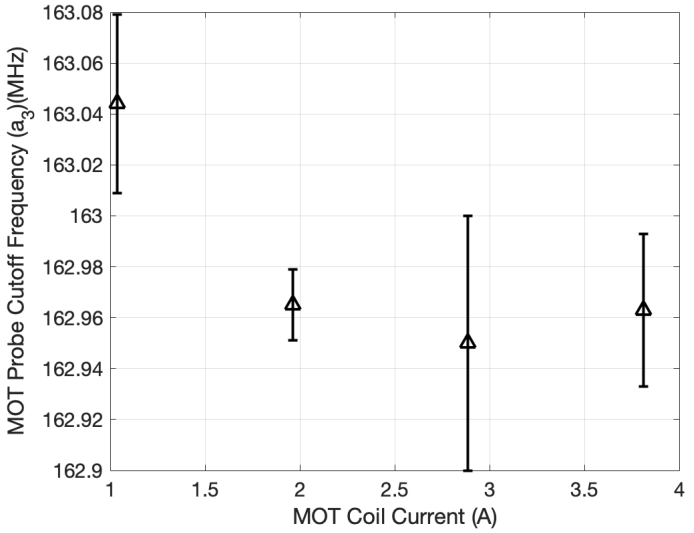

(b) MOT cutoff frequency dependence on the MOT probe B-field power supply current in ^{226}Ra.

Figure 5.9: The MOT cutoff frequencies for ^{226}Ra is plotted against different values of MOT probe laser powers and MOT B-field power supply current. Using the largest possible values of the differences in MOT cutoff frequencies for each systematic effect, we place a limit on the size of the effect.

This is consistent with the value calculated from previously available spectroscopic data for radium [64] of 2629.0 ± 8.6 MHz, and is a factor of 29 more precise. Additionally, along with the known hyperfine splitting between the $F = 1/2$ and the $F = 3/2$ levels of $^3P_1$, we can use our measurement of the difference in the MOT transitions between ^{226}Ra and ^{225}Ra to calculate the

isotope shift $\Delta\nu_{\text{iso}}$ between these two isotopes for the $^1S_0$ to $^3P_1$ transition.

$$\Delta\nu_{\text{iso}} = \frac{1}{3}\Delta\nu_{\text{hfs}} - \Delta\nu \tag{5.12}$$

$$= \frac{14691}{3} - 2630 \tag{5.13}$$

$$= 2267.0 \pm 2.2\,\text{MHz} \tag{5.14}$$

This is a factor of 8 more precise than the isotope shift of 2268 ± 17 MHz that can be determined from Ref. [64]. It should be noted that Wendt *et al.* [64] measured the isotope shifts for the $^1S_0$ to $^3P_1$ transition for a range of radium isotopes with respect to ^{214}Ra. Therefore, it is possible that the uncertainty of 17 MHz propagated on this isotope shift between ^{226}Ra and ^{225}Ra could be overestimated. However, since, to the best of our knowledge, no direct measurements of this isotope shift is reported, we take the above calculated value and its propagated uncertainty to be the currently best available measurement.

Table 5.1: Summary of the systematic uncertainties in our measurement of the MOT cutoff frequencies of ^{226}Ra and ^{225}Ra.

Systematic Effect	Uncertainty (MHz)
MOT Probe Power Drift	0.18
MOT B-field Gradient Drift	0.18
Total	0.254

5.4 Conclusion

We have demonstrated the implementation of a broadband tunable ESB offset lock using an IQ modulation scheme. The ESB offset lock on our 483 nm ECDL1 laser is compared to a PDH lock on the same laser to characterize the ESB locks performance. We find that the noise level for the ESB lock is about 1.5dB higher in the sub-MHz region compared to the PDH lock. In our 714 nm laser, we do not notice any significant change in the laser linewidth and intend to inspect any effects measuremeable in the ECDL1 483 nm laser.

Suggestions for optimizing the ESB locks are provided. RAM in the system can introduce significant drifts in the error signal DC offset. Adjusting the EOM temperature and tuning the input polarization has been shown to be most effective in reducing RAM in our system. Photo refractive damage is a serious concern for low wavelength EOMs such as our 714 nm phase modulator and appropriate limit on the input optical power needs to be placed.

The tunability of the lock allows for precision spectroscopy of different systems. Using this scheme, with a 714 nm laser locked to a ULE optical cavity, we determine the frequency shift required for the MOT transition frequencies between ^{226}Ra ($^1S_0$ to $^3P_1$) and ^{225}Ra ($^1S_0$ $[F = 1/2]$ to $^3P_1$ $[F = 3/2]$) to be 2630.0 ± 0.3MHz. Our measurement is a factor of 29 more precise than what can be calculated from the previously available spectroscopic data on radium. Using this measurement and the available hyperfine splitting in $^3P_1$, we determine the isotope shift for the $^1S_0$ to $^3P_1$ transition between ^{226}Ra and ^{225}Ra to be $\Delta\nu_{\mathrm{iso}} = 2267.0 \pm 2.2$ MHz. This is a factor of 8 better than the currently available value. We note that the currently available value is propagated from the measurements of isotope shifts done for this transition for the two isotopes of interest with respect to ^{214}Ra and therefore the uncertainty on the calculated value that we use for comparison could potentially be overestimated. However, since there is no direct measurement of this isotope shift between ^{226}Ra and ^{225}Ra, we take this value and its uncertainty as the best available measurement.

CHAPTER 6

THE RADIUM EDM SEARCH EXPERIMENT

This chapter describes the experimental apparatus for the radium EDM search experiment, the data collection and summarizes the results that set the latest limit on the size of the radium atomic EDM. It concludes with a brief discussion of the proposed upgrades for an improved measurement of the radium atomic EDM.

6.1 Producing a Beam of Radium Atoms

6.1.1 Radium Oven

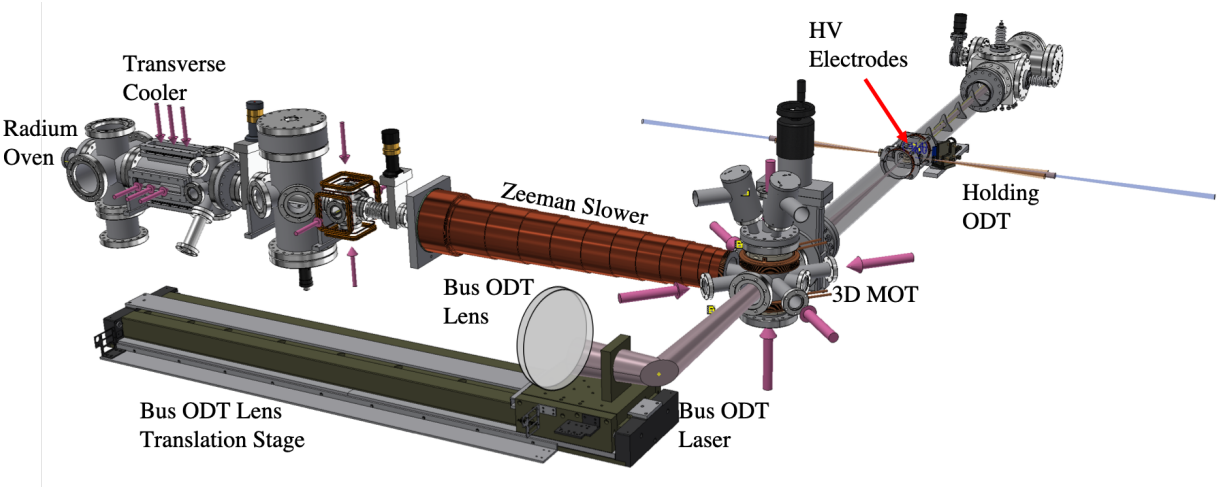

Figure 6.1: The full beam line for the radium EDM experiment. The radium atomic beam produced from the oven is transversely cooled and collimated before entering the zeeman slower for slowing its longitudinal motion, and is finally trapped in the 3D MOT. The 'bus' beam ODT helps transport the atoms into the science chamber where they are held in between the HV electrodes by the 'holding' ODT for experimentation.

Fig. 6.1 depicts the full vacuum system for the radium EDM experiment. The radium atomic beam is generated by the effusive oven at the very left of the vacuum system. The oven is radiatively heated by surrounding copper filaments. A water-cooled jacket surrounds the filaments and acts as a heat sink. A thermocouple at the rear of the oven chamber monitors the oven temperature. The

oven chamber is continuously pumped by an ion pump (Varian, Vacion150). More details on the oven design can be found in Ref. [65].

6.1.2 Radium Oven Crack

Each time we load more radium into the oven, we follow a standard procedure for "cracking" the oven to ensure that we have a steady atomic beam out of the new oven. This involves gradually increasing the oven temperature and monitoring the atomic beam fluorescence. To prepare for an oven load, the gate valve from the oven and the transverse cooling chamber to the rest of the vacuum system is closed to ensure we maintain vacuum in the rest of the system. The oven ion pump is pneumatically sealed off from the chamber it pumps on. The chamber is instead pumped by a combination of a mechanical roughing pump and a turbo-molecular pump. The pumps are shut down shortly before a load and the chamber vented with argon to prepare for the new load of radium. The procedure is generally the same for loading any of the isotopes currently used in our lab. ^{225}Ra is obtained in the form of $RaNO_3$ solution. It is deposited on an aluminum foil the day before the load to allow it to evaporate and reduce the vacuum contamination. A small piece of metalic barium is added to the foil and inserted into the reservoir segment of the oven, shortly before the load. The sample is prepared in a separate lab and transported to the radium lab for the load. The new oven is installed and the heater power supply turned on, and the pumps engaged. As the temperature is slowly raised, we monitor the oven chamber pressure using a residual gas analyzer (RGA) to keep it in the mid-10^{-6} Torr range.

As the atomic beam exits the oven, we monitor the atomic beam fluorescence on the $^1S_0 \leftrightarrow {}^3P_1$ transition. A laser beam ($\sim 500\,\mu$W, ~ 3 mm) supplied by the 714 nm Ti:Sapphire laser, illuminates the atomic beam orthogonally from the top. The atomic beam fluorescence is focused by a 2" diameter lens and collected on a photomultiplier tube (PMT) (Hamamatsu, H7421-50) with a 714 nm interference filter at the input. Since the $^3P_1$ has a lifetime of 420 ns, the 714 nm light is modulated at 1 MHz (50% duty cycle) with a double-passed AOM, such that the light is on for only 500 μs. The data from the PMT is collected at 20 MHz on a data aquisition (DAQ) card (NI-

USB6341). It is then gated so as to collect the data only when the 714 nm light is off. This greatly enhances the signal-to-noise ratio (SNR). The AOM modulation frequency is scanned to determine the atomic resonance. We monitor this beam fluorescence signal and study the atomic beam flux as we turn up the oven temperature. Fig. 6.2 shows a typical oven crack data. In this example, the beam fluorescence is low up till 594 C and rapidly increases such that by 600 C, we have > 50 kCounts. At this point, the oven temperature is quickly reduced and we notice a hysteresis in the beam fluorescence counts at lower temperatures, i.e., we observe higher counts than before. The oven is then declared "cracked". This procedure ensures that we see steady output from the oven and have healthy number of trapped atoms in our MOT. The actual details of the ensuing chemistry that enables the 'cracking' of the oven is not fully understood, however we believe it involves the redox reaction between metallic barium and the radium nitrate ($Ra(N0)_3$) molecules that helps produce the beam of atomic radium.

6.2 Trapping a MOT of Radium Atoms

The segment of the experiment used for trapping a MOT of radium atoms can be subdivided into three parts: the transverse cooling, the zeeman slower and the MOT segments. The laser beams used in all three segments are tuned to the $7s^2\ {}^1S_0 \leftrightarrow\ 7s7p\ {}^1P_1$ ($\Gamma = 2\pi \times 380$ kHz, $I_s = 140\,\mu\mathrm{W/cm^2}$), $(J = 0) \leftrightarrow (J = 1)$ transition for ^{226}Ra, and $(F = 1/2) \leftrightarrow (F = 3/2)$ transition for ^{225}Ra.

The atomic beam out of the effusive oven has a measured divergence of < 50 mrad. The transverse cooling reduces the atomic motion orthogonal to the beam direction. The transverse cooling section consists of 150 mW of 714 nm beam expanded to ~ 2 cm diameter and split into two parts that are orthogonal to the atomic beam. One part of the beam is horizontally incident on the atoms while the other is vertically incident. A pair of 2.5 cm by 18 cm mirrors in each direction reflect the beams such that they pass through the atomic beam multiple times. This helps collimate the atomic beam, and when tuned up, the gain in the fluorescence signal from the MOT atoms is a factor of $\approx 80 - 90$.

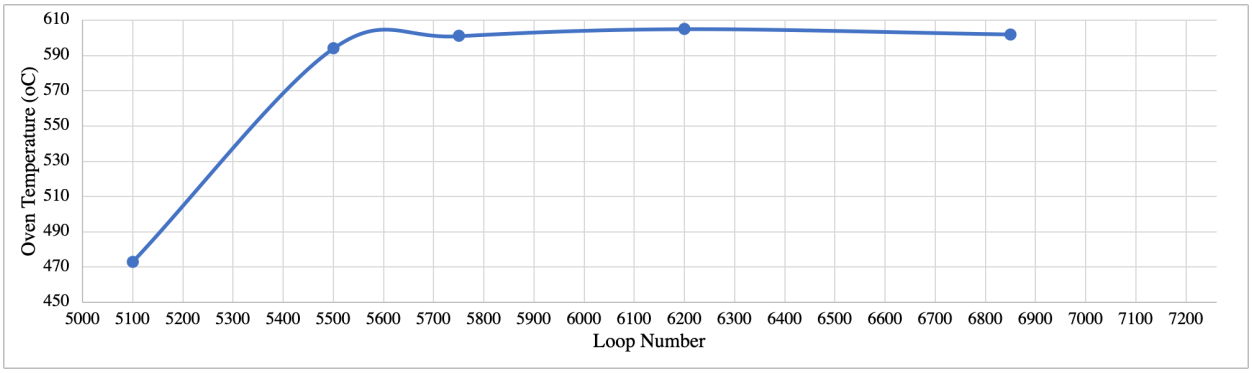

(a) Radium oven temperature

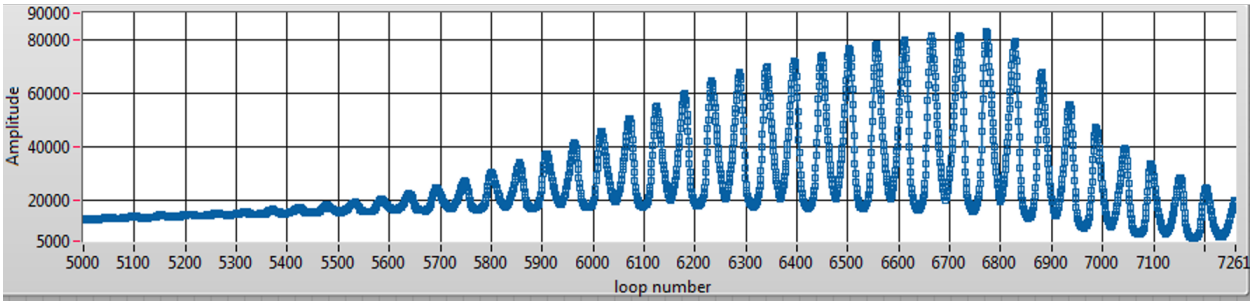

(b) Radium atomic beam fluorescence as recorded on the PMT (in arbitrary units).

Figure 6.2: A typical radium oven 'crack'. The atomic beam fluorescence is monitored as the temperature is steadily increased. We begin seeing a noticeable signal at around 500 C. On further increasing the temperature, we notice a rapid increase in the fluorescence signal. On turning down the temperature to <500 C, we notice a hysteresis in the fluorescence counts, indicating that the oven has been 'cracked'.

The collimated atomic beam enters the 0.9m long zeeman slower region. As shown in Fig. 6.1, the tapered solenoid creates the requisite $B-$field profile and the atoms are longitudinally slowed by $\approx$ 35 mW of 714 nm laser beam. Co-propagating with the slowing beam, we also apply a repump beam at 1428 nm. More details on the zeeman cooler can be found in Ref. [66]. With the current "red slower" scheme, we slow atoms with longitudinal speeds up to 60 m/s. For a typical oven temperature of 500 C, this corresponds to 0.5% of the atomic velocity distribution.

The atoms then enter the 3D MOT region. The 3D MOT consists of anti-Helmholtz coils that create the necessary $B-$field gradient. A 714 nm laser beam with $\approx$ 40 mW is split into orthogonal beams. Each beam is retro-reflected to produce a pair of counter-propagating beams with opposite circular polarization along the three spatial directions. Along with the $B-$field the beams create the necessary trap for confining the slowed atoms. The MOT chamber is pumped by an ion pump

(Gamma Vacuum, 45S) and is connected to a titanium sublimation pump (TSP). Occasionally firing the TSP ensures that the pressure in the chamber is maintained at mid-10^{-10} Torr. The MOT lifetime is typically measured to be ≈ 40 s. The oven to MOT trapping efficiency is 1 ppm owing mostly to the use of the weaker 714 nm transition for atom slowing. Typically in the MOT, we trap $\approx 10^5$ ^{226}Ra and $\approx 10^3$ ^{225}Ra atoms cooled to $40 \pm 15\,\mu$K [67].

The MOT operates in three different phases: the 'load', the 'probe' and the 'cooling' phase. The 'load' phase is optimized for trapping atoms in the MOT. The 'probe' phase allows for optimal imaging of the atoms in the MOT. The 'cooling' phase allows for optimal transfer of atoms from the MOT into the 'Bus' ODT for atom transport. During the 'load' phase, the laser intensity is the greatest ($\approx 1.5\,\mathrm{mW/cm^2}$), while the $B-$field gradient is the smallest ($B = 1$ G/cm) and the laser frequency is red-detuned by 2.8 MHz. During the 'probe' phase, the laser intensity is reduced (to $\approx 0.5\,\mathrm{mW/cm^2}$) and the field gradient increased ($B = 2 - 3$ G/cm). The laser frequency detuning is reduced to 2 MHz. This ensures tighter confinement of the atoms and reduces the background scattering, resulting in a better SNR for a MOT fluorescence measurement. A 10 cm focal length lens (NA = 0.009) placed 10cm from the trap center focuses the MOT signal on to a CCD camera (Andor, Luca) and processed using a LabView program that displays the real-time, background subtracted atom images and the MOT counts in a pre-defined region of interest (ROI). A typical image of a MOT of ^{226}Ra atoms is shown in Fig. 6.3. During the 'cooling' phase, the laser intensity is further reduced to $40\,\mu\mathrm{W/cm^2}$ and the detuning decreased to 1 MHz. The $B-$field is kept the same as during the 'probe' phase.

The relevant laser beam parameters for the transverse cooler, the zeeman slower, and the different MOT phases are shown in Table 6.1. The laser beam intensities are expressed in terms of the saturation intensity I_s for the 714 nm transition. The frequency detunings δ are expressed in terms of the natural linewidth of the 714 nm transition, Γ.

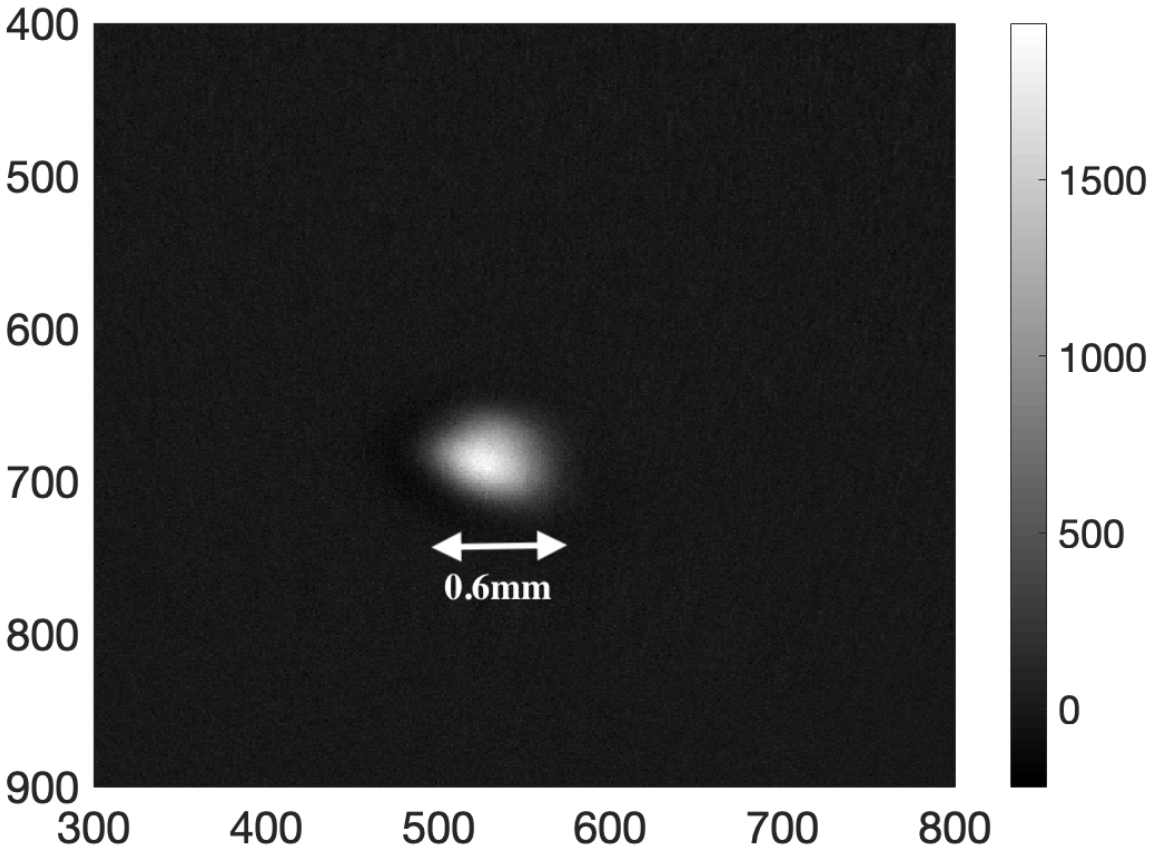

Figure 6.3: A MOT of ^{226}Ra atoms trapped after loading for 30 s.

Table 6.1: Typical laser intensities I and frequency detuning δ used for the different segments of the laser cooling and trapping setup.

	I/I_s	δ/Γ
TC	50	-3
ZS	30	-12
MOT Load	12	-8
MOT Probe	3.6	-5
MOT Cooling	0.3	-3

6.3 Transporting atoms to the science chamber

Having trapped atoms in the 3D MOT, the next step is to transport them into the science chamber for - amongst other experimentation - EDM measurement. This requires a transport of the atoms over a distance of $\approx$ 1082 mm. This is achieved by overlapping the MOT with the focus of the

'Bus' ODT and moving the focus from the MOT chamber to the science chamber, in between the HV electrodes. The choice of the ODT wavelength of 1550 nm was dictated by the fact that this is predicted to be the 'magic wavelength'[1] for the intercombination transition used for laser cooling and trapping [68], and is therefore optimal for atom transfer from the MOT to the ODT. As described in the chapter 4, this is constructed with a 50 W 1550 nm laser (IPG ELR-50-1550). The output beam of the laser is expanded, and focused to a beam waist of $\approx 100\,\mu$m by a 10 cm diameter, 2 m focal length lens. During the 'cooling' phase of the MOT, the atoms are loaded into the 'bus' ODT with typical transfer efficiencies of $60 - 80\%$. As shown in Fig. 6.1, the lens is mounted on a translation stage (Aerotech ABL2000) that moves the focus of the ODT with a well-defined motion profile. A sinusoidal motion profile was found to optimize the atom transfer efficiency [69].

From time to time, we notice 'noisy' transfer of atoms from the MOT to the science chamber. There are certainly many contributing factors, one of which is the jitter in the stage motion and the stage arrival time (the time it takes for the stage to move the lens and therefore the focus of the Bus beam from the MOT to the science chamber). To rule out instabilities in the stage motion, we devised a simple interferometer, as shown in Fig. 6.4, that helped monitor both the distance traveled by the stage as well as the time taken to cover that distance.

A beam from a HeNe laser is split along the two arms of the interferometer. A beamsplitter (BS) splits the laser beam into two paths x_1 and x_2. The beams are reflected back by two right-angled prisms $P1$ and $P2$ along each path. The beams then recombine at the beamsplitter and interfere to produce an interference fringe pattern. In fact, one can vary the differential optical path lengths (OPL) along the two arms of the interferometer and notice the fringes move corresponding to how much the OPL changes by. The relation between the OPL and the fringes, and hence the wavelength λ of the laser light is given by

[1] A highly intense ODT laser beam induces a dynamic stark shift of the atomic energy levels that depends on the laser frequency. Due to the different stark shifts of the two levels coupled by an optical transition, this results in a frequency shift of the atomic resonance. At certain wavelengths of the ODT beam, the differential stark shift is close to zero, resulting in very small shifts in the transition resonance. Such a wavelength is called the 'magic wavelength' for the transition.

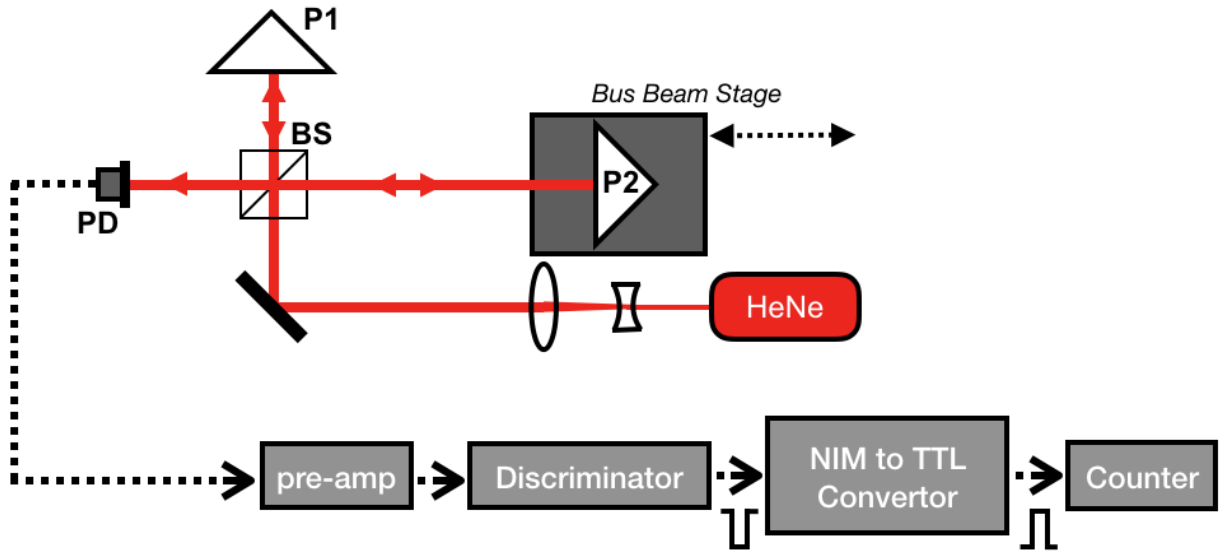

Figure 6.4: The interferometer setup used for measuring the distance traveled by the stage. The interference fringes move as the optical path length (OPL) is changed by moving $P2$. We can then use the knowledge of the wavelength λ of the laser to determine the actual distance Δx traveled by $P2$ and therefore the stage. The fringes are counted using a counter by amplifying the photodiode (PD) signal and using a discriminator to output a logic signal every time the stage moves by half a fringe.

$$OPL = N\lambda$$
$$2\Delta x = N\lambda \tag{6.1}$$

Where $\Delta x = |x_2 - x_1|$, and the factor of 2 accounts for the round-trip of the laser light as it reflects off of $P2$, and N is the number of fringes moved as the OPL is changed by $2\Delta x$. In our case, we move $P2$, which is attached to the moving stage. Hence counting the number of fringes allows us to determine the distance Δx traveled by the prism $P2$ and therefore the stage.

We use a 632.816 nm HeNe laser as our coherent light source. The interference pattern is collected on a photodiode (PD). This is then amplified and sent into a discriminator (NIM Model 623B Octal Updating Discriminator). The discriminator outputs a negative NIM logic whenever the PD signal exceeds its threshold. This NIM logic is converted to a TTL pulse and fed into a counter which counts how many fringes the interferometer has moved, and records them on a DAQ

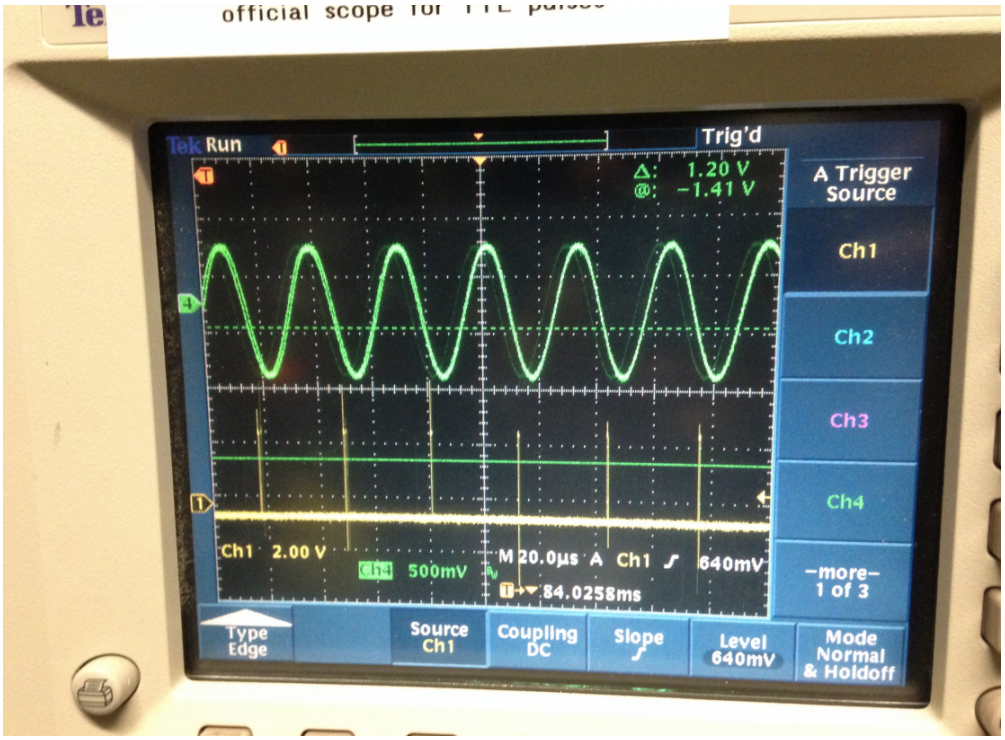

Figure 6.5: The green trace shows the sinusoidal interferometer signal as the stage moves and the optical path length changes. Each peak corresponds to the prism $P2$ moving by a half a wavelength of the laser. The yellow trace shows the fringe peaks as detected by the discriminator and the corresponding TTL pulse generated. Each TTL pulse corresponds to a fringe moved.

card (NI PXIe-6341 card). The counter gives us N in Eq. 6.1. We can then use it to determine the distance traveled by the stage.

As a test, we move the prism $P2$ by translating the bus beam stage from its initial position $x_i = 549$ mm to $x_f = -400$ mm; a total displacement of 949 mm. We ensure that the discriminator is triggered all the while the stage moves and count the fringes on a counter. Fig. 6.5 shows what such a signal looks like. The green trace shows the output from the photodiode (PD) as fringes move from one bright peak to another. In the yellow trace we have the TTL pulses generated by the discriminator as it sees the fringes (triggered as the green trace surpasses its threshold). We send these TTL outputs into a counter that then counts the fringes moved. We use the total fringes moved N to determine the total displacement of the stage. For the above displacement, the counter registers $N = 2999396$ counts. With the HeNe wavelength of $\lambda = 632.816$ nm, using Eq. 6.1, we can figure out how much the stage moved by:

$$\begin{aligned}\Delta x &= N\lambda/2 \\ &= (2999396)(632.816\,\text{nm})/2 \\ &= 949.033\,\text{mm}\end{aligned} \tag{6.2}$$

The noise we see on the counts from the counter is on the order of 20 counts which correspond to $\approx 10\,\mu$m which is about 10 ppm. Our measured value, accounting for the spurious counts, is within $20\,\mu$m of the distance the stage is programmed to move by. For the purposes of atom transfer, a jitter at this scale is insignificant.

Satisfied with the performance of the interferometer, we use it to monitor the jitters in the stage motion throughout the course of a day. We take a series of measurements of the stage distance traveled and the time it takes the stage to complete the motion at 10am, 3pm and 6pm. The results are shown in Fig. 6.6. As can be seen, the stage is consistent in its arrival time within 20 ms, and the overall motion is repeatable within $10\,\mu$m. This enabled us to rule out instabilities in our atom transfer efficiency due to the stage final position and arrival time jitters.

The stage motion might deteriorate over time in which case, this interferometer setup should help verify whether the stage is traveling the same distance (within a few tens of μm, and whether it arrives at the same time within a few tens of μs). We can also plot the overall motion profile of the stage from the interferometer data collected. Fig. 6.7 shows the displacement and the speed of the stage as it moves from the MOT to science chamber. The velocity profile is sinusoidal as expected.

Having transported the atoms into the science chamber, the next step is to transfer them into the 'holding' beam ODT that holds the atoms at its focus in between the HV electrodes. To ensure efficient transfer we compress the atoms along the longitudinal direction of the 'Bus' ODT by using a 1D MOT setup. A pair of coils arranged in the anti-Helmholtz configuration along the direction of the vacuum glass tube generates the $B-$field gradient of $\approx$0.75 G/cm. We apply a short (170 ms) 714 nm pulse along the longitudinal direction of the 'Bus' beam. Fig. 6.8a shows an image of the atoms compressed in the presence of the 1D MOT. This figure presents the background subtracted

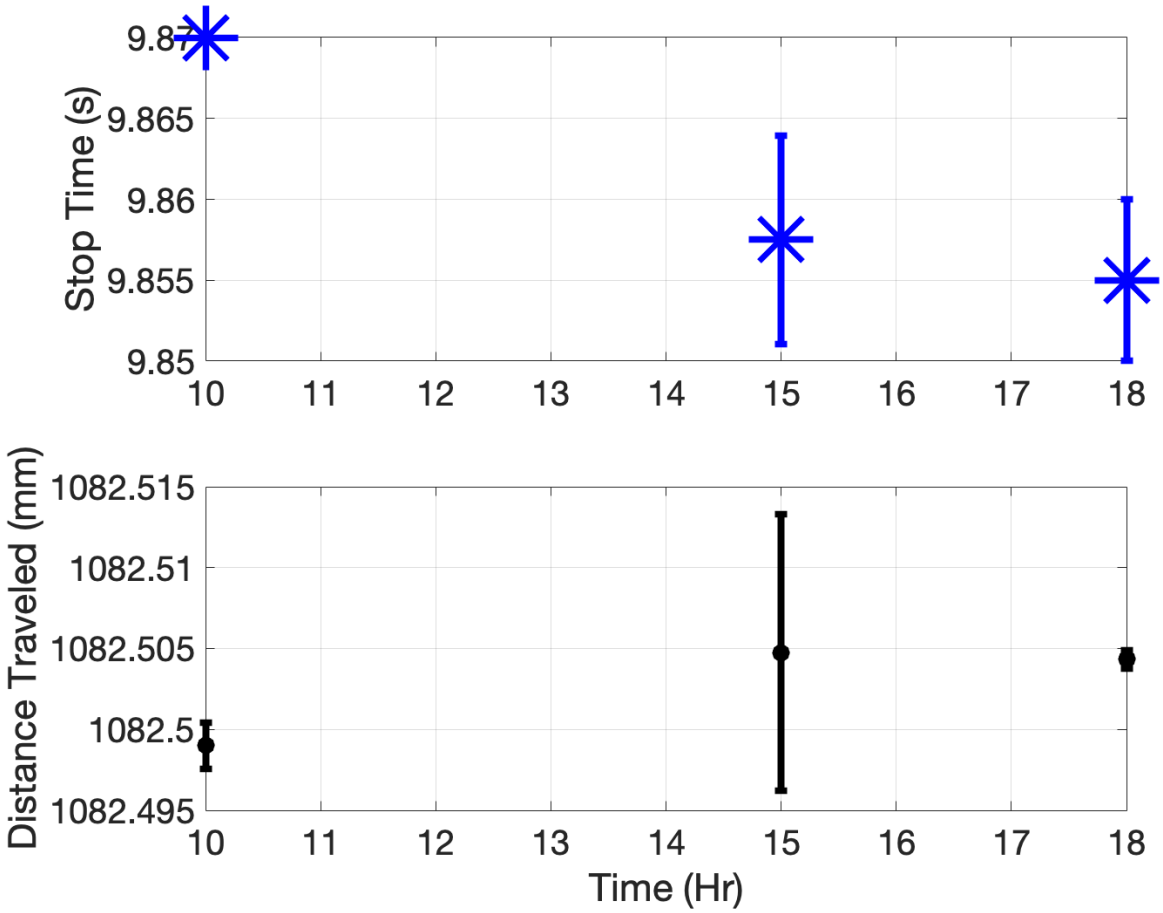

Figure 6.6: The stage motion data throughout the course of a day. We notice that the stage arrives at the same time within 20ms, and the overall jitter in the distance travelled is within 10μm.

absorption image of the atoms in the 1D MOT, which is inverted for better visibility. The details of the absorption imaging and the background subtraction used, will be provided later in this chapter.

The 1D MOT compression facilitates the transfer of atoms into the 'Holding' ODT. Once the 1D MOT compressed atom cloud is close enough to the focus of the 'Holding' ODT, we begin noticing some transfer of atoms into the 'Holding' ODT, as shown in Fig. 6.8b. Here we notice atoms beginning to populate the 'Holding' ODT, but we also see some of the atoms that remain in the 1D MOT. Once the overlap between the 1D MOT and the 'Holding' ODT is optimized, we see a clear transfer of atoms as shown in Fig. 6.8c. It should be noted that the 1D MOT beam, as well as the 1D MOT $B-$field is turned off after the optimal overlap. The 1D MOT coils have independent power supplies that and relay controls that isolate the power supply from the coils and

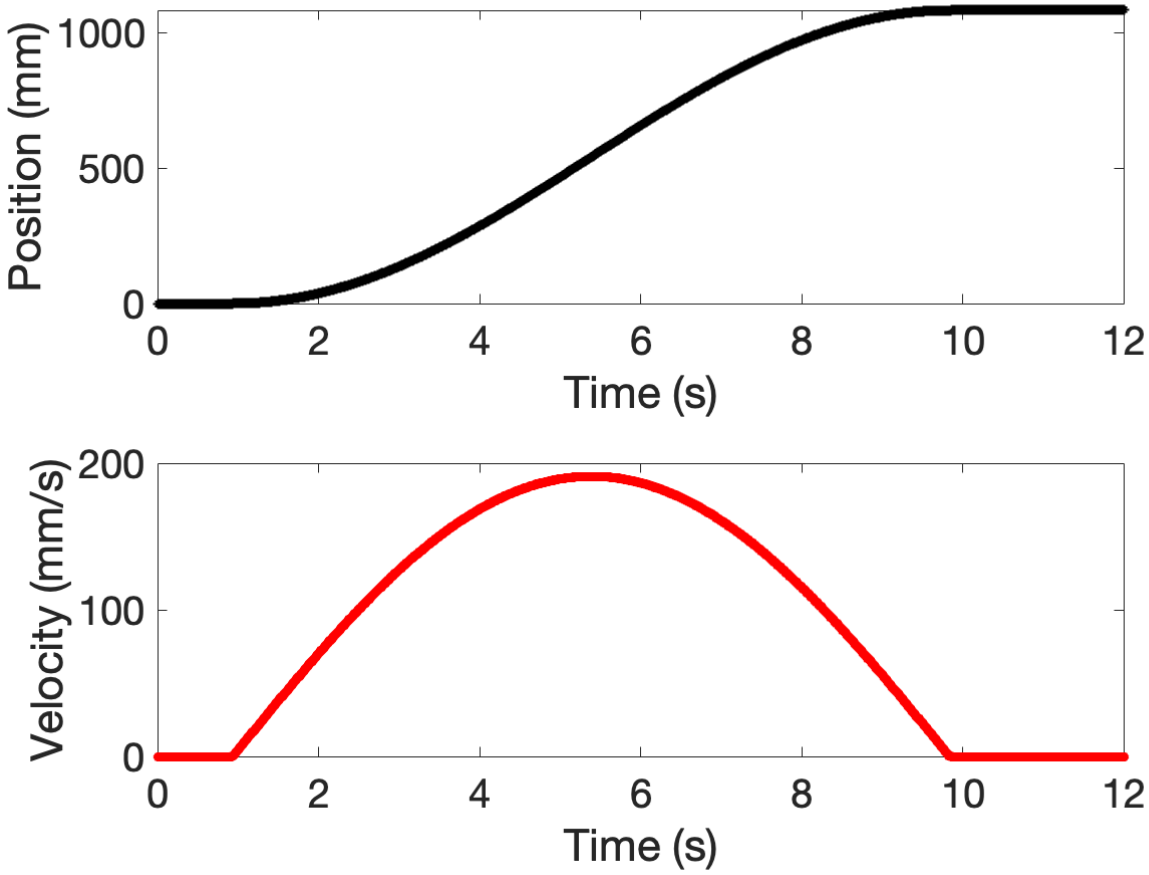

Figure 6.7: The stage position and the velocity as measured by the interferometer for a total displacement of 1082.5 mm.

greatly reduces magnetic field noise in the apparatus, which is crucial during an EDM measurement. Depending on the experiment, we either hold the atoms in a cross-trap formed by the 'Bus' and the 'Holding' ODTs, or hold the atoms in the 'Holding' ODT in either a travelling wave or a standing wave configuration.

6.4 Science Chamber

The EDM measurement takes place inside the science chamber as shown in Fig. 6.9. This chamber comprises of a vacuum glass tube that houses the HV electrodes that generate the electric field required for the experiment. The glass tube was chosen to reduce ferromagnetism and therefore $B-$field instabilities and inhomogeneity at the atoms. An ion pump (Gamma Vacuum 150T with a

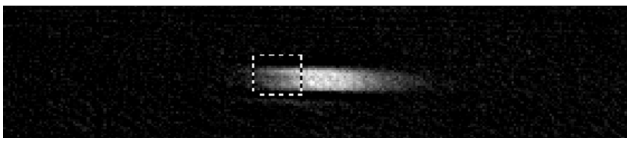

(a) Atoms compressed in the 1D MOT

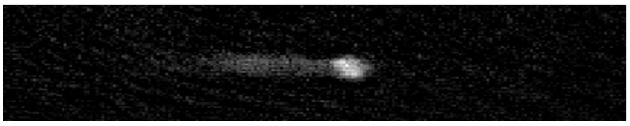

(b) Interaction between the 1D MOT and the 'Holding' ODT.

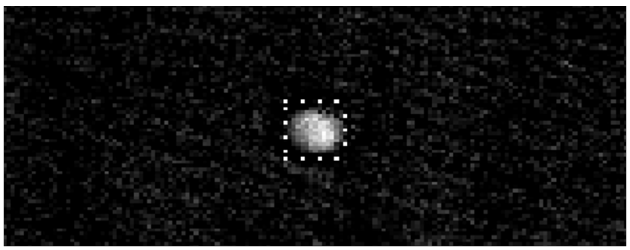

(c) Optimal overlap between the 1D MOT and the 'Holding' ODT

Figure 6.8: The atoms in the 'Bus' ODT is compressed using a 1D MOT for optimal transfer into the 'Holding' ODT. The 1D MOT is formed by a 170 ms long 714 nm laser pulse that is retro-reflected to have opposite polarization, in the presence of a quadrupolar $B-$field.

TSP) attached to the glass tube maintains a typical pressure of low-10^{-11} Torr in the glass tube.

For the latest EDM measurements, a pair of copper electrodes were used to generate the required $E-$field. As shown in the inset in Fig. 6.9, the electrodes were held in a Macor holder at a separation of 2.3 ± 0.1 mm. Prior to their installment in the glass tube, the electrodes were electropolished to minimize surface inhomogenieties. Once in the glass tube, one of the electrodes was connected to the high voltage power supply and the other to a leakage current monitor. Such a current generates a magnetic field that the magnetic moment of the atom couples to and affects its spin precession frequency. The direction of the leakage current depends on the polarity of the $E-$field and therefore creates a frequency shift that is indistinguishable from the effects of the atomic EDM. This is a potential source of systematic uncertainty and is monitored using a leakage current monitor connected to the uncharged/grounded electrode. To ensure we get as high of an $E-$field as feasible, after their installation, the electrodes are subjected to a process known as 'high voltage conditioning'. This entails ramping the charged electrode to high voltages and observing

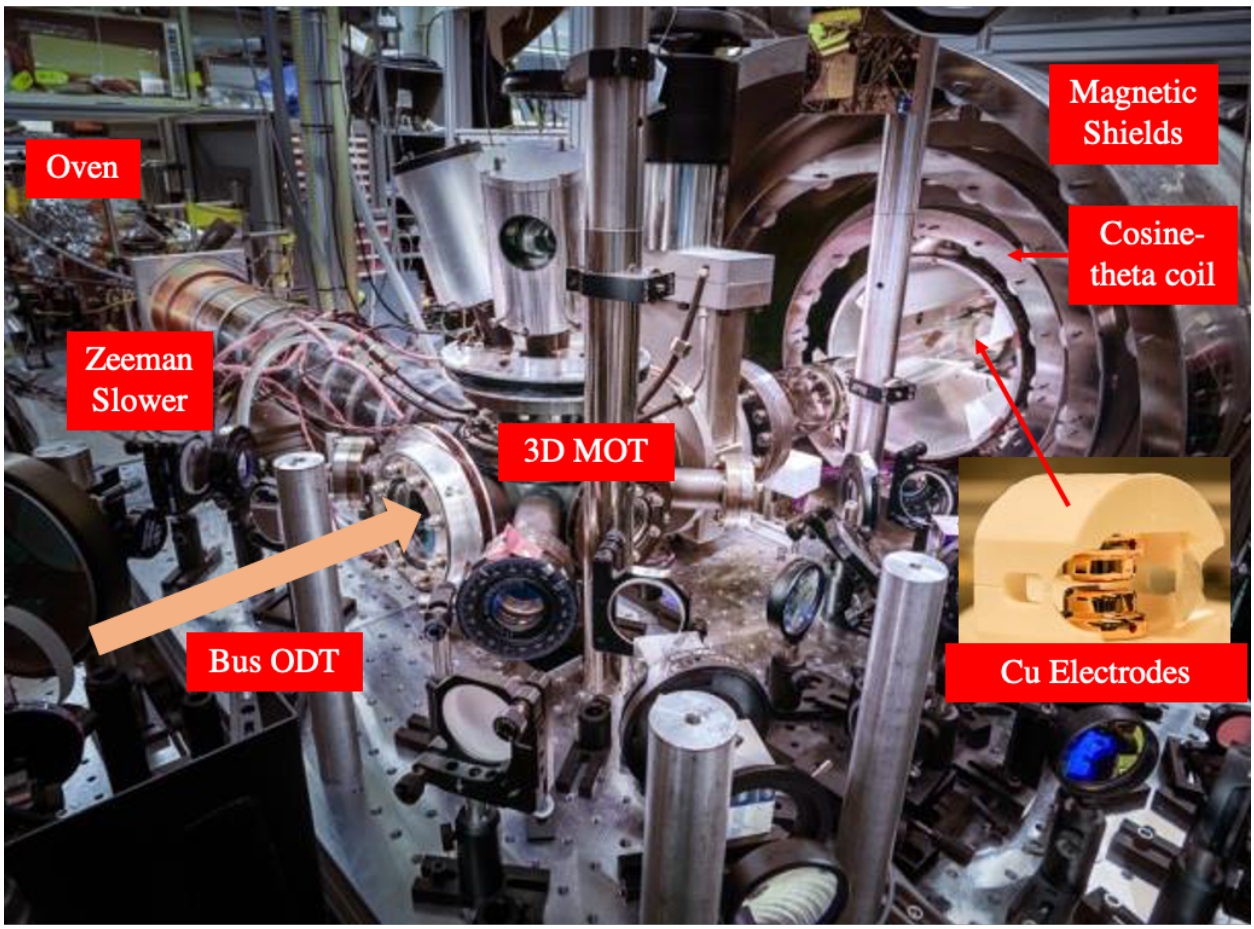

Figure 6.9: Figure displaying the science chamber. The copper electrodes are held in a vacuum glass tube to create the required $E-$field. It is surrounded by the cosine-theta coil that generates the stable, homogeneous $B-$field. The entire setup is covered by three sets of mu-metal magnetic shields. Image courtesy of Kevin Bailey.

the leakage current monitor data to see if we notice any electrical discharges. These are short (few ms long, tens of nA) leakage current bursts that happen when the electrodes are held at high voltages. Typically, the discharge rate either decreases, in which case we gradually increase the voltage, or they increase, in which case we decrease the voltage to a level where the discharges settle or die down. Eventually, this process of ramping the voltage and maintaining a low discharge rate enables the electrodes to be charged to high voltages without electrical breakdowns. For the set of copper electrodes, a field of 67 kV/cm was achieved and used for the EDM measurement. The resultant steady state leakage current was measured to be < 100 pA. More details on the $E-$field generation setup used in the last EDM measurement can be found in Ref. [65].

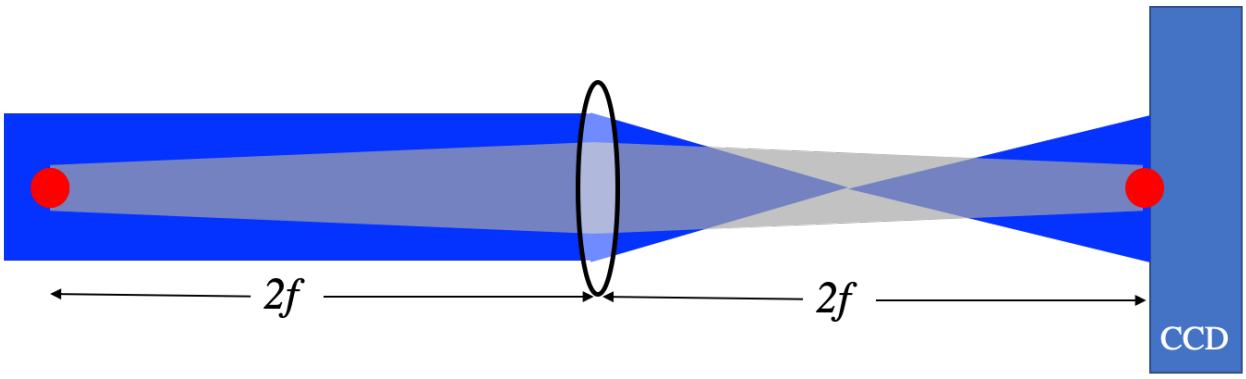

Figure 6.10: The radium spin precession imaging setup using 483 nm imaging laser. We use a $f = 50$ cm imaging lens for 1-to-1 atom shadow imaging.

The $B-$field required for nuclear spin precession of the ground state is produced by a cosine-theta coil wrapped around a 32 cm diameter, 65 cm height cylinder that is concentric to the glass tube. The current in the coil follows a cosine-theta distribution, creating a uniform vertical $B-$field. The current is supplied by a laser diode power supply (ILX Lightwave LDC3724B). The spatial variation of the $B-$field was verified to be $< 0.1\%/\text{cm}$. For an atom cloud of $\approx 50\,\mu$m diameter, this results in a $0.2\,\mu$G variation in the field over the atom cloud. Further details on the stability and the spatial homogeneity of the $B-$field is provided in Ref. [63, 65, 66].

The science chamber is enclosed in three layers of mu-metal magnetic shields for reducing the effects of external $B-$fields on the magnetic field stability and homogeneity inside the science chamber. Without any degaussing, the shielding factor was measured to be 8×10^3. Therefore, we degauss the shields by passing an exponentially decaying (with a time constant of 300 s) 50 Hz sinusoidal current through a pair of coils wrapped around the mu-metal shields. The waveform for programming the power supply is generated by a LabView VI. The key is to ensure that there is no residual current at the end of the degaussing process. This is achieved by inserting an isolation transformer between the supply and the coils. With degaussing the suppression of external fields is improved to a factor a 2×10^4.

6.5 Laser Absorption Imaging

Once the atoms are trapped in between the electrodes, we image them using absorption imaging on the ${}^1S_0\,(J=0) \leftrightarrow {}^1P_1(J=1)$ transition for ^{226}Ra and the ${}^1S_0(F=1/2) \leftrightarrow {}^1P_1(F=3/2)$ transition for ^{225}Ra. A schematic of the atom imaging setup is shown in Fig. 6.10. A collimated beam of 483 nm light illuminiates the atom cloud. At resonance, the atoms absorb some of the light and create an atom cloud shadow that is imaged one-to-one using a 50 cm focal length lens, on a CCD camera (Andor Clara CCD). The atom images for ^{226}Ra contain enough signal to be seen without any image processing, however, for ^{225}Ra since the signal is dominated by the photon shot noise it necessitates background subtraction.

6.5.1 Background Subtraction

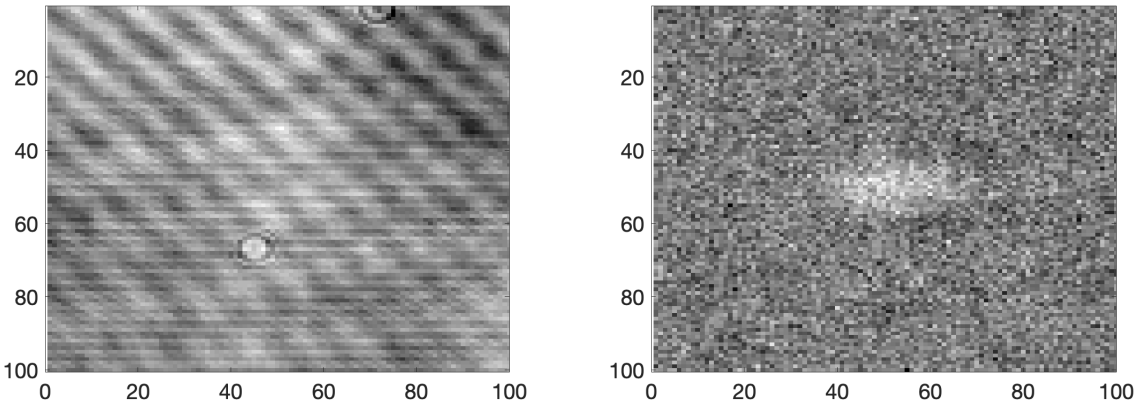

(a) Raw image of ^{225}Ra atoms

(b) Background subtracted image of ^{225}Ra atoms

Figure 6.11: Background subtraction using the 'least square' method for ^{225}Ra atom images. (a) shows the raw atom image where the background fluctuation due to interference and diffraction off of optical elements dominate the atom signal. (b) shows the background subtracted image where the atom cloud is clearly visible. The residual background fluctuation is $\approx 2\times$ the photon shot noise.

Fig. 6.11a shows the raw image of a cloud of ^{225}Ra atoms as collected on the camera. It is clear that the underlying atom signal is obscured by the different noises in the image caused by the various optical elements in the path of the imaging beam. These elements cause interference and

diffraction that result in the fringing of the imaging light. Moreover, these aberrations fluctuate shot to shot and therefore simply subtracting one background (containing no atoms) image from the atom image does not address this issue fully.

Instead, we follow the routine outlined in Ref. [70]. We begin by creating a background Q for an atom image A that is a linear combination of all the reference background images R_k. We then subtract the background from the atom image to get the background subtracted atom image: $\tilde{A} = A - Q$. The background can be written as

$$Q_x = \sum_k c_k R_{x,k} \tag{6.3}$$

where Q_x is the $x-$th pixel of the background image, and c_k is the coefficient of the $k-$th reference background R_k. To determine the coefficients c_k, we minimize the least square difference between the background Q and the atom image A: $\sum_x m_x (A_x - Q_x)^2$, where we impose the mask m_x on the images to exclude the atoms ($m_x = 0$ for pixels containing atoms, and $m_x = 1$ elsewhere). Taking the partial derivative with respect to c_j and setting it to zero, we obtain

$$\begin{aligned}
\frac{\partial}{\partial c_j} \sum_x m_x (A_x - Q_x)^2 &= 0 \\
\frac{\partial}{\partial c_j} \sum_x m_x (A_x - \sum_k c_k R_{x,k})^2 &= 0 \\
\sum_k c_k \sum_x m_x R_{x,k} R_{x,j} &= \sum_x m_x (A_x R_{x,j}) \\
\sum_k c_k B_{k,j} &= \sum_x m_x (A_x R_{x,j}) \\
B\vec{c} &= \vec{y}
\end{aligned} \tag{6.4}$$

where $B_{k,j}$ is a square matrix and can be decomposing as $B = LU$, with L and U being the respective lower and upper triangular matrices. This then allows us to solve Eq. 6.4 for the coefficient vector $\vec{c}$. With this 'least square' method of background subtraction, the residual background fluctuations is easily reduced to $1.2-2\times$ the photon shot noise. As shown in Fig. 6.11b,

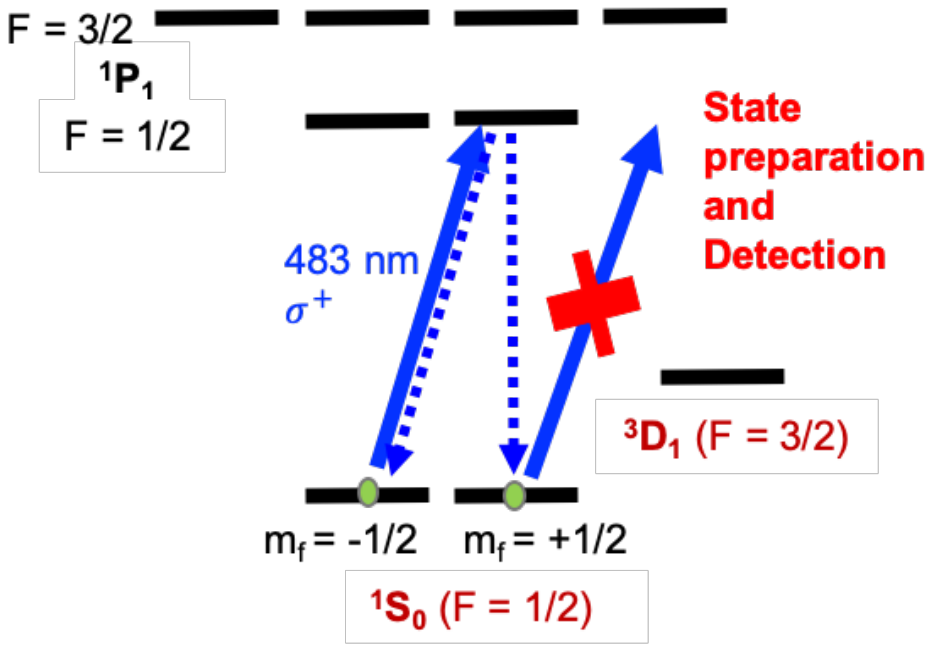

Figure 6.12: Ground state preparation and detection in ^{225}Ra for an EDM measurement. The same σ^+ polarized laser beam tuned to the $^1S_0(F = 1/2) \leftrightarrow {}^1P_1(F = 1/2)$ transition spin polarizes the atoms into the 'dark' $m_F = +1/2$ sublevel, and images them when in the 'bright' $m_F = -1/2$ sublevel.

this then enables us to see the atom signal and proves very important when working with small atom numbers as is the case with ^{225}Ra. This background subtraction routine is implemented in two places. It is implemented on the LabView program that processes the camera images in real-time. Here the number of reference background images used is limited to 25 to avoid overloading the computer memory. We also implement it in image processing via `MATLAB`, where we use all the reference backgrounds taken for creating the background Q.

6.6 Nuclear Spin Precession Detection

Clearly, for an EDM measurement, we cannot use the above imaging transition for ^{225}Ra due to its lack of ground state spin selectivity. Instead, we employ the $^1S_0(F = 1/2) \leftrightarrow {}^1P_1(F = 1/2)$ transition in ^{225}Ra for both ground state preparation as well as detection.

As shown in Fig. 6.12, using a σ^+ polarized 483 nm light, we spin polarize the ground state by optically pumping the atoms into the $m_F = +1/2$ sublevel. We then use the same laser light to

image the atoms. The $m_F = +1/2$ sublevel, in our current choice of polarization, is the 'dark' state, since the atoms in this state do not scatter the imaging light, while the $m_F = -1/2$ sublevel is the 'bright' state, since it does. In the presence of a magnetic field orthogonal to the quantization axis (in this case, set by the laser propagation direction), the precession of the spin polarized atoms can be detected using this scheme, hence allowing us to measure its precession frequency and therefore an EDM induced phase shift.

The key to this technique is the polarization quality of the polarization/imaging pulse. In our lab, we adjust the light to be 99% circularly polarized as measured by a polarimeter setup after the laser beam passes through the vacuum glass tube.

6.7 The Radium EDM Limit

6.7.1 EDM Measurement

With the above choice of atom imaging transition, the atoms in the 'bright' state scatter on average 3 photons before decaying to the 'dark' state. The SNR of the detection scheme is optimized when we scatter on an average 2.1 photons per atom. This limits our detection pulse duration to 60 μs. The atom polarization pulse is set to 150 μs. In the last EDM measurement experiment, the pulse sequence shown in Fig. 6.13 was used. A polarization pulse is applied, followed by an imaging pulse (Im#1) applied at a delay of ΔT_1. Another polarization pulse is applied and the atoms allowed to precess in the presence of both magnetic and electric fields. The electric field is ramped up for 19.2 s, either parallel or antiparallel to the magnetic field. An atom image (Im#2) is taken at a delay of ΔT_2 after the polarization pulse. Another pair of polarization and imaging pulses (Im#3) are applied, separated by a delay of ΔT_3. This is used to normalize Im#2. Another polarization pulse is applied and the atoms allowed to precess with the electric field off for a duration of ΔT_4, followed by an imaging pulse (Im#4). Finally, a pair of polarization and imaging pulses (Im#5) are applied, separated by ΔT_5. This is used to normalize Im#4. For images 1, 3 and 5, $\Delta T_{1,3,5} = 17.4$ ms, which is half the precession period and ensures that the atoms are entirely in the 'bright' state and that the atom signal is maximum. For images 2 and 4, $\Delta T_{2,4} = 20000 + \delta$ ms, and δ is varied

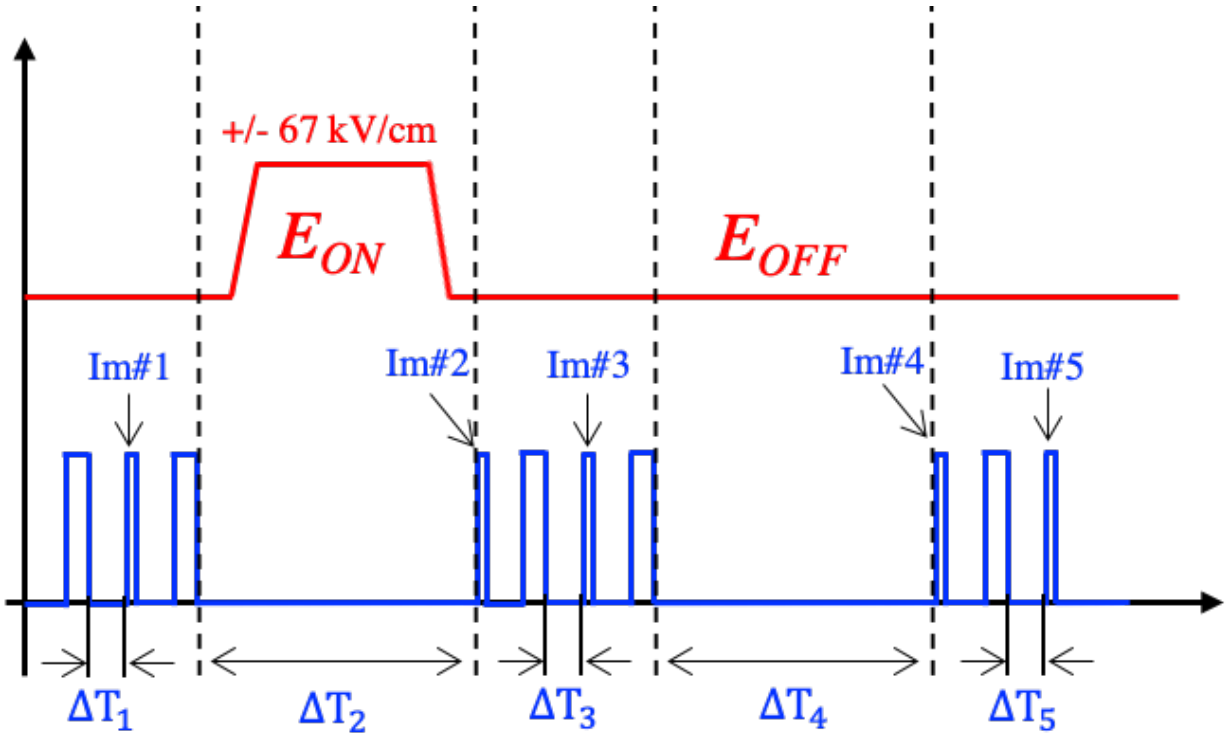

Figure 6.13: The pulse sequence for one experimental cycle of an EDM measurement of ^{225}Ra atoms. The wider 150μs 483nm pulses correspond to ground state polarization pulses. The narrower 60μs 483nm pulses are the atom imaging pulses used for mapping the ground state nuclear spin precession.

from -10 ms to +40 ms to capture at least one entire fringe of the ground state precession.

6.7.2 The Latest Ra EDM Limit

Fig. 6.14 shows the data collected with the electric field parallel, antiparallel to the magnetic field, and with the electric field off. The data collected is then fit to the following pair of fit functions

$$y_{\text{off}} = \frac{A}{1+P}[1 - P\cos(\omega\Delta T_4)],$$
$$y_{\text{parralel(antiparallel)}} = \frac{A}{1+P}[1 - P\cos(\omega\Delta T_2 + \theta \pm \Delta\phi/2)] \quad (6.5)$$

Here A is a normalization constant, P is the signal contrast, ω is the angular frequency of precession, θ is the phase difference the $E-$field on and off data, and $\Delta\phi$ is the differential phase shift between the $E-$field parallel and antiparallel data. This last quantity is the parameter of

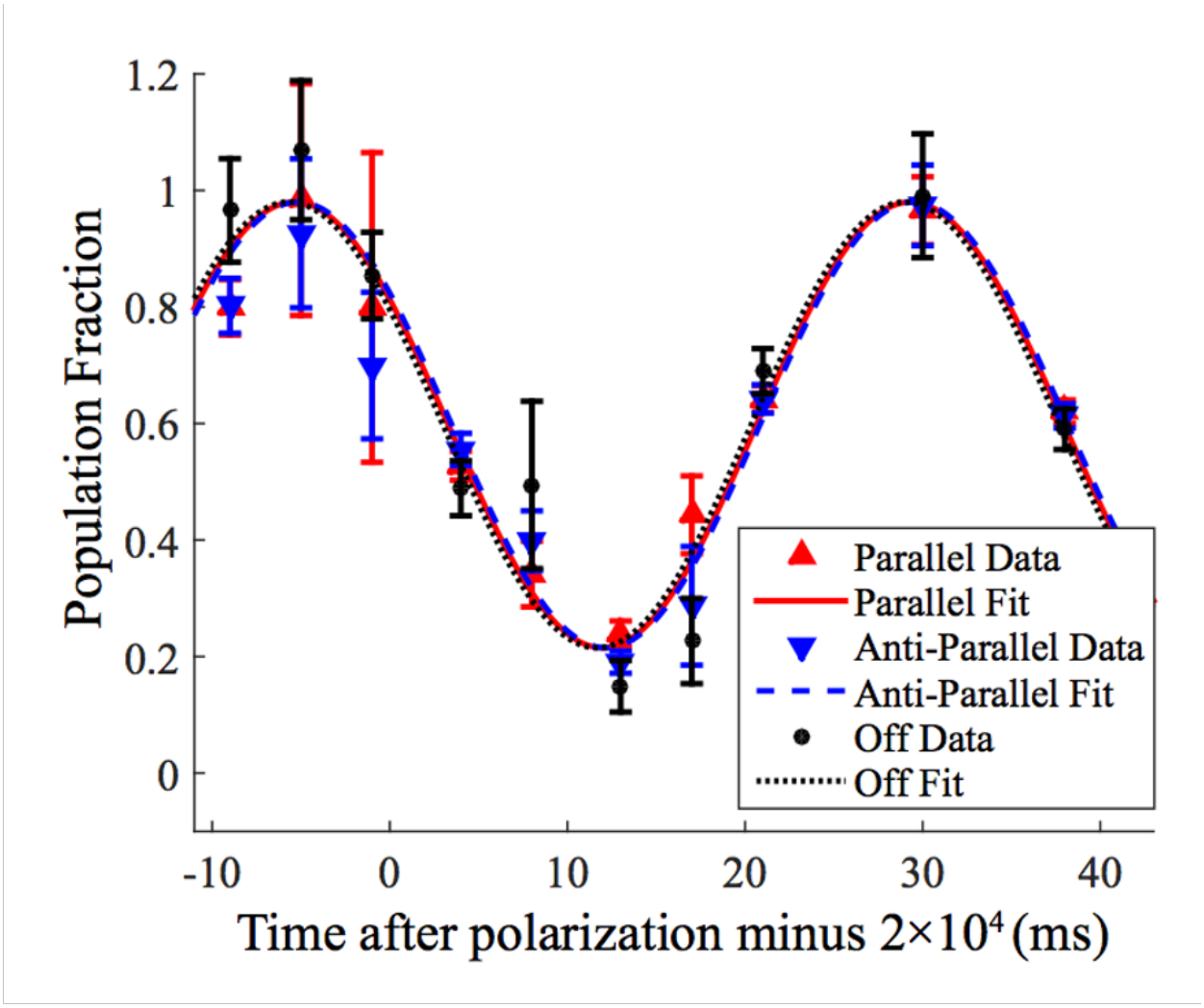

Figure 6.14: The ground state nuclear spin precession of ^{225}Ra atoms. The normalized 'bright' state population is plotted against the adjustable delay δ. The plot shows data taken with the $E-$field parallel to the $B-$field, $E-$field antiparallel to the $B-$field, and with the $E-$field off. The best fits to the data are obtained using the functions given in Eq. 6.5. The figure is taken from [63].

interest and is proportional to the atomic EDM 'd'. The differential phase accumulated over a total precession time of τ is given by $\Delta\phi = 4dE\tau/\hbar$. The best fit value of $\Delta\phi$ from the latest experimental data results in a 95% confidence upper limit of $\left|d(^{225}\mathrm{Ra})\right| < 1.4 \times 10^{-23} e \cdot \mathrm{cm}$[63] and is the current best limit on the atomic EDM of radium.

6.7.3 Systematic Effects

Table 6.2: The relevant sources of systematic uncertainties in the radium EDM measurement. As shown, at the current level of sensitivity, the systematic effects are at least two orders of magnitude smaller than the 95% upper confidence limit. With improved statistics at the level of $10^{-26} e \cdot \mathrm{cm}$ EDM sensitivity, we will further constrain these sources of systematic effects. Taken from Ref. [63].

Systematic Effect	Current Sensitivity	Improved Statistics ($10^{-26} e \cdot \mathrm{cm}$)
E-squared effects	1×10^{-25}	7×10^{-29}
B-field correlations	1×10^{-25}	5×10^{-27}
Holding ODT power corr.	6×10^{-26}	9×10^{-30}
Stark Interference	6×10^{-26}	2×10^{-27}
E-field ramping	9×10^{-28}	2×10^{-29}
Blue laser power corr.	7×10^{-28}	1×10^{-31}
Blue laser frequency corr.	4×10^{-28}	8×10^{-30}
$E \times v$ effects	4×10^{-28}	7×10^{-30}
Leakage current	3×10^{-28}	9×10^{-29}
Geometric phase	3×10^{-31}	7×10^{-30}
Total	2×10^{-25}	5×10^{-27}

The upper limit on the atomic EDM of radium is currently dominated by the statistical uncertainty of the measurement. The relevant sources of systematic uncertainties are shown in Table 6.2 and are not discussed here. Details on the sources of these systematics and how they are estimated can be found in Ref. [63]. As can be seen, at the current level of sensitivity, the systematic effects are at least two orders of magnitude smaller than the radium EDM upper limit. With the proposed improvements to the experiment, at a statistical sensitivity of $10^{-26} e \cdot \mathrm{cm}$, the systematic effects are anticipated to decrease even further, as illustrated in the third column of Table 6.2.

6.8 Upgrades for an Improved Measurement

Having stressed the fact that currently we are limited by the statistical uncertainty in our data, we estimate what the expected statistical uncertainty should be. Following the derivation in Ref. [66], we obtain

$$\sigma_d = \frac{\hbar\sqrt{2}}{8E\tau}\sqrt{\frac{1}{N} + 5\frac{N_\gamma}{M_\gamma^2 N^2}}\sqrt{\frac{\tau + T_d}{T}} \tag{6.6}$$

where E is the magnitude of the applied electric field, τ is the spin precession time, T_d is the total dead time, and T is the total integration time. N is the total number of atoms, N_γ is the average number of photons in the imaging pulse, and M_γ is the average number of photons scattered per atom.

Currently, a number of upgrades to the experiment are underway to improve the statistical sensitivity of the radium EDM limit by another two to three orders of magnitude. Considerable effort has gone into improving the detection signal-to-noise-ratio (SNR). This is the subject of the next chapter in which it will be explained in detail. However, to briefly summarize our strategy, our current detection SNR is limited by the use of the ${}^1S_0(F = 1/2) \leftrightarrow {}^1P_1(F = 1/2)$ transition which limits our optimal SNR to only about 1.2. With the atom numbers N kept the same, using the ${}^1S_0(F = 1/2) \leftrightarrow {}^1P_1(F = 3/2)$ transition would increase our SNR to 20. At the atom shot noise limit, the EDM sensitivity is given by

$$\sigma_d = \frac{\hbar\sqrt{2}}{8E\tau}\left(\sqrt{\frac{1}{N}}\right)\sqrt{\frac{\tau + T_d}{T}} \tag{6.7}$$

To see the sensitivity enhancement due to this improvement, we set $N = 500$, $E = 68$ kV/cm, $\tau = 20$ s, $T_d = 48$ s, and $T = 2$ days in Eq. 6.6 and calculate the EDM sensitivity at the different values of SNR. As shown in Table 6.3, at our current level of SNR, we are a factor of $\times 40$ above the atom shot noise limit. With the improved SNR, we expect to be within a factor of $\times 2$ of the atom shot noise at the current number of atoms.

Table 6.3: The effect of detection scheme SNR upgrade on the radium EDM sensitivity. For comparison we add the atom shot noise limit with $N = 500$.

SNR	M_γ	N_γ	σ_d ($e \cdot$ cm)
1.2	2.5	1×10^6	2.7×10^{-23}
20	1000	4×10^8	1.5×10^{-24}
Atom Shot Noise Limit			6.8×10^{-25}

So, imaging on the cycling transition, we greatly improve our EDM sensitivity. However since the transition itself is not ground state spin-selective (regardless of our choice of laser polarization), the imaging laser beam cannot be used for state preparation. Instead, we want to implement an electron shelving technique that will selectively depopulate one of the ground state sublevels. This technique called stimulated raman adiabatic passage (STIRAP) will be described in the next chapter.

Since the last EDM measurement, our group has developed new pairs of electrodes to increase the electric fields applied to the atoms. Experimenting both with new materials as well as surface preparation techniques we find that electrodes fabricated out of large grain niobium prove the most promising. A pair of niobium electrodes held at a distance of 1mm apart have shown to generate electric fields as large as 200 kV/cm, with low levels (<25 pA) of steady state leakage currents, which is a factor of 3.1 larger than what was achieved with the pair of copper electrodes. This pair of electrodes has been installed in our science chamber at Argonne National Laboratory and is ready for use in the next EDM measurement. The preparation and the testing of the new pair of electrodes will be compiled into a publication soon, and will also be detailed in Roy Ready's thesis.

With these two upgrades we expect a factor of ≈ 60 in our EDM sensitivity putting the 95% upper limit on the radium EDM at the $10^{-25} e \cdot$ cm level.

Another upgrade underway focuses on increasing the number of trapped atoms that are interrogated for an EDM measurement, N. This involves changing our atom cooling scheme. The idea is to cool the atoms on the stronger dipole allowed 483 nm $^1S_0 \leftrightarrow {}^1P_1$ transition instead of the weaker 714nm $^1S_0 \leftrightarrow {}^3P_1$ transition currently used in our setup. Currently with a 1m long zeeman slower using the 714 nm transition, we slow atoms moving with velocities up to 60

m/s. With a 20 cm slower using the 483 nm transition, we expect to slow atoms moving as fast as 310 m/s, resulting in a factor of 100 improvement in the atom trapping efficiency. This upgrade and the relevant spectroscopy of the states of interest is the subject of chapter 8. Along with the two upgrades to the detection SNR and the $E-$field, this will enhance the radium atomic EDM sensitivity to the $10^{-26}\, e \cdot \text{cm}$ level, as summarized in Table 6.4.

Table 6.4: The upgrades to the radium EDM experiment, and the anticipated enhancement of the radium atomic EDM sensitivity.

	Currently	Upgrade Goal
Electric Field (E)	65 kV/cm	200 kV/cm
Atom Detection SNR	1.2	20
Atom Number (N)	500	5×10^4
σ_d ($e \cdot$ cm)	10^{-23}	10^{-26}

CHAPTER 7

DETECTION SCHEME UPGRADE

At the current level of statistical uncertainty, the Ra EDM sensitivity scales linearly with the SNR (signal-to-noise-ratio). This chapter highlights a proposed upgrade for enhancing our photon absorption signal from the same amount of atoms trapped in an ODT, using the STIRAP technique.

7.1 Electron Shelving for Nuclear Spin Precession Measurement

As detailed in the previous chapter, with the current scheme for detecting the nuclear spin precession in ^{225}Ra on the $7s^2\,{}^1S_0(F = 1/2) \longleftrightarrow 7s7p\,{}^1P_1(F = 1/2)$ transition, we scatter on average 2.1 photons per atom. As a result, our atom signal is photon shot noise limited, while we would like to reach the atom shot noise limit instead. The $7s^2\,{}^1S_0(F = 1/2) \longleftrightarrow 7s7p\,{}^1P_1(F = 3/2)$ transition on the other hand allows for up to 2000 photon scattering events per atom, three orders of magnitude more than what we currently achieve. If used, this would provide a factor of $\approx$ 20 enhancement in our SNR. The transition is however not spin-selective as both the ground state hyperfine sublevels are excited and therefore cannot - on its own - be used for spin precession detection. What we require in addition, is a mechanism to selectively deplete the atoms out of one of the ground state sublevels to ensure spin-selective atom precession detection using this transition.

The presence of the low lying metastable $D-$ states in Radium, and other alkaline-earth metals, provide a convenient avenue for shelving the electrons from one of the ground state sublevels making them insensitive to the detection light. Nuclear spin precession detection therefore requires that the electron shelving be spin-selective. This then ensures that we can use the above transition for spin precession detection. One such technique is the stimulated raman adiabatic passage (STIRAP).

As shown in Fig. 7.1, typically, STIRAP consists of the coherent transfer of the population from one lower lying state $|1\rangle$ to another $|3\rangle$ via an excited state $|2\rangle$. Each individual lower lying state is connected to the excited state $|2\rangle$ by a radiative transition that can be excited by a laser. The laser that connects the state $|1\rangle$ in which the atoms begin to the excited state $|2\rangle$ is called the

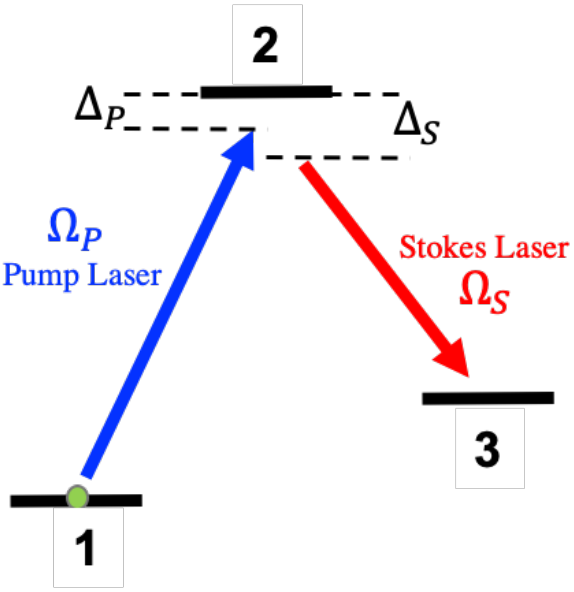

Figure 7.1: The Λ-type three-level system with the lower-lying states $|1\rangle$, $|3\rangle$ and the excited intermediate state $|2\rangle$. The states are connected by the pump transition $|1\rangle \leftrightarrow |2\rangle$ and the Stokes transition $|3\rangle \leftrightarrow |2\rangle$ with individual one-photon detunings Δ_p and Δ_s.

pump laser, while the laser that connects the final state $|3\rangle$ to the excited state $|2\rangle$ is called the Stokes laser. In their pioneering work on this technique, Gaubatz *et al.* [71] presented both the fundamental theory behind this method as well as experimental data showing STIRAP. Their work featured the non-intuitive spatial arrangement of the pump and Stokes laser beams - where the Stokes beam precedes the pump - demonstrating selective population transfer between vibrational levels in sodium dimer. Since then, STIRAP has been demonstrated in a variety of atomic [72–77], molecular, and ionic systems[78, 79], using spatially separated laser beams as well as temporally differentiated pulses. Applications of STIRAP in atomic and ionic systems range from precision isotope shift measurements, state preparation for quantum computation, atom interferometry, to creation of coherent superposition states. In molecular physics, it has been used in - among other applications - the creation of ultracold molecules and Bose-Einstein condensates[80–82].

In our case, we intend to use STIRAP for selectively shelving the electrons from one of the ground sublevels of ^{225}Ra, $7s^2\,{}^1S_0(F = 1/2)$ into the meta-stable $7s7d\,{}^3D_1$ state. If the spin polarized atoms happen to be in the state sensitive to the STIRAP lasers, they will be shelved into the ${}^3D_1$ state and will not be detected by the imaging light. If they are in the sublevel insensitive to

the STIRAP lasers, they will remain in the ground state and be imaged by the detection light. This then allows us to use the stronger imaging transition ($7s^2\,{}^1S_0(F = 1/2) \longleftrightarrow 7s7p\,{}^1P_1(F = 3/2)$) to detect the spin precession of the ground state.

7.1.1 STIRAP

Here we develop the basic concepts underlying the STIRAP technique. We use a simple 3-state system with two lower-lying states ($|1\rangle$ and $|3\rangle$) and one excited state ($|2\rangle$). Fig. 7.1 shows the typical Λ-type system used in the earliest theoretical work on STIRAP [71]. The population is transferred with near unity efficiency from one low-lying state $|1\rangle$ to another $|3\rangle$ via an excited intermediate state $|2\rangle$, without any loss to the excited state. We assume that the initial state $|1\rangle$ is energetically lower than the final state $|3\rangle$. For simplicity, we ignore the effects of spontaneous emission from the intermediate state $|2\rangle$, or radiative decays from the final state $|3\rangle$ to the initial state $|1\rangle$. The latter is justified - in our case - by the long lifetime (longer than the atom-light interaction time)[1] of the final state $|3\rangle$. We will however incorporate the spontaneous decay of population from the intermediate state $|2\rangle$ in our simulations. The initial state $|1\rangle$ is coupled to the intermediate state $|2\rangle$ by the pump laser with frequency ω_P, while the Stokes laser with frequency ω_S couples the final state $|3\rangle$ to the intermediate state $|2\rangle$. The pump laser is frequency detuned from the transition resonance by $\Delta_p = \omega_{12} - \omega_p$, where $E_{12} = E_2 - E_1 = \hbar\omega_{12}$ is the energy difference between states $|2\rangle$ and $|1\rangle$. Similary, the Stokes laser is frequency detuned by $\Delta_s = \omega_{32} - \omega_s$ from the single photon resonance, where $E_{32} = E_2 - E_3 = \hbar\omega_{32}$ is the energy difference between states $|2\rangle$ and $|3\rangle$. The two-photon detuning is then defined as $\delta = \Delta_p - \Delta_s$. The coherent light-atom interaction is fully described by the following time-dependent Schrödinger equation

$$i\hbar\frac{d}{dt}\Psi(t) = \mathcal{H}(t)\Psi(t) \tag{7.1}$$

where $\Psi(t) = [c_1(t), c_2(t), c_2(t)]^T$ is the three component state vector, $\mathcal{H}(t) = \mathcal{H}_0 + \mathcal{H}_{int}(t)$

[1]The $7s7d\,{}^3D_1$ state has a lifetime of 510(60)μs [50], which is more than two orders of magnitude longer the STIRAP pulse durations of a few μs.

is the total Hamiltonian, $\mathcal{H}_0$ is the unperturbed bare-atom Hamiltonian, and $\mathcal{H}_{int}(t)$ describes the atom-light interaction.

The bare-atom Hamiltonian can be simply written as

$$\mathcal{H}_0 = \frac{p^2}{2m} + \hbar\omega_{12} |2\rangle \langle 2| + \hbar\omega_{13} |3\rangle \langle 3| \tag{7.2}$$

where m is the mass of the atom, p is the center-of-mass momentum, and $\hbar\omega_{13} = E_3 - E_1$ is the energy difference between states $|3\rangle$ and $|1\rangle$.

We now formulate the interaction part of the Hamiltonian $\mathcal{H}_{int}(t)$. We closely follow the treatment of three level systems in Ref. [83], although we differ in defining the ground state $|1\rangle$ as our energy reference, instead of the intermediate state $|2\rangle$. To describe the atom-light interaction we begin by writing the combined optical field of the pump and Stokes lasers in the "long-wavelength limit"[2] as

$$\vec{E}(t) = \vec{E}_p(t) + \vec{E}_s(t) \tag{7.3}$$

$$= \hat{\varepsilon}_p E_{0p}(t) \cos(\omega_p t) + \hat{\varepsilon}_s E_{0s}(t) \cos(\omega_s t) \tag{7.4}$$

where $\hat{\varepsilon}_p$ and $\hat{\varepsilon}_s$ are the respective polarization vectors for the pump and Stokes lasers. $E_{0p}(t)$ and $E_{0s}(t)$ are the slowly time-varying amplitudes of the pump and Stokes lasers. At this point, it is instructive to express the combined optical field in terms of the co- and counter-rotating frequency terms:

$$\vec{E}(t) = \vec{E}^{(+)}(t) + \vec{E}^{(-)}(t) \tag{7.5}$$

$$= \left(\hat{\varepsilon}_p E_{0p}(t)\, e^{-i\omega_p t} + \hat{\varepsilon}_s E_{0s}(t)\, e^{-i\omega_s t}\right) + \left(\hat{\varepsilon}_p E_{0p}(t)\, e^{+i\omega_p t} + \hat{\varepsilon}_s E_{0s}(t)\, e^{+i\omega_s t}\right) \tag{7.6}$$

[2]In the long-wavelength limit, we ignore the spatial variation of the optical field. The spatial part of the laser field contains exponentials of the form $e^{i\vec{k}\cdot\vec{r}} \approx 1 + i\vec{k}\cdot\vec{r}$ where we only keep the first term. This is valid since the wavelength of the optical field 'λ' is much larger than the size of the atom 'R': $|R/\lambda| << 1$.

The atom-light interaction can then be expressed as

$$\mathcal{H}_{int}(t) = -\vec{d} \cdot \vec{E}(t) \tag{7.7}$$

where $\vec{d} = e\vec{r}$ is the light induced electric dipole moment between the connected states. We now express the induced electric dipole moment in terms of the co- and counter-rotating frequency terms as

$$\begin{aligned}
\vec{d} &= \vec{d}^{(+)} + \vec{d}^{(-)} && (7.8)\\
&= \vec{d}_{12}^{(+)} + \vec{d}_{32}^{(+)} + \vec{d}_{12}^{(-)} + \vec{d}_{32}^{(-)} && (7.9)\\
&= \left(\langle 1|\, \vec{d}\, |2\rangle\, \sigma_1\right) + \left(\langle 3|\, \vec{d}\, |2\rangle\, \sigma_3\right) + \left(\langle 1|\, \vec{d}\, |2\rangle\, \sigma_1^\dagger\right) + \left(\langle 3|\, \vec{d}\, |2\rangle\, \sigma_3^\dagger\right) && (7.10)
\end{aligned}$$

where $\sigma_\alpha = |\alpha\rangle\langle 2|$ is the annihilation/lowering operator that lowers an atom in the excited state $|2\rangle$ to the lower lying state $|\alpha\rangle$ ($\alpha = 1, 3$), and $\sigma^\dagger$ is the corresponding creation/raising operator.

To understand why $\vec{d}^{(+)}$ is the co-rotating term, we inspect the time evolution of the expectation value of this operator connecting states $|1\rangle$ and $|2\rangle$, $\vec{d}_{12}^{(+)}$. Using the Ehrenfest's Theorem[84]:

$$\begin{aligned}
-i\hbar\frac{d}{dt}\left\langle \vec{d}_{12}^{(+)} \right\rangle &= \left\langle \left[\mathcal{H}_0, \vec{d}^{(+)}\right] \right\rangle && (7.11)\\
&= \left\langle \hbar\left[\left(\omega_{12}\,|2\rangle\langle 2| + \omega_{13}\,|3\rangle\langle 3|\right), \left(\langle 1|\, \vec{d}\, |2\rangle\, \sigma_1\right)\right] \right\rangle && (7.12)\\
&= -\hbar\left\langle \vec{d}_{12}^{(+)} \right\rangle && (7.13)
\end{aligned}$$

Solving for the time-evolution of the expectation value of the $\vec{d}_{12}^{(+)}$ gives

$$\left\langle \vec{d}_{12}^{(+)} \right\rangle (t) = \left\langle \vec{d}_{12}^{(+)} \right\rangle (0)\, e^{-i\omega_{12}t} \tag{7.14}$$

As we can see, the time-evolution carries the positive (co-rotating) frequency ω_{12}. The same is true of the expectation value of $\vec{d}_{32}^{(+)}$. The expectation value of the $\vec{d}_{12}^{(-)}$ term on the other hand depends on the negative (counter-rotating) frequency $-\omega_{12}$ as can be similarly shown.

The interaction term can now be written in terms of the co- and counter-rotating terms as

$$\mathcal{H}_{int}(t) = -\vec{d} \cdot \vec{E}(t) \tag{7.15}$$

$$= \left(\vec{d}^{(+)} + \vec{d}^{(-)}\right) \cdot \left(\vec{E}^{(+)}(t) + \vec{E}^{(-)}(t)\right) \tag{7.16}$$

$$= \vec{d}^{(+)} \cdot \vec{E}^{(+)}(t) + \vec{d}^{(+)} \cdot \vec{E}^{(-)}(t) + \vec{d}^{(-)} \cdot \vec{E}^{(+)}(t) + \vec{d}^{(-)} \cdot \vec{E}^{(-)}(t) \tag{7.17}$$

Here we further simplify the system. We observe that the expectation values of the $\vec{d}^{(+)} \cdot \vec{E}^{(+)}(t)$ and the $\vec{d}^{(-)} \cdot \vec{E}^{(-)}(t)$ terms contain the complex exponential with frequencies $\pm\omega_{\alpha 2} \pm \omega_{p,s}$ ($\alpha = 1, 3$). Assuming that $|\omega_{\alpha 2} + \omega_{p,s}| >> |\omega_{\alpha 2} - \omega_{p,s}|$ ($\alpha = 1, 3$), we can ignore the above "fast-rotating" terms and only keep the cross-terms in Eq. 7.17. This is famously known as the rotating wave approximation (RWA), under which, the atom-light interaction can then be expressed as

$$\mathcal{H}_{int}(t) = \vec{d}^{(+)} \cdot \vec{E}^{(-)}(t) + \vec{d}^{(-)} \cdot \vec{E}^{(+)}(t) \tag{7.18}$$

$$= \hbar\frac{\Omega_p}{2}\left(\sigma_1\, e^{-i\omega_p t} + \sigma_1^\dagger\, e^{i\omega_p t}\right) + \hbar\frac{\Omega_s}{2}\left(\sigma_3\, e^{-i\omega_s t} + \sigma_3^\dagger\, e^{i\omega_s t}\right) \tag{7.19}$$

where $\Omega_{p,s}(t) = -\langle\alpha|\, \hat{\varepsilon}_{p,s} \cdot \vec{d}\, |2\rangle\, E_{0p,s}(t)/\hbar$ is the Rabi frequency for the pump and Stokes transitions connecting the relevant lower level $|\alpha\rangle$ ($\alpha = 1, 3$) and the excited level $|2\rangle$.

Before proceeding with the solution to Eq. 7.1, we make a unitary transform of the atomic state into the rotating frames of the optical fields, using the ground state $|1\rangle$ as the energy reference. The time dependent probability amplitudes in the rotating frame can be written as

$$\tilde{c}_1(t) = c_1(t) \tag{7.20}$$

$$\tilde{c}_2(t) = c_2(t)\, e^{-i\omega_p t} \tag{7.21}$$

$$\tilde{c}_3(t) = c_3(t)\, e^{-i(\omega_p - \omega_s)t} \tag{7.22}$$

In the rotating frame, the bare-atom Hamiltonian is given by

$$\tilde{H}_0 = \frac{p^2}{2m} + \hbar\Delta\, |2\rangle\langle 2| + \hbar\delta\, |3\rangle\langle 3| \tag{7.23}$$

where we define $\Delta = \Delta_p$ as the one-photon detuning. The atom-light interaction term in the rotating frame is given by

$$\tilde{H}_{int} = \hbar\frac{\Omega_p(t)}{2}\left(\sigma_1 + \sigma_1^\dagger\right) + \hbar\frac{\Omega_s(t)}{2}\left(\sigma_3 + \sigma_3^\dagger\right) \tag{7.24}$$

Combining them together and ignoring the center-of-mass motion, the Hamiltonian in the rotating frame is given by

$$\tilde{H} = \tilde{H}_0 + \tilde{H}_{int}(t) \tag{7.25}$$

$$= \hbar\begin{pmatrix} 0 & \frac{1}{2}\Omega_p(t) & 0 \\ \frac{1}{2}\Omega_p(t) & \Delta & \frac{1}{2}\Omega_s(t) \\ 0 & \frac{1}{2}\Omega_s(t) & \delta \end{pmatrix} \tag{7.26}$$

Assuming two-photon resonance ($\delta = 0$), we can solve for the eigenvalues and the eigenstates of this Hamiltonian. The three eigenvalues λ_0, $\lambda_\pm$ are

$$\lambda_0 = 0 \tag{7.27}$$

$$\lambda_\pm = \frac{1}{2}\left(\Delta \pm \sqrt{\Delta^2 + \Omega_{rms}(t)^2}\right) \tag{7.28}$$

where $\Omega_{rms}(t) = \sqrt{\Omega_p(t)^2 + \Omega_s(t)^2}$.

The corresponding adiabatic eigenstates $|a_0\rangle$, $|a_\pm\rangle$ are given by

$$|a_0\rangle = \cos\theta(t)\,|1\rangle - \sin\theta(t)\,|3\rangle \tag{7.29}$$

$$|a_+\rangle = \sin\theta(t)\sin\phi(t)\,|1\rangle + \cos\phi(t)\,|2\rangle + \cos\theta(t)\sin\phi(t)\,|3\rangle \tag{7.30}$$

$$|a_-\rangle = \sin\theta(t)\cos\phi(t)\,|1\rangle - \sin\phi(t)\,|2\rangle + \cos\theta(t)\cos\phi(t)\,|3\rangle \tag{7.31}$$

where the mixing angles are defined as

$$\tan\theta(t) = \frac{\Omega_p(t)}{\Omega_s(t)} \tag{7.32}$$

$$\tan 2\phi(t) = \frac{\Omega_{rms}(t)}{\Delta} \tag{7.33}$$

We now focus our attention on the adiabatic eigenstate $|a_0\rangle$ corresponding to the null eigenvalue $\lambda_0 = 0$. What should be striking is how this state is decoupled from the intermediate excited state $|2\rangle$. For this reason, this state is also known as the "dark" state or the "coherent population trapping" state. This is precisely what enables the STIRAP technique. An atom prepared in the initial state $|1\rangle$ and kept aligned with the "dark" state $|a_0\rangle$ will ensure complete transfer of population into the final state $|3\rangle$ without any loss to the intermediate state $|2\rangle$, given the two-photon resonance ($\delta = 0$) and the adiabaticity conditions are met. We shall elaborate more on the latter below. We note that to ensure that we stay in the "dark" state, we need to align it with the initial bare-atomic state $|1\rangle$ by beginning with the mixing angle θ at 0. This is achieved by requiring that only the Stokes laser is present at the start of our STIRAP process. This then explains the need for the "non-intuitive" arrangement of the two lasers. It is non-intuitive in the sense that the atoms are initially illuminated with photons that do not - in a two-level system - cause any radiative transitions.

Fig. 7.2 shows the results of a typical STIRAP process with the two-photon detuning $\delta = 0$. Fig. 7.2(a) shows the temporal ordering of the STIRAP pulses with the Stokes pulse preceding the pump pulse. Fig. 7.2(b) shows the three dressed-state energy eigenvalues of the system. We remain in the energy eigenstate $|a_0\rangle$ with the null eigenstate $\lambda_0 = 0$. Fig. 7.2(d) shows the population in the three bare-atom states. Under optimal STIRAP conditions, we remain in the "dark" adiabatic state $|a_0\rangle$ throughout the STIRAP process and the atomic population is completely transferred from the intial state $|1\rangle$ into the final state $|3\rangle$ without any loss into the intermediate state $|2\rangle$. Fig. 7.2(c) shows the adiabatic time-evolution of the mixing angle θ from 0 to $\pi/2$ critical to the optimal functioning of this technique.

We conclude this section by commenting on the required "adiabaticity" of the STIRAP process. Kuklinski *et al.* [85] derived the "local" condition for the adiabatic evolution of the atomic population

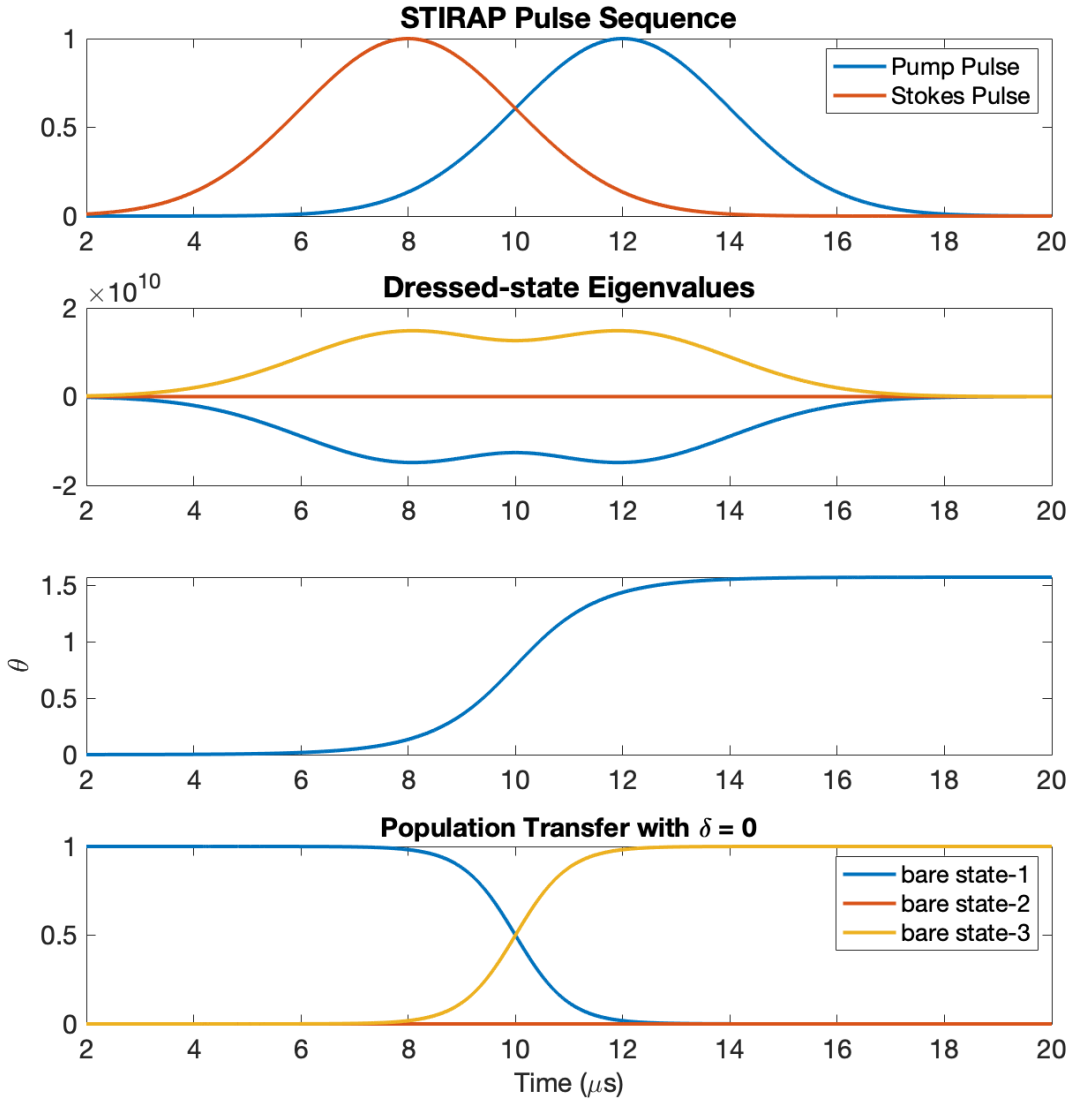

Figure 7.2: STIRAP in the Λ-type three-level system shown in Fig. 7.1. (a) shows the STIRAP pulse sequence with the Stokes pulse preceding the pump pulse. (b) shows the three energy eigenvalues. Under ideal STIRAP conditions, the atom evolves adiabatically in the "dark" state $|a_0\rangle$ with the null eigenvalue $\lambda_0 = 0$. (c) shows the mixing angle as a function of time. As desired, the mixing angle θ begins at 0 and ends at $\pi/2$. (d) shows the time-evolution of the population in the three bare-atom states. Under ideal STIRAP conditions, the population is transferred from the intial state $|1\rangle$ into the final state $|3\rangle$ without any loss into the intermediate state $|2\rangle$.

during the STIRAP process as

$$\Omega_{rms}(t) >> |\dot{\theta}(t)| \tag{7.34}$$

This condition states that rate of change of the mixing angle $\theta(t)$ has to be much slower than the effective Rabi frequency Ω_{rms}, hence the use of the term 'adiabatic'. In other words, it requires a 'smooth' transition of the STIRAP pulses from the Stokes to the pump pulse. It also requires sufficient overlap between the two pulses to ensure that this local condition is met throughout the adiabatic passage of the atomic population. For smooth laser pulses, such as Gaussian pulses, Eq. 7.34 can be integrated over the interaction duration to obtain what is called the "global" adiabaticity condition

$$\Omega_{max}\tau > 10 \tag{7.35}$$

where Ω_{max} is the peak Rabi frequency and τ is the pulse duration (assuming we use pulses of equal durations).

7.1.2 Proposed Application to the Radium EDM Experiment

It is this highly efficient transfer of atomic population between states in a Λ-type three-level system that makes STIRAP an attractive candidate for electron shelving in radium. Our objective is to shelve the population in one of the magnetic sublevels of the $^1S_0$ ground state of ^{225}Ra to ensure spin-selective atom imaging for mapping the nuclear spin-precession. For this purpose, one proposed STIRAP scheme for ^{225}Ra is shown in Fig. 7.3.

Here we employ STIRAP with the following choices of pump and Stokes transitions. Pump laser with σ^+ polarization is tuned to the $^1S_0\ (F = 1/2, m_F = -1/2) \leftrightarrow {}^1P_1\ (F = 1/2, m_F = +1/2)$ transition, while the Stokes laser with σ^+ polarization is tuned to the $^3D_1\ (F = 3/2, m_F = -1/2) \leftrightarrow {}^1P_1\ (F = 1/2, m_F = +1/2)$ transition. This ensures that we selectively deplete only the $^1S_0\ (F = 1/2, m_F = -1/2)$ sublevel. This, as shown in Fig. 7.4, is the state preparation step. Suppose we spin polarize the ground state by optically pumping the atoms into the $^1S_0\ (F = 1/2, m_F = +1/2)$

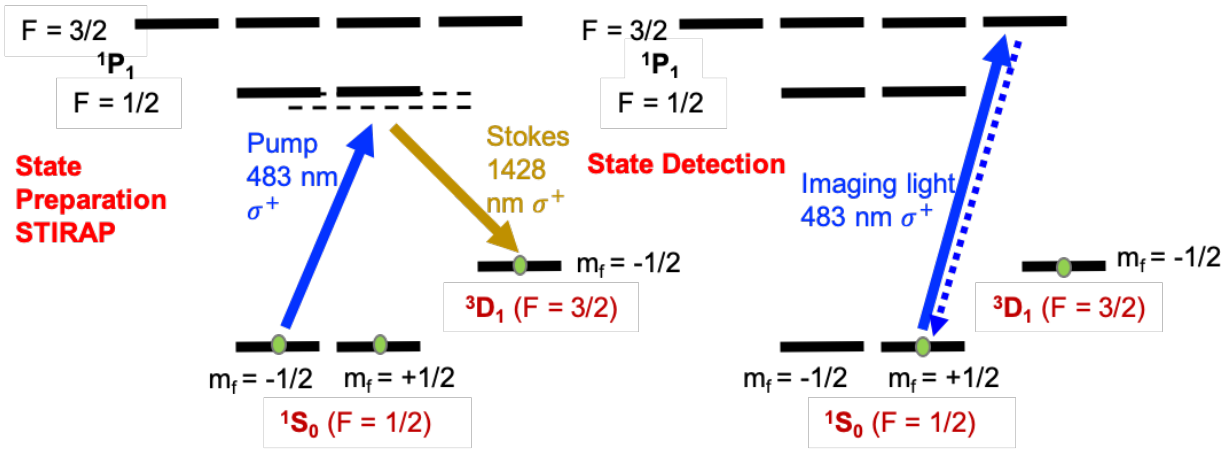

Figure 7.3: Proposed STIRAP scheme for ^{225}Ra. The ground state atomic population from the $^1S_0\,(F = 1/2, m_F = -1/2)$ sublevel is shelved into the meta-stable $^3D_1\,(F = 3/2, m_F = -1/2)$ state via the excited $^1P_1\,(F = 1/2, m_F = +1/2)$ state. The spin precession of the population in the ground state sublevel is imaged on the $^1S_0\,(F = 1/2, m_F = +1/2) \leftrightarrow {}^1P_1\,(F = 3/2, m_F = +3/2)$ transition.

sublevel. If we apply the STIRAP pulses at multiples of half the precession period, the atoms are in the STIRAP "bright"(sensitive) $^1S_0\,(F = 1/2, m_F = -1/2)$ state and are shelved into the $^3D_1$ state. However, if the STIRAP pulses are applied at multiples of a full precession period, the atoms are in the STIRAP "dark"(insensitive) $^1S_0\,(F = 1/2, m_F = +1/2)$ state and therefore remain in the ground state. This then allows us to selectively image the ground state sublevel and map the nuclear spin precession using the stronger imaging transition. This, as shown in Fig. 7.4, is the state detection step. Although this example illustrates the use of STIRAP for spin-selective electron shelving in ^{225}Ra, it is not the only possible scheme for achieving ground state spin selectivity.

7.2 Simulating STIRAP in Radium Isotopes

To determine the feasibility of using STIRAP in radium, we conducted a number of simulation studies in the different isotopes of radium of interest. We studied the effects of STIRAP in ^{226}Ra, ^{225}Ra, and ^{223}Ra.

7.2.1 ^{226}Ra

Fig. 7.4 shows the seven states used to simulate STIRAP in ^{226}Ra.

We consider the following set of states for the purposes of simulating STIRAP

1. One Initial state: $|1\rangle := {}^1S_0\,(J=0, m_J=0)$

2. Three Intermediate states: $|2\rangle := {}^1P_1\,(J=1, m_J=-1)$, $|3\rangle := {}^1P_1\,(J=1, m_J=0)$, and $|4\rangle := {}^1P_1\,(J=1, m_J=+1)$.

3. Three Final states: $|5\rangle := {}^3D_1\,(J=1, m_J=-1)$, $|6\rangle := {}^3D_1\,(J=1, m_J=0)$, and $|7\rangle := {}^3D_1\,(J=1, m_J=+1)$.

As an example, we set the pump laser frequency resonant on the ${}^1S_0\,(m_J=0) \leftrightarrow {}^1P_1(m_J=+1)$ transition and the Stokes laser frequency resonant on the ${}^3D_1\,(m_J=0) \leftrightarrow {}^1P_1(m_J=+1)$ transition.

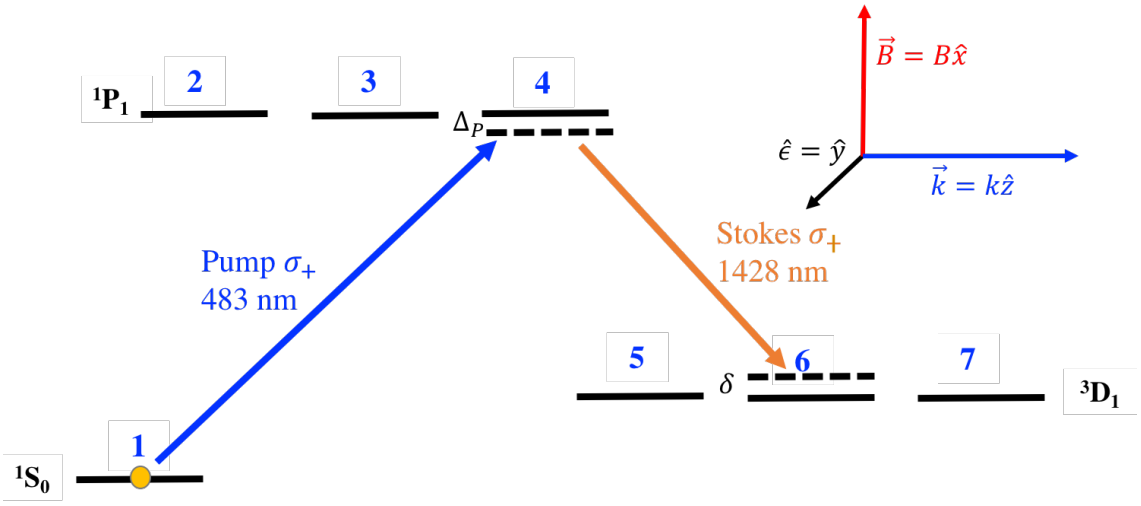

Figure 7.4: The seven levels involved in the simulation of STIRAP in ^{226}Ra are labelled. A possible STIRAP scheme for ^{226}Ra is shown. Also shown are the 1-photon detuning Δ_P and the 2-photon detuning δ. The direction of pulse propagation $\vec{k}$, the magnetic field $\vec{B}$ and the polarization of our optical dipole trap (ODT) $\hat{\epsilon}$ are as shown.

In our simulation, the ^{226}Ra atoms are held in an optical dipole trap (ODT), in the presence of an external magnetic field $B = B\hat{x}$. The Hamiltonian for this system can be written as $\mathcal{H} = \mathcal{H}_\Omega + \mathcal{H}_B$, where $\mathcal{H}_\Omega$ is the light-atom interaction part, and $\mathcal{H}_B$ is the interaction with the external magnetic field B.

In the rotating wave approximation (RWA) the atom-light interaction part of the Hamiltonian $\mathcal{H}_\Omega$ can be written as the following 7×7 matrix

$$\mathcal{H}_\Omega = \frac{\hbar}{2}\begin{pmatrix} -\delta & \Omega_{P,12}(t) & \Omega_{P,13}(t) & \Omega_{P,14}(t) & 0 & 0 & 0 \\ \Omega_{P,12}(t) & 2\Delta + i\gamma/2 & 0 & 0 & \Omega_{S,25}(t) & \Omega_{S,26}(t) & \Omega_{S,27}(t) \\ \Omega_{P,13}(t) & 0 & 2\Delta + i\gamma/2 & 0 & \Omega_{S,35}(t) & \Omega_{S,36}(t) & \Omega_{S,37}(t) \\ \Omega_{P,14}(t) & 0 & 0 & 2\Delta + i\gamma/2 & \Omega_{S,45}(t) & \Omega_{S,46}(t) & \Omega_{S,47}(t) \\ 0 & \Omega_{S,25}(t) & \Omega_{S,35}(t) & \Omega_{S,45}(t) & \delta & 0 & 0 \\ 0 & \Omega_{S,26}(t) & \Omega_{S,36}(t) & \Omega_{S,46}(t) & 0 & \delta & 0 \\ 0 & \Omega_{S,27}(t) & \Omega_{S,37}(t) & \Omega_{S,47}(t) & 0 & 0 & \delta \end{pmatrix} \tag{7.36}$$

where $\Delta = \Delta_P = \omega_{14} - \omega_P$ is the one-photon detuning, $\hbar\omega_{14}$ is the energy difference between the states $|1\rangle$ and $|4\rangle$, and ω_P is the pump laser frequency. We define the two-photon detuning as $\delta = \omega_{46} - \Delta_P - \omega_S$, where ω_S is the Stokes laser frequency and $\hbar\omega_{46}$ is the energy splitting between states $|4\rangle$ and $|6\rangle$. In this simulation we also take into account spontaneous decay of atoms from the excited (intermediate) state manifold ($|2\rangle, |3\rangle, |4\rangle$). γ is the spontaneous emission rate out of the excited state $^1P_1$ manifold to states other than the ones included in this simulation.

The Rabi frequency for a laser induced transition between a lower level $|i\rangle$ and an excited state $|j\rangle$ is given by $\Omega_{ij}(t) = -\vec{d}_{ij} \cdot \vec{E}(t)/\hbar$, where $\vec{d}_{ij}$ is the E1-transition dipole moment, and $\vec{E}(t)$ is the electric field of the laser pulse.

In our case, we use gaussian pulses with electric fields given by

$$\vec{E}(t) = \vec{E}_0 e^{-(t-\Delta t)^2/2\tau^2} \tag{7.37}$$

where $\vec{E}_0$ is the peak pulse electric field, Δt is the pulse delay and τ is the pulse width/duration.

The transition dipole moment d_{ij} is given by

$$d_{ij} = \langle i||d||j\rangle \times k_{ij} \tag{7.38}$$

where $\langle i||d||j\rangle$ is the reduced matrix element that only depends on the radial part of the wavefunctions for state $|i\rangle$ and $|j\rangle$ and is common for states of the same orbital angular momentum 'l'.

k_{ij} gives the angular part of the transition dipole moment. For ^{226}Ra where we take into consideration the fine structure of the atom, it is given by

$$k_{ij} = (-1)^{L'+S-M'_J}\sqrt{(2J+1)(2J'+1)} \times \begin{Bmatrix} L' & J' & S \\ J & L & 1 \end{Bmatrix} \begin{pmatrix} J & 1 & J' \\ M_J & q & -M'_J \end{pmatrix} \tag{7.39}$$

For ^{225}Ra and ^{223}Ra where we take into account the hyperfine structure, the relevant expression for k_{ij} is given by

$$k_{ij} = (-1)^{1+L'+S+J+J'+I-M'_F}\sqrt{(2J+1)(2J'+1)(2F+1)(2F'+1)} \tag{7.40}$$

$$\times \begin{Bmatrix} L' & J' & S \\ J & L & 1 \end{Bmatrix} \begin{Bmatrix} J' & F' & I \\ F & J & 1 \end{Bmatrix} \begin{pmatrix} F & 1 & F' \\ M_F & q & -M'_F \end{pmatrix} \tag{7.41}$$

where relevant, L is the total orbital angular momentum, S is the total electron spin, $\vec{J} = \vec{L} + \vec{S}$ is the total electron angular momentum with z-component M_J, I is the nuclear spin, and $\vec{F} = \vec{J} + \vec{I}$ is the total angular momentum, with z-component M_F of the lower lying state $|i\rangle$. The primed $'$ quantities correspond to the excited state $|j\rangle$. $q = 0, \pm 1$ corresponds to the polarization (0: linear, +: right circular and -: left circular) of the optical field. The quantity with the curly brackets {} corresponds to the Wigner 6-j symbol, while the one with the parenthesis () corresponds to the Wigner 3-j symbol for angular momentum addition.

The interaction $\mathcal{H}_B$ of an atom with magnetic moment $\vec{\mu}$ with the external magnetic field $\vec{B}$ is given by $\mathcal{H}_B = -\vec{\mu} \cdot \vec{B}$. In our case, the direction of the laser propagation $\vec{k} = k\hat{z}$ is taken as the quantization axis. Therefore the B-field lying along the x-axis, causes precession of states in each degenerate manifold with total angular momentum J. For the three different states connected by STIRAP with orbital angular momentum 'l', we write $\mathcal{H}_B$ as a direct sum over the interactions of

individual states with the magnetic field: $\mathcal{H}_B = \bigoplus_{l=1}^{2} \mathcal{H}_B^{(l)}$. For instance, for the ${}^1P_1(l=1)$ state, the interaction term with a magnetic field $\vec{B} = B\hat{x}$ is given by $\mathcal{H}_B^{(l=1)} = -\vec{\mu}\cdot\vec{B} = g_J\mu_B B J_x/\hbar$, where μ_B is the Bohr magneton and g_J is the Landé g-factor for the state with a total angular momentum J and $x-$component J_x given by

$$g_J = \frac{3}{2} + \frac{S(S+1) - L(L+1)}{2J(J+1)} \tag{7.42}$$

The total 7×7 matrix for the interaction of the different STIRAP connected states ^{226}Ra with an external magentic field B is given by

$$\mathcal{H}_B = \bigoplus_{l=1}^{2} \mathcal{H}_B^{(l)} \tag{7.43}$$

$$= \frac{\mu_B}{\hbar} B \begin{pmatrix} g_{(J=0)}J_x^{(0)} & & \\ & g_{(J=1)}J_x^{(1)} & \\ & & g_{(J=1)}J_x^{(1)} \end{pmatrix} \tag{7.44}$$

$$= \frac{\mu_B}{\sqrt{2}} B \begin{pmatrix} 0 & 0 & 0 & 0 & 0 & 0 & 0 \\ 0 & 0 & 1 & 0 & 0 & 0 & 0 \\ 0 & 1 & 0 & 1 & 0 & 0 & 0 \\ 0 & 0 & 1 & 0 & 0 & 0 & 0 \\ 0 & 0 & 0 & 0 & 0 & 1/2 & 0 \\ 0 & 0 & 0 & 0 & 1/2 & 0 & 1/2 \\ 0 & 0 & 0 & 0 & 0 & 1/2 & 0 \end{pmatrix} \tag{7.45}$$

where each block $J_x^{(j)}$ is a $(2j+1)\times(2j+1)$ block matrix representing the x-component of the total angular momentum J. All the other matrix elements outside the block matrices, $J_x^{(j)}$ are zero.

We are now ready to solve for the time-evolution of the 7-component state vector of ^{226}Ra, $\Psi(t) = [c_1(t), c_2(t), c_3(t), c_4(t), c_5(t), c_6(t), c_7(t)]^T$, using Eq. 7.1. To solve the first order ordinary differential equation (ODE) we use the ODE solver `ODE23` on `MATLAB`. The script used for simulating STIRAP in ^{226}Ra is shown in Appendix A.

7.2.1.1 STIRAP Laser Polarization Dependence

We first begin by simulating a STIRAP in ^{226}Ra with $\Delta = 0$ and $\delta = 0$. The pump and the Stokes laser pulses are 2μs wide. The Stokes laser pulse precedes the pump laser pulse by 4μs. We set the pump laser peak power to 1μW while the Stokes laser power is set to 2mW. The results of this simulation are shown in Fig. 7.5. Fig. 7.5(a) shows the STIRAP pulse sequence. The pulse amplitudes are normalized with respect to the pulse peak. Fig. 7.5(b) shows the population in the different atomic states. The population is initialized in the ground state $|1\rangle$ and fully transferred into the final state $|6\rangle$ without any loss to the intermediate state manifold $(|2\rangle, |3\rangle, |4\rangle)$. Under these conditions we see successful transfer of the atomic population using STIRAP.

If we change the polarization of the Stokes laser from σ^+ to σ^-, there is no allowed transition from the relevant intermediate state $|4\rangle$ to the final state manifold $(|5\rangle, |6\rangle, |7\rangle)$. Therefore as shown in Fig. 7.6, we see no STIRAP and hence no transfer of the atomic population. Fig. 7.6(b) shows the rapidly oscillating Rabi flops between the ground state $|1\rangle$ and the excited state $|4\rangle$. The decay of the Rabi flop is due to the loss of the population via spontaneous decay of the atomic population to states outside of the STIRAP states. We note that there is no transfer of atoms into the final state manifold $(|5\rangle, |6\rangle, |7\rangle)$.

7.2.1.2 STIRAP Laser Power Dependence

We next study the effect of pump laser power on the STIRAP transfer efficiency. The transfer efficiency is defined as the fraction of population that is transferred into the final state manifold $(|5\rangle, |6\rangle, |7\rangle)$. We simulate the STIRAP transfer over a range of pump laser powers. The Stokes laser power is set to 10mW, $\Delta = 2\pi \times 400$MHz, $\delta = 0$MHz and the pulse duration and separations the same as before. The results are shown in Fig. 7.7. We notice in our simulations that at the current choice of Δ, the transfer efficiency drops dramatically for pump laser powers below 20μW. What is also worth noting is the decline in the STIRAP transfer efficiency as we increase the pump laser power. We notice that it drops down to 80% for pump pulse powers of 6mW. We suspect this occurs because, at high pump laser powers, there is a significant amount of pump light present

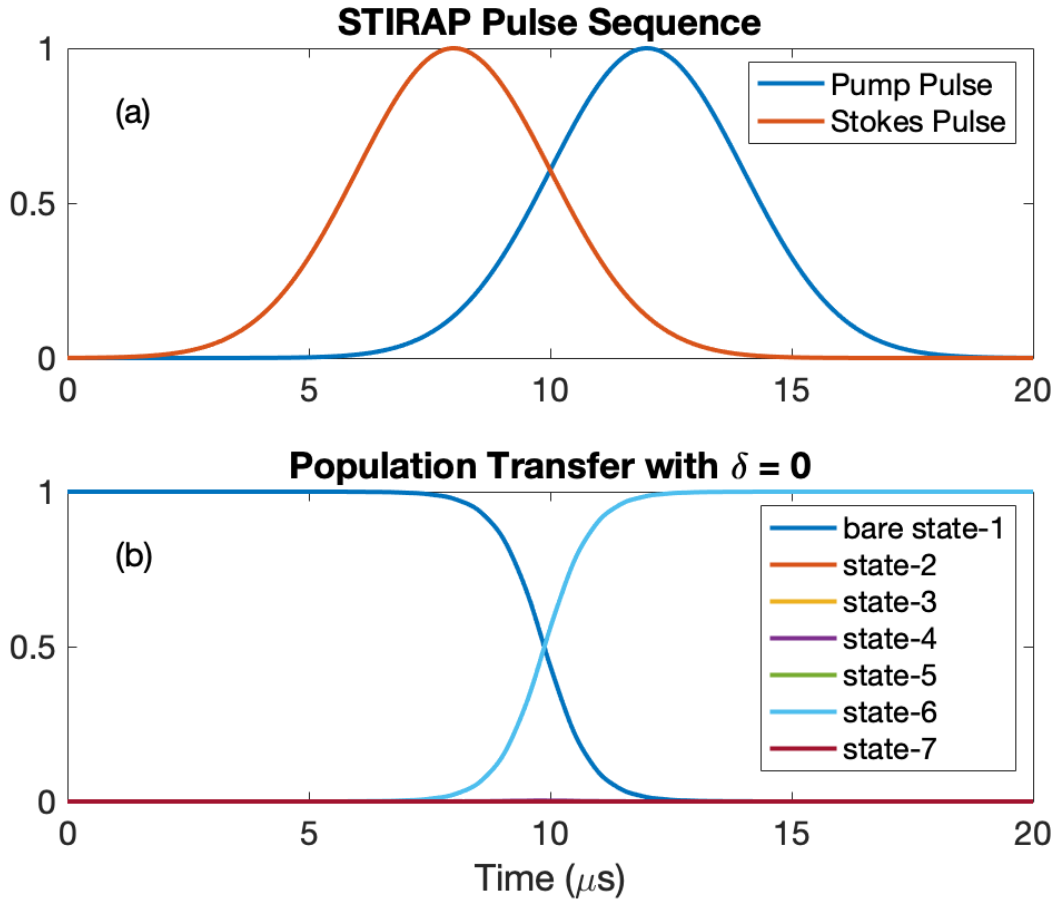

Figure 7.5: Simulation of population transfer from the ground state $|1\rangle$ into the final state $|6\rangle$ using STIRAP in ^{226}Ra, with $\Delta, \delta = 0$. The pump and the Stokes laser powers are set to 1μW and 2mW respectively. The pulse duration τ is set to 2μs and the pulses are separated by 4μs. (a) The STIRAP pulse sequence is shown for the pump and Stokes laser pulses. (b) The population is completely transferred without any loss to the excited state manifold ($|2\rangle, |3\rangle, |4\rangle$).

initially along with the Stokes laser. This disrupts the formation of the "dark" state required for ideal STIRAP transfer of atoms. This can be remedied by increasing the Stokes laser power to 30mW, and almost complete STIRAP transfer efficiency is recovered.

We then simulate STIRAP at different values of the Stokes laser power. The pump laser power is set to 0.1mW, and the rest of the parameters are the same as before. As shown in Fig. 7.8, we notice that the transfer efficiency saturates at about 10mW Stokes laser power. We also notice that unlike its dependency on the pump laser power, the STIRAP efficiency does not decrease with increasing Stokes laser power. This agrees with our observation that too high a pump laser power

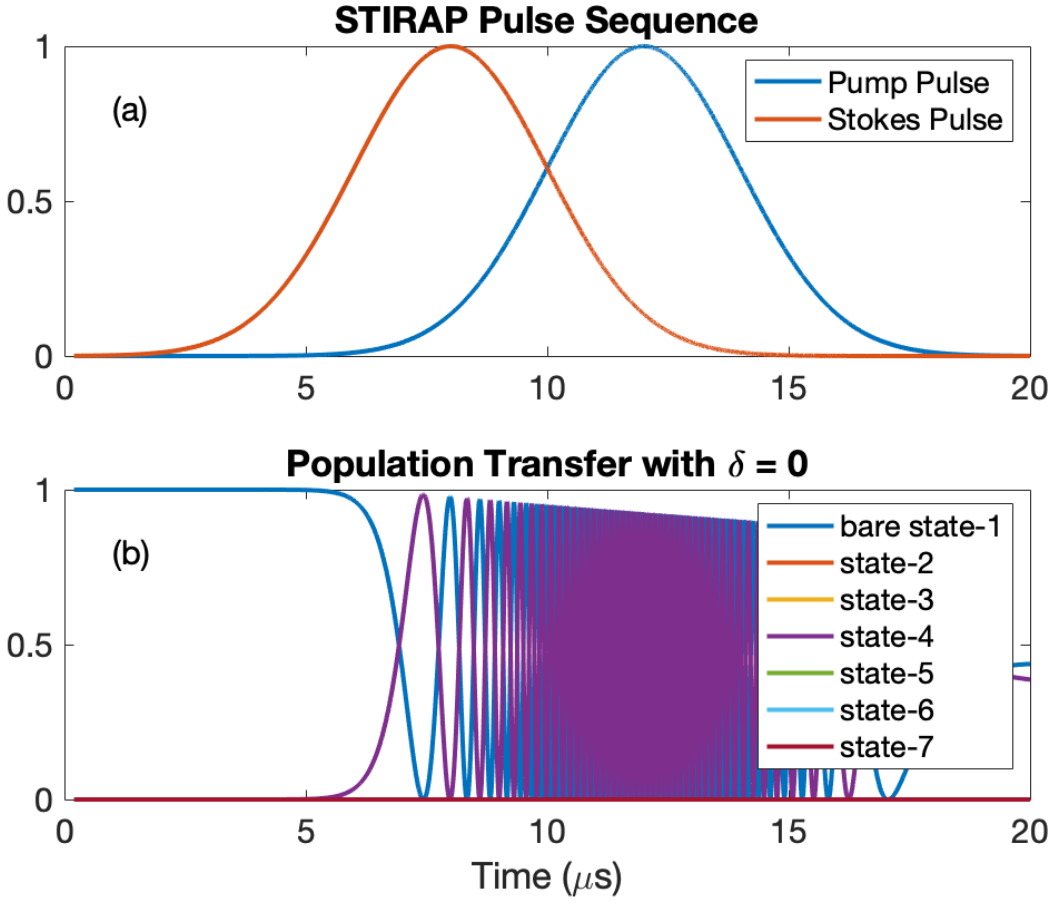

Figure 7.6: Simulation of STIRAP in ^{226}Ra with all the parameters the same as in Fig. 7.5, we change the circular polarization of the Stokes pulse from σ^+ to σ^-. Consequently we do not observe successful STIRAP in ^{226}Ra and instead see Rabi oscillations between states $|1\rangle$ and $|4\rangle$. The decay of the total population is due to the spontaneous decay to states not coupled by the STIRAP lasers.

interferes with the initial formation of the "dark" state for STIRAP population transfer.

7.2.1.3 STIRAP Dependence on One-Photon Detuning

We next investigate the effect of one-photon detuning Δ on the STIRAP transfer efficiency in ^{226}Ra. The pump laser power is set to 0.1mW, while the Stokes laser power is at 10mW, and the two-photon detuning δ = 0MHz. Fig. 7.9 shows the decrease in the STIRAP transfer efficiency for values of $\Delta/2\pi$ over 800MHz. At $\Delta = 2\pi \times 3$GHz, we have only about 40% transfer efficiency.

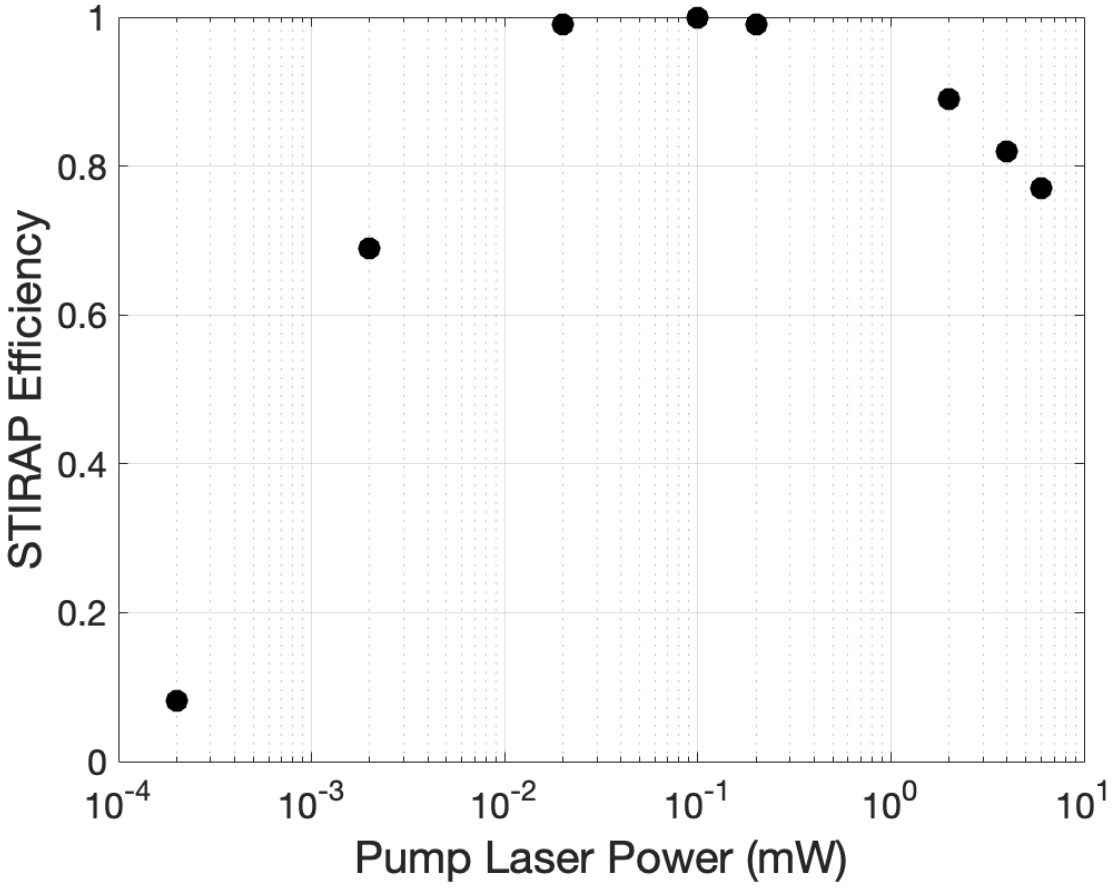

Figure 7.7: The simulated STIRAP efficiency in ^{226}Ra is plotted as a function of the pump laser power. The Stokes laser power is set to 10mW, $\Delta = 2\pi \times 400$MHz and $\delta = 0$MHz. With the rest of the parameters the same as in Fig. 7.5, we notice that the STIRAP efficiency decreases to below 70% for pump powers below 20μW. We also note that the efficiency drops as we increase the pump power. At 6mW the efficiency drops to 80%. This is due to the imbalance between the Stokes and pump laser powers at the beginning of the STIRAP process. Increasing the pump power eventually is detrimental to the formation of the STIRAP "dark" state and therefore leads to decrease in the transfer efficiency.

7.2.1.4 STIRAP Dependence on Pulse Separation

We then simulate the effects of pulse separation on the STIRAP transfer efficiency in ^{226}Ra. Fig. 7.10 illustrates the dependence of STIRAP transfer efficiency on the pulse separation in ^{226}Ra. Positive separation means the Stokes pulse precedes the pump pulse and vice versa. The Stokes laser power is set to 4mW, and the pump at 2mW. The one-photon detuning is set to $\Delta = 2\pi \times 400$MHz and we maintain two-photon resonance $\delta = 0$MHz. As expected, STIRAP is optimal when the

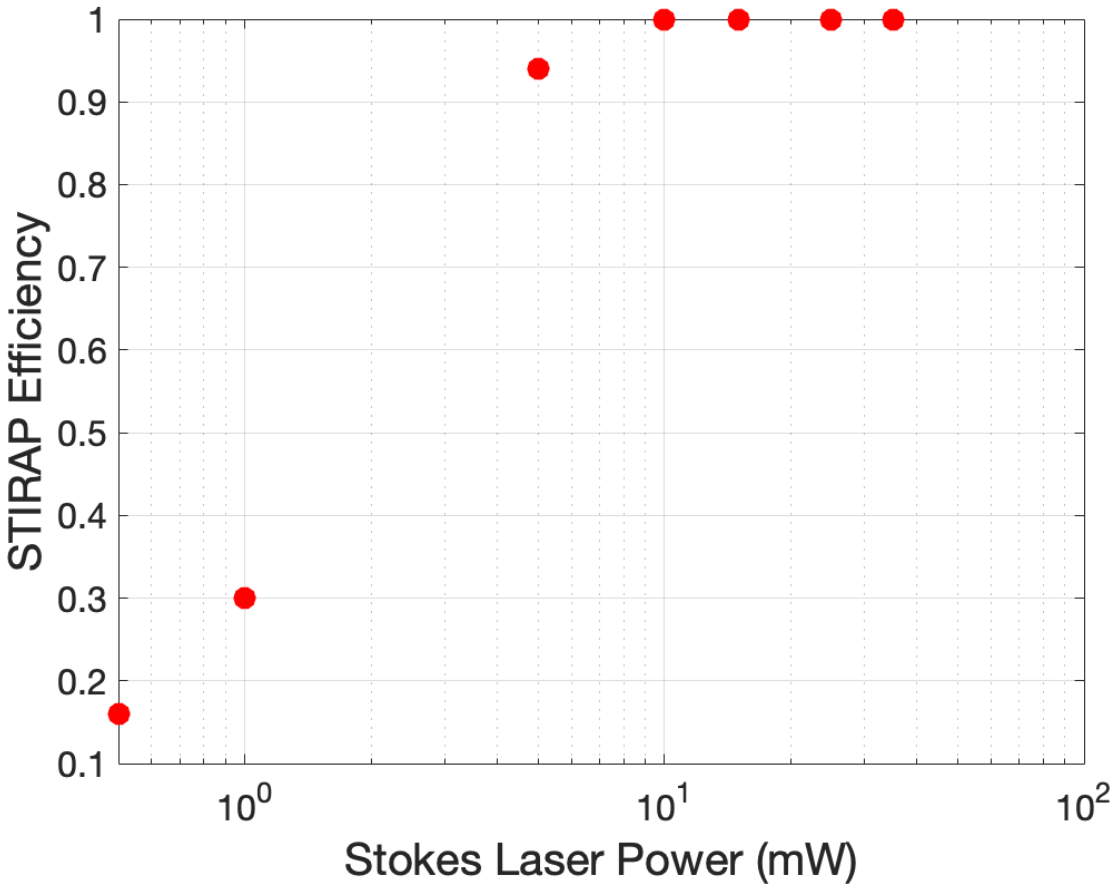

Figure 7.8: The simulated STIRAP efficiency in ^{226}Ra is plotted as a function of the Stokes laser power. The pump laser power is set to 0.1mW. The rest of the parameters are the same as in Fig. 7.7. We notice that the STIRAP efficiency saturates to unity at 10mW Stokes laser power.

Stokes pulse precedes the pump pulse while maintaining sufficient overlap with it. This ensures that the adiabaticity condition is met throughout the STIRAP process. As the pulses cease to overlap, the STIRAP process is unsuccessful. We also note the secondary maximum at a pulse delay of -2μs, with the pump pulse preceding the Stokes. This has been observed before[71] and is a consequence of the large one-photon detuning used, in this case $\Delta = 2\pi \times 400$MHz.

7.2.1.5 STIRAP Dependence on Two-Photon Detuning

We also study the effects of two-photon detuning δ on the STIRAP transfer efficiency in ^{226}Ra. As shown in Fig. 7.11, with the pump laser power at 0.1mW, Stokes laser power at 10mW, and

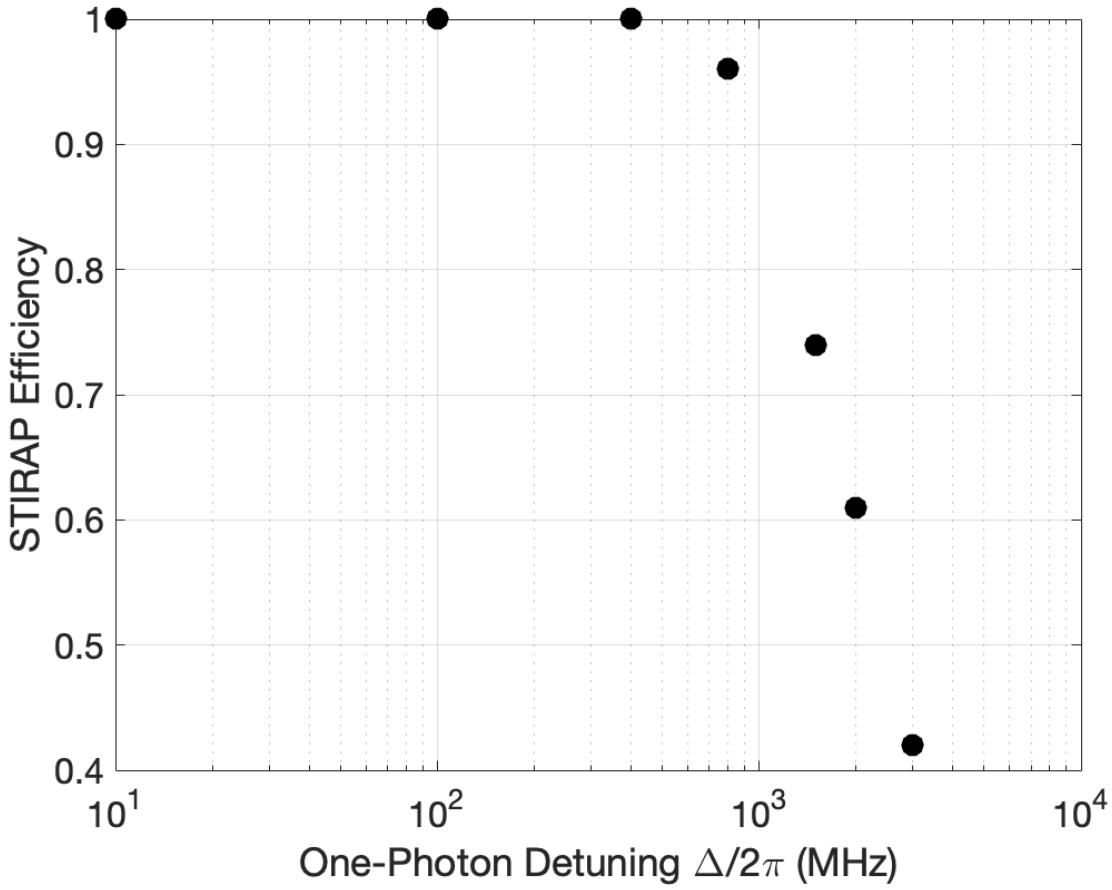

Figure 7.9: The simulated STIRAP transfer efficiency is plotted as a function of the one-photon detuning $\Delta/2\pi$. The Stokes laser power is set to 10mW, and the pump laser power to 0.1mW.

the one-photon detuning $\Delta = 0$MHz, we see that the STIRAP efficiency is symmetric about $\delta = 0$. It drops to below 40% at $\delta = \pm 10$MHz. Fig. 7.10 and Fig. 7.11 illustrate the essential features of STIRAP. They show that STIRAP is not only a two-photon process and requires $\delta = 0$, but also requires the "non-intuitive" pulse sequence for the formation of the STIRAP "dark" state for optimal population transfer.

7.2.1.6 STIRAP Dependence on Laser Frequency Noise

We conclude this section by discussing the effects of laser frequency fluctuations on the STIRAP efficiency. This will be particularly relevant when we compare results of our simulations to the experimental data obtained for STIRAP in ^{226}Ra. Any laser has a finite 'linewidth' that depends

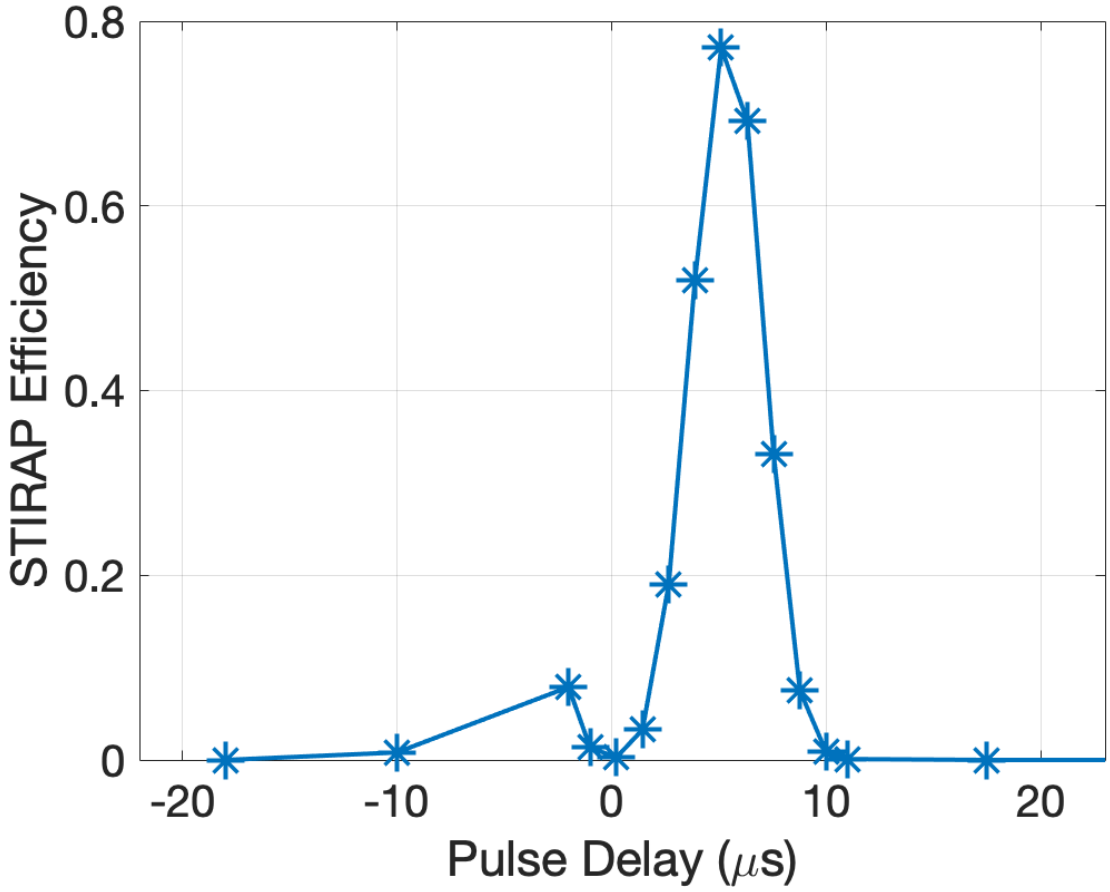

Figure 7.10: The simulated STIRAP transfer efficiency is plotted against the separation of the Stokes and pump pulses. Positive delay indicates that the Stokes pulse precedes the pump pulse. As expected, we notice that the STIRAP is optimal at a positive pulse separation with the Stokes pulse preceding the pump pulse but with sufficient overlap between the two pulses to ensure that the adiabaticity condition is maintained. The Stokes laser power is set to 4mW, and the pump at 2mW. The one-photon detuning is set to $\Delta = 2\pi \times 400$MHz.

on its gain material, cavity length, and its overall design. Consdirable effort goes into either 'narrowing' the free-running laser frequency linewidth or 'stabilizing' the frequency jitters. This can be achieved by using techniques for stabilizing the laser frequency to an optical frequency reference by feeding back on a tunable component that controls the laser frequency. The imaging transition ${}^1S_0 \leftrightarrow {}^1P_1$ for instance, has a frequency linewidth of $2\pi \times 28.9$MHz, so laser frequency jitters at the scale of a MHz do not significantly effect the imaging signal. However, the STIRAP resoance as will be shown in the experimental data below, is as narrow as $\approx$ 1MHz. This requires that the two-photon detuning be stable to within $\approx$ 1MHz. In the following we investigate the

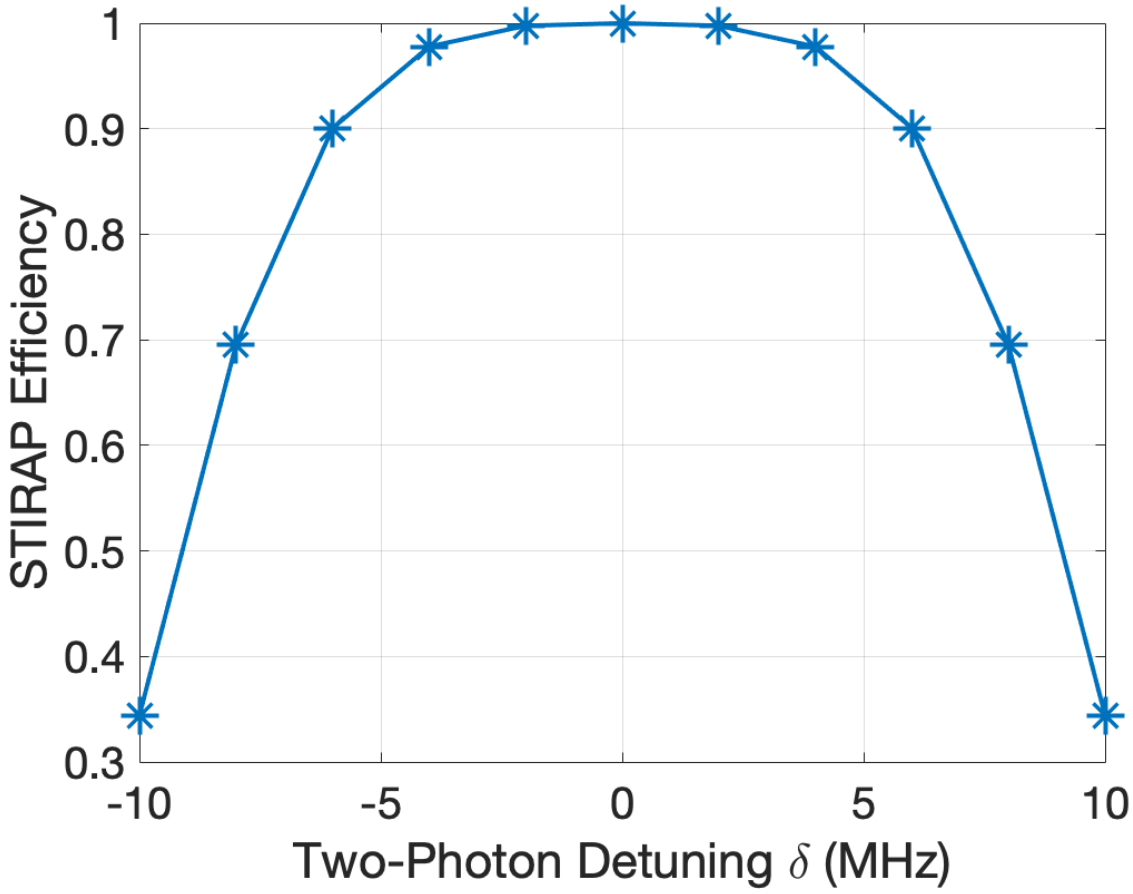

Figure 7.11: The simulated STIRAP transfer efficiency is plotted against the two-photon detuning δ. Pump laser power is set to 0.1mW, the Stokes laser power is set to 10mW, one-photon detuning is set to $\Delta = 0$. The STIRAP transfer efficiency is symmetric about $\delta = 0$, and drops to below 40% at $\delta = \pm 10$MHz.

impacts of laser frequency fluctuations on the STIRAP transfer efficiencies in ^{226}Ra.

We follow the treatment of the effect of laser frequency noise on STIRAP as adopted by Kuhn *et al.* [86]. They use an exponentially correlated colored noise (Omstein-Uhlenbeck process[87]) to model the laser frequency fluctuations. This model assumes zero mean and no cross-correlation in the frequency fluctuations in the two lasers:

$$\left\langle \xi_j(t) \right\rangle = 0, \qquad \left\langle \xi_j(t)\xi_k(t') \right\rangle = \begin{cases} D_j G_j \exp\{-G_j|t-t'|\}, & j = k \\ 0, & j \neq k \end{cases} \tag{7.46}$$

where $\xi_{j=p,s}(t)$ denotes the time-dependent laser frequency fluctuation for the pump and Stokes

lasers. $D_{j=p,s}$ is the spectral density of the noise and $G_{j=p,s}$ is the frequency noise bandwidth for the pump and the Stokes laser pulses. G^{-1} is the auto-correlation time.

The frequency noise in the individual lasers is generated by following the Box-Mueller algorithm as outlined by Fox *et al.* [88]. The total simulation time T is divided into N intervals separated by time-step $\Delta t = T/N$, such that the $i+1-$th discrete time is given by $t_{i+1} = t_i + \Delta t$. The frequency noise $\xi(t_{i+1})$ at time t_{i+1} is then correlated to the noise $\xi(t_i)$ at time t_i given by

$$\xi(t_{i+1}) = \xi(t_i)e^{-G\Delta t} + h(t_i) \tag{7.47}$$

where $h(t_i)$ has a zero mean and satisfies gaussian statistics with a variance given by

$$\left\langle h^2(t_i)\right\rangle = DG\left(1 - e^{-2G\Delta t}\right) \tag{7.48}$$

$h(t_i)$ is given by

$$h(t_i) = \cos\left(2\pi b(t_i)\right)\sqrt{-2DG\left(1 - \exp\{-2G\Delta t\}\right)\ln\left(a(t_i)\right)} \tag{7.49}$$

where a and b are randomly generated numbers in the range $0 < a, b \leq 1$. The initial - gaussian distributed - value for the frequency noise is given by

$$\xi(0) = \cos\left(2\pi b\right)\sqrt{-2DG\exp\{-2G\Delta t\}\ln\left(a\right)} \tag{7.50}$$

We can now generate the frequency noise for the pump and Stokes lasers using the procedure outlined in Eq. 7.47. The laser frequency noise ξ satisfies a normal distribution given by

$$\mathbb{P}(\xi) = \frac{1}{\sqrt{2\pi DG}}\exp\left(-\frac{\xi^2}{2DG}\right) \tag{7.51}$$

with a width given by $\sigma = \sqrt{DG}$. We incorporate these frequency fluctuations of the pump and Stokes lasers into our simulation by replacing 'δ' by '$\delta + \xi_{p,s}$' in the atom-light interaction part of the Hamiltonian $\mathcal{H}_\Omega$ given by Eq. 7.36.

To illustrate the effects of laser frequency noise on STIRAP in ^{226}Ra, we simulate noise in the STIRAP lasers with the following paramters:

- $G_p = 31.4$MHz and $D_p = 0.5$MHz, with $\sigma_p = 2\pi \times 0.2$MHz
- $G_s = 31.4$MHz and $D_s = 1.5$MHz, with $\sigma_s = 2\pi \times 1.1$MHz

The simulated pump and Stokes frequency noise are shown in Fig. 7.12. All the other parameters such as the laser pulse powers, the one- and two-photon detunings, the pulse widths, and the pulse separation are the same as used for simulating Fig. 7.5.

The simulation results are shown in Fig. 7.13. The population evolution of the different atomic states is noisier with laser frequency noise than without. We notice that the STIRAP transfer efficiency drops from 100% to 53% in the presence of the laser frequency noise on the STIRAP lasers as chosen above.

For a fixed frequency noise with width 'σ_p' on the pump laser, we simulate STIRAP to study the dependence of the STIRAP transfer effiency in ^{226}Ra on the Stokes laser frequency noise with width 'σ_s'. This simulation was carried with the two-photon detuning set to $\delta = 0$ MHz, and the one-photon detuning set to $\Delta = 2\pi \times 200$MHz. The results are shown in Fig. 7.14. Each data set is the average of five simulations at the same STIRAP parameters. The error bars indicate the uncertainty on the mean. For our current noise model, we notice that the STIRAP efficiency drops to 50% for Stokes frequency noise > 1MHz. So, laser frequency jitters at the level of 1 MHz becomes significant and can be deterimental to the STIRAP efficiency.

7.2.2 ^{225}Ra

We now adapt the STIRAP simulations developed in ^{226}Ra on the isotope used in our EDM search experiment, ^{225}Ra.

We consider the following states for simulating STIRAP in ^{225}Ra as shown in Fig. 7.15:

1. Two Initial state: $|1\rangle \coloneqq {}^1S_0\,(F = 1/2, m_F = -1/2)$, $|2\rangle \coloneqq {}^1S_0\,(F = 1/2, m_F = +1/2)$

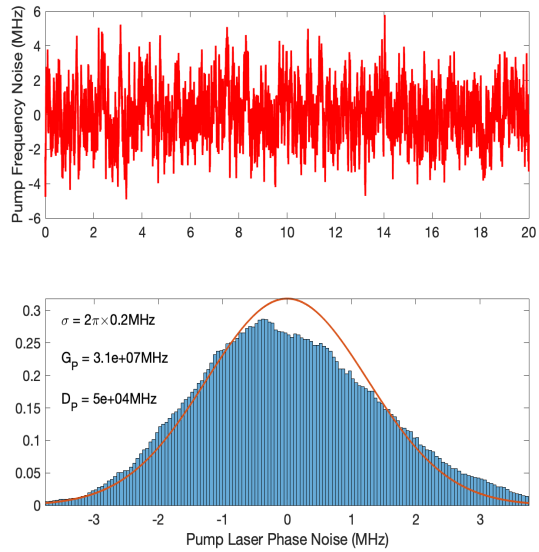

(a) Simulated pump laser frequency noise with G_p = 31.4MHz and D_p = 0.5MHz, with $\sigma_p = 2\pi\times0.2$MHz

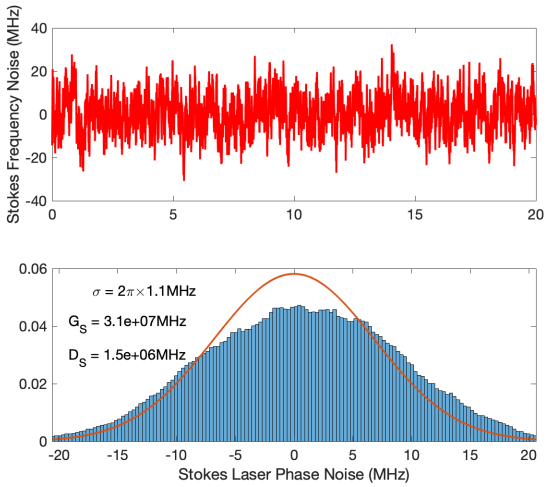

(b) Simulated Stokes laser frequency noise with G_s = 31.4MHz and D_s = 1.5MHz, with $\sigma_s = 2\pi\times1.1$MHz

Figure 7.12: Simulated frequency noise in the pump and Stokes laser for studying the effect of frequency fluctuations on STIRAP transfer efficiency in ^{226}Ra. The red traces are the gaussian fits with the respective choice of σ for each laser.

2. Six Intermediate states: $|3\rangle := {}^1P_1\,(F = 3/2, m_F = -3/2)$, $|4\rangle := {}^1P_1\,(F = 3/2, m_F = -1/2)$, $|5\rangle := {}^1P_1\,(F = 3/2, m_F = +1/2)$, $|6\rangle := {}^1P_1\,(F = 3/2, m_F = +3/2)$, $|11\rangle := {}^1P_1\,(F = 1/2, m_F = -1/2)$, and $|12\rangle := {}^1P_1\,(F = 1/2, m_F = +1/2)$.

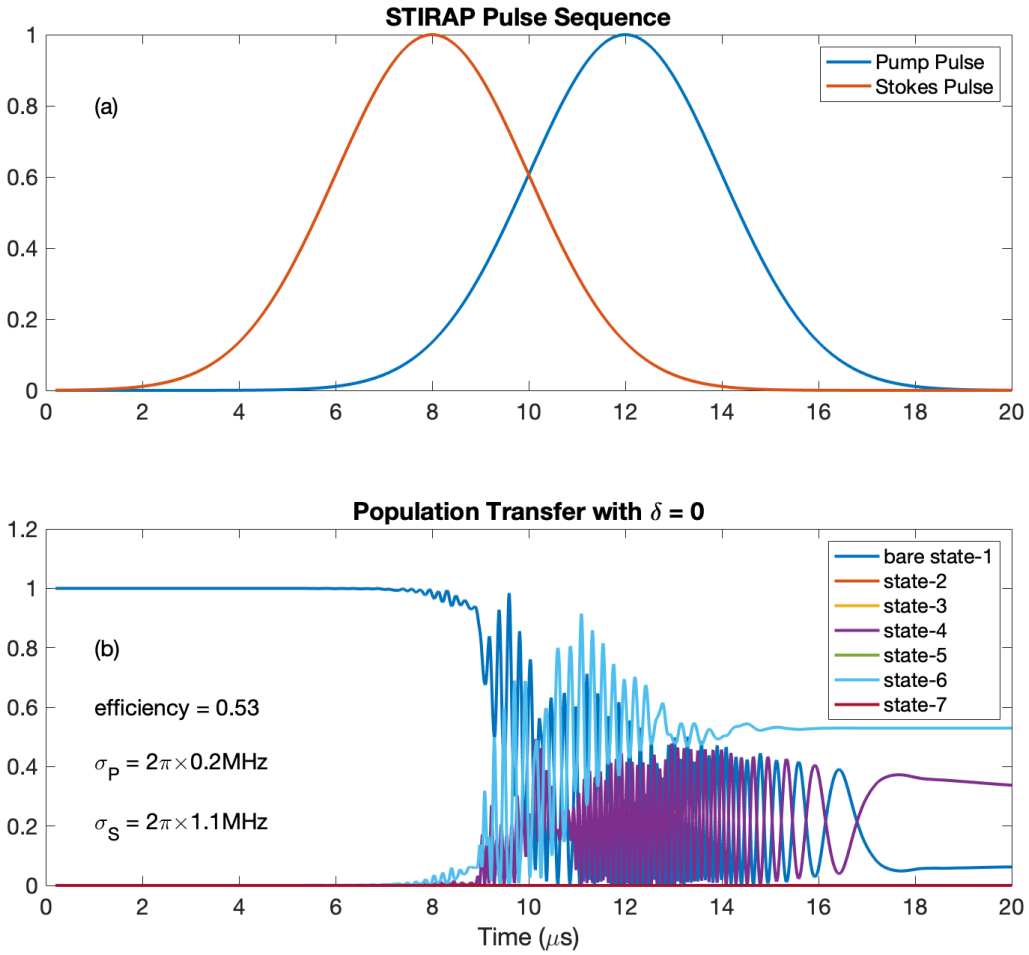

Figure 7.13: Simulation of STIRAP in ^{226}Ra with frequency noise on the pump and Stokes laser as shown in Fig. 7.12. (a) shows the STIRAP pulse sequence. (b) gives the time-evolution of the atomic state populations. We observe that the evolution is noisier with frequency fluctuations, and the STIRAP efficiency is 53%, reduced from 100% without frequency noise.

3. Four Final states: $|7\rangle := {}^3D_1\,(F = 3/2, m_F = -3/2)$, $|8\rangle := {}^3D_1\,(F = 3/2, m_F = -1/2)$, $|9\rangle := {}^3D_1\,(F = 3/2, m_F = +1/2)$, and $|10\rangle := {}^3D_1\,(F = 3/2, m_F = +3/2)$.

We then formulate the relevant Hamiltonian for ^{225}Ra, $\mathcal{H} = \mathcal{H}_\Omega + \mathcal{H}_B$ as we did for ^{226}Ra. The Hamiltonian $\mathcal{H}$ is a 12×12 matrix and its construction follows the procedure outlined for ^{226}Ra and is therefore not shown here.

Here we omit results of our simulations in ^{225}Ra that are qualitatively similar to what we have already discussed in ^{226}Ra, such as the dependence of the STIRAP transfer efficiency on the laser

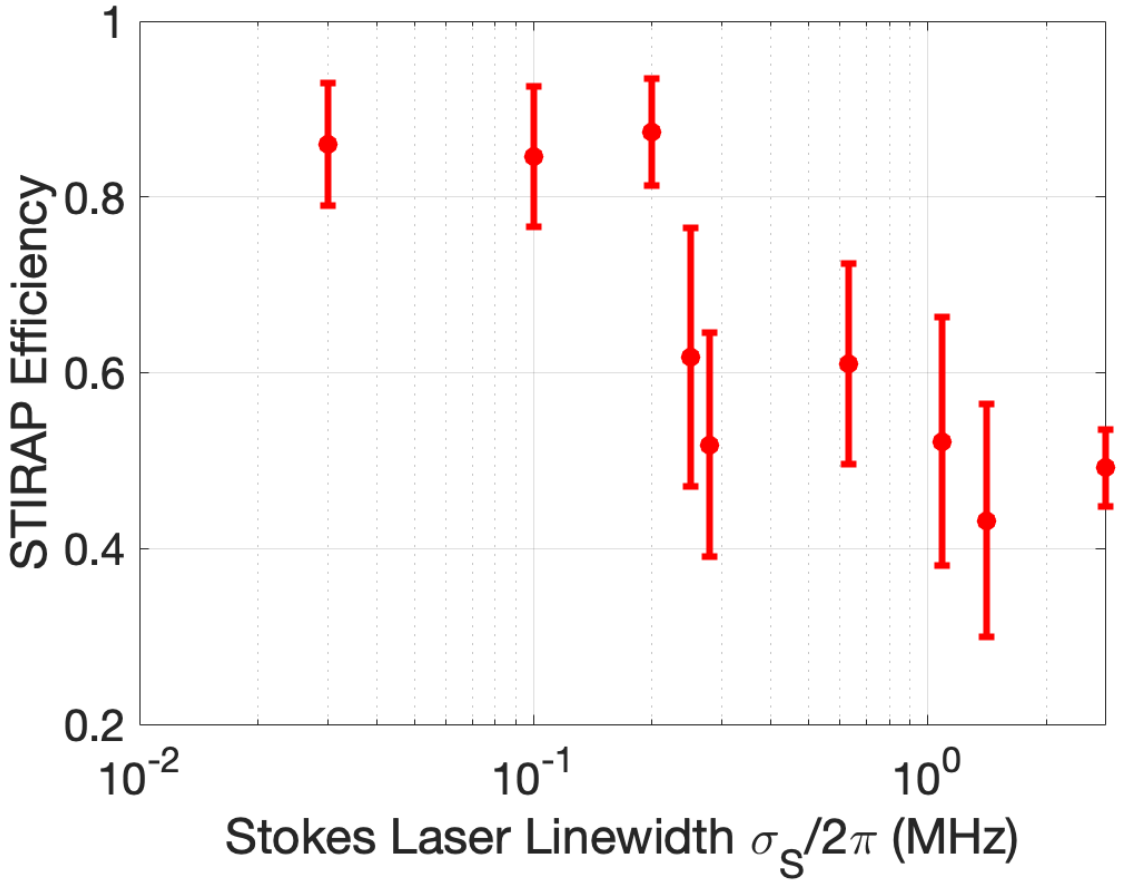

Figure 7.14: Simulated STIRAP transfer efficiency in ^{226}Ra as a function of Stokes laser frequency noise width σ_s. We set $\Delta = 200$MHz, $\delta = 0$MHz, $\sigma_p = 2\pi \times 0.2$MHz. We notice that the transfer efficiency drops to $\approx 50\%$ over widths of 1MHz.

polarizations, pulse powers, one- and two-photon detunings, and pulse separations. Instead we show the spin-selectivity of the STIRAP scheme chosen for ^{225}Ra. Fig. 7.15 shows the choice of STIRAP pump and Stokes transitions for this particular example. Population in state $|1\rangle$ is transferred into state $|10\rangle$ via the intermediate state $|12\rangle$ using STIRAP. The pump laser is frequency detuned by Δ_p with respect to the $^1S_0\,(F = 1/2) \leftrightarrow {}^1P_1(F = 1/2)$ transition. STIRAP transfer of population out of state $|2\rangle$ is forbidden in two ways. First, as is clear in this case, the choice of σ^- polarization for the Stokes laser prohibits STIRAP transfer as there is no state in the $^3D_1$ manifold to shelve the electrons into. Second, even with a possible final state to transfer the atoms into, the choice of the σ^+ polarization for the pump laser ensures that the pump transition is 4196MHz + Δ_p frequency

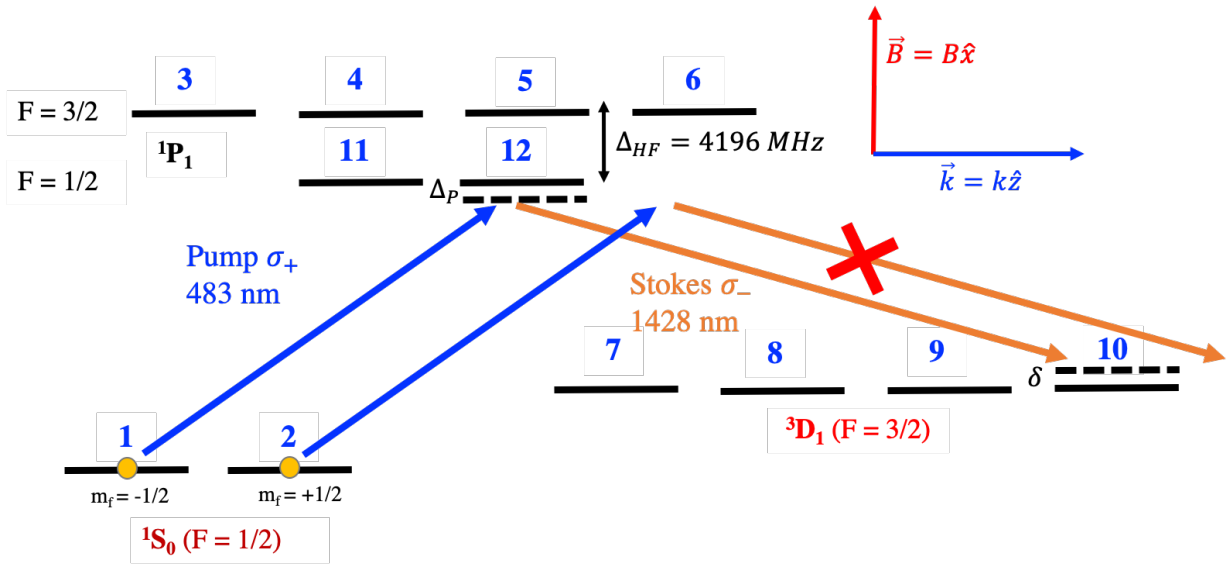

Figure 7.15: The twelve levels involved in the simulation of STIRAP in ^{225}Ra are labelled. A possible spin-selective scheme for electron shelving using STIRAP for ^{225}Ra is shown. Δ_P and δ are the one- and two-photon detunings respectively.

detuned from the $^1S_0\,(F = 1/2, m_F = +1/2) \leftrightarrow {}^1P_1(F = 3/2, m_F = +3/2)$ transition and is therefore highly inefficient as illustrated in Fig. 7.9 for ^{226}Ra.

Fig. 7.16 simulates successful STIRAP transfer in ^{225}Ra. The pump laser power is set to 0.1mW, and the Stokes laser to 10mW. We assume both one- and two-photon resonance; $\Delta = 0$ and $\delta = 0$. The atoms start off in the state $|1\rangle$ and are fully transferred into the state $|10\rangle$, with no loss to the intermediate states.

Now, with the same set of laser parameters, we initialize the atoms in the state $|2\rangle$. As discussed earlier, we should not observe any STIRAP transfer out of this state. This is exactly what we note in Fig. 7.17. The population remains in state $|2\rangle$ throughout the STIRAP process and is unperturbed.

To wrap up our discussion of STIRAP simulations in ^{225}Ra, we simulate the ground state nuclear spin precession. In the absence of any laser pulses, and in the presence of an external magnetic field $B = B\hat{x}$, the atoms in the ground state undergo spin precession. With an external magnetic field of 30 mG, with a nuclear magnetic moment $\mu_I = -0.7338\mu_N$, the ^{225}Ra atoms undergo spin precession with a period of 29.8ms, as shown in Fig. 7.18.

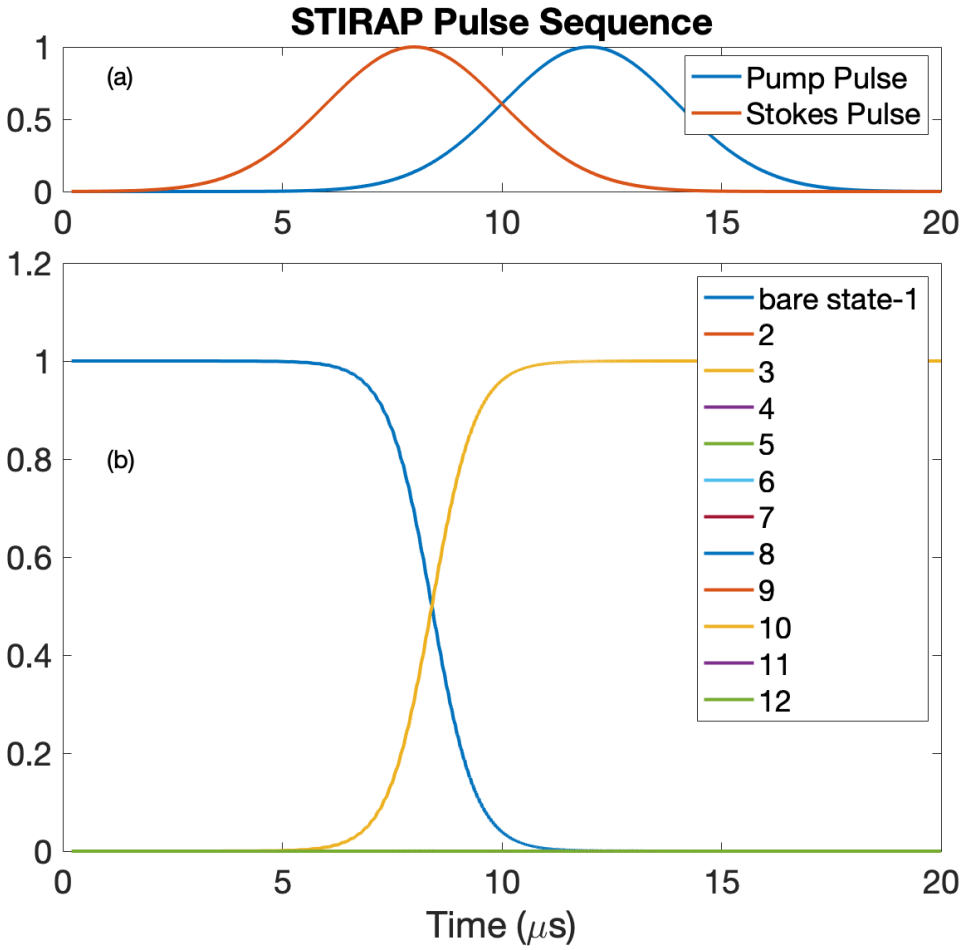

Figure 7.16: Simulation of successful STIRAP in ^{225}Ra. (a) shows the necessary pulse sequence for STIRAP. (b) shows the transfer of atoms from state $|1\rangle$ to $|10\rangle$ without any loss to the intermediate states. The pump laser power is set to 0.1mW, and the Stokes to 10mW. The one- and two-photon detunings are both set to zero. ($\Delta = \delta = 0$)

7.2.3 ^{223}Ra

We now turn our attention to another isotope of radium, ^{223}Ra, with potential applications to searches for *CP*-violating physics. With a nuclear spin $I = 3/2$, ^{223}Ra is significantly different from ^{226}Ra and ^{225}Ra. In this section, we focus on the application of ^{223}Ra as a candidate for an EDM search experiment.

To simulate STIRAP in ^{223}Ra, we consider 28 different states as shown in Fig. 7.19. These states include all the hyperfine levels of the $^1S_0$, $^1P_1$ and the $^3D_1$ states:

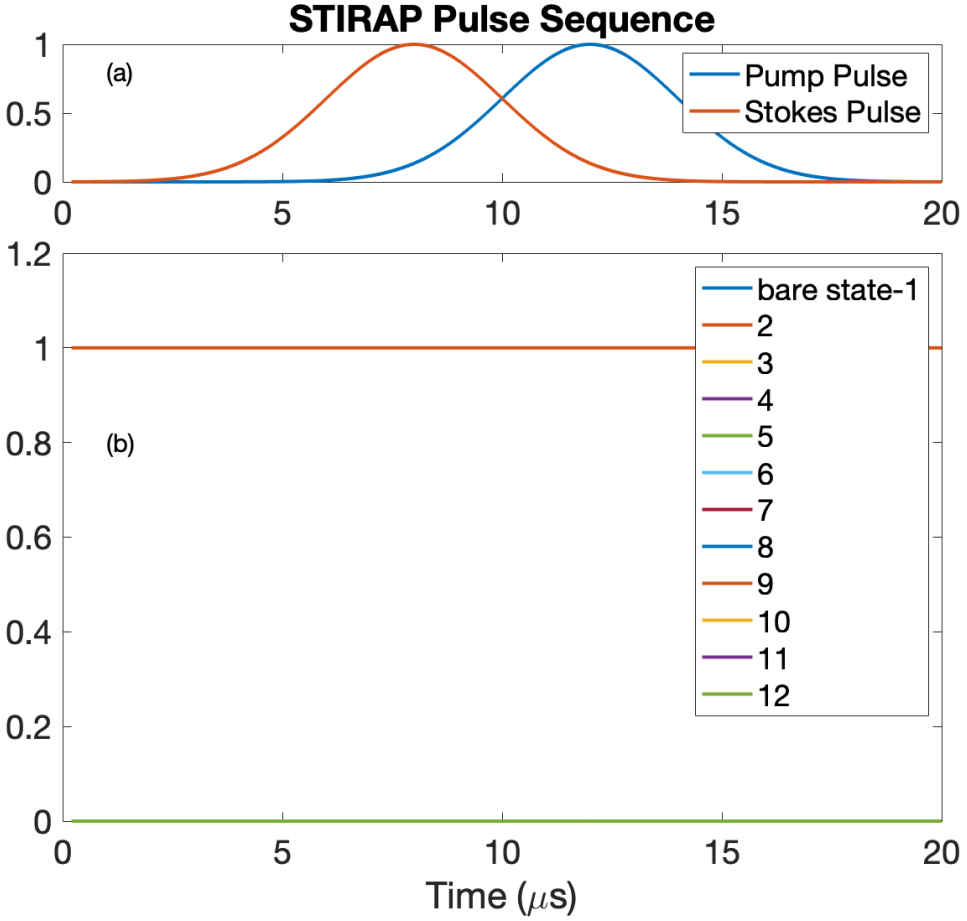

Figure 7.17: Simulation of unsuccessful STIRAP in ^{225}Ra. (a) shows the pulse sequence for STIRAP. (b) shows the population of the different atomic states. We note that the population remains entirely in the initial state $|2\rangle$ throughout the STIRAP process. In this case, STIRAP is forbidden by our choice of pump and Stokes laser polarisation.

1. Four Initial state: $|1\rangle := {}^1S_0\,(F = 3/2, m_F = -3/2)$, $|2\rangle := {}^1S_0\,(F = 3/2, m_F = -1/2)$, $|3\rangle := {}^1S_0\,(F = 3/2, m_F = +1/2)$, and $|4\rangle := {}^1S_0\,(F = 3/2, m_F = +3/2)$

2. Twelve Intermediate states: $|5\rangle := {}^1P_1\,(F = 5/2, m_F = -5/2)$, $|6\rangle := {}^1P_1\,(F = 5/2, m_F = -3/2)$, $|7\rangle := {}^1P_1\,(F = 5/2, m_F = -1/2)$, $|8\rangle := {}^1P_1\,(F = 5/2, m_F = +1/2)$, $|9\rangle := {}^1P_1\,(F = 5/2, m_F = +3/2)$, $|10\rangle := {}^1P_1\,(F = 5/2, m_F = +5/2)$, $|17\rangle := {}^1P_1\,(F = 3/2, m_F = -3/2)$, $|18\rangle := {}^1P_1\,(F = 3/2, m_F = -1/2)$, $|19\rangle := {}^1P_1\,(F = 3/2, m_F = +1/2)$, $|20\rangle := {}^1P_1\,(F = 3/2, m_F = +3/2)$, $|21\rangle := {}^1P_1\,(F = 1/2, m_F = -1/2)$, $|22\rangle := {}^1P_1\,(F = 1/2, m_F = +1/2)$.

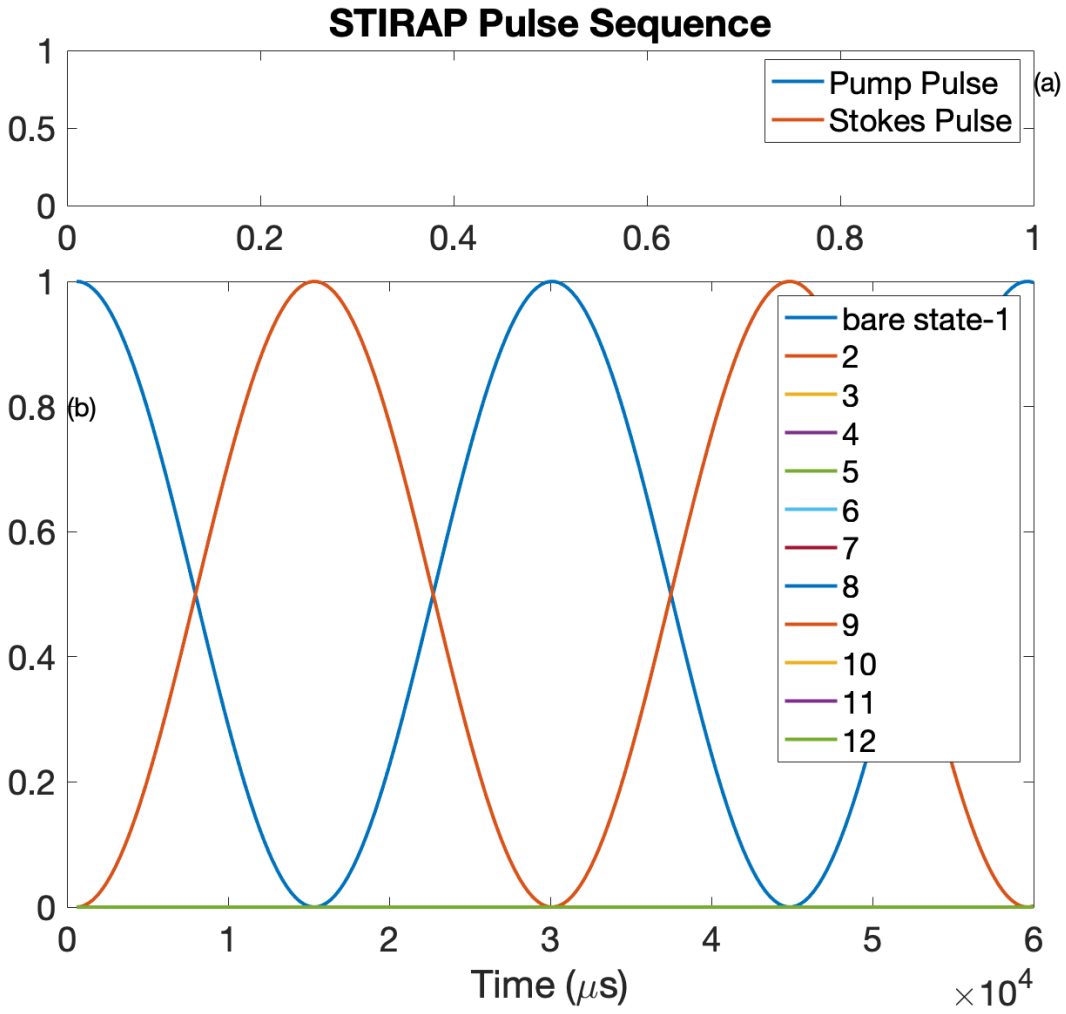

Figure 7.18: Simulation of ground state nuclear spin precession in ^{225}Ra. With an external magnetic field of $B = 30$mG, the atoms precess with a period of 29.8ms.

3. Twelve Final states: $|11\rangle := {}^3D_1\,(F = 5/2, m_F = -5/2)$, $|12\rangle := {}^3D_1\,(F = 5/2, m_F = -3/2)$, $|13\rangle := {}^3D_1\,(F = 5/2, m_F = -1/2)$, $|14\rangle := {}^3D_1\,(F = 5/2, m_F = +1/2)$, $|15\rangle := {}^3D_1\,(F = 5/2, m_F = +3/2)$, $|16\rangle := {}^3D_1\,(F = 5/2, m_F = +5/2)$, $|23\rangle := {}^3D_1\,(F = 3/2, m_F = -3/2)$, $|24\rangle := {}^3D_1\,(F = 3/2, m_F = -1/2)$, $|25\rangle := {}^3D_1\,(F = 3/2, m_F = +1/2)$, $|26\rangle := {}^3D_1\,(F = 3/2, m_F = +3/2)$, $|27\rangle := {}^3D_1\,(F = 1/2, m_F = -1/2)$, and $|28\rangle := {}^3D_1\,(F = 1/2, m_F = +1/2)$.

The simulation accounts for all the intermediate states, but selects a particular hyperfine level in the final states ${}^3D_1$ manifold. We follow the same procedure as for ^{226}Ra, and ^{225}Ra to construct

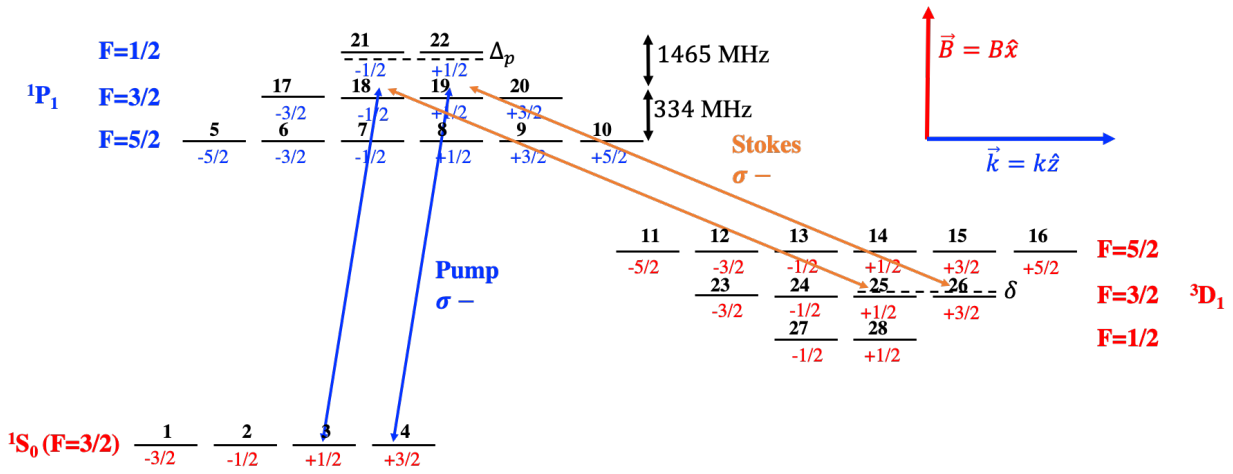

Figure 7.19: The relevant levels for STIRAP simulation in ^{223}Ra. The hyperfine splitting in the intermediate state manifold $^1P_1$ is shown. We can selectively choose the final state hyperfine level for population shelving.

the 28×28 Hamiltonian $\mathcal{H} = \mathcal{H}_\Omega + \mathcal{H}_B$ for ^{223}Ra.

Again, we do not elaborate on many of the tests done to validate successful STIRAP transfer in ^{223}Ra. Our primary objective is to determine a STIRAP scheme in ^{223}Ra that selectively shelves electrons from the ground state sublevels. After some investigation we identify one such scheme that allows for spin-selective atom transfer. The scheme that we test has the pump frequency set to the $^1S_0(F = 3/2) \leftrightarrow {}^1P_1(F = 1/2)$ transition, and the Stokes frequency set to the $^3D_1(F = 3/2) \leftrightarrow {}^1P_1(F = 1/2)$ transition. Due to the higher density of states, it is particularly difficult to find a STIRAP scheme that selectively transfers atoms out of only one of the four ground state sublevels. To ensure STIRAP selectivity, we need to ensure that it is heavily preferred out of one of the sublevels compared to the other three. The above choice of pump and Stokes transitions satisfy this requirement. The STIRAP efficiency is higher when the atoms are in the $^1S_0\,(F = 3/2, m_F = +3/2)$ than in the other sublevels. Transfer of atoms in the $^1S_0\,(F = 3/2, m_F = +1/2)$ state is also allowed by the choice of our laser polarizations but disfavoured by the much weaker pump and Stokes transition strengths. STIRAP of atoms in the other two sublevels ($^1S_0\,(F = 3/2, m_F = -1/2)$ and $^1S_0\,(F = 3/2, m_F = -3/2)$) are allowed via the $^1P_1(F = 3/2)$ hyperfine level, but disfavored due to the Δ_p + 1465MHz one-photon frequency detuning.

To illustrate the STIRAP spin selectivity, we initialize the atoms in the state $|4\rangle$ as shown in Fig. 7.20a. The pump and Stokes laser polarizations are set to σ^- at 4 mW and 6 mW respectively. The one-photon detuning is set to $+2\pi \times 200$ MHz, and we maintain two-photon resonance ($\delta = 0$). The transfer efficiency is 99% into the state $|26\rangle$.

We next initialize the atoms in the state $|3\rangle$ and observe a decreased STIRAP transfer efficiency of 60% into state $|25\rangle$, as shown in Fig. 7.20b.

STIRAP transfer efficiency when the atoms are initially in state $|1\rangle$ is even further reduced to 16% as shown in Fig. 7.20c. When initially in state $|2\rangle$ the transfer efficiency is only 1% as shown in Fig. 7.20d.

The above discussion elucidates the partially spin-selective nature of this choice of STIRAP scheme. To investigate its feasibility for nuclear spin precession measurement in ^{223}Ra, we calculate the contrast in our atom absorption imaging signal. To do so, we begin by deriving the precession of the ground state sublevels in the presence of an external magnetic field $\vec{B} = B\hat{x}$. We assume that the atoms are initially in the state $|4\rangle$. To make the calculation simpler, we work in the $x-$basis of our angular momentum operator, in which the atom-field interaction is given by $\mathcal{H}_B = -\vec{\mu}^{223} \cdot \vec{B}$, where $\vec{\mu}^{223}$ is the total magnetic moment for a ^{223}Ra atom and is given by $\vec{\mu}^{223} = 2\mu_I^{223}\vec{I}$ for the ground state. I is the total nuclear angular momentum, and $\mu_I^{223} = 0.2705\mu_N$ [89] is the nuclear magnetic moment of a ^{223}Ra atom. The Zeeman energy shift due to the interaction of the hyperfine levels of the ground state of ^{223}Ra (with total angular momentum $F = 3/2$ and $x-$component m_F) with the external magnetic field B is therefore given by $\Delta E(m_F) = -2\mu_I^{223} B m_F$. We can express the energy in terms of the Larmor frequency 'ω_L' as $\Delta E(m_F) = -\hbar\omega_L m_F$.

We now write the state $|4\rangle$ in terms of the $x-$basis states $\{|x_1\rangle, |x_2\rangle, |x_3\rangle, |x_4\rangle\}$, where the $x-$component of the total angular momentum for each state is given by m_F = -3/2, -1,2, +1/2, +3/2 respectively. In this basis our initial state $|\Psi(0)\rangle = |4\rangle$ is given by

$$|\Psi(0)\rangle = \frac{1}{\sqrt{8}}|x_1\rangle + \sqrt{\frac{3}{8}}|x_2\rangle + \sqrt{\frac{3}{8}}|x_3\rangle + \frac{1}{\sqrt{8}}|x_4\rangle \tag{7.52}$$

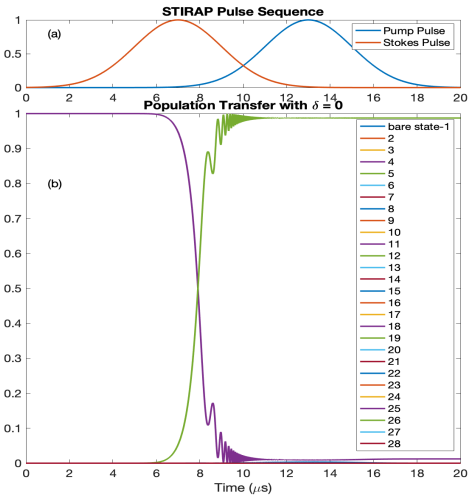

(a) Atoms initially in state $|4\rangle$

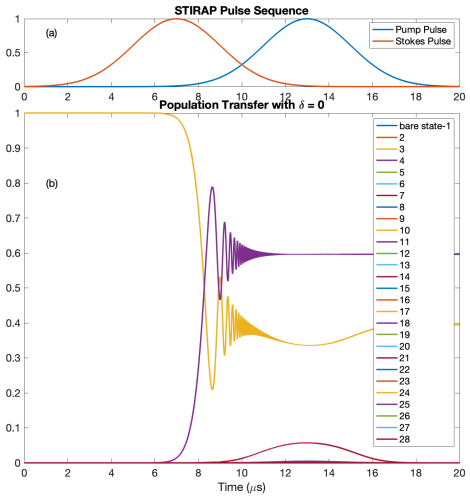

(b) Atoms initially in state $|3\rangle$

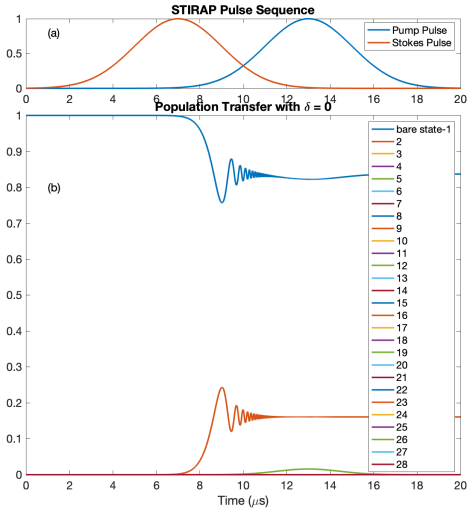

(c) Atoms initially in state $|1\rangle$

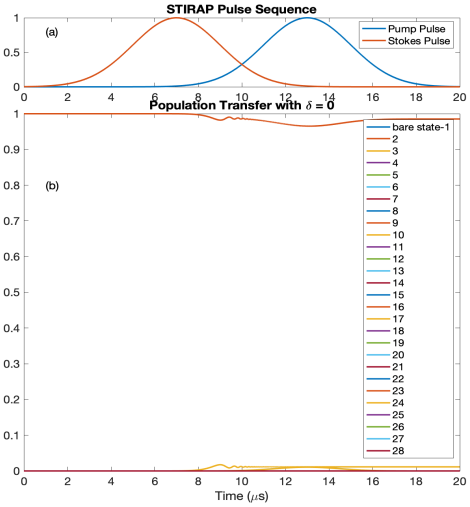

(d) Atoms initially in state $|2\rangle$

Figure 7.20: Simulation of STIRAP in ^{223}Ra with the atoms initialized in the different ground state sublevels. The pump and Stokes laser powers are set to 4mW and 6mW respectively. The one- and two-photon detunings are $\Delta_p = 2\pi \times 200$MHz, and the $\delta = 0$MHz respectively.

Using our expression for $\Delta E(m_F)$, the state evolution of the atom is given by

$$|\Psi(t)\rangle = \frac{1}{\sqrt{8}}|x_1\rangle\, e^{+3i\omega_L t/2} + \sqrt{\frac{3}{8}}|x_2\rangle\, e^{+i\omega_L t/2} + \sqrt{\frac{3}{8}}|x_3\rangle\, e^{-i\omega_L t/2} + \frac{1}{\sqrt{8}}|x_4\rangle\, e^{-3i\omega_L t/2} \quad (7.53)$$

The probability $\mathbb{P}(t)$ of finding the atom in the initial state $|4\rangle$ at a time 't' is then given by

$$\mathbb{P}(t) = |\langle 4|\Psi(t)\rangle|^2 \tag{7.54}$$

$$= \frac{1}{32}\left[\cos\left(3\omega_L t\right) + 6\cos\left(2\omega_L t\right) + 7\cos\left(\omega_L t\right) + 10\right] \tag{7.55}$$

As a check we simulate the spin precession of the atoms initially in the state $|4\rangle$ in the presence of a 200 G magnetic field. The result is shown in Fig. 7.21. The analytical solution in this case is given by Eq. 7.55. The numerical solution is the result of the simulation. This validates that our simulation accurately describes the nuclear spin precession of the ground state sublevels of ^{223}Ra.

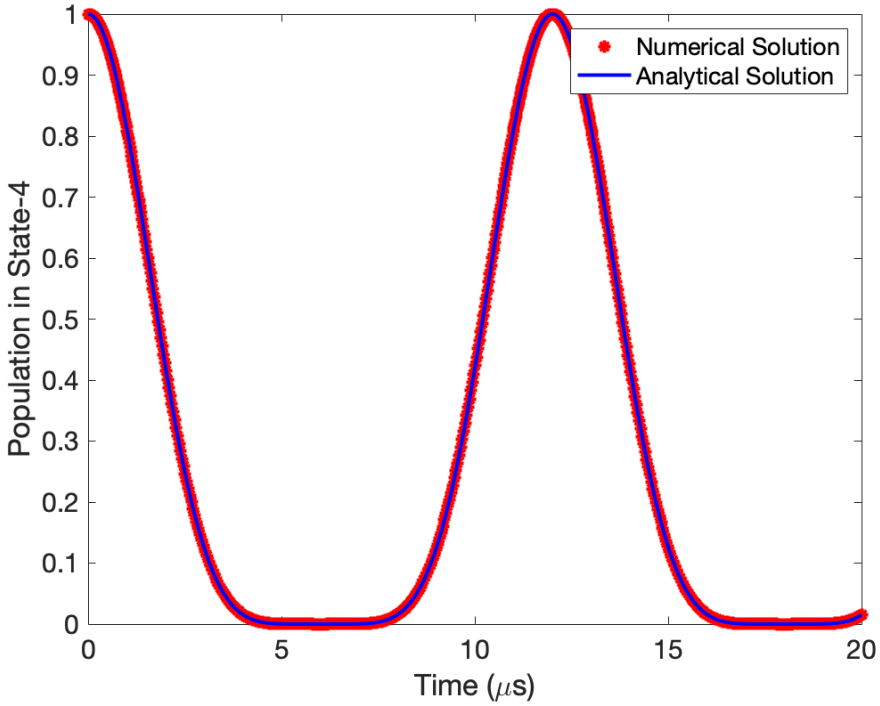

Figure 7.21: The simulated ground state spin precession in ^{223}Ra with B = 200G. The nuclear precession of the atomic population in state $|4\rangle$ is plotted along with the analytical solution derived in Eq. 7.55.

To quantify the degree of contrast that can be achieved in our precession signal as a result of the STIRAP scheme under consideration for ^{223}Ra, we simulate the spin precession curve at different values of the time delay (Δt) at which STIRAP pulses are applied. Here we assume that STIRAP pulse durations are much smaller compared to the Larmor frequency ω_L. The total population in

the ground state is plotted as a function of Δt in Fig. 7.22. Here we observe 98% contrast in the ground state population depending on when the STIRAP pulses are applied. This indicates that our choice of STIRAP scheme for ^{223}Ra is quite promising for a nuclear spin precession measurement in this isotope.

This then concludes this section on the simulation of STIRAP in the three different isotopes of radium (^{226}Ra, ^{225}Ra, ^{223}Ra). In ^{225}Ra, and ^{223}Ra it has provided valuable insights into the possible STIRAP schemes for achieving ground state spin selectivity. For ^{226}Ra, as will be shown in the following section, it has helped understand some of our experimental results and demonstrations of STIRAP in radium.

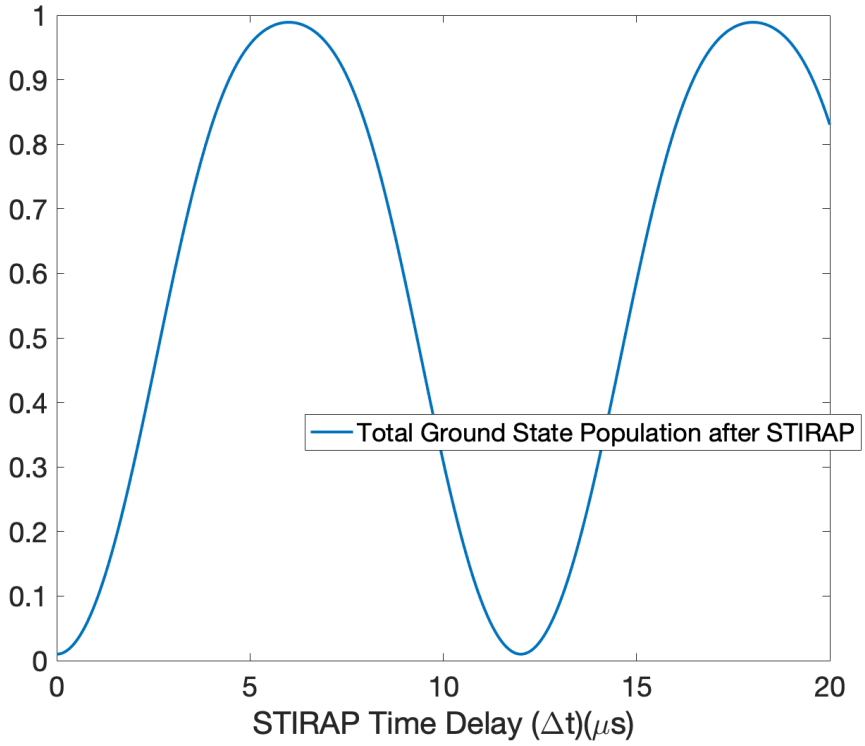

Figure 7.22: The simulated precession of the total population in the ground state of ^{223}Ra after the STIRAP pulses are applied at different delays Δt. To illustrate the ground state spin precession in the presence of an external field, we apply a magnetic field of B = 200G. This indicates that the atoms are selectively more susceptible to STIRAP in certain ground state sublevels than others. With the choice of our STIRAP scheme in ^{223}Ra we observe up to 98% contrast in the ground state spin precession signal.

7.3 STIRAP Demontrations in Radium

In the following section we show experimental data demonstrating STIRAP in both ^{226}Ra and ^{225}Ra. As with any new upgrades to the experiment, we implement and test them first in our 'test' isotope ^{226}Ra, before proceeding with our 'EDM' isotope ^{225}Ra. Although we explain the experimental setup used for ^{226}Ra, much of it remains the same for ^{225}Ra. Wherever necessary, any differences in the setups are explained.

7.3.1 The Experimental Setup

The schematic of the relevant portion of our experiment for STIRAP is shown in Fig. 7.23. ^{226}Ra atoms are held in between the electrodes in the 'holding' ODT made of a retroreflected 20 W 1550 nm IPG Photonics fiber laser, which is far red-detuned in frequency from the relevant STIRAP transition frequencies. The STIRAP pump, Stokes, and the imaging pulses co-propagate along the direction of the ODT and interact with the atoms. For STIRAP, the Stokes laser pulse precedes the pump laser as shown in Fig. 7.23. The 1428 nm Stokes light is generated by a Fara-Banafsh FBG (Fiber Bragg Grating) laser. We typically achieve about 15 mW Stokes laser power at the atoms. In our first demonstration of STIRAP in ^{226}Ra, the 483 nm STIRAP pump as well as the imaging pulses were generated by a home-built 966 nm ECDL in Littrow configuration, which was frequency doubled by passing it through a HC Photonics PPNL waveguide to produce the 483 nm light. This typically produced about 100 μW for the imaging pulse and about 80 μW for the STIRAP at the atoms - after taking into account all the losses in the optical beam path. Both of these lasers are frequency stabilized to zerodur glass optical reference cavities. The cavities are housed in a vacuum chamber held at 1×10^{-9} Torr, and temperature stabilized to drifts of < 10 mK/day. This corresponds to thermal drifts in frequency of < 700 kHz for the pump laser and < 237 kHz for the Stokes. In mid-2017, the 966 nm ECDL was replaced by two separate 483 nm lasers for independently supplying the STIRAP pump and the atom imaging pulses. The STIRAP pump laser is currently generated by a Toptica DL Pro ECDL which is frequency stabilized to the

zerodur optical cavity. The 483 nm imaging laser is produced by a Moglabs cateye laser (CEL) which is frequency stabilized using the optical beat signal obtained with the frequency stabilized 483 nm Toptica DL Pro ECDL. The demonstration of STIRAP in ^{225}Ra used the two separate STIRAP pump and imaging lasers.

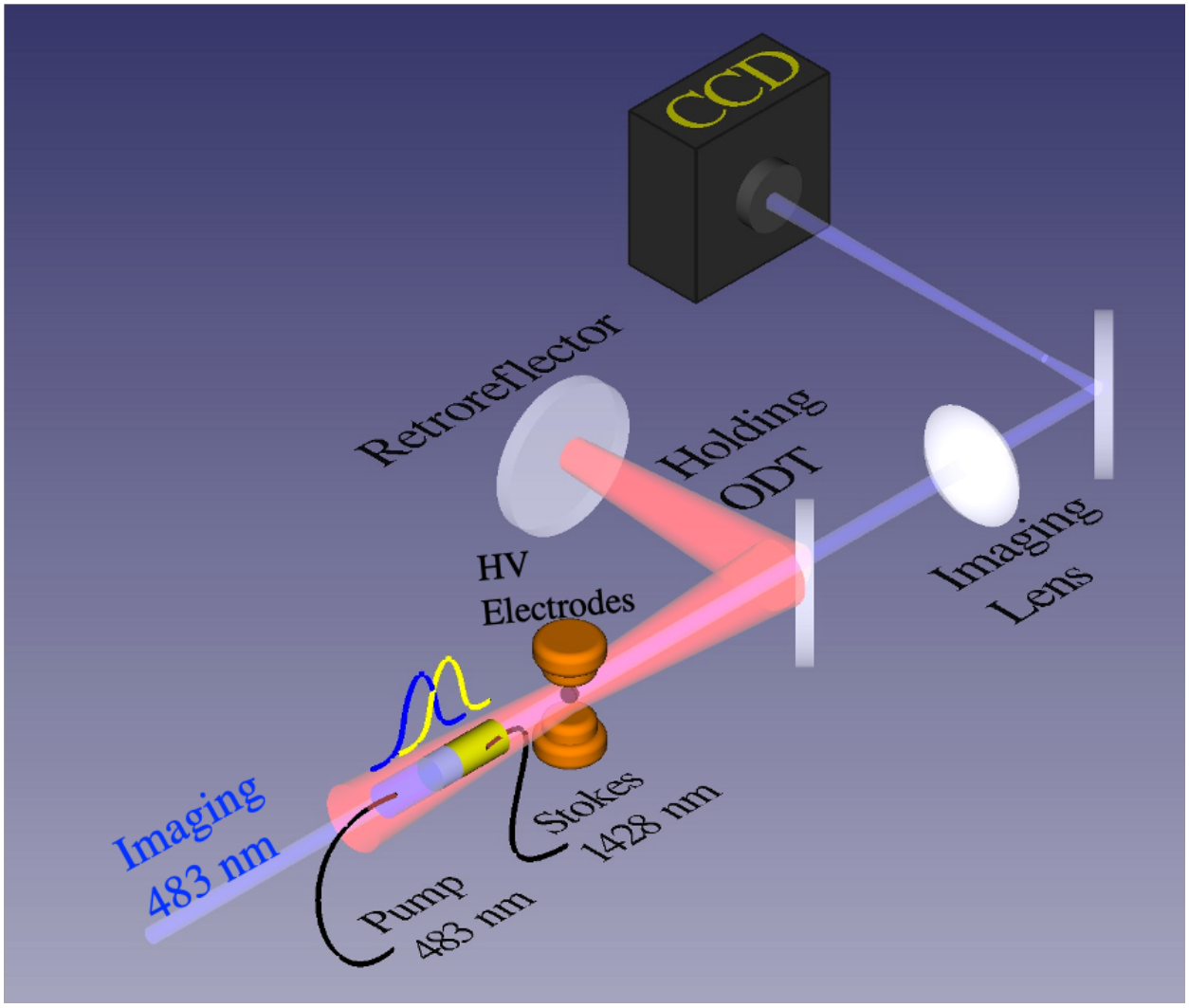

Figure 7.23: The experimental setup for demonstrating STIRAP in radium isotopes. The atoms are held in an ODT in between our high voltage electrodes. They are then irradiated with the pump and Stokes pulses. The atoms are imaged using the 483 nm imaging laser on a CCD camera.

The atomic beam out of the oven is collimated using transverse cooler (TC), slowed and trapped using the Zeeman slower (ZS) and the 3D magneto-optical trap (MOT). The atoms are transferred into the 'bus' ODT using a 50 W 1550 nm IPG Photonics fiber laser and transported, a distance

of 1 m, to the electrodes by moving the focus of the 'bus' ODT by translating the focusing lens mounted on a translation stage. The atoms are then overlapped with the 'holding' ODT and are ready to be probed by the STIRAP pulses.

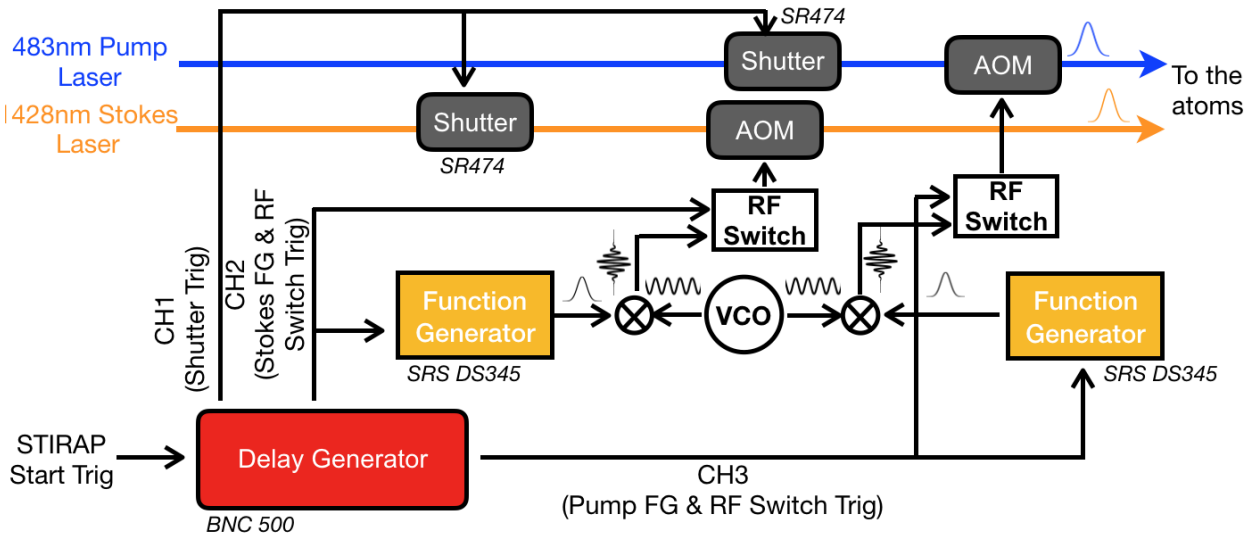

Figure 7.24: The electronic setup for generating the STIRAP pulses. A STIRAP start trigger is sent to the delay generator (BNC-500 pulse generator). Channel 1 triggers the laser shutters for the STIRAP lasers. Channel 2 and 3 trigger the function generators (SRS DS345) and RF switches for the Stokes and pump lasers respectively. The pulse separation is controlled by changing the relative delay between the two channels. The output of each function generator is mixed with the output of a VCO and sent to the RF switch. It is then amplified and fed to the relevant AOM, which then generates the STIRAP pulses.

We now describe how the STIRAP pulses are generated. As shown in Fig. 7.24, the STIRAP start trigger is sent to a BNC 500 pulse generator. Channel 1 of the delay generator supplies the required triggers for the STIRAP pump and Stokes laser shutters. Channel 2 and 3 trigger the SRS DS345 function generators and the RF switches for the Stokes and pump lasers respectively. Each SRS DS345 is programmed using a National Instruments Labview VI to output a gaussian pulse of a specified amplitude and temporal width. The output of the function generator is mixed with the output of a voltage controlled oscillator (VCO) at 80 MHz and sent to an RF amplifier via an RF switch and finally to the relevant acousto-optic modulator (AOM) for generating the STIRAP laser pulses. The relevant settings for the delay generator are shown below:

- `CH1`: Triggers both the pump and Stokes STIRAP shutters

`Delay`: 0 s

`Width`: 2.1 ms

- `CH2`: Triggers the Stokes pulse shaping FG and the AOM RF switch

  `Delay`: 7.35 ms

  `Width`: 200 μs

- `CH3`: Triggers the pump pulse shaping FG and the AOM RF switch

  `Delay`: 7.3542 ms (corresponds to a pulse delay of 2 μs)

  `Width`: 200 μs STIRAP shutters

The pulse separation between the STIRAP pump and Stokes pulses is programmed using the `Delay` option for channel 3 on the delay generator. We monitor the output pulses from the AOMs on photodiodes and determine that a `Delay` = 7.3542 ms on channel 3 results in a 2 μs pulse separation between the Stokes and pump pulses, with the Stokes preceding the pump. There is an inherent delay of 2.2 μs caused by the accumulated delay in the different cable lengths used for generating the two pulses.

For ^{226}Ra, where we use the same laser for both the STIRAP pump and the imaging pulse, we tune the AOM for the STIRAP pump laser to maximize diffraction into the -1 order, and the AOM for the imaging laser to maximize diffraction into the +1 order. This ensures that the STIRAP pump laser frequency is $\approx$ 160 MHz (one-photon detuning $\Delta_p = -160$ MHz) red-detuned from the the pump transition. So, unless otherwise noted, the one-photon detuning is set to -160 MHz. For ^{225}Ra, since we use two separate lasers, the one-photon detuning can be tuned widely by adjusting the reference frequency for our optical beatlock setup. To find the correct STIRAP Stokes frequency and therefore the STIRAP resoance, we scan the frequency of the Stokes laser by simply adjusting the EOM offset frequency in our electronic sideband (ESB) locking scheme. This allows us to tune the STIRAP Stokes laser frequency over >1 GHz. At each STIRAP Stokes laser frequency, we follow the following sequence of steps every experimental cycle:

1. We take a normalization atom image (image#1) of the atoms in the 'holding' ODT on an Andor Clara CCD camera

2. We trigger the STIRAP pulses

3. We take another atom image (image#2)

4. We turn on the atom killing pulse and "drop" (turn off) the 'holding' ODT for a few seconds to ensure none of the atoms survive in between the electrodes.

5. We take 5 backgrounds before and 20 backgrounds after the STIRAP and imaging pulses for background subtraction purposes

6. We take the ratio of the counts in background subtracted image#2 to image#1 to get the atom survival fraction: sf = $\text{counts}_{(\text{image2})}/\text{counts}_{(\text{image1})}$

The survival fraction 'sf' gives the fraction of atoms that remain in the 'holding' ODT after the STIRAP pulses interact with the atoms. This helps account for the atom losses due to finite 'holding' ODT trap lifetime, scattering with the imaging photons, and other loss mechanisms common to every experimental cycle.

7.3.2 Results

To demonstrate STIRAP in ^{226}Ra, Fig. 7.25 shows the result of a Stokes laser frequency scan. We scan the Stokes laser EOM offset and measure the survival fraction as detailed above. We notice a $\approx$ 2 MHz wide resonance peaking at 901 MHz, with a survival fraction of 8.7%. At 5 MHz either side of the peak, the survival fraction rises to about 50%. As expected, the STIRAP process is highly sensitive to two-photon detuning.

Next, we study the dependence of STIRAP process in ^{226}Ra on the pulse separation Δt between the Stokes and the pump pulses, all the while maintaining two-photon resonance. Fig. 7.26 shows the atom survival fraction (sf) at different values of pulse delay times (Δt). Just to remind ourselves,

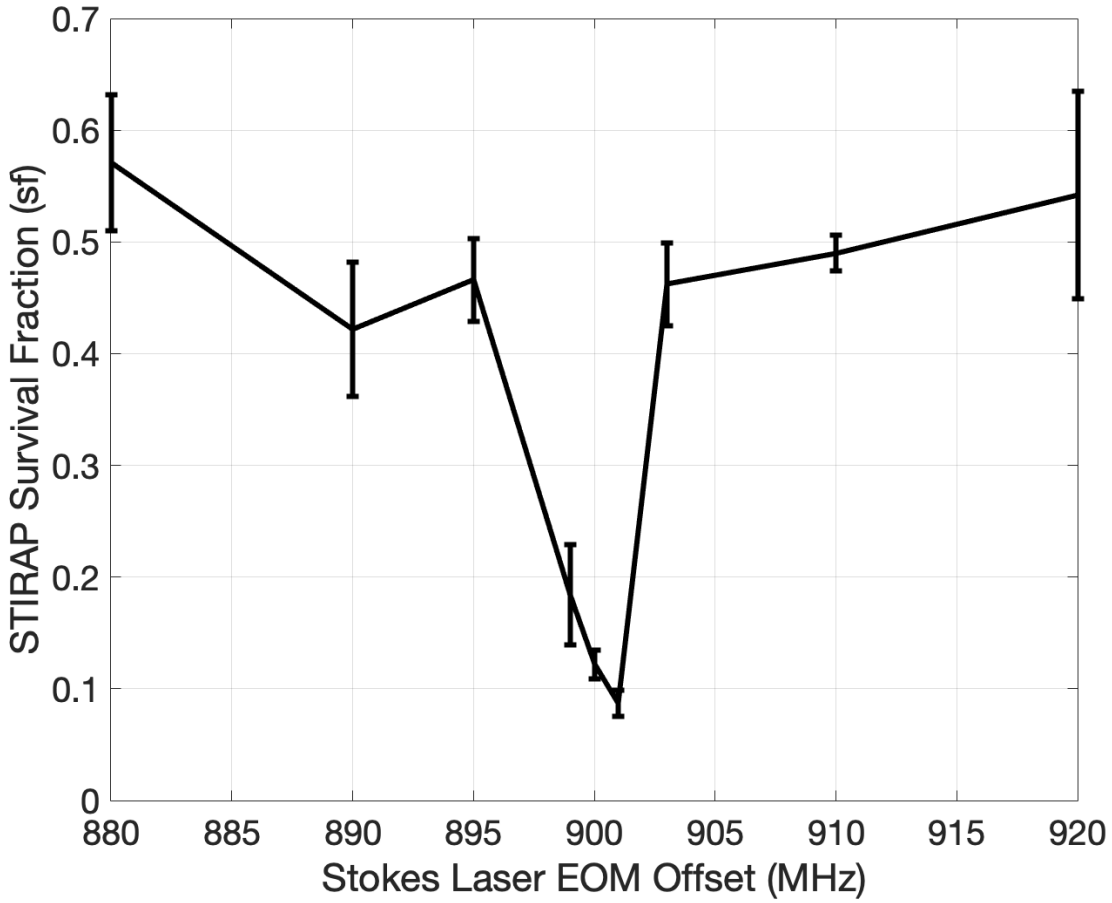

Figure 7.25: The experimentally observed post-STIRAP population survival fraction in the ground state at different values of Stokes laser frequencies in ^{226}Ra. This effectively corresponds to scanning the two-photon detuning δ. We observe the narrow two-photon resonance at the Stokes laser EOM offset frequency of 901MHz.

$\Delta t > 0$ indicates that the Stokes pulse precedes the pump pulse. As expected, we observe optimal STIRAP (lowest survival fraction) at a positive delay with $\Delta t = 2\,\mu$s.

To quantify the STIRAP process, we define the STIRAP efficiency '$\varepsilon(\Delta t)$' at a given pulse separation 'Δt' as

$$\varepsilon(\Delta t) = \frac{\mathrm{sf}(22\mu\mathrm{s}) - \mathrm{sf}(\Delta t)}{\mathrm{sf}(22\mu\mathrm{s})} \tag{7.56}$$

where $\mathrm{sf}(22\,\mu\mathrm{s})$ is the STIRAP survival fraction with the pulse separation at $22\,\mu$s. This is $> 10\tau$ and the overlap of the two pulses is negligible, and consequently we do not observe

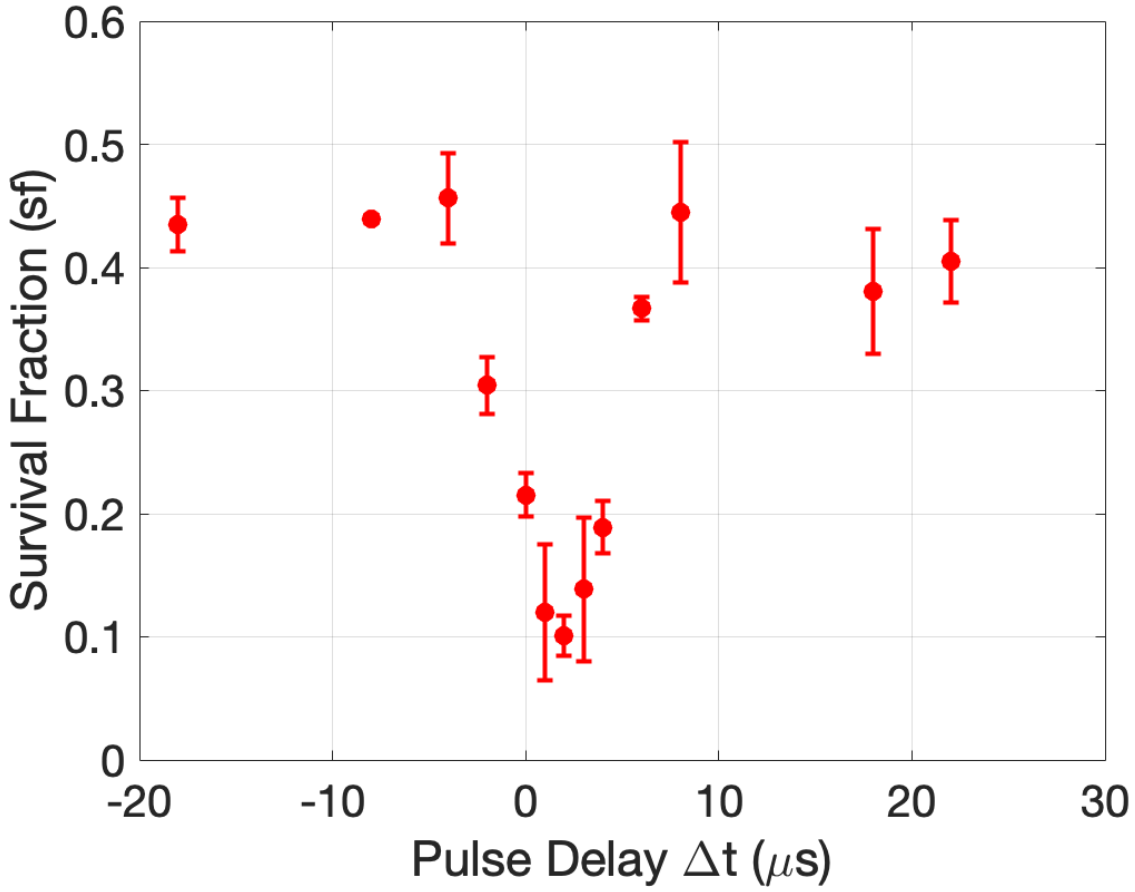

Figure 7.26: Experimental observation of STIRAP in ^{226}Ra at different values of pulse separations Δt. $\Delta t > 0$ indicates that the Stokes pulse precedes the pump pulse. We observe an optimal pulse delay of 2 μs.

STIRAP. sf(22μs) is therefore taken as the baseline survival fraction for computing the STIRAP efficiency. In Fig. 7.27 we plot the measured STIRAP transfer efficiency in ^{226}Ra at different pulse delay times Δt. For comparison, we simulate the expected STIRAP efficiencies in ^{226}Ra at different pulse separations. We incorporate laser frequency fluctuations using the exponentially correlated colored-noise model developed earlier. We consider laser frequency noise widths of $\sigma_p = 2\pi \times 0.25$MHz and $\sigma_s = 2\pi \times 1.1$MHz for the pump and Stokes lasers respectively.

The red data points in Fig. 7.27 shows the calculated STIRAP efficiency $\epsilon(\Delta t)$ at different pulse delays Δt. The blue shaded band is the result of our STIRAP simulation, incorporating the laser frequency noise as specified above. Each simulated data point is the average of four simulations

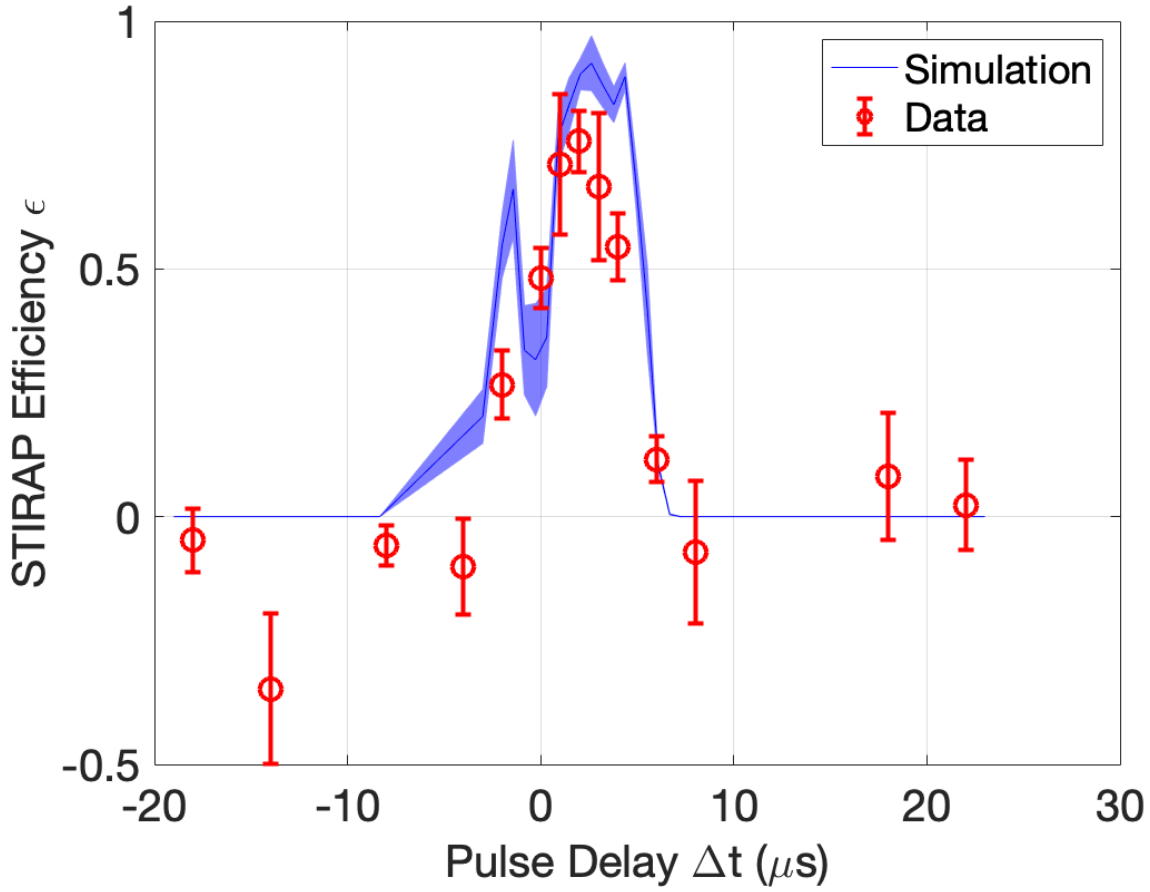

Figure 7.27: STIRAP transfer efficiency ϵ at different values of pulse delays Δt. We maintain two-photon resonance and a one-photon detuning of $\Delta = 2\pi \times 160$ MHz. The peak pump power is set to 100 μW, and the peak Stokes power is set to 10 mW. With 1 μs pulses, the red experimental data shows an optimal delay of 2 μs. The blue line represents the simulated data points with the 68% uncertainty band. We observe that the simulation generally agrees with the experimental data and show similar resonance width, as well as optimal delay time.

performed with randomly sampled frequency noise parameters, as detailed in Sec. 6.2.1.6, and the error bars are the uncertainties on the mean. Overall, the simulation agrees well with the data except for the secondary peak at the pulse delay of $\Delta t = -2\,\mu$s. The simulation shows a much lower transfer efficiency than observed at $\Delta t = 0\,\mu$s, and much higher transfer efficiencies at $\Delta t = \pm 4\,\mu$s. We briefly mentioned in our discussion on the simulation of STIRAP at different pulse delays, the appearance of a secondary peak at large one-photon detuning. It is however unclear why at a one-photon detuning of $\Delta = 2\pi \times 160$ MHz, we do not see an obvious peak in the experimental data. Perhaps the secondary peak is less than a MHz wide and therefore was not resolved. However, it is

possible that there are other factors that are unaccounted for in our simulation.

The dependence of the ground state population survival fraction in ^{226}Ra on the two-photon detuning δ (Stokes laser frequency offset) and the STIRAP pulse separations conclusively indicate that the atoms in the ground state $^1S_0$ are transferred into the $^3D_1$ final state with the aid of STIRAP. This is the first ever demonstration of STIRAP transfer of atoms from the ground state into a meta-stable state in radium.

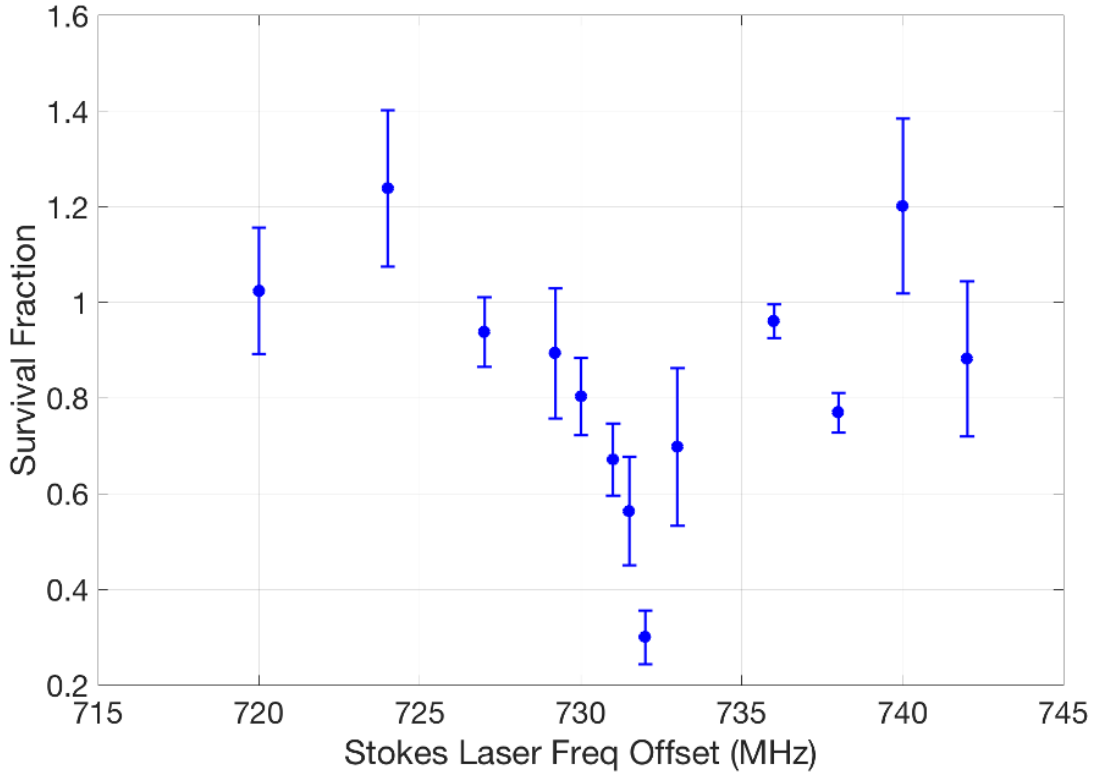

Figure 7.28: The experimentally observed STIRAP survival fraction in ^{225}Ra as a function of the Stokes laser frequency.

We also performed a number of preliminary STIRAP resonance searches in ^{225}Ra. For a proof of principle demonstration of STIRAP in ^{225}Ra we choose a scheme that is not necessarily ground state spin-selective. Instead of the spin-selective scheme outlined in Fig. 7.15, where we use the $^1P_1(F = 1/2)$ as the intermediate state, we use the $^1P_1(F = 1/2)$ state for STIRAP transfer of the ground state atoms. We also switch the Stokes laser polarization from σ^- to σ^+. This ensures that both the ground state sublevels are sensitive to the STIRAP pulses, hence maximizing our STIRAP

signal. The scheme chosen for demonstration of STIRAP in ^{225}Ra is shown in Fig. 7.29.

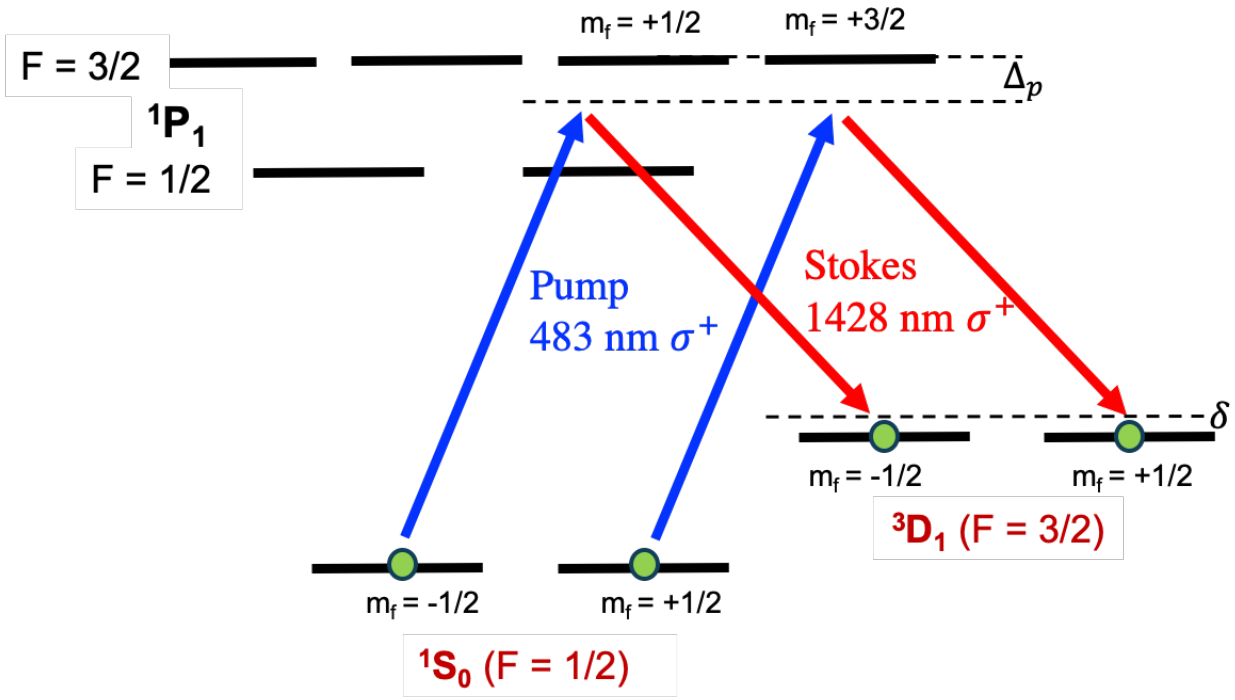

Figure 7.29: Scheme for demonstrating STIRAP in ^{225}Ra. This differs from the spin-selective scheme shown in Fig. 7.15 in two respects. We use the $^1P_1(F = 3/2)$, instead of the $^1P_1(F = 1/2)$ level as our intermediate state. We also switch the Stokes laser polarization from σ^- to σ^+. This ensures STIRAP transfer from both the ground state sublevels for maximal STIRAP signal.

We then scan the Stokes laser frequency to find the two-photon resonance. Fig. 7.28 shows the ground state survival fraction in ^{225}Ra at different Stokes laser frequencies. At the two-photon resonance, the survival fraction drops to $\approx$ 30%. Although we did not scan the pulse delay, the differences in the two-photon resonance frequencies between ^{226}Ra and ^{225}Ra quite conclusively ascertains that we have observed STIRAP in ^{225}Ra. Our attempts at ground state spin-selective STIRAP in ^{225}Ra were hampered by unexpected laser frequency instability issues that required significant rebuilding of our optical reference cavity chamber, as well as the temperature controlling circuit. We also had to replace our 'bus' ODT laser since the power in the last one dropped by $\approx$ 40% to 30 W and was no longer intense enough for successful atom transport into the science chamber to the 'holding' ODT. Furthermore, the limited supply of ^{225}Ra has prompted our investigations into ^{223}Ra as a suitable candidate for an atomic EDM search experiment. Currently efforts are

underway to laser cool and trap ^{223}Ra atoms in our system. Upon the availability of more ^{225}Ra we will resume our efforts at spin-selective shelving of ground state electrons in this isotope.

This concludes our investigation into the STIRAP technique and its applicability to radium isotopes for electron shelving from the ground state. Table 7.1 shows a list of suggested choices of initial STIRAP parameters (pump and Stokes laser peak powers, and the pulse separation) for a search for successful STIRAP in the ^{226}Ra, ^{225}Ra, and ^{223}Ra isotopes. For ^{226}Ra the choice of the STIRAP scheme is as shown in Fig. 7.4. For ^{225}Ra, we use the STIRAP scheme shown in Fig. 7.15. For ^{223}Ra, we consider the scheme shown in Fig. 7.19. We assume the pulses to be 2 μs wide, a one-photon detuning of $\Delta = 2\pi \times 200$ MHz, and two-photon resonance ($\delta = 0$ MHz). We exclude considerations of the laser frequency noise since they were not simulated in ^{225}Ra, and ^{223}Ra.

Table 7.1: Suggestions for the choice of pump and Stokes peak pulse powers, and the pulse delay for the three different isotopes of radium. We assume pulse widths of $\tau = 2\,\mu$s, one-photon detuning of $\Delta \sim 2\pi \times 200$ MHz, and two-photon resonance ($\delta = 0$ MHz).

Isotope	Pump Peak Power (mW)	Stokes Peak Power (mW)	Pulse Separation (μs)
^{226}Ra	0.1	6	4
^{225}Ra	0.1	6	4
^{223}Ra	4	6	4

Our extensive simulation studies in ^{226}Ra, highlight the characteristic dependence of the STIRAP process to the different parameters such as the pulse powers, the two-photon detuning (δ), the pulse separation, and the effect of laser frequency fluctuations on the STIRAP transfer efficiency. We find reasonable agreement between our experimental observation of STIRAP in ^{226}Ra and our simulation conducted with parameter values similar to the experimental conditions. We note that laser frequency fluctuation plays an important role, and in the case of ^{226}Ra might have led to sub-unity atom transfer efficiencies.

We intend on using STIRAP for spin polarizing the ground state in ^{225}Ra for an EDM measurement using nuclear spin precession of the ground state. Thus far, we have observed non-(ground state) spin selective atom transfer via STIRAP in ^{225}Ra. Our simulations of STIRAP in ^{225}Ra

indicate that the prospect of STIRAP assisted ground state spin-selective population transfer is promising.

^{223}Ra is another isotope of interest for an EDM measurement experiment. A nuclear spin of $I = 3/2$ makes it challenging to find a STIRAP scheme that spin polarizes the ground state resulting in a good enough contrast in the spin precession of the ground state. We have identified one such possible STIRAP scheme, as shown in Fig. 7.19, and our simulations suggest that STIRAP transfer of ground state population in ^{223}Ra can achieve spin precession contrast of up to 98%.

CHAPTER 8

RADIUM ATOM SLOWING SCHEME UPGRADE

This chapter details the spectroscopic study and lifetime measurement of the $6d7p\ ^3F_2^o$ state of radium with particular applications to devising an improved atom slowing scheme for trapping more radium atoms in our MOT. I contributed to the experimental design, the data collection runs, data analysis and in the writing of the following published manuscript[90], which is presented in this chapter:

Booth, D. *et al.* Spectroscopic Study and Lifetime Measurement of the $6d7p\ ^3F_2^o$ state of radium. *Spectrochimica Acta Part B* **172** (2020)

8.1 Introduction

A non-zero permanent electric dipole moment (EDM) in a non-degenerate system would indicate a new, clean signature of charge-parity (*CP*) violation and contribute to our current understanding of the observed baryon asymmetry in the Universe. Octupole deformation and the nearly degenerate parity doublet in the nuclear ground state of the ^{225}Ra atom enhances its intrinsic nuclear Schiff moment, making it an ideal candidate for an atomic EDM search [30, 32, 38, 91, 92]. The best limit on the atomic EDM of ^{225}Ra comes from the cold atom experiment at the Argonne National Laboratory [63].

Precise measurements of oscillator strengths and the branching fractions provide effective tests of atomic structure calculations, especially where electron correlation effects [93] and relativistic corrections [94] are important. They are also important for atomic parity non-conservation searches in the unified electro-weak theories [95]. Oscillator strengths can be determined either directly or indirectly. Direct measurements rely on absolute measurements of absorption, emission, or dispersion of relevant transitions, while indirect methods include combined measurements of the branching fractions and the lifetimes of the relevant higher states.

As a first step in trapping Ra, we must first reduce the longitudinal momentum of the atomic

beam. Currently, with a 1 m long Zeeman slower, using the $7s^2\ ^1S_0 \leftrightarrow 7s7p\ ^3P_1^o$ transition at 714 nm ("red slower" scheme), as shown in Fig. 8.1a, we slow atoms moving at speeds up to 60 m/s. The proposed upgrade to the cooling scheme will use the stronger dipole allowed $7s^2\ ^1S_0 \leftrightarrow 7s7p\ ^1P_1^o$ transition at 483 nm ("blue slower" scheme), enabling us to trap atoms with speeds up to 310 m/s, resulting in an estimated two orders of magnitude more atoms. This would improve the statistical sensitivity of our EDM measurement by an order of magnitude. The improved slowing scheme is shown in Fig. 8.1b. This slowing scheme, along with other upgrades underway, will enable the ^{225}Ra EDM limit to set one of the most stringent constraints on the hadronic CP violating parameters [23].

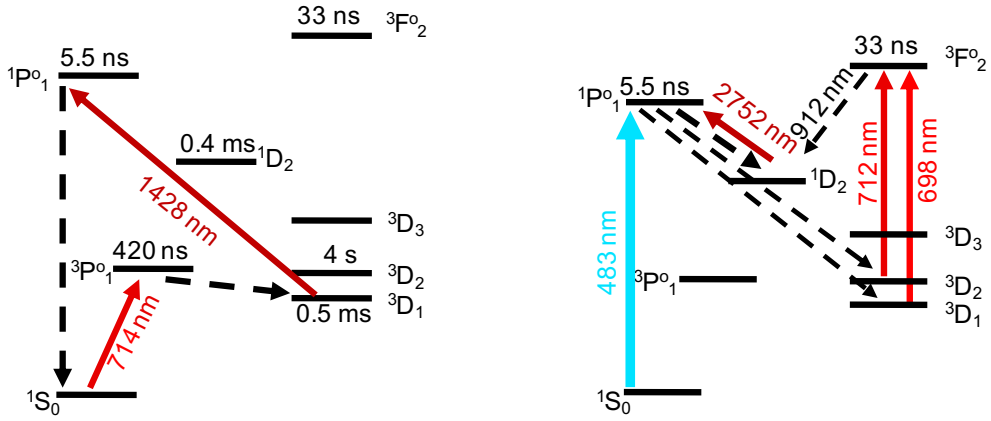

(a) red slower. (b) blue slower.

Figure 8.1: Relevant energy levels of neutral radium along with the current and proposed improved atom slowing schemes are shown. (a) Current slowing scheme: red slower, uses the 714 nm, inter-combination line along with one repump laser at 1428 nm to longitudinally cool and slow the atoms. (b) Proposed improved slowing scheme: blue slower, will use the stronger dipole allowed 483 nm transition. The $^3F_2^o$ state has a theoretically determined lifetime of 33 ns. It will be used as a spin flipping channel to transfer atoms from the ^3D_J states into the $^1D_2$ state, from where they are excited to the $^1P_1^o$ state, returning them into the cooling cycle.

As shown in Fig. 8.1a, we currently cool and trap the atoms using the $7s^2\ ^1S_0 \leftrightarrow 7s7p\ ^3P_1^o$ inter-combination line instead of the stronger dipole allowed $7s^2\ ^1S_0 \leftrightarrow 7s7p\ ^1P_1^o$ transition. This has the advantage of requiring only one 'repump' laser at 1428 nm to depopulate the $^3D_1$ state back into the cooling cycle.

The blue slower upgrade to our atom slowing scheme will use the stronger dipole allowed

transition, as shown in Fig. 8.1b. However, the atoms excited to the $^1P_1^o$ state decay to the long-lived (hundreds of μs) $^1D_2$, $^3D_1$, and $^3D_2$ states. This requires additional lasers to depopulate these states. A naïve repumping scheme would transfer the atoms directly from the various D-states into the $^1P_1^o$ state, returning them into the cooling cycle. This presents several challenges. The additional repump transitions have significantly different magnetic moments, making it impossible to design a magnetic field profile that simultaneously compensates for the associated Doppler shifts for a Zeeman slower. In addition, given the weak transition strengths from the ^3D_J manifold to the $^1P_1^o$ state, we would require higher laser powers than are readily available. Thus the direct repumping scheme is treated to be insufficient.

Theoretical studies of the low lying atomic levels of Radium suggest a strong spin-orbit interaction in the $6d7p\ ^3F_2^o$ state [68]. The E1-transition amplitude for the spin forbidden $^3F_2^o \rightarrow {}^1D_2$ transition is enhanced, while the spin allowed $^3F_2^o \rightarrow {}^3D_3$ transition is greatly suppressed. These properties are consistent with a *j-j* coupled state having the term symbol $(6d_{3/2}7p_{1/2})$. The proposed blue slower scheme will employ this strong spin-orbit coupling in the $^3F_2^o$ state, using it as a spin flipping channel to transfer atoms from the ^3D_J states into the $^1D_2$ state, from which they can be excited to the $^1P_1^o$ state, returning them to the cooling cycle.

Of the four transitions involved, the $^3F_2^o \rightarrow {}^1D_2$ and the $^3F_2^o \rightarrow {}^3D_3$ transitions have not been experimentally observed before [89, 96]. Knowledge of the oscillator strengths of these transitions is necessary for designing the Zeeman slower, as these oscillator strengths determine the repumper laser powers needed. This necessitated a spectroscopic study of the $^3F_2^o$ state, which involved measuring the oscillator strengths of the transitions to this state from the relevant D-states and the respective branching fractions.

Direct measurements of the oscillator strengths require the knowledge of the sample number density as well as local thermodynamic equilibrium [95]. However, since the $^3F_2^o$ state has large branching fractions to several long-lived states, it is suitable for a novel method of measuring the oscillator strengths that circumvent these requirements.

8.2 Method

The method that we employ for measuring the oscillator strengths of the transitions from the different D-states to the $^3F_2^o$ state requires that when 'probed' on a certain D-state to the $^3F_2^o$ state transition, the atoms scatter only a few photons from the probe laser before they decay into a meta-stable dark state. The lifetimes of the $^1D_2$ and $^3D_1$ states are measured to be 385(45) μs [97] and 510(60) μs [50] respectively, and the calculated lifetime of the $^3D_2$ state is determined to be 4 s [98]. By comparison, the average transit time of the atoms through the beam is 38 μs.

For the $^3D_3$ we set an upper bound on the branching fraction by comparing the fluorescence signal as the atom decays into this state, compared to the fluorescence signal as it decays into the $^1D_2$ state. For the rest, we selectively probe the atoms in the three different states, $^1D_2$, $^3D_2$ and $^3D_1$ by exciting them into the $^3F_2^o$ state and observing the fluorescence as they decay to one of the other non-probed states.

Since we use an atomic beam, an atom that decays into an unprobed or "dark", long-lived D-state, is not re-excited by the probe beam. For instance, the $^3F_2^o$ state decays with a maximum branching fraction of about 60% into the $^3D_2$ state, which corresponds to on average only 2.5 photons/atom scattered on this transition before going dark. The probability with which the atom scatters a probe photon is therefore Poissonian. Additionally, an atom that decays from the $^3F_2^o$ state to the probe state k with a probability p_{ik}, has a geometric probability of $p_{ik}^{n-1}(1 - p_{ik})$ of decaying into a dark state after n scattering events [99].

The cumulative distribution function, $\mathrm{CDF}(\Lambda, n)$, for a Poissonian distribution with a rate Λ that describes our probing process, is the probability that up to n probe photons are scattered. It is given by

$$\mathrm{CDF}(\Lambda, n) = \frac{\Gamma[\mathrm{floor}(n+1), \Lambda]}{\mathrm{floor}(n)!}, \tag{8.1}$$

where Γ is the upper incomplete gamma function.

1 – CDF then represents the probability that the probe laser power is sufficient to scatter at least

n photons. Therefore, the probability p that after scattering n probe photons the atom decays into our signal state is given by the cumulative term

$$p = p_{ik}^{n-1}(1 - p_{ik})[1 - \mathrm{CDF}(\Lambda, n)] \tag{8.2}$$

Thus, the overall process is described by a Poisson and geometric distribution. The Poissonian rate Λ is dependent on the oscillator strength of the transition, as well as the natural linewidth of the $^3F_2^o$ state, which is proportional to the sum of the oscillator strengths of all its possible decay channels. Therefore, if we probe all the relevant transitions to the excited state of interest, we can fit for every oscillator strength.

This is significantly different from the method of “equivalent widths" for oscillator strength measurement [100, 101]. Although the emission lineshapes indirectly depend on the Lorentzian lineshape of the underlying transition, they are nevertheless described by a Poissonian cumulative distribution function due to the small number of photons scattered per atom. This is due to the finite exposure time of the atoms as they pass through the probe beam and the optical pumping of the atoms into dark states, limiting the number of photon scattering events. Our sensitivity to the oscillator strength comes not from the absolute intensity of light emitted by the atoms, but instead from the line broadening that occurs due to the saturation-like effect that occurs as a result of the optical pumping. In addition, we observe a different transition than we are probing on, meaning only one photon at that wavelength is emitted per atom.

We also need to know the oven temperature, although it will be shown later that this does not need to be very precise. It also requires a measurement of the probe beam profile and the probe beam powers. Apart from these, this method circumvents the need for atomic flux calibration and the absolute efficiency of various parts of the experimental setup.

As for the $^3F_2^o$ state, this provides an effective technique for oscillator strength measurements in an atomic beam, where one probes a state directly inaccessible from the ground state, and with significant branching fractions to several lower lying, long-lived states.

8.3 Experimental Setup

The measurements presented in this work were performed on ^{226}Ra ($t_{1/2}$ = 1600 y, I = 0). This isotope is selected due to its relative abundance compared to ^{225}Ra. The experimental setup is shown in Fig. 8.2. We load 3 μCi of ^{226}Ra in the form of radium nitrate salt along with two 25 mg pieces of metallic barium into the oven and radiatively heat it. The barium helps chemically separate the radium from the radium salt, allowing a steady flux of atomic radium out of the nozzle. The nozzle geometry limits the divergence of the atomic beam to 50 mrad [63]. About 30 cm from the nozzle, the atoms are excited into the $^1P_1^o$ state using 3 mW of 483 nm 'pump' light produced by a Toptica DL Pro diode laser which is frequency stabilized to a zerodur optical cavity. The pump laser linewidth is 150 kHz, and the zerodur cavity is stable to drifts of $\sim$ 700 kHz/day. The atoms, after being excited by the pump laser, then decay to the long-lived D-states as shown in the inset of Fig. 8.2. The probe laser beams at 912 nm, 712 nm and 698 nm for respectively probing the $^1D_2$, $^3D_2$, and $^3D_1$ state are produced by a Sirah Matisse Ti:Sapphire ring cavity laser which is frequency stabilized to a high finesse ultra-low expansion (ULE) glass optical cavity. The linewidth of the probe laser is 70 kHz, and the ULE cavity is stable to drifts on the order of $\sim$ 10 kHz/day. For instance, in Fig. 8.2, we probe the atoms in the $^3D_2$ state by resonantly exciting the atoms into the $^3F_2^o$ state with a 712 nm probe beam and observing the subsequent decay of the atoms into the $^3D_1$ state at 698 nm. We collect line-shape data for a given probe transition and laser power by scanning the probe laser frequency. This is repeated for a range of different probe powers.

We scan the frequency of the probe laser by double passing it through an acousto-optic modulator (AOM) and scanning its input RF frequency. The fluorescence signal is collected by a 2" diameter, 10 cm focal length lens, filtered and focused onto a photo-multiplier tube (PMT) (Hamamatsu, H7421-50). The PMT output is sent to a data acquisition (DAQ) card (NI- USB6341). The pump laser is shuttered a rate of 0.5 Hz to subtract any scattered background from the probe light on the PMT in the fluorescence signal. This is repeated for all the probe transitions of interest. The probe beam intensity profile is measured using a Thorlabs DCC1545M CMOS camera (1280 $\times$ 1024 pixels).

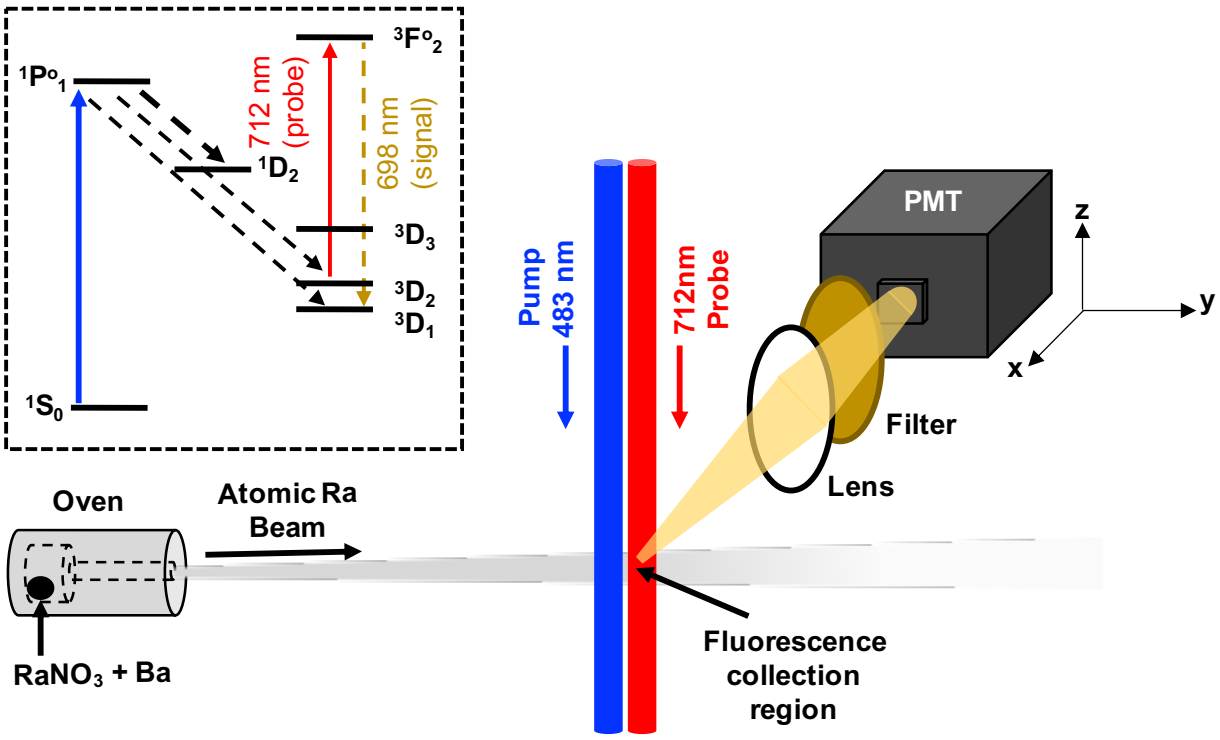

Figure 8.2: Spectroscopy measurement setup (not to scale). The atoms exiting the oven are pumped into the $^1P^o_1$ state from which they decay into the D-states. Here, we probe the atoms in the $^3D_2$ state with a resonant 712 nm probe laser beam which excites them into the $^3F^o_2$ state and the resultant fluorescence 698 nm is filtered and detected by a PMT. Inset: the relevant energy levels and the transitions involved for probing the atoms in the $^3D_2$ state and detecting the fluorescence as the atoms decay from $^3F^o_2 \rightarrow {}^3D_1$.

To limit the branching fraction of the $^3F^o_2 \rightarrow {}^3D_3$ transition, with the probe laser at 912 nm, probing the $^1D_2 \rightarrow {}^3F^o_2$ transition, we compare the signal at 750 nm (decay to the $^3D_3$ state), with the signal strength at 698 nm (decay to the $^3D_1$ state) using narrow bandwidth filters. Using the value we obtain for the 698 nm branching fraction from our analysis, we convert the relative limit on the branching ratio of $^3D_3 \rightarrow {}^3F^o_2$ transition to an absolute limit.

8.4 Data Analysis

We collect lineshape data for 8 different powers with the probe laser wavelength at 712 nm and 5 different powers each with the probe laser wavelength at 698 nm and 912 nm, for a total of 18 lineshape data sets. For each of the lineshape data sets measured, we fit the fluorescence counts at

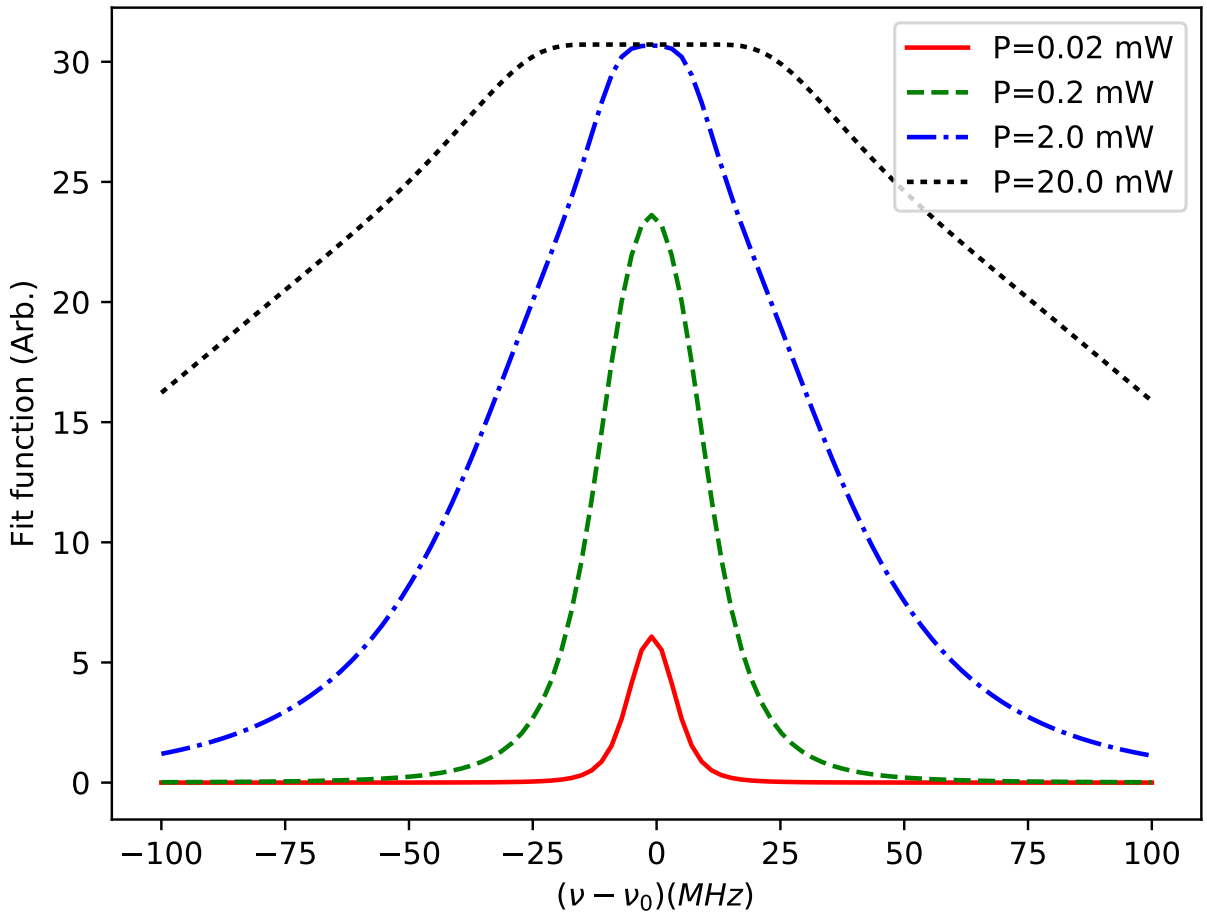

Figure 8.3: An example of the behavior of the fit function as the probe beam power is increased. This example is shown for the 712 nm probe transition, which has an oscillator strength $f_{ik} = 0.32(12)$.

the signal transition to a function 'F' to extract the oscillator strengths:

$$F = A \sum_{n=1}^{n_{\max}} p_{ik}^{n-1}(1 - p_{ik})\,[1 - \mathrm{CDF}(\Lambda, n)] + C_0, \tag{8.3}$$

where n is the number of photons scattered before the atom decays into the signal state, p_{ik} is the branching fraction from the ${}^3F_2^o$ state to the probe state k, A is an amplitude extracted from the fit, and C_0 is a constant offset. The term $p_{ik}^{n-1}(1-p_{ik})[1-\mathrm{CDF}]$ is the probability that after scattering n probe photons the atom decays into our signal state, as given by Eq. 8.2. The nominally infinite sum is truncated to $n_{\max}$ and checked for convergence.

The shape of the probe beam is incorporated into the expression for the Poissonian weight, Λ,

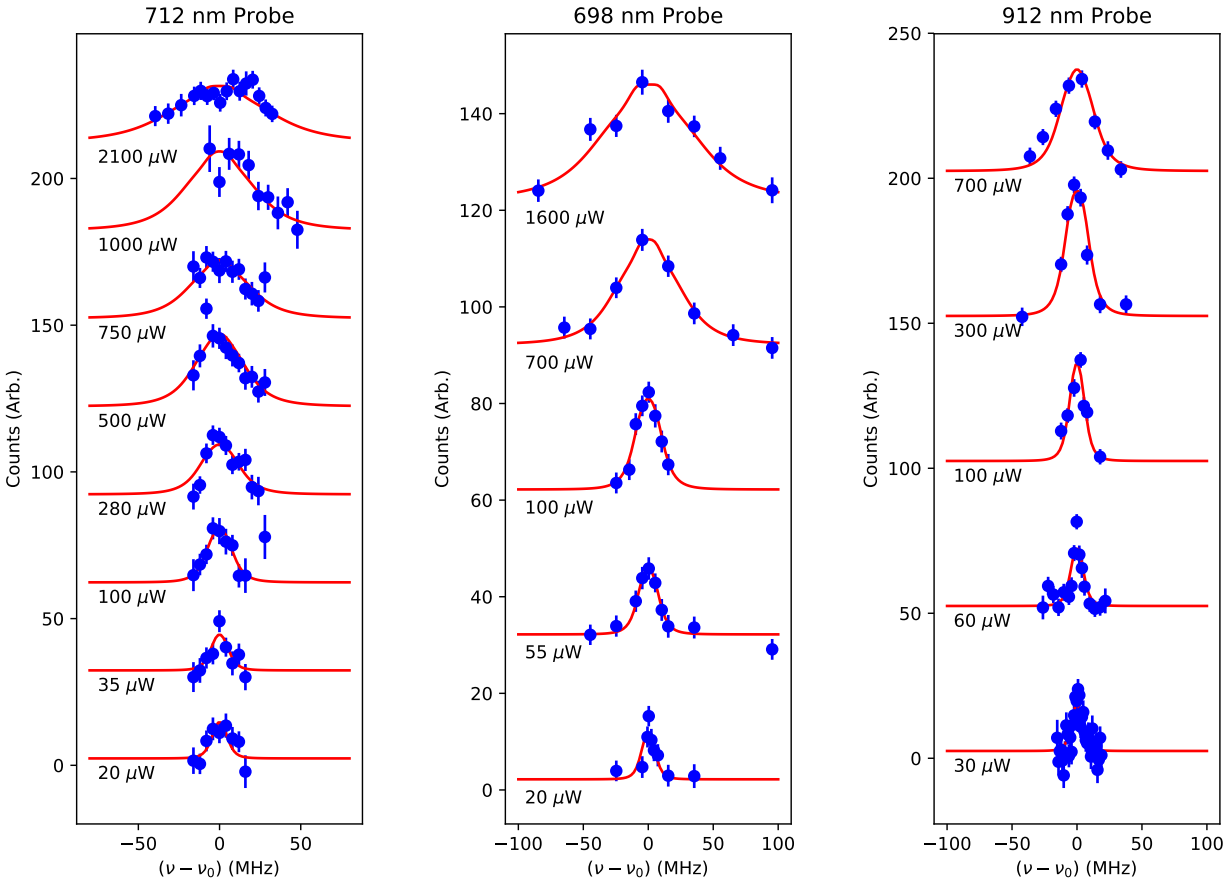

Figure 8.4: Waterfall plot of the data and the fits for each of the lineshapes measured in the experiment. The count rate for a particular probe transition at a given power is plotted against the detuning $(\nu - \nu_0)$ from resonance. The lineshapes are offset vertically for clarity.

given by:

$$\Lambda = \sum_y \tau \bar{n}(y) f \sigma_0 g(\nu - \nu_0; \Gamma, \gamma_D), \tag{8.4}$$

where τ is the interaction time as the atom passes through one pixel of the laser beam image of width Δy, f is the oscillator strength, ν is the laser frequency, ν_0 is the line center, and $\sigma_0 = \pi r_e c = 2.654 \times 10^{-2} \mathrm{cm}^2/s$, where r_e is the classical electron radius and c is the speed of light [102]. g is the lineshape function and $\bar{n}(y)$ is the photon intensity at a given y-pixel. The interaction time is determined by the velocity distribution of the beam:

$$\tau = \Delta y \left\langle \frac{1}{v} \right\rangle \tag{8.5}$$

$$\left\langle \frac{1}{v} \right\rangle = \int_0^\infty B(v;T) \frac{1}{v} dv, \tag{8.6}$$

where the Boltzmann velocity distribution $B(v;T)$ is defined as [103]:

$$B(v;T) = 2\frac{u^2}{\bar{v}} e^{-u^2} \tag{8.7}$$

$$u = v/\bar{v}, \tag{8.8}$$

where $\bar{v}$ is the most probable speed.

The photon intensity observed by an atom at horizontal position y, $\bar{n}(y)$ is:

$$\bar{n}(y) = \frac{P}{h\nu\Delta y^2} \frac{\sum_x I(x,y)}{\sum_{x,y} I(x,y)}, \tag{8.9}$$

where P is the total power in the laser beam, Δy is the width on one pixel on the beam image (5.2 μm), and $I(x,y)$ is the beam strength at pixel (x,y).

The lineshape function $g(\nu - \nu_0; \Gamma, \gamma_D)$ is a Voigt profile, with the Gaussian width γ_D determined, by a measurement of the Doppler-broadened linewidth on the narrow 714 nm, ${}^1S_0 \rightarrow {}^3P_1^o$ transition ($\Gamma_{714} = 2\pi \times 380\,\text{kHz}$), to be 2.32 MHz. The Lorentzian width of the Voigt profile is a dependent parameter of the fit:

$$\Gamma = \sum_i A_{ki} = \frac{2\pi^2 r_e c}{2J_k + 1} \sum_i \frac{2J_i + 1}{\lambda_{ik}^2} f_{ik}, \tag{8.10}$$

where A_{ki} is the spontaneous decay transition rate from an upper state k to a lower state i, and J_i and J_k are the total angular momenta of states i and k respectively. The branching fractions p_{ik} can be expressed in terms of A_{ki} as:

$$p_{ik} = \frac{A_{ki}}{\Gamma}. \tag{8.11}$$

The parameters of the fit are the oscillator strengths f_{ik}, the peak amplitudes A, the peak centers ν_0, and the offsets C_0. The offsets, peak centers, and oscillator strengths are common for fits of peaks from the same transition. The amplitudes vary between different lineshapes due to variations in the atom flux from the oven. The offsets are to account for various background sources. Examples of the effect of the oscillator strength on the fit function are shown in Fig. 8.3. As the power increases, it results in a broader peak for a fixed oscillator strength. This line broadening happens due to the Poissonian nature of the probe process. As soon as the atom scatters a few probe photons, it decays into the signal state and is lost from the probe cycle.

The lineshapes for each power taken for each transition are cumulatively fit, using a least squares method using the curve fitter from the scipy library, version 1.1.0, in Python.

8.5 Results

Fits for each of the lineshapes measured are shown in Fig. 8.4. The reduced chi-squared for the cumulative fit is $\chi^2_\nu = 1.13$, (179 degrees of freedom). Results for the oscillator strengths and branching fractions are shown in Table 8.3. From these oscillator strengths we can determine the linewidth of the $^3F_2^o$ state to be 10.4 ± 2.7 MHz.

Convergence of the sum in Eqn. 8.3 is tested by varying the upper limit on n, testing the values $n_{\max} = [5, 10, 20, 40]$. Results of this test are shown in Table 8.1. For $n_{\max} = 10$ and above, there is strong convergence for all of the oscillator strengths. This is as expected, since the atoms scatter only a few probe photons before decaying into a dark state, and is responsible for the saturation of the peak seen in Fig 8.3.

$n_{\max}$	$^3F_2^o \rightarrow {}^3D_2$	$^3F_2^o \rightarrow {}^3D_1$	$^3F_2^o \rightarrow {}^1D_2$
1	0.247(44)	0.234(39)	0.046(7)
5	0.294(71)	0.254(65)	0.042(7)
10	0.318(105)	0.243(79)	0.041(8)
20	0.318(119)	0.245(87)	0.041(9)
40	0.317(120)	0.245(87)	0.041(9)

Table 8.1: Convergence of the oscillator strengths as a function of the number of terms, $n_{\max}$, in the sum in Eqn. 8.3.

T(°C)	$^3F_2^o \rightarrow {}^3D_2$	$^3F_2^o \rightarrow {}^3D_1$	$^3F_2^o \rightarrow {}^1D_2$
420	0.317(120)	0.239(85)	0.040(9)
470	0.318(119)	0.245(87)	0.041(8)
520	0.319(119)	0.251(88)	0.042(9)

Table 8.2: The oscillator strengths as a function of the temperature of the Radium oven, with $n_{\max} = 20$.

Table 8.3: Wavenumbers, Oscillator strengths (f_{ik}), and branching fractions (BF) for the transitions out of the $^3F_2^o$ state. Theory values for the branching fraction from [68] are shown for comparison. For more discussion of the transition to $^3D_3$, see section 8.6.

Transition	Wavenumber (cm^{-1})	f_{ik} (theory)	f_{ik}	BF
$^3F_2^o \rightarrow {}^1D_2$	10956.7095(5)	0.054	0.041(9)	0.050(11)
$^3F_2^o \rightarrow {}^3D_2$	14044.0875(5)	0.074	0.32(12)	0.64(24)
$^3F_2^o \rightarrow {}^3D_1$	14322.2340(5)	0.202	0.25(8)	0.31(11)
$^3F_2^o \rightarrow {}^3D_3$	13330.7 [68]	9.3×10^{-5}	< 0.002	$< 4 \times 10^{-3}$

An additional factor that may affect our results is the temperature of the radium oven source. There can be uncertainty in this temperature due to temperature gradients between inside of the oven crucible and the monitor thermocouple at the rear of the crucible. This would cause a systematic shift in the Boltzmann factor $B(v;T)$, which affects the interaction time τ of the atoms with the laser beam in Eqn. 8.4. To test this, we fit the data using $n_{\max} = 20$ and $T = [420, 470, 520]$°C. Results of this test are shown in Table 8.2. We find both of these systematic effects to be negligible.

Effects such as radiation trapping and collisional effects are negligible in our case due to the low beam density. With the number of atoms in our oven and our operational temperature, we have a beam density of about 10^3/cm^3. This is many orders of magnitude below the densities at which these effects become significant. Our experiment is performed at low magnetic field, but the light polarization still affects the directionality of the emission. This directionality affects the fluorescence observed, unless the detector is at the magic angle (54.7 degrees) [104]. However, the oscillator strength is not extracted from the integral of the detected fluorescence, but rather from the linewidth, which is broadened by the total scattering over all angles. Therefore, the polarization of the probe beam does not affect our calculation of the oscillator strength.

A limit on the $^3F_2^o \rightarrow {}^3D_3$ branching fraction was determined by comparing the strength of

the signal at 750 nm from this transition to the $^3D_1$ signal strength at 698 nm. A 105-minute integration of the 750 nm signal level resulted in 2.5 ± 0.75 counts per second, compared to a 10 minute integration at 698 nm, where we had a signal level of 73 ± 2.9 counts per second.

A source of systematic error in this measurement that had to be accounted for is the leakage of 483 nm light through the 750 nm filter. This leakage causes a constant offset on the signal level, which is accounted for in the lineshape fitting by adding a constant offset. In the 750 nm measurement, however, this error can appear as a false detection of atoms decaying on this decay channel. To determine the effect of 483 nm leakage, we measured the PMT signal in the absence of probe light for a period of 14 hours, yielding a signal level of 2.43 ± 0.28 counts per second. After removing this effect, the result at 750 nm is 0.08 ± 0.81 counts per second, which we interpret as an upper limit of 0.4% (68% confidence limit) on the branching fraction to $^3D_3$. This upper bound is computed using the Feldman-Cousins contruction of confidence intervals for a Gaussian distribution constrained to have a non-negative mean. [105]

8.6 Discussion

Although differing in detail from the prediction in [68], the overall picture of strong spin-orbit coupling in $^3F_2^o$ is confirmed. The $^3D_3$ is found to be highly suppressed, and the $^1D_2$, while still weak compared to $^3D_2$, is strongly enhanced compared to the normal dipole selection rules for a $^3F_2^o$ state. The oscillator strength of the $^3D_2$ channel is found to be significantly higher than predicted, although the others are in good agreement. It should be noted, however, that the $^3F_2^o \rightarrow {}^1D_2$ transition is a forbidden transition in the absence of relativistic effects with its branching fraction component coming from the strong spin-orbit interaction in the $^3F_2^o$ state.

For the $^3F_2^o \rightarrow {}^3D_3$ transition, the branching fraction from the dipole matrix elements from [68] is 3.6×10^{-4}, which is an order of magnitude below our upper bound of 4×10^{-3} (68% confidence limit).

The theoretical value for the lifetime of the $^3F_2^o$ state is 33 ns [68], which differs from our experimental lifetime (derived from the natural linewidth) of 15.3 ± 4.0 ns, by about a factor of two.

The differences with theory could be due to either uncertainty in the theory, as the $^3F_2^o$ level has little previous spectroscopic data and a strong spin-orbit coupling, or it could also be due to an unknown systematic error due to the novelty of our method. The latter could be tested for by using a system with more previously-existing spectroscopic data.

Our results for the branching fractions out of the $^3F_2^o$ confirm the viability of our scheme for repumping the blue Zeeman slower. The branching fraction to the $^1D_2$ state is sufficient to make repumping through this state reasonable, despite being lower than the theoretical branching fraction. With a branching fraction of 0.05, 20 excitations would be needed on average to bring an atom into the $^1D_2$ state.

8.7 Conclusions

We have measured the oscillator strengths and the branching fractions of the decay channels of the $^3F_2^o$ state. We employ what we believe to be a novel technique that is used in an atomic beam measurement and requires that the atom excited to a higher energy level decays into several long-lived states, and therefore scatters only a few photons on the transition of interest. This technique requires measuring lineshape data for a number of powers for all the transitions involved. The cumulative fit to all the data is a function of the oscillator strengths of all the transitions to the excited state. This method avoids the need for knowledge of the atomic number density, as well as the absolute calibration of the efficiencies of the different parts of the experimental setup.

The systematic effects due to the oven temperature uncertainty and the finite sum over the photon scattering events n in the fit function Eq. 8.3 up to an upper limit $n_{\max}$ were studied. Both of these effects are negligible compared to the statistical uncertainties in the oscillator strengths. The main limitation on the maximum number of photons is computation time. Our implementation of the fitting algorithm took about a day to run with $n_{max} = 40$ on a laptop computer with an Intel i7-7700HQ CPU.

The strong decay channel to $^1D_2$, along with the strong suppression of the branching ratio to the $^3D_3$ state compared to the $^1D_2$ state supports the theoretical prediction of strong spin-orbit

coupling in the $^3F_2^o$ state in radium.

The above spectroscopic study of the $^3F_2^o$ state supports our proposal of using this state as a spin flipping channel for implementing the blue slower upgrade to our atom slowing and cooling apparatus. This will improve our atom trapping efficiency by two orders of magnitude and enhance our sensitivity to the atomic EDM of ^{225}Ra by at least a factor of 10, setting very stringent limits on the hadronic *CP*-violating parameters.

CHAPTER 9

CONCLUSION AND OUTLOOK

With its octupole deformed nuclear structure, resulting in an enhanced nuclear Schiff moment, ^{225}Ra is an excellent probe for *CP*-violation arising from the atomic nucleus. Two to three orders of magnitude improvement in the radium EDM limit will help further constrain the allowed values of the various *CP*-violating parameters, such as C_T. This thesis outlines the work conducted at Argonne National Laboratory on the upgrades to the radium EDM search apparatus for an improved measurement of the atomic EDM of ^{225}Ra.

Since the radium EDM experiment employs laser cooling and trapping of atoms, the technique itself and the different laser systems used in the experiment are described in chapter 4. In chapter 5, we describe a broadband laser frequency stabilization scheme that was implemented in many of our lasers. Owing to its broadband frequency tunability, we apply this technique for precision spectroscopy in radium and measure the frequency difference between the MOT transitions for ^{226}Ra, and ^{225}Ra, by a factor of 29 better than what can be determined from previously available spectroscopic data. This measurement, along with the hyperfine splitting in the $^1P_1$ level in ^{225}Ra allow us to determine the isotope shift for this transition between the two isotopes a factor of 8 more precisely compared to the available spectroscopic data.

Since the radium EDM limit is currently limited by the statistical uncertainties, several upgrades are in different phases of installation and implementation for improving the statistical sensitivity of the experiment. Efforts toward enhancing the detection sensitivity of the apparatus using the STIRAP electron shelving technique, as detailed in chapter 6, intends on using STIRAP for spin polarizing the ground state in ^{225}Ra. This involved simulation studies of the feasibility of STIRAP in ^{226}Ra, ^{225}Ra, and ^{223}Ra. Experimental observation of STIRAP in ^{226}Ra showed sub-unity STIRAP transfer efficiency, which was simulated and explained using a correlated color noise model incorporated into our STIRAP Stokes and pump lasers frequencies. Non-nuclear spin selective STIRAP has been experimentally observed in ^{225}Ra. Nuclear spin-selective schemes

have been identified for ^{225}Ra which when implemented will allow us to spin polarize the ground state for use in an EDM experiment. We have also identified a nuclear spin selective STIRAP scheme in ^{223}Ra for use in a potential EDM measurement experiment.

Chapter 8 details our work on improving the atom slowing and cooling using the "blue slower" scheme. We identify the higher lying $6d7p\ ^3F_2^o$ as a potential spin flipping channel for efficient repumping of atoms out of the meta-stable $^3D_1$, and $^3D_2$ states. We performed spectroscopic study of the $^3F_2^o$ state and measure the oscillator strengths for transitions to the lower lying $^3D_1$, $^3D_2$, and $^1D_2$ states and set a 68% upper limit on the oscillator strength for the transition to $^3D_3$ state. We also measure the lifetime of the $^3F_2^o$ state to be 15.3 ± 4.0 ns. These results suggest a strong spin-orbit coupling in the $^3F_2^o$ state and supports our proposal to use of this state in the "blue slower" upgrade for improving the atom trapping efficiency by a factor of 100.

Along with the demonstrated factor of ~ 4 increase in the electric field, when implemented, these upgrades are expected to improve the limit on the atomic EDM of ^{225}Ra by three orders of magnitude to $10^{-26}\ e \cdot$cm level. At this level, in the global analysis interpretation, the ^{225}Ra EDM limit will not only set stringent limits on several of the *CP*-violating parameters inside the atomic nucleus, but also start significantly constraining the nucleon-electron interaction parameter C_T.

9.1 Personal Contributions to the Work Presented in this Thesis

- I was involved in implementing STIRAP electron transfer in ^{226}Ra and participated in the data runs that resulted in the first ever observation of STIRAP in ^{226}Ra as well as ^{225}Ra.

- I rebuilt our zerodur optical cavity setup, for improved laser frequency stability for our STIRAP searches in ^{225}Ra. This involved adding additional layers of insulation and temperature control, and rebuilding the temperature control circtuit for temperature controlling the inner vacuum chamber that houses the zerodur cavity.

- I simulated STIRAP electron transfer efficiencies in ^{226}Ra, ^{225}Ra, and ^{223}Ra and studied its dependence on the power and polarization of the STIRAP Stokes and pump lasers. I also simulated fluctuations in the STIRAP Stokes laser frequency using an exponentially

correlated colored noise and studied its effects on the STIRAP transfer efficiency in ^{226}Ra and compared it against our experimental data. I also verified the feasibility of STIRAP transfer in ^{223}Ra for nuclear spin-selectivity and identified a particular pair of STIRAP Stokes and pump transitions that achieves this.

- I participated in the planning and the taking of data for the spectroscopic study of the $^3F_2^o$ state in radium. In the preliminary stages, I helped set up the 912 nm external cavity diode laser described in chapter 4, that enabled us to find the relevant $^1D_2 \leftrightarrow {}^3F_2^o$ transition frequency. I also participated in the analysis of the collected spectroscopic data and helped compile the manuscript that was eventually accepted for publication.

- Our collaborators have performed extensive Monte Carlo simulation of the radium atom slowing and trapping setup to better understand the atom trapping efficiencies. Related to this effort, I helped take some experimental data to verify the dependence of the number of atoms trapped in the MOT on the external magnetic field in the transverse cooling region. This work is detailed in Ref. [103].

- For broadband laser frequency tunability, I helped implement the ESB offset frequency stabilization scheme on our different laser systems. I characterized its performance against our typically used PDH laser frequency stabilization scheme. I applied this to the precise measurement of the MOT frequency difference between ^{226}Ra and ^{225}Ra, which also allowed us to more precisely determine the isotope shift for this transition between the two isotopes.

APPENDICES

APPENDIX A

MATLAB CODES FOR STIRAP SIMULATION IN ^{226}Ra

The following MATLAB code simulates STIRAP in ^{226}Ra.

```
%%% This script simulates STIRAP in Ra-226 involving the 1S0, 1P1 and 3D1
% levels. There are 7 states in total. This also takes into account laser
% frequency noise.
% The levels are labelled as following: (2S+1)L(J) (J,mJ)
%                                       1: 1S0
%                                       2: 1P1(1/2,-1/2)
%                                       3: 1P1(1/2,0)
%                                       4: 1P1(1/2,+1/2)
%                                       5: 3D1(1/2,-1/2)
%                                       6: 3D1(1/2,0)
%                                       7: 3D1(1/2,+1/2)

clear
clc
close all

%% Defining Constants Used in the Simulation
c0 = 299792458; % Speed of Light in vacuum in m/s
h = 6.626e-34; % Planck's Constant in SI units
hbar = h/(2*pi);
e0 = 8.854187e-12; % Vacuum permittivity in SI units
muB = 9.3e-24; % Bohr magneton in SI units

%% Parameters of the Pump and Stokes Beams
% factor1 = 0.08;
% factor2 = 15;
```

```
27 l = 20; % number of pulse widths to simulate for
28 factor1 = 0.8;
29 factor2 = 1;
30 pumppwr = factor1*1e-3; % pump laser pulse power in Watts
31 stokespwr = factor2*1e-3; % stokes laser pulse power in Watts
32 pumpInt = 2*pumppwr/(pi*(100e-6)^2); % pump laser pulse peak intensity in ...
       Watts/m^2. Here we assume the laser beam is Gaussian
33 stokesInt = 2*stokespwr/(pi*(100e-6)^2); % stokes laser pulse peak ...
       intensity in Watts/m^2
34 ompump = 0.5*sqrt(2*pumpInt/(e0*c0))/hbar; % Pump peak Rabi freq in SI units
35 omstokes = 0.5*sqrt(2*stokesInt/(e0*c0))/hbar; % Stokes peak Rabi freq in ...
       SI units
36 pulse = 1e-6; % This is the STIRAP pulse width in second, common to both ...
       pump and stokes pulses.
37 % delayp = 5*pulse+2e-6; % Pump Laser Pulse Delay/pulse width
38 delays = (l/2)*pulse-2e-6; % Stokes Laser Pulse Delay/pulse width
39 delayp = delays+2e-6;
40 % Set the polarizations of the STIRAP pulses. +1: +ve circular, -1: -ve
41 % circular, 0: linearly polarized
42 polp = 1; % Pump laser polarization (corresponds to 1<-->4 transition)
43 pols = 1; % Stokes laser polarization (corresponds to 6<-->4 transition)
44 pol = [polp, pols];
45 branchingratio = 1-1100/1101; % branching ratio from the intermediate ...
       state to states other than the STIRAP states
46 gamma = branchingratio*1/(2*pi*5.5e-9); % Natural linewidth of the ...
       intermediate (1P1) state for Radium
47 Δpump = -2*pi*160e6; % Single photon detuning between for the 1S0 <--> 1P1 ...
       transition, set the sign -ve for red-detuned, and +ve for blue-detuned.
48 detune = 50*2*pi*1e6; % 2 photon detuning
49 pts = linspace(-10e6,10e6,20)*2*pi; % List of two photon detunings used ...
       for creating the STIRAP 2 photon lineshape
50 cwp = 0; % set cw = 1 for cw laser and 0 for pulsed laser
51 cws = 0;
```

```
52 zeeman = 0; % This sets the zeeman splitting between the sub-levels
53 GausstoT = 1e-4; % Tesla to Gauss conversion
54 B = 0*30e-3*GausstoT; % B-field strength
55 ODTState = 0; % 0 for ODT OFF and 1 for ON
56 ODT = ODTState*20; % ODT power in Watts
57
58
59 %% Frequency noise generation
60 PPN = 0; % set to 1 for pump freq noise on
61 SPN = 0; % set to 1 for stokes freq noise on
62 GP = PPN*2*pi*1e1/pulse; % pump laser freq noise temporal correlation term
63 DP = PPN*2*pi*0.5e6/pulse/GP; % pump laser freq noise diffusion term
64 GS = SPN*2*pi*1e1/pulse; % stokes laser freq noise temporal correlation term
65 DS = SPN*2*pi*15e6/pulse/GS; % stokes laser freq noise diffusion term
66 delt = l*pulse/1e6; % temporal step size for generating freq noise.
67 time = 0:delt:l*pulse; % total time over which to generate the freq noise. ...
       This should be the same as the total integratigration time for the ode ...
       solver
68 epsP = zeros(1,length(time));
69 epsS = zeros(1,length(time));
70 % epsP(1) = sqrt(DP*GP)*randn;
71 % epsS(1) = sqrt(DS*GS)*randn;
72
73 % generate frequency noise for pump laser using the algorith provided in ...
       L. P. Yatsenko et al, PHYSICAL REVIEW A, VOLUME 65, 043409
74 if PPN == 1
75     epsP(1) = sqrt(-2*DP*GP*log(rand))*cos(2*pi*rand); %Taken from Fox et ...
           al, PRA, 38(11), 1988
76     for i = 2:length(time)
77     % epsP(i) = epsP(i-1)*exp(-GP*delt) + ...
           sqrt(DP*GP*(1-exp(-2*GP*delt)))*rand;
78     epsP(i) = epsP(i-1)*exp(-GP*delt) + ...
           sqrt(-2*DP*GP*(1-exp(-2*GP*delt))*log(rand))*cos(2*pi*rand);
```

```
79      end
80  else
81      epsP;
82  end
83
84  % generate frequency noise for stokes laser
85  if SPN == 1
86      epsS(1) = sqrt(-2*DS*GS*log(rand))*cos(2*pi*rand);
87      for i = 2:length(time)
88      % epsS(i) = epsS(i-1)*exp(-GS*delt) + ...
            sqrt(DS*GS*(1-exp(-2*GS*delt)))*randn;
89      epsS(i) = epsS(i-1)*exp(-GS*delt) + ...
            sqrt(-2*DS*GS*(1-exp(-2*GS*delt))*log(randn))*cos(2*pi*randn);
90      end
91  else
92      epsS;
93  end
94
95  epsP = real(epsP);
96  epsS = real(epsS);
97
98  %% Solving for the Time-Dependent Populations in Each State
99  % vopt = odeset('RelTol', 1e-8, 'MaxStep', l*pulse/100, 'AbsTol', 1e-6, ...
        'InitialStep', 1e-3, 'Stats', 'off');
100 vopt = odeset('RelTol', 1e-6, 'AbsTol', 1e-8, 'InitialStep', 1e-6, ...
        'MaxStep', l*pulse/10, 'Stats', 'on');
101 % vopt = odeset('Stats', 'on');
102 init = [1,0,0,0,0,0,0]; % Initial population distribution for Ra-226 ...
        STIRAP setup
103 % Solving the Differential Equation for the Time-Dependent State Vectors
104 tic
105 hamon = 1; % Turns the laser-dependent part of the hamiltonian On or Off
```

```
106 ev = @(t, psi) evolverad226_v3(psi, t, hamon, pulse, ompump, delayp, ...
        omstokes, delays, Δpump, detune, gamma, zeeman, B, pol, ODT, cwp, cws, ...
        delt, epsP, epsS);
107 [t,y] = ode23(ev, [1*pulse/100, 1*pulse], init, vopt);
108 Y = y.*conj(y); % This gives the population in each bare state
109 stirap_eff = Y(end,5)+Y(end,6)+Y(end,7); % STIRAP efficiency is defined as ...
        the total population in the final state, D-state, manifold
110 tot = sum(Y,2); % Total population in all the states. Unless spontaneous ...
        emission is turned on, this should be as close to 1 as possible. ...
        Otherwise, it suggests the ODE solver is introducing significant ...
        errors in the solutions.
111 toc
112
113 %% Solving for the eigenstates, eigenvalues of the STIRAP dressed-state ...
        hamiltonian
114 stokes = omegastokes(t, pulse, omstokes, cws, delays); % The stokes laser ...
        pulse
115 pump = omegapump(t, pulse, ompump, cwp, delayp); % The pump laser pulse
116 % [pumpom,stokesom] = CalcOm226(ompump,omstokes,pol);
117 % str1 = num2str(abs(pumpom*pulse),2);
118 % str2 = num2str(abs(stokesom*pulse),2);
119 str3 = num2str(stirap_eff,2);
120 disp(['stirap efficiency is ', str3])
121
122 %% generating frequency noise histogram gaussian fit
123 % pump laser
124 fP = linspace(min(epsP/1e6),max(epsP/1e6),10000);
125 mu = 0;
126 sigma1P = sqrt(DP*GP)/1e6;
127 % sigma2 = sigma1*(1-exp(-2*GP/1e6*delt));
128 prob1P = exp(-(fP-mu).^2./(2*sigma1P^2))./(sigma1P*sqrt(2*pi));
129 % prob2 = exp(-(f-mu).^2./(2*sigma2^2))./(sigma2*sqrt(2*pi));
130 % prob = prob1+prob2;
```

```
131
132 % stokes laser
133 fS = linspace(min(epsS/1e6),max(epsS/1e6),10000);
134 mu = 0;
135 sigma1S = sqrt(DS*GS)/1e6;
136 % sigma2 = sigma1*(1-exp(-2*GP/1e6*delt));
137 prob1S = exp(-(fS-mu).^2./(2*sigma1S^2))./(sigma1S*sqrt(2*pi));
138 % prob2 = exp(-(f-mu).^2./(2*sigma2^2))./(sigma2*sqrt(2*pi));
139 % prob = prob1+prob2;
140
141 %% Plotting the Simulation Results
142 % Plotting the STIRAP laser pulses and the individual bare atomic states ...
       as functions of time
143 figure(1)
144 subplot(2,1,1)
145 plot(t/1e-6,pump/ompump,t/1e-6,stokes/omstokes,'LineWidth',2)
146 title('STIRAP Pulse Sequence','FontSize',15)
147 text(1,0.8,'(a)','FontSize',15)
148 % text(11,0.5,['\Omega_{P}\tau = ', str1],'FontSize',15)
149 % text(6,0.5,['\Omega_{S}\tau = ', str2],'FontSize',15)
150 legend('Pump Pulse','Stokes Pulse')
151 ax = gca;
152 set(gcf,'Color','w')
153 ax.FontSize = 15;
154
155 subplot(2,1,2)
156 plot(t/1e-6,Y,'LineWidth',2)
157 text(l*pulse*1e6/20,0.6,['efficiency = ', str3],'FontSize',15)
158 text(l*pulse*1e6/20,0.4,['\sigma_P = 2\pi\times', ...
       num2str(sigma1P/(2*pi),2), 'MHz'],'FontSize',15)
159 text(l*pulse*1e6/20,0.2,['\sigma_S = 2\pi\times', ...
       num2str(sigma1S/(2*pi),2), 'MHz'],'FontSize',15)
160 % semilogy(t/1e-6,Y,'LineWidth',2)
```

```
161 title('Population Transfer with \Δ = 0','FontSize',15)
162 xlabel('Time (\mus)','FontSize',15)
163 text(1,0.8,'(b)','FontSize',15)
164 legend('bare ...
       state-1','state-2','state-3','state-4','state-5','state-6','state-7')
165 ax = gca;
166 set(gcf,'Color','w')
167 ax.FontSize = 15;
168
169 % figure(2)
170 % plot(t/1e-6,E,'LineWidth',2)
171 % xlabel('Time (\mus)','FontSize',15)
172 % title('Dressed-state Eigenvalues','FontSize',15)
173 % ax = gca;
174 % set(gcf,'Color','w')
175 % ax.FontSize = 15;
176
177 % Plotting the total probability of finding the atom in one of the 7 bare ...
       atomic states. This should be equal to or very close to 1. Any deviation
178 % indicates inaccuracies in the ODE solver.
179 figure(3)
180 plot(t/1e-6,tot,'LineWidth',2)
181 xlabel('Time (\mus)','FontSize',15)
182 ax = gca;
183 set(gcf,'Color','w')
184 ax.FontSize = 15;
185
186 % plotting the frequency noise
187 % pump laser
188 figure(4)
189 subplot(2,1,1)
190 plot(time/1e-6,epsP/1e6,'r-','LineWidth',2)
191 ylabel('Pump Frequency Noise (MHz)')
```

```
ax = gca;
set(gcf,'Color','w')
ax.FontSize = 15;
subplot(2,1,2)
histogram(epsP/1e6,'Normalization','pdf')
hold on
% plot(f,prob,'LineWidth',2)
plot(fP,prob1P,'LineWidth',2)
% plot(f,prob2,'LineWidth',2)
xlabel('Pump Laser Phase Noise (MHz)')
text(mu-2.8*sigma1P,0.9*max(prob1P),['\sigma = 2\pi\times', ...
    num2str(sigma1P/(2*pi),2), 'MHz'],'FontSize',15)
text(mu-2.8*sigma1P,0.7*max(prob1P),['G_P = ', num2str(GP,2), ...
    'MHz'],'FontSize',15)
text(mu-2.8*sigma1P,0.5*max(prob1P),['D_P = ', num2str(DP,2), ...
    'MHz'],'FontSize',15)

ax = gca;
set(gcf,'Color','w')
ax.FontSize = 15;
ax.XLim = ([mu-3*sigma1P, mu+3*sigma1P]);

% stokes laser
figure(5)
subplot(2,1,1)
plot(time/1e-6,epsS/1e6,'r-','LineWidth',2)
ylabel('Stokes Frequency Noise (MHz)')
ax = gca;
set(gcf,'Color','w')
ax.FontSize = 15;
subplot(2,1,2)
histogram(epsS/1e6,'Normalization','pdf')
hold on
```

```
% plot(f,prob,'LineWidth',2)
plot(fS,prob1S,'LineWidth',2)
% plot(f,prob2,'LineWidth',2)
xlabel('Stokes Laser Phase Noise (MHz)')
text(mu-2.5*sigma1S,0.9*max(prob1S),['\sigma = 2\pi\times', ...
    num2str(sigma1S/(2*pi),2), 'MHz'],'FontSize',15)
text(mu-2.8*sigma1S,0.7*max(prob1S),['G_S = ', num2str(GS,2), ...
    'MHz'],'FontSize',15)
text(mu-2.8*sigma1S,0.5*max(prob1S),['D_S = ', num2str(DS,2), ...
    'MHz'],'FontSize',15)
ax = gca;
set(gcf,'Color','w')
ax.FontSize = 15;
ax.XLim = ([mu-3*sigma1S, mu+3*sigma1S]);
```

The following is the MATLAB script 'evolverad226_v3' used for simulating the atom-light photon interaction.

```
%% This script includes STIRAP evolution in Ra-226 with laser frequency noise
function y = evolverad226_v3(psi, t, hamon, pulse, ompump, delayp, ...
    omstokes, delays, Δ, detune, gamma, zeeman, B, pol, ODT, cwp, cws, ...
    delt, epsP, epsS)
     y = 1i*hamrad226_v4(t, hamon, pulse, ompump, delayp, omstokes, delays, ...
         Δ, detune, gamma, zeeman, B, pol, ODT, cwp, cws, delt, epsP, ...
         epsS)*psi;
end
```

The Hamiltonian for the atom-light dynamics is generated by the following MATLAB script:

```
%%% This script calculates the hamiltonian for the bare-state evolution in
%%% Ra-226 and incorporates laser frequency noise

```

```
function h = hamrad226_v4(t, hamon, pulse, ompump, delayp, omstokes, ...
    delays, Δ, detune, gamma, zeeman, B, pol, ODT, cwp, cws, delt, epsP, epsS)
     stokes = omegastokes(t, pulse, omstokes, cws, delays); % this defines ...
        the time-dependent stokes pulse shape
     pump = omegapump(t, pulse, ompump, cwp, delayp); % pump pulse shape
     eps12 = epsP(int64(round(t/delt))); % this defines the freq noise on ...
        the pump laser pulse
     eps32 = epsS(int64(round(t/delt))); % stokes laser pulse freq noise
    %% The following chooses the appropriate transitions for the choices of ...
       STIRAP laser pulse polarizaions
    polp = pol(1); % Pump laser pulse polarization
    pols = pol(2); % Stokes laser pulse polarization
    if abs(polp) > 0
       c = 1; % Allows only Δ m = +/-1 pump transitions
    else
       c = 0; % Allows only Δ m = 0 pump transitions
    end
    if abs(pols) > 0
       d = 1; % Allows only Δ m = +/-1 stokes transitions
    else
       d = 0; % Allows only Δ m = 0 stokes transitions
    end
    %% Defining constants used in generating the dressed-state hamiltonian
    c0 = 299792458;
    au = 8.5e-30; % a.u. to SI unit conversion for electric dipole moment (C*m)
    e0 = 8.854187e-12;
    Int = 2*ODT/(pi*(100e-6)^2);
    E0 = sqrt(2*Int/(e0*c0));
    pau = 1.648e-41;
    h = 6.626e-34;
    hbar = h/(2*pi);
    muB = 9.3e-24;

```

```
33  %% Assigning the prefactors kij for i<-->j STIRAP pump or stokes ...
       transition dipole moments
34  redMEsp = 5.504*au; % reduced ME for transition dipole moment taken ...
       from Dzuba and Flambaum, J. Phys. B: At. Mol. Opt. Phys. 40 (2007) ...
       227?236
35  redMEdp = 0.437*au;
36
37  k12 = redMEsp*sqrt(1/3)*(1-polp)*c/2;
38  k13 = redMEsp*sqrt(1/3)*(1-abs(polp));
39  k14 = redMEsp*sqrt(1/3)*(1+polp)*c/2;
40  k25 = -0.5*redMEdp*sqrt(1/6)*(1-abs(pols));
41  k26 = 0.5*redMEdp*sqrt(1/6)*(1-pols)*d/2;
42  k27 = 0;
43  k35 = -0.5*redMEdp*sqrt(1/6)*(1+pols)*d/2;
44  k36 = 0*redMEdp*(1-abs(pols));
45  k37 = 0.5*redMEdp*sqrt(1/6)*(1-pols)*d/2;
46  k45 = 0;
47  k46 = -0.5*redMEdp*sqrt(1/6)*(1+pols)*d/2;
48  k47 = 0.5*redMEdp*sqrt(1/6)*(1-abs(pols));
49  %% Zeeman splitting for the magnetic sub-levels
50  zeemanshift = zeeman;
51  zeemanshift2 = zeeman;
52  %% Scalar Stark Shifts due to the ODT
53  as0s = 284;
54  ap0s=-204;
55  ap2t = -557;
56  ad0s = 262;
57  ad2t = -4;
58  as0 = as0s/sqrt(3);
59  ap0 = ap0s/3;
60  ap2 = -ap2t/(3*sqrt(5));
61  ad0 = ad0s/3;
62  ad2 = -ad2t/(3*sqrt(5));
```

```
63  %% Constructing the STIRAP dressed-state hamiltonian
64  % contributions from the pump and stokes pulses
65  y = zeros(7,7);
66  y(1,:) = ...
        [-(detune+zeemanshift-2*eps12)/2,pump*k12,pump*k13,pump*k14,0,0,0];
67  y(2,:) = ...
        [pump*k12,(Δ+zeemanshift2)+1i*gamma/2,0,0,stokes*k25,stokes*k26,stokes*k27];
68  y(3,:) = ...
        [pump*k13,0,(Δ+zeemanshift2)+1i*gamma/2,0,stokes*k35,stokes*k36,stokes*k37];
69  y(4,:) = ...
        [pump*k14,0,0,(Δ+zeemanshift2)+1i*gamma/2,stokes*k45,stokes*k46,stokes*k47];
70  y(5,:) = ...
        [0,stokes*k25,stokes*k35,stokes*k45,(detune-zeemanshift+2*eps32)/2,0,0];
71  y(6,:) = [0,stokes*k26,stokes*k36,stokes*k46,0,(detune+2*eps32)/2,0];
72  y(7,:) = ...
        [0,stokes*k27,stokes*k37,stokes*k47,0,0,(detune+zeemanshift+2*eps32)/2];
73  % contributions from the magnetic field B
74  Fx = zeros(7,7);
75  gj1p1 = 1;
76  gj3d1 = 0.5;
77  Jx0 = 0;
78  Jx1 = (1/sqrt(2))*[0,1,0;1,0,1;0,1,0];
79  Fx(1,1) = Jx0; %1S0
80  Fx(2:4,2:4) = (muB/hbar)*gj1p1*Jx1; %1P1
81  Fx(5:7,5:7) = (muB/hbar)*gj3d1*Jx1; %3D1
82  Jy1 = (1/sqrt(2))*[0,1i,0;-1i,0,1i;0,-1i,0];
83  Jsq1 = 2*eye(3);
84  % Contribution from the ODT laser
85  Stark = zeros(7,7);
86  Stark(1,1) = -((abs(E0))^2/(4*hbar))*pau*as0;
87  Stark(2:4,2:4) = ...
        -((abs(E0))^2/(4*hbar))*(ap0*eye(3)+ap2*0.5*(6*Jy1^2-2*Jsq1))*pau;
88  Stark(5:7,5:7) = ...
```

```
        -((abs(E0))^2/(4*hbar))*(ad0*eye(3)+ad2*0.5*(6*Jy1^2-2*Jsq1))*pau;
89      % The comined hamiltonian
90      h = hamon*y-B*Fx-Stark;
91  end
```

BIBLIOGRAPHY

BIBLIOGRAPHY

1. Dirac, P. A. M. The quantum theory of the electron. *Proc. R. Soc. Lond. A* **117,** 610–624 (1928).

2. Anderson, C. D. The Positive Electron. *Phys. Rev.* **43** (1933).

3. Komatsu, E. *et al.* Seven-year wilkinson microwave anisotropy probe (WMAP*) observations: Cosmological interpretation. *Astrophysical Journal, Supplement Series* **192** (2011).

4. Sakharov, A. D. Violation of *CP* invariance, *C* asymmetry, and baryon asymmetry of the universe. *Sov. Phys. Usp.* **34,** 392–393 (1991).

5. Huet, P. & Sather, E. Electroweak baryogenesis and standard model CP violation. *Phys. Rev. D* **51** (1995).

6. Lee, T. D. & Yang, C. N. Question of Parity Conservation in Weak Interactions. *Phys. Rev.* **104** (1956).

7. Wu, C. S., Ambler, E., Hayward, R. W., Hoppes, D. D. & Hudson, R. P. Experimental Test of Parity Conservation in Beta Decay. *Phys. Rev.* **105** (1957).

8. Landau, L. On the conservation laws for weak interactions. *Nuclear Physics* **3,** 127–131 (1957).

9. Gell-Mann, M. & Pais, A. Behavior of Neutral Particles under Charge Conjugation. *Nuclear Physics* **97** (1955).

10. Christenson, J. H., Cronin, J. W., Fitch, V. L. & Turlay, R. Evidence for the 2π Decay of the K_2^0 Meson. *Phys. Rev. Lett.* **13** (1964).

11. Lees, J. P. *et al.* Observation of Time-Reversal Violation in the B^0 Meson System. *Phys. Rev. Lett.* **109,** 211801 (2012).

12. Engel, J., Ramsey-Musolf, M. J. & van Kolck, U. Electric dipole moments of nucleons, nuclei, and atoms: The Standard Model and beyond. *Progress in Particle and Nuclear Physics* **71,** 21–74 (2013).

13. Hänsch, T. W. Nobel Lecture: Passion for precision. *Rev. Mod. Phys.* **78** (2006).

14. Bennett, G. W. *et al.* Improved limit on the muon electric dipole moment. *Phys. Rev. D* **80,** 052008. `https://link.aps.org/doi/10.1103/PhysRevD.80.052008` (5 Sept. 2009).

15. Inami, K. *et al.* Search for the electric dipole moment of the τ lepton. *Physics Letters B* **551,** 16–26 (2003).

16. Pondrom, L. *et al.* New limit on the electric dipole moment of the Λ hyperon. *Phys. Rev. D* **23,** 814–816. https://link.aps.org/doi/10.1103/PhysRevD.23.814 (3 Feb. 1981).

17. Purcell, E. M. & Ramsey, N. F. On the Possibility of Electric Dipole Moments for Elementary Particles and Nuclei. *Phys. Rev.* **78** (1950).

18. Smith, J. H., Purcell, E. M. & Ramsey, N. F. Experimental Limit to the Electric Dipole Moment of the Neutron. *Phys. Rev.* **108** (1957).

19. Abel, C. *et al.* Measurement of the Permanent Electric Dipole Moment of the Neutron. *Phys. Rev. Lett.* **124,** 081803. https://link.aps.org/doi/10.1103/PhysRevLett.124.081803 (8 Feb. 2020).

20. Hudson, J. J. *et al.* Improved measurement of the shape of the electron. *Nature* **473,** 493–496 (2011).

21. Andreev, V. *et al.* Improved limit on the electric dipole moment of the electron. *Nature* **562,** 355–360 (2018).

22. Cairncross, W. B. *et al.* Precision Measurement of the Electron's Electric Dipole Moment Using Trapped Molecular Ions. *Phys. Rev. Lett.* **119** (2017).

23. Chupp, T., Fierlinger, P., Ramsey-Musolf, M. & Singh, J. T. Electric dipole moments of atoms, molecules, nuclei, and particles. *Rev. Mod. Phys.* **91** (2019).

24. Graner, B., Chen, Y., Lindahl, E. & Heckel, B. Reduced Limit on the Permanent Electric Dipole Moment of ^{199}Hg. *Phys. Rev. Lett.* **116** (2016).

25. Peccei, R. D. & Quinn, H. R. CP conservation in the presence of pseudoparticles. *Phys. Rev. Lett.* **38,** 1440–1443 (1977).

26. Chupp, T. & Ramsey-Musolf, M. Electric dipole moments: A global analysis. *Phys. Rev. C* **91,** 035502. https://link.aps.org/doi/10.1103/PhysRevC.91.035502 (3 Mar. 2015).

27. Schiff, L. I. Measurability of Nulcear Electric Dipole Moments. *Phys. Rev.* **132** (1963).

28. Sandars, P. The electric dipole moment of an atom. *Physics Letters* **14,** 194–196. ISSN: 0031-9163. http://www.sciencedirect.com/science/article/pii/0031916365905834 (1965).

29. Salpeter, E. E. Some Atomic Effects of an Electronic Electric Dipole Moment. *Phys. Rev.* **112,** 1642–1648. https://link.aps.org/doi/10.1103/PhysRev.112.1642 (5 Dec. 1958).

30. Spevak, V., Auerbach, N. & Flambaum, V. V. Enhanced T-odd, P-odd electromagnetic moments in reflection asymmetric nuclei. *Phys. Rev. C* **56,** 1357–1369. https://link.aps.org/doi/10.1103/PhysRevC.56.1357 (3 Sept. 1997).

31. Flambaum, V. V. & Zelevinsky, V. G. Enhancement of nuclear Schiff moments and time-reversal violation in atoms due to soft nuclear octupole vibrations. *Phys. Rev. C* **68,** 035502. https://link.aps.org/doi/10.1103/PhysRevC.68.035502 (3 Sept. 2003).

32. Dobaczewski, J. & Engel, J. Nuclear Time-Reversal Violation and the Schiff Moment of ^{225}Ra. *Phys. Rev. Lett.* **94** (2005).

33. Moller, P., Nix, J., Myers, W. & Swiatecki, W. Nuclear Ground-State Masses and Deformations. *Atomic Data and Nuclear Data Tables* **59,** 185–381 (1995).

34. Helmer, R., Lee, M., Reich, C. & Ahmad, I. Intrinsic reflection asymmetry in ^{225}Ra: Additional information from a study of the α-decay scheme of ^{229}Th. *Nuc. Phys. A* **474,** 77–113 (1987).

35. Dzuba, V. A., Flambaum, V. V. & Porsev, S. G. Calculation of (P,T)-odd electric dipole moments for the diamagnetic atoms ^{129}Xe, ^{171}Yb, ^{199}Hg, ^{211}Rn, and ^{225}Ra. *Phys. Rev. A* **80,** 032120. https://link.aps.org/doi/10.1103/PhysRevA.80.032120 (3 Sept. 2009).

36. Singh, Y. & Sahoo, B. K. Rigorous limits on the hadronic and semileptonic *CP*-violating coupling constants from the electric dipole moment of ^{199}Hg. *Phys. Rev. A* **91,** 030501. https://link.aps.org/doi/10.1103/PhysRevA.91.030501 (3 Mar. 2015).

37. Yamanaka, N. *et al.* Probing exotic phenomena at the interface of nuclear and particle physics with the electric dipole moments of diamagnetic atoms: A unique window to hadronic and semi-leptonic CP violation. *Eur. Phys. J. A* **53** (2017).

38. Singh, Y. & Sahoo, B. K. Electric dipole moment of ^{225}Ra due to P- and T-violating weak interactions. *Phys. Rev. A* **92** (2015).

39. Prasannaa, V. S., Mitra, R. & Sahoo, B. K. Reappraisal of P, T-odd parameters from the improved calculation of electric dipole moment of ^{225}Ra atom. *J. Phys. B: At. Mol. Opt. Phys.* **53** (2020).

40. Fleig, T. $\mathcal{P},\mathcal{T}$-odd tensor-pseudotensor interactions in atomic ^{199}Hg and ^{225}Ra. *Phys. Rev. A* **99,** 012515. https://link.aps.org/doi/10.1103/PhysRevA.99.012515 (1 Jan. 2019).

41. Latha, K. V. P., Angom, D., Das, B. P. & Mukherjee, D. Probing CP Violation with the Electric Dipole Moment of Atomic Mercury. *Phys. Rev. Lett.* **103,** 083001. https://link.aps.org/doi/10.1103/PhysRevLett.103.083001 (8 Aug. 2009).

42. Latha, K. V. P. & Amjith, P. R. Electric dipole moments of atomic Xe, Ra, and Yb with core-polarization effects. *Phys. Rev. A* **87,** 022509. https://link.aps.org/doi/10.1103/PhysRevA.87.022509 (2 Feb. 2013).

43. Jackson, J. D. *Classical Electrodynamics* (John Wiley and Sons, Inc., 1962).

44. Foot, C. J. *Atomic Physics* (Oxford University Press, 2005).

45. Metcalf, H. J. & van der Straten, P. *Laser Cooling and Trapping* (Springer, 1999).

46. Phillips, W. D. & Metcalf, H. Laser Deceleration of an Atomic Beam. *Phys. Rev. Lett.* **48** (1982).

47. Phillips, W. D. Laser cooling and trapping of neutral atoms. *Rev. Mod. Phys.* **70** (1998).

48. Raab, E. L., Prentiss, M., Cable, A., Chu, S. & Pritchard, D. E. Trapping of Neutral Sodium Atoms with Radiation Pressure. *Phys. Rev. Lett.* **59** (1987).

49. Grimm, R., Weidemüller, M. & Ovchinnikov, Y. B. *Optical dipole traps for neutral atoms* 1999. arXiv: physics/9902072 [physics.atom-ph].

50. Guest, J. R. *et al.* Laser Trapping of ^{225}Ra and ^{226}Ra with Repumping by Room-Temperature Blackbody Radiation. *Phys. Rev. Lett.* **98** (2007).

51. Lasertechnik, S. *Datasheet Matisse 2 TS* http://www.sirah.com/wp-content/uploads/pdfs/Matisse-2-TS.pdf (2020).

52. Gibson, B. M. & McCall, B. J. Tilt-tuned etalon locking for tunable laser stabilization. *Opt. Lett.* **40,** 2696–2698. http://ol.osa.org/abstract.cfm?URI=ol-40-12-2696 (June 2015).

53. Allard, F., Maksimovic, I., Abgrall, M. & Laurent, P. Automatic system to control the operation of an extended cavity diode laser. *Rev. of Sci. Inst.* **75,** 54–58 (2004).

54. Black, E. An introduction to Pound–Drever–Hall laser frequency stabilization. *Am. J. Phys.* **69,** 490–505 (2001).

55. Drever, R. W. P. *et al.* Laser phase and frequency stabilization using an optical resonator. *Appl. Phys. B* **31,** 97–105 (1983).

56. Bondu, F., Fritschel, P., Man, C. N. & Brillet, A. Ultrahigh-spectral-purity laser for the VIRGO experiment. *Opt. Lett.* **21,** 582–584 (1997).

57. Conti, L., Rosa, M. D. & Marin, F. High-spectral-purity laser system for the AURIGA detector optical readout. *J. Opt. Soc. Am. B* **20,** 462–468 (2003).

58. Ye, J. & Hall, J. L. Optical phase locking in the microradian domain: potential applications to NASA spaceborne optical measurements. *Opt. Lett.* **24,** 1838–1840 (1999).

59. Thorpe, J. I., Numata, K. & Livas, J. Laser frequency stabilization and control through offset sideband locking to optical cavities. *Opt. Express* **16,** 15980–15990 (2008).

60. Bai, J., Wang, J., He1, J. & Wang, J. Electronic sideband locking of a broadly tunable 318.6 nm ultraviolet laser to an ultra-stable optical cavity. *J. Opt.* **19** (2017).

61. Li, L., Liu, F., Wang, C. & Chen, L. Measurement and control of residual amplitude modulation in optical phase modulation. *Rev. Sci. Instrum.* **83** (2012).

62. Zhang, W. *et al.* Reduction of residual amplitude modulation to 1×10^{-6} for frequency modulation and laser stabilization. *Opt. Lett.* **39,** 1980–1983 (2014).

63. Bishof, M. *et al.* Improved limit on the ^{225}R electric dipole moment. *Phys. Rev. C* **94** (2016).

64. Wendt, K. *et al.* On the hyperfine structure and isotope shift of radium. *Z. Phys. D: At., Mol. Clusters* **4** (1987).

65. Kalita, M. R. *Search for a Permanent Electric Dipole Moment of Ra-225* PhD thesis (University of Kentucky, 2015).

66. Parker, R. *First EDM Measurement of Radium* PhD thesis (University of Chicago, 2015).

67. Parker, R. H. *et al.* First Measurement of the Atomic Electric Dipole Moment of ^{225}Ra. *Phys. Rev. Lett.* **114** (2015).

68. Dzuba, V. A. & Flambaum, V. V. Calculation of energy levels and transition amplitudes for barium and radium. *J. Phys. B: At. Mol. Opt. Phys.* **40** (2007).

69. Parker, R. H. *et al.* Efficient, tightly-confined trapping of ^{226}Ra. *Phys. Rev. C* **86** (2012).

70. Ockeloen, C. F., Tauschinsky, A. F., Spreeuw, R. J. C. & Whitlock, S. Detection of small atom numbers through image processing. *Phys. Rev. A* **82** (2010).

71. Gaubatz, U., Rudecki, P., Schiemann, S. & Bergmann, K. Population transfer between molecular vibrational levels by stimulated Raman scattering with partially overlapping laser fields. A new concept and experimental results. *J. Chem. Phys.* **92** (1990).

72. Pillet, P., Valentin, C., Yuan, R. L. & Yu, J. Adiabatic population transfer in a multilevel system. *Phys. Rev. A* **48,** 845 (1990).

73. Goldner, L. S. *et al.* Coherent transfer of photon momentum by adiabatic following in a dark state. *Quantum Opt.* **6,** 387 (1994).

74. Weitz, M., Young, B. C. & Chu, S. Atom manipulation based on delayed laser pulses in three- and four-level systems: Light shifts and transfer efficiencies. *Phys. Rev. A* **50,** 2438 (1994).

75. Kulin, S. *et al.* Coherent Manipulations of Atomic Wave Packets by Adiabatic Transfer. *Phys. Rev. Lett.* **78,** 4185 (1997).

76. Esslinger, T., Sander, F., Weidemüller, M., Hemmerich, A. & Hänsch, T. W. Subrecoil Laser Cooling with Adiabatic Transfer. *Phys. Rev. Lett.* **76,** 2432 (1996).

77. Martin, J., Shore, B. W. & Bergmann, K. Coherent population transfer in multilevel systems with magnetic sublevels. III. Experimental results. *Phys. Rev. A* **54,** 1556 (1996).

78. Sørensen, J. L. *et al.* Efficient coherent internal state transfer in trapped ions using stimulated Raman adiabatic passage. *New J. Phys.* **8,** 261 (2006).

79. Gebert, F. *et al.* Precision Isotope Shift Measurements in Calcium Ions Using Quantum Logic Detection Schemes. *Phys. Rev. Lett.* **115,** 053003 (2015).

80. Javanainen, J. & Mackie, M. Coherent photoassociation of a Bose-Einstein condensate. *Phys. Rev. A* **59** (1999).

81. Vardi, A., Shapiro, M. & Bergmann, K. Complete population transfer to and from a continuum and the radiative association of cold Na atoms to produce translationally cold Na2 molecules in specific vib-rotational states. *Opt. Express* **4,** 91–106 (1999).

82. Drummond, P. D., Kheruntsyan, K. V., Heinzen, D. J. & Wynar, R. H. Stimulated Raman adiabatic passage from an atomic to a molecular Bose-Einstein condensate. *Phys. Rev. A* **65** (2002).

83. Steck, D. A. *Quantum and Atom Optics* 2017. `http://steck.us/teaching`.

84. Ehrenfest, P. Bemerkung über die angenäherte Gültigkeit der klassischen Mechanik innerhalb der Quantenmechanik. *Z. Physik* **45,** 455–457 (1927).

85. Kuklinski, J. R., Gaubatz, U., Hioe, F. T. & Bergmann, K. Adiabatic population transfer in a three-level system driven by delayed laser pulses. *Phys. Rev. A* **40,** 6741(R) (1989).

86. Kuhn, A. *et al.* Population transfer by stimulated Raman scattering with delayed pulses using spectrally broad light. *J. Chem. Phys.* **96,** 4215–4223 (1992).

87. Uhlenbeck, G. E. & Ornstein, L. S. On the Theory of the Brownian Motion. *Phys. Rev.* **36** (1930).

88. Fox, F., Gatland, I. R., Roy, R. & Vemuri, G. Fast, accurate algorithm for numerical simulation of exponentially correlated colored noise. *Phys. Rev. A* **38,** 5938–5940 (1988).

89. Dammalapatia, U., Jungmann, K. & Willmann, L. Compilation of Spectroscopic Data of Radium (Ra I and Ra II). *J. Phys. Chem. Ref. Data* **45** (2016).

90. Booth, D. *et al.* Spectroscopic Study and Lifetime Measurement of the $6d7p\ ^3F_2^o$ state of radium. *Spectrochimica Acta Part B* **172** (2020).

91. Auerbach, N., Flambaum, V. & Spevak, V. Collective T- and P-Odd Electromagnetic Moments in Nuclei with Octupole Deformations. *Phys. Rev. Lett.* **76** (1996).

92. Dzuba, V., Flambaum, V., Ginges, J. & Kozlov, M. Electric dipole moments of Hg, Xe, Rn, Ra, Pu, and TlF induced by the nuclear Schiff moment and limits of time-reversal violating interactions. *Phys. Rev. A* **66** (2002).

93. Hibbert, A. Developments in atomic structure calculations. *Rep. Prog. Phys.* **38** (1975).

94. Hibbert, A. Recent Advances in the Calculation of Oscillator Strengths. *Phys. Scr.* **16** (1977).

95. Huber, M. C. E. & Sanderman, R. J. The measurement of oscillator strengths. *Prog. Phys.* **49** (1986).

96. Rasmussen, E. Das Bogenspektrum des Radiums. *Z. Phys.* **86** (1934).

97. Trimble, W. L. *et al.* Lifetime of the $7s6d\ ^1D_2$ atomic state of radium. *Phys. Rev. A* **80** (2009).

98. Bieroń, J., Fischer, C. F., Fritzsche, S. & Pachucki, K. Lifetime and hyperfine structure of the $^3D_2$ state of radium. *J. Phys. B: At. Mol. Opt. Phys.* **37** (2004).

99. Ross, S. in. 8th ed., 143–155 (Pearson Prentice Hall, 2010).

100. Thorne, A., U.Litezen & Johansson, S. *Spectrophysics Principles and Applications* (Springer-Verlag, Berlin, 1999).

101. Tojo, S., Fujimoto, T. & Hasuo, M. Precision measurement of the oscillator strength of the cesium $6\,^2S_1 \rightarrow 5\,^2D_{5/2}$ electric quadrupole transition in propagating and evanescent wave fields. *Phys. Rev. A* **71** (2004).

102. Axner, O., Gustafsson, J., Omenetto, N. & Winefordner, J. D. Line strengths, A-factors and absorption cross-sections for fine structure lines in multiplets and hyperfine structure components in lines in atomic spectrometry - a user's guide. *Spectrochimica Acta Part B* **59** (2004).

103. Potterveld, D. H. *et al. Characterizing the Optical Trapping of Rare Isotopes by Monte Carlo Simulation* 2019. eprint: `arXiv:1903.07798`.

104. Fischer, A. & Hertel, I. Alignment and orientation of the hyperfine levels of a laser excited Na-atom beam. *Z. Phys. A-Atoms and Nuclei* **304** (1982).

105. Feldman, G. J. & Cousins, R. D. Unified approach to the classical statistical analysis of small signals. *Phys. Rev. D* **57** (1998).